

Spring 2015

Development of Superconducting Spoke Cavities for High-Velocity Applications

Christopher Shawn Hopper
Old Dominion University

Follow this and additional works at: https://digitalcommons.odu.edu/physics_etds



Part of the [Electrical and Electronics Commons](#), and the [Physics Commons](#)

Recommended Citation

Hopper, Christopher S.. "Development of Superconducting Spoke Cavities for High-Velocity Applications" (2015). Doctor of Philosophy (PhD), dissertation, Physics, Old Dominion University, DOI: 10.25777/ydbm-9d84
https://digitalcommons.odu.edu/physics_etds/62

This Dissertation is brought to you for free and open access by the Physics at ODU Digital Commons. It has been accepted for inclusion in Physics Theses & Dissertations by an authorized administrator of ODU Digital Commons. For more information, please contact digitalcommons@odu.edu.

**DEVELOPMENT OF SUPERCONDUCTING SPOKE
CAVITIES FOR HIGH-VELOCITY APPLICATIONS**

by

Christopher Shawn Hopper
BS, Saginaw Valley State University, 2005
MS, Central Michigan University, 2008

A Dissertation Submitted to the Faculty of
Old Dominion University in Partial Fulfillment of the
Requirements for the Degree of

DOCTOR OF PHILOSOPHY

PHYSICS


OLD DOMINION UNIVERSITY


May 2015

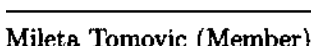
Approved by:


Jean-R. Delayen (Director)


Jozef Dudek (Member)


Alexander Godunov (Member)


Geoffrey Krafft (Member)


Mileta Tomovic (Member)

ABSTRACT

DEVELOPMENT OF SUPERCONDUCTING SPOKE CAVITIES FOR HIGH-VELOCITY APPLICATIONS

Christopher Shawn Hopper
Old Dominion University, 2015
Director: Dr. Jean R. Delayen

To date, superconducting spoke cavities have been designed, developed, and tested for particle velocities up to $\beta_0 \sim 0.6$, but there is a growing interest in possible applications of spoke cavities for high-velocity applications. The first task is to explore the design parameter space for low-frequency, high-velocity, single- and double-spoke superconducting cavities in order to determine how each design parameter affects the electromagnetic properties, in particular the surface electromagnetic fields and the shunt impedance. Once an electromagnetically optimized, high-velocity spoke cavity is designed, there are several other characteristics that need to be investigated. These include multipacting scenarios, higher-order mode excitation and suppression, multipole analysis of the accelerating field, and mechanical properties. Finally, the cavity fabrication and testing is performed and evaluated. In this dissertation, we present a detailed account of the full development process for the first high-velocity single-spoke cavity operating at 325 MHz and double-spoke cavity operating at 500 MHz.

Copyright, 2015, by Christopher Shawn Hopper, All Rights Reserved.

ACKNOWLEDGEMENTS

I would first like to thank my advisor Professor Jean Delayen for providing me with the opportunity and resources to complete this work. Without his guidance and support, this project would not have been possible. I also thank Professors Geoff Krafft, Jozef Dudek, Alex Godunov, and Mileta Tomovic for being on my committee. In addition, they provided formal instruction in electrodynamics, quantum mechanics, and computational physics, for which I am most grateful.

My colleagues here at ODU deserve a great deal of thanks as well. Subashini De Silva, Alejandro Castilla, Kevin Mitchel, Rocio Olave, and HyeKyoung Park have taught me so much throughout this process. Suba, in particular, has been my mentor from the very beginning.

Many people at Jefferson Lab have been invaluable to this project. While there are too many to name individually, I would be remiss not to mention Tom Powers, Kirk Davis, Danny Forehand, Steve Castagnola, Chris Dreyfuss, Roland Overton, Chris Tennant, and Bill Clemens. From fabrication to cleaning to calibration, I gained so much practical knowledge from these individuals and their teams that I can hardly begin to thank them enough.

Finally, I would like to express my deepest thanks to my parents, Mary Ann and Bill, my siblings, Traci and Richard, and my partner, Jenni. They have stood by and supported me throughout this process.

TABLE OF CONTENTS

	Page
LIST OF TABLES	ix
LIST OF FIGURES	xvi
 Chapter	
1. INTRODUCTION	1
1.1 HISTORICAL OVERVIEW	1
1.2 FEATURES OF THE SPOKE CAVITY	2
1.3 APPLICATIONS FOR HIGH-VELOCITY SPOKE CAVITIES	4
2. SUPERCONDUCTING RADIO FREQUENCY CAVITIES	8
2.1 SUPERCONDUCTIVITY	8
2.2 EARLY CAVITY DEVELOPMENT	15
2.3 THE PILLBOX CAVITY	16
2.4 TEM-CLASS CAVITIES	21
2.5 FIGURES OF MERIT	22
2.6 CAVITY PERFORMANCE LIMITATIONS	25
3. CAVITY FUNDAMENTALS	31
3.1 CAVITY MODES	31
3.2 MULTIPACTING	32
3.3 HIGHER ORDER MODES	35
3.4 BEAM INTERACTION WITH HIGHER ORDER MODES	38
3.5 WAKE FIELDS	43
3.6 BEAM INSTABILITIES DUE TO HIGHER-ORDER MODE EXCITATION	45
3.7 MULTIPOLE COMPONENTS OF THE ACCELERATING FIELD ..	48
3.8 MECHANICAL PROPERTIES	51
4. ELECTROMAGNETIC OPTIMIZATION	55
4.1 DESIGN GOALS	55
4.2 DESIGN STRATEGY	57
4.3 DEPENDENCE OF RF PROPERTIES ON GEOMETRIC PARAMETERS	58
4.4 COUPLER PLACEMENT	72
4.5 RESULTS	79

5. MULTIPACTING ANALYSIS.....	87
5.1 SIMULATION PARAMETERS	87
5.2 EMITTING SITES AND RESONANT LOCATIONS.....	88
5.3 IMPACT ENERGIES	91
5.4 COUPLERS	94
5.5 MULTIPACTING REDUCTION	96
6. HIGHER ORDER MODE ANALYSIS	101
6.1 IDENTIFICATION OF MODE TYPES	101
6.2 GEOMETRIC SHUNT IMPEDANCE (R/Q)	104
6.3 VELOCITY DEPENDENCE	106
6.4 BEAM LOADING	111
6.5 REGENERATIVE BEAM BREAKUP	114
6.6 HIGHER ORDER MODE COUPLERS	117
6.7 HIGHER ORDER MODE DAMPING.....	120
7. MECHANICAL ANALYSIS.....	124
7.1 PRESSURE SENSITIVITY.....	125
7.2 MECHANICAL MODES	129
8. MULTIPOLE ANALYSIS.....	131
8.1 500 MHZ DOUBLE-SPOKE CAVITY.....	132
8.2 325 MHZ SINGLE-SPOKE CAVITY.....	137
9. FABRICATION.....	140
9.1 SPOKE FORMING	140
9.2 OUTER CONDUCTOR.....	142
9.3 TRIM-TUNING AND THE BEAD-PULL	143
9.4 FINAL ROOM TEMPERATURE CAVITY	149
10. CAVITY PROCESSING	151
10.1 BULK CHEMICAL ETCHING	151
10.2 HEAT TREATMENT.....	153
10.3 LIGHT CHEMICAL ETCHING	156
10.4 HIGH PRESSURE RINSING	158
10.5 LOW TEMPERATURE HEATING	159
11. CRYOGENIC TESTING RESULTS.....	162
11.1 VERTICAL TEST AREA AT JEFFERSON LAB	162
11.2 CALIBRATION OF INPUT AND PICKUP PROBES.....	164
11.3 GRADIENT MEASUREMENTS	165
11.4 SURFACE RESISTANCE MEASUREMENTS	178
11.5 PRESSURE SENSITIVITY.....	180
12. CONCLUSION	182

BIBLIOGRAPHY 197

APPENDIX 198

VITA..... 203

LIST OF TABLES

Table	Page
1. 500 MHz, $\beta_0 = 1$ Port Losses	79
2. Cavity Parameters, 352 MHz, $\beta_0 = 0.82$ and $\beta_0 = 1$	81
3. RF Properties, 352 MHz, $\beta_0 = 0.82$ and $\beta_0 = 1$	82
4. Cavity Parameters, 325 MHz, $\beta_0 = 0.82$ and $\beta_0 = 1$	82
5. RF Properties, 325 MHz, $\beta_0 = 0.82$ and $\beta_0 = 1$	82
6. RF Properties, 352 MHz, $\beta_0 = 0.82$ and $\beta_0 = 1$ cavities optimized for higher shunt impedance	84
7. RF Properties, 325 MHz, $\beta_0 = 0.82$ and $\beta_0 = 1$ cavities optimized for higher shunt impedance	84
8. Cavity Parameters, 325 MHz, $\beta_0 = 0.82$ and 500 MHz, $\beta_0 = 1$	85
9. RF Properties, 325 MHz, $\beta_0 = 0.82$ and 500 MHz, $\beta_0 = 1$	86
10. Multipacting Simulation Parameters	88
11. Location of Multipactors for Various Electric Field Gradients	91
12. Electric field gradient range for multipactors of order 1-4	93
13. Cut-off frequencies of the single-spoke and double-spoke cavities	104
14. Deflection Angle of Degenerate Deflecting Mode Pairs	111
15. Beam Parameters: ODU Inverse Compton Source	111
16. Specifications of the required proton beam for C-ADS	114
17. Pressure Sensitivity by area	128
18. Pressure sensitivity by number of end cap ribs	129
19. Components of the Transverse Deflecting Voltage	132
20. Normal Multipole Coefficients of the 500 MHz Double-Spoke Cavity with a Racetrack Aperture	136

21.	Multipole Components, 500 MHz, $\beta_0 = 1$	137
22.	CMM measurements of spoke assembly.....	142
23.	325 MHz Single-Spoke Cavity Field Flatness.....	146
24.	Simulated and Measured Geometric Shunt Impedance.....	148
25.	Frequency Changes by Process.....	150
26.	500 MHz Chemical Etching	152
27.	Calibrated and measured pickup probe Q_{ext}	166
28.	HOM Properties: 500 MHz, $\beta_0 = 1$ Double-Spoke Cavity	198
29.	HOM Properties: 325 MHz, $\beta_0 = 0.82$ Single-Spoke Cavity	202

LIST OF FIGURES

Figure	Page
1. 325 MHz, $\beta_0 = 1$ double-spoke cavity.	2
2. Layout of an Inverse Compton Source	6
3. Longitudinal space occupied by spoke and elliptical cavities.....	7
4. Temperature dependence of the critical field.	9
5. Phase boundaries for Type-II superconductors.	12
6. Geometry of a pillbox cavity.....	16
7. Pillbox TM_{010} mode electric and magnetic fields.....	19
8. Electric field of the 0 mode and π mode of a 2 cell elliptical cavity.	20
9. Frequency relation for 7 coupled oscillators.	21
10. Electric and magnetic field of the fundamental TEM mode in a half-wave resonator.	22
11. Electric field of the fundamental TEM mode in a half-wave resonator with beam pipes and drift tube.	23
12. SRF cavity limitations	26
13. Energy diagram of a metal-vacuum interface.	28
14. Secondary electron yield curve parameters.....	33
15. A point charge trailing another.	44
16. Examples of common multipole field patterns.	51
17. Effect of the Lorentz force on the cell shape of an elliptical cavity.....	54
18. Frequency convergence in CST [®]	55
19. Geometric parameters of the spoke.	58
20. Dependence of the normalized magnetic field on the spoke base length. ..	59
21. Cut-away view of a two-spoke 500 MHz, $\beta_0 = 1$ cavity.....	60

22.	Dependence of normalized fields on spoke base length.	61
23.	Dependence of the geometric shunt impedance on spoke base length.	61
24.	Dependence of the energy content on the spoke base length.	62
25.	Dependence of normalized fields for transverse spoke base length (single-spoke).	62
26.	Dependence of normalized field on spoke base width.	63
27.	Dependence of geometric shunt impedance on spoke base width.	63
28.	Dependence of normalized field on base width (single-spoke).	64
29.	Dependence of geometric shunt impedance on base width (single-spoke).	64
30.	Dependence of the normalized electric and magnetic fields, shunt impedance, and energy content on the aperture length.	65
31.	Dependence of the normalized electric and magnetic fields, shunt impedance, and energy content on the aperture width.	67
32.	Dependence of the normalized electric and magnetic fields on the aperture height.	68
33.	End view of a single spoke showing the spoke angle ϕ	69
34.	On-axis electric field profiles for different spoke angle ϕ	69
35.	Dependence of the normalized magnetic field and RR_s on the parameter h_{out}	70
36.	Dependence of magnetic field and RR_s on the parameter H	71
37.	Dependence of electric field and RR_s on the parameter H	71
38.	Dependence of electric field and RR_s on the parameter h_{in}	72
39.	Edges for rounding at the outer conductor and spoke base.	72
40.	Dependence of B_p/E_{acc} on the outer conductor edge rounding.	73
41.	Dependence of B_p/E_{acc} on the spoke base rounding radius.	73
42.	Locations for coupler ports.	76

43. Standard coaxial and hook used for power coupling.	77
44. RF power per cavity from various frequency shifts.	78
45. CST MWS [®] depiction of the surface magnetic and electric fields.	80
46. Dependence of RR_s on the ratio of cavity surface area to volume.	83
47. Secondary emission yield of niobium for various surface treatments.	87
48. 500 MHz double-spoke cavity divisions for multipacting simulations.	88
49. Emitting and resonant location of the double-spoke cavity.	89
50. Emitting and resonant location of the single-spoke cavity.	90
51. Field gradient for at which multipacting takes place.	91
52. Two-point resonant electron trajectory in the end cap of the cavity.	92
53. Dependence of resonant electron energy on electric field gradient.	92
54. Single-spoke cavity enhancement counter.	94
55. Double-spoke cavity enhancement counter.	95
56. Secondary emission yield of copper.	96
57. Electric field and multipacting in the fundamental power coupler.	98
58. Electric field and multipacting in the higher order mode coupler.	99
59. Dependence of resonant electron energy on electric field gradient.	100
60. Influence of rounding radii on multipacting.	100
61. On-axis field profiles for the first three accelerating modes of the 500 MHz, $\beta_0 = 1$ double-spoke cavity.	102
62. On-axis field profiles for TE-type, hybrid modes, and a pair of degenerate deflecting modes of the 500 MHz, $\beta_0 = 1$ double-spoke cavity.	103
63. On-axis field profiles for the fundamental mode and the first deflecting mode of the 325 MHz, $\beta_0 = 0.82$ single-spoke cavity.	104
64. Geometric shunt impedance vs. frequency for the single- and double-spoke cavities.	106

65. Velocity acceptance of a single- and double-spoke cavities compared to a 5-cell elliptical cavity.	107
66. Dependence of geometric shunt impedance on particle velocity.	108
67. Velocity dependence of selected accelerating and deflecting modes.	109
68. Direction specific velocity dependence of $(R/Q)_{x,y}$	110
69. Loss factor of accelerating modes and deflecting modes for the 500 MHz double-spoke cavity.	112
70. Loss factor of accelerating modes and deflecting modes for the 325 MHz single-spoke cavity.	113
71. Loss factor of all accelerating modes, only high (R/Q) modes, the contribution from the fundamental mode and that of all other accelerating modes considered.	114
72. Accumulated induced voltage due to HOM excitation.	115
73. Integrated wall dissipation due to HOM excitation.	115
74. Deflecting mode impedance for various I_{th}	117
75. Threshold current for all higher order deflecting modes at various levels of damping.	118
76. Transmission curve of a notch filter.	119
77. Circuit diagram and schematic of the notch filter.	120
78. Accelerating and deflecting modes damped by the FPC alone.	121
79. Surface electric field of two pairs of deflecting modes.	122
80. Damping by the FPC and HOM coupler.	123
81. Stress/strain curve for a typical metal.	124
82. von-Mises stress under 1 and 1.4 atm vacuum load.	126
83. von-Mises stress on the single-spoke cavity with the external support structure.	127
84. von-Mises stress of the double-spoke cavity.	127
85. 3 mm cavity with 4 mm thick spokes and end cap stiffening ribs.	128

86.	Change in frequency by number of end cap stiffening ribs.	129
87.	Double-spoke cavity deformation due to mechanical modes.	130
88.	Transverse cross-section of the mesh used for multipole analysis.	131
89.	Components of the transverse fields as a function of z	133
90.	Dependance of normalized transverse voltage on offset position from the beam symmetry axis.	134
91.	Quadrupole component of the 500 MHz double-spoke cavity.	134
92.	$E_z^{(4)}$ and $E_z^{(6)}$ components of the 500 MHz double-spoke cavity fundamen- tal accelerating mode.	135
93.	Various spoke aperture geometries studied.	136
94.	Dependence of transverse voltage on transverse offset.	136
95.	$E_z^{(2)}$ and $E_z^{(4)}$ for various aperture geometries.	137
96.	Components of the transverse fields as a function of distance from the beam axis for the single-spoke cavity.	138
97.	Dependance of normalized transverse voltage on offset position from the beam symmetry axis.	139
98.	Time independent multipole field components.	139
99.	Engineering drawing, welded parts, and assembled spoke for the 325 MHz single-spoke cavity.	141
100.	Spoke die in the press and the fully formed and welded spoke.	142
101.	Welded spoke and CMM results showing deviations from the model.	143
102.	325 MHz outer conductor parts.	144
103.	Frequency changes due to trimming the outer conductor of the 325 MHz single-spoke cavity.	145
104.	Simulated and measured field profile of the single-spoke cavity.	145
105.	325 MHz single-spoke end cap deformation.	146
106.	Trim tuning of the 500 MHz double-spoke cavity.	147

107. Simulated and measured field flatness from trimming the double-spoke cavity outer conductor.	147
108. Fabricated 325 MHz single-spoke and 500 MHz double-spoke cavities.	149
109. Bulk BCP removal amounts at the measured locations on the 500 MHz double-spoke cavity.	153
110. Bake process for the single-spoke resonator.	155
111. RGA data collected during the baking process.	155
112. RGA Spectrum at the beginning and end of the two bakes.	156
113. RGA data for 10 hour 600 °C bake.	157
114. Schematic view of the Jefferson Lab high pressure rinsing cabinet.	159
115. Acid residue still present in the 325 MHz single-spoke cavity.	160
116. Schematic of the HPR nozzle in the single-spoke cavity.	160
117. Gas pressure and temperature during the first and second 120 °C bake of the 325 MHz single-spoke cavity.	161
118. Schematic of cavity in vertical test cryostat.	163
119. SEL block diagram.	164
120. Various coupling schemes.	167
121. Reflected power for critically, over, and under coupled.	168
122. 325 MHz single-spoke cavity initial test results.	170
123. Schematic diagram of the setup used for helium processing.	171
124. Test results before and after helium processing.	172
125. Single-spoke cavity test results after the second light etching.	173
126. Magnetic field in the region of the dewar where the cavity sits.	174
127. Comparison of 2 K tests before and after helium processing.	175
128. Initial 500 MHz double-spoke cavity gradient measurements.	176

129. Typical transmitted power during a multipacting event compared to an actual quench.	177
130. Double-spoke cavity gradient measurements at 4.2 and 2 K.	178
131. Surface resistance measurements and fitting.	179
132. Pressure sensitivity measurements.	180
133. Cell-to-cell coupling for an optimized double-spoke cavity.	183
134. Field profiles for non-uniform cell lengths.	184

CHAPTER 1

INTRODUCTION

1.1 HISTORICAL OVERVIEW

One of the first application of superconducting radio frequency (SRF) technology to particle accelerators was for a proton accelerator [1] and, until the late 1980s, superconducting accelerating cavities were separated into two distinct velocity classes. The low-velocity structures, designed for the acceleration of protons and heavy ions, extended to the $\beta_0 = v_0/c \sim 0.2$ regime, where v_0 is the particle velocity and c is the speed of light. They were usually based on resonant transmission lines and are often referred to as TEM structures. This is because the operating mode is a transverse electric and magnetic mode with respect to the inner conductor(s). Among them are the quarter-wave resonator [2], the coaxial half-wave resonator [3, 4], and the spoke resonator [3–6]. The high-velocity cavities were used almost exclusively for the acceleration of electrons or positrons and were restricted to $\beta_0 \sim 1$. These structures were made of a series of coupled cells operating in the TM_{010} mode and are therefore referred to as TM structures.

Since the late 1980s there has been a growing interest in higher velocity protons and ions [3, 5], and TEM structures have been designed for higher and higher velocities [7], while TM structures have been designed for lower and lower velocities, until the two have overlapped in what is referred to as the medium-velocity region corresponding to $\beta_0 \sim 0.5-0.6$ [8, 9].

The majority of superconducting accelerating structures in use or under development, and included in the medium- β_0 regime, fall under these two broad categories. Accelerating charged particles from $\beta_0 \sim 0.6$ to $\beta_0 = 1$ is typically accomplished using TM cavities. The TM cavities used in the medium-velocity region are essentially similar to the ones in this high-velocity region, but compressed in the longitudinal direction. For low-frequency, low-velocity applications, TM cavities are large and potentially mechanically unstable, but for high-velocity applications, they remain dominant in operational accelerators. The reasons for this include the geometrical

simplicity (which has led to good design, modeling, and simulation tools), extensive knowledge base (both in research institutions and industry), and low surface fields at high- β_0 [10]. While basic TEM-type cavities, i.e. those with cylindrical loading elements, may also be easy to design, model, and fabricate, the improved mechanical properties (e.g. low microphonics and minimal sensitivity to He pressure) are only accomplished with more advanced engineering and fabrication techniques [11, 12].

Spoke and other low-frequency, low-velocity cavities were primarily intended for 4.2 K operation, however recent developments in fabrication and processing techniques [7, 13, 14] have produced results which indicate that 2 K operation may be more economical for large machines, even taking into account the differences in refrigerator efficiency [9]. For smaller machines, on the other hand, 2 K operation may not be practical, in which case, spoke cavities offer a viable 4.2 K option [15]. The concept for a $\beta_0 = 1$ double-spoke cavity is shown in Fig. 1.



FIG. 1: 325 MHz, $\beta_0 = 1$ double-spoke cavity.

1.2 FEATURES OF THE SPOKE CAVITY

A single spoke cavity is a variation of the coaxial half-wave geometry; in its fundamental mode of operation, the spoke sustains a TEM mode where the length of the spoke is approximately half of the rf wavelength. The loading elements of multi-spoke cavities, operate out of phase with their nearest neighbor by π and, for improved mode separation and lower surface fields, are usually oriented perpendicularly to each other.

Here we summarize the features of spoke cavities which make them particularly attractive in the low- to mid-velocity regime. These features, as will be shown in the rest of the paper, are still present in the high-velocity regime, although in some cases the advantages TEM cavities offer in other velocity regimes are reduced.

1.2.1 SIZE

The diameter of a simple spoke cavity (with uniform spokes) is on the order of half the rf wavelength, whereas the diameter of a TM cavity is about twice that. This allows for either smaller physical dimensions at the same operating frequency or close to half the operating frequency for the same physical diameter. While this is true at low β_0 and for simple spoke geometries, higher- β_0 -optimized geometries result in this factor of 2 being reduced. Nonetheless, since the BCS surface resistance is proportional to the square of the rf frequency, accelerators can be designed to operate at lower frequencies (and have fewer elements with different fundamental frequencies) where 4.2 K operation is practical while maintaining cavities of a reasonable size. Furthermore, at half the frequency of a TM cavity of the same β_0 , a multi-spoke cavity of the same length would have half the number of cells. This results in a larger velocity acceptance causing the cavity to be useful over a wider range of velocities. Lower frequency would also lead to a higher longitudinal acceptance, which could prove beneficial in high-current applications.

1.2.2 CELL-TO-CELL COUPLING

In elliptical cavities, the cell-to-cell coupling occurs through the iris opening, but in spoke cavities, which are more open, the magnetic field lines couple all cells [16].

The cell-to-cell coupling in multi-spoke cavities, with simple geometries, is high and they are much more robust as compared to TM cavities with respect to manufacturing inaccuracies. Tuning to achieve field profile balance is important in TM cavities but is usually not necessary in multi-spoke cavities. We will see in Chapter 9 that it was necessary for these cavities, however.

Even in velocity-of-light multi-spoke cavities, the fundamental mode is the lowest frequency mode, which allows for simpler damping and extraction of higher-order modes. Also, unlike TM cavities, the stronger cell-to-cell coupling together with the small number of spokes, implies that the accelerating mode will be well separated from the nearest mode.

1.2.3 SURFACE FIELDS AND ENERGY CONTENT

As was mentioned previously, the spokes in a multi-spoke cavity operate out of phase by π from each other in a TEM-like mode. As such, the fields are concentrated around the spoke and decay rapidly moving away from them. TM elliptical cavities have a larger volume which is uniformly filled with electromagnetic energy. As a result, spoke cavities tend to have a smaller energy content and higher shunt impedance. The fields on the outer surface can be relatively small; this also allows for both the fundamental power coupler and higher-order mode extraction couplers to be located on the outer surface rather than on the beam line [17-20], which is customary for elliptical cavities.

One disadvantage is that for a given gradient defined by using the inside length of the cavity as the reference length, the peak surface fields are higher in a spoke cavity compared to those in an elliptical cavity, at least in the high- β regime [8]. However, in light of the fact that there is no need to use the beamline for couplers in a spoke cavity, it is not clear that the surface fields would be significantly higher at a constant real estate gradient. Additionally, spoke cavities are intended to be used mostly in relatively high-current and/or continuous wave applications where the operating gradients would be modest and not limited by peak surface fields [15].

1.3 APPLICATIONS FOR HIGH-VELOCITY SPOKE CAVITIES

As the interest in TEM structures has increased and their design advanced, more and more spoke cavities have been built and tested [14, 21-27]. With the advantages that spoke cavities can offer, there is recent interest in the design and development of these structures for the high-velocity regime. Some applications include, but are not limited to, small, low-energy electron accelerators for compact light sources [28, 29], non-destructive assay system of nuclear materials in spent fuel using nuclear resonance fluorescence [30, 31], and GeV-scale proton accelerators such as spallation sources [32]. Spoke cavities have currently been built and tested for up to $\sim \beta_0 = 0.6$ [21], but are now under development for up to $\beta_0 = 1$ [33].

1.3.1 HIGH-VELOCITY PROTONS AND IONS

The development of proton and ion beams was enabled by the invention of the cyclotron by Lawrence and Livingston in the 1930s [34]. Linear accelerators (linacs),

while being used as early as 1931 [35], began playing a prominent role in this research in 1957, with the development of the Lawrence Radiation Laboratory linac used to deliver 10 MeV/amu beams with masses up to 40 amu [36].

In the 1970s, developments in electrostatic accelerators led to terminal voltages of up to 30 MV [37]. With the development of negative heavy-ion sources [38], tandem Van de Graaff accelerators were now able to complement cyclotrons and linacs in the area of heavy-ion nuclear physics research.

Around this time, experiments with heavy relativistic ions began when the proton synchrotrons at Princeton [39] and Berkeley [40] were converted to perform this function. The beams produced by these machines were limited in intensity and ion species by the injectors they used since they were developed for protons. These issues were eventually solved, which increased the available energy range from 100 MeV to 2.4 GeV per nucleon.

Over the past several decades, proton and heavy-ion beams have become extremely important tools used in scientific research. The investigations carried out range from the production of radioactive isotopes [41], basic nuclear physics research, biology [42], and medicine [43–45]. Superconducting radio frequency (srf) accelerators are well suited for this task because they can effectively create excellent quality beams and operate in continuous wave (cw) mode which eliminates transients that can be introduced in pulsed operation [46].

For these applications, the accelerator must be able to accelerate particles through a wide range of velocities, in addition to handle multiple ions, each with different velocity profiles. Additionally, high power linacs require that the beam losses should be ≤ 1 Watt/meter [14]. The low frequencies that spoke cavities offer results in a large velocity acceptance (both transverse and longitudinal), which can be useful in addressing these needs. For applications such as accelerator driven systems (ADS), reliability of the accelerator is critical. This high degree of fault tolerance can be accommodated by the fact that superconducting cavities in general, and spoke cavities in particular, can be independently powered, allowing for the linac to be retuned if one or more of the cavities becomes temporarily inoperable.

Typically, the low energy section of an accelerator operates at low frequency, and successive energy stages operate at increasing multiples of that frequency. At each frequency transition, there is a chance for beam losses. GeV-scale spallation sources, such as the ESS Linac proposal, could benefit from using spoke cavities [32]. By

using low frequency spoke cavities, there would be little need for using multiple frequencies, thus minimizing the associated losses.

1.3.2 ELECTRON ACCELERATORS

Current state-of-the-art linacs in operation around the world are designed for large facilities. The design choices made are vastly different than for a compact, relatively low-cost cw source of electrons. In the latter case, the refrigeration requirements are perhaps the most important parameter which can be used for cost reduction.

As was mentioned previously, the low frequency of spoke cavities allows for operation at 4.2 K (why this is true will be discussed in the next chapter), which is why they are being considered for small electron accelerators where 2 K operation may not be practical. The improved thermal and mechanical efficiency can allow for a reduced wall-plug power of four times. In addition, their proven mechanical stability could also be beneficial for cw operation in an environment not as isolated as the tunnel of a large accelerator.

One example of such a machine is shown in Fig. 2. This is an x-ray source based on Inverse Compton Scattering which was first proposed by MIT [28]. This concept for the electron gun, linac, and bunch compression system is currently being developed at ODU/Jefferson Lab [29]. In order to minimize cryogenic losses, a low frequency, modest gradient, and high shunt impedance will be necessary. These are all characteristics of spoke cavities, which is why they are well-suited for such a machine.

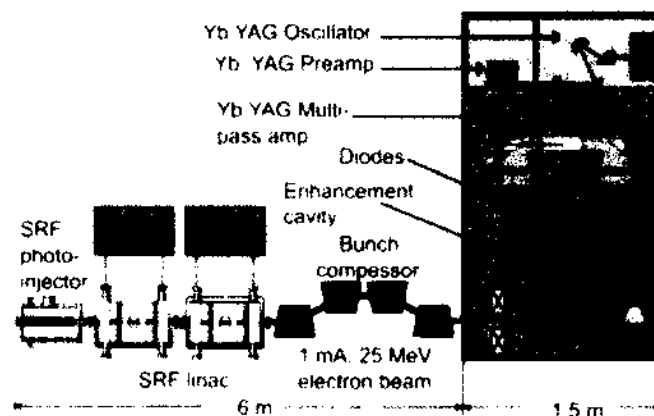


FIG. 2: Layout of an Inverse Compton Source [28].

Another application is being proposed in Japan. In this case, an Energy Recover Linac (ERL) would be used to accelerate a low emittance, high current beam to generate a high quality light source for the purposes of producing monochromatic x/ γ -rays to be used in non-destructive assay system of nuclear materials [31]. In this case, laser Compton scattering would produce the γ -rays which would then be utilized in nuclear resonance fluorescence to non-destructively detect nuclear materials such as uranium, plutonium, and minor actinide elements found in spent nuclear reactor fuels. Because this would be a high current beam, instabilities due to higher order modes can be particularly destructive to the beam current of the ERL. As was previously mentioned, the spoke cavity allows for higher order mode couplers to be located on the outer conductor, which preserves the longitudinal compactness, as seen in Fig. 3 [31].

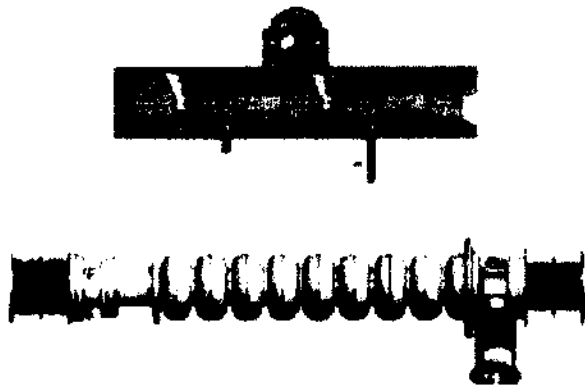


FIG. 3: Schematic comparison of the longitudinal space occupied by a spoke cavity (top) and an equivalent elliptical cavity (bottom) [31].

Even GeV-scale cw electron accelerators with a low repetition bunch frequency could be considered as a possible application for high-velocity spoke cavities. The low repetition bunch frequency, as would be customary in light sources, would benefit by using the low frequencies associated with spoke cavities. They could therefore provide a low-frequency alternative while maintaining reasonable transverse and longitudinal dimensions [47].

CHAPTER 2

SUPERCONDUCTING RADIO FREQUENCY CAVITIES

In this chapter, we will provide an overview of the theoretical tools needed to understand our results. We will begin by briefly outlining the historically significant discoveries that have led to our current use of superconducting radio frequency (srf) cavities, as outlined in [48] and [49]. We will then discuss some of the basic characteristics of such cavities, and conclude with descriptions and derivations of the most important figures of merit.

2.1 SUPERCONDUCTIVITY

The advent of liquefied helium facilitated the discovery of superconductivity by H. Kamerlingh Onnes in 1911 [50, 51]. This liquefied helium allowed for the cooling of metals such as lead, mercury, and tin to just a few degrees Kelvin. Under these conditions, Onnes observed that the electrical resistance of the metals completely disappeared for a small range of temperatures around a material-specific temperature, now referred to as the critical temperature, T_c . This perfect conductivity is a signature property of superconductors and is the reason that they can be so useful in numerous applications.

It was not until 1933 that Meissner and Ochsenfeld discovered the second signature property of superconductors, namely, perfect diamagnetism in a bulk sample [52]. This perfect diamagnetism is not simply a result of the perfect conductivity, as would be the case if the magnetic field were merely excluded from the bulk material, but it is actually *expelled* from the bulk as the temperature is lowered below T_c . This is known as the Meissner effect, and its existence suggests that there should be a magnetic field for which superconductivity breaks down. In fact, this is the case and the field is referred to as the critical field $H_c(T)$. This field has been found to be reliably approximated by [48]

$$H_c(T) \approx H_c(0) \left[1 - \left(\frac{T}{T_c} \right)^2 \right]. \quad (1)$$

The temperature dependence of the critical field is illustrated in Fig. 4.

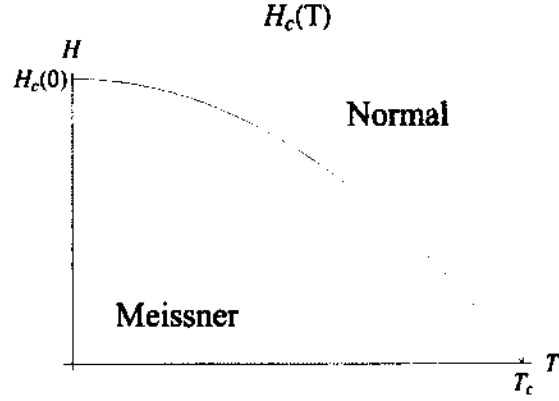


FIG. 4: Temperature dependence of the critical field.

In 1935, F. and H. London proposed governing equations for the microscopic electric and magnetic fields [53].

$$\mathbf{E} = \frac{\partial}{\partial t}(\Lambda \mathbf{J}_s) \quad (2)$$

$$\mathbf{B} = -(\vec{\nabla} \times \Lambda \mathbf{J}_s) \quad (3)$$

$$\text{where } \Lambda = \frac{m}{n_s e^2}, \quad (4)$$

where m is the electron mass, e is the electron charge, and the subscript s denotes that we are talking about superconducting electrons, therefore, n_s is the density of such electrons. The subscript n will therefore denote normal conducting electrons, their density, and the associated current. The two current densities satisfy

$$\frac{\partial \mathbf{J}_s}{\partial t} = \frac{n_s e^2}{m} \mathbf{E} \quad (\mathbf{J}_s = -en_s \mathbf{v}_s) \quad (5)$$

$$\mathbf{J}_n = \sigma_n \mathbf{E} \quad (\mathbf{J}_n = -en_n \mathbf{v}_n) \quad (6)$$

These equations follow from what is known as the Two-Fluid model in which the electrons in a metallic material can be classified as either normal conducting or superconducting, thus the total number of electrons is given by $n = n_s + n_n$. If we now apply Ampere's Law to Eq. (3), and insert $\nabla \times \mathbf{B} = (4\pi/c)\mathbf{J}_s$, we get

$$\nabla \times (\nabla \times \mathbf{B}) = -\frac{4\pi n_s e^2}{mc^2} \mathbf{B} = -\frac{1}{\lambda_L^2} \mathbf{B}, \quad (7)$$

where λ_L is the London penetration depth,

$$\lambda_L = \sqrt{\frac{mc^2}{4\pi n_s e^2}}. \quad (8)$$

Using the vector identity $\nabla \times (\nabla \times \vec{B}) = \nabla(\nabla \cdot \vec{B}) - \nabla^2 \vec{B}$ along with the fact that $\nabla \cdot \vec{B} = 0$, we obtain

$$\nabla^2 \mathbf{B} = \frac{1}{\lambda_L^2} \mathbf{B}. \quad (9)$$

A one-dimensional solution to Eq. (9) would be $B(z) = B_0 e^{-z/\lambda_L}$. This tells us that the penetration depth describes an exponential decay of the magnetic field as it enters a superconductor. It is this penetration depth that explains the phenomenon exhibited by superconductors to exclude and expel an external magnetic field.

The density of superconducting electrons depends on the temperature, so the penetration depths should as well. Empirically, this dependence can be approximated as

$$\lambda_L(T) \approx \lambda(0) \left[1 - \left(\frac{T}{T_c} \right)^4 \right]^{-1/2}. \quad (10)$$

There are numerical discrepancies between the London model and experimental measurements of the penetration depth. This discrepancy was explained by Pippard in 1953 [54].

The London equations describe a local phenomenon, but superconductivity involves coherent behavior of superconducting electrons at a non-local level. What Pippard introduced was a length for which this coherent behavior operated, known as the coherence length, ξ_0 [48]. This coherence length, however, relied on the material being clean, i.e. it did not account for defects. Instead, Pippard introduced a new length ξ

$$\frac{1}{\xi} = \frac{1}{\xi_0} + \frac{1}{\ell}, \quad (11)$$

where $\ell = v_F \tau = 2\pi v_F / \omega_D$, which is the mean free path with v_F being the Fermi velocity and ω_D is the Debye frequency. This allowed for a phenomenologically generalized expression for the supercurrent

$$\mathbf{J}_s = -\frac{3}{4\pi\xi_0} \frac{e^2 n_s}{mc} \int d^3 r' \frac{\boldsymbol{\rho}(\boldsymbol{\rho} \cdot \mathbf{A}(\mathbf{r}'))}{\rho^4} e^{-\rho/\xi}, \quad (12)$$

where $\boldsymbol{\rho} = \mathbf{r} - \mathbf{r}'$, and \mathbf{A} is a vector potential. In the same way Eq. (9) was derived, we find that

$$\nabla^2 \mathbf{B} = \frac{1}{\lambda^2} \mathbf{B}, \quad (13)$$

with the penetration depth

$$\lambda = \sqrt{\frac{mc^2}{4\pi e^2 n_s}} \sqrt{\frac{\xi_0}{\beta \ell}} = \lambda_L \sqrt{\frac{\xi_0}{\beta \ell}}. \quad (14)$$

Thus, in what is known as the dirty limit (when $\lambda \gg \ell \approx \xi_0$), the penetration depth is increased by a factor of order $\sqrt{\xi_0/\ell}$.

In the 1950s, the theory of superconductors became even more sophisticated when Ginzburg and Landau introduced a theory describing the transition between the normal and superconducting phases [55]. To do this, they proposed the order parameter

$$\psi(x) = |\psi| e^{i\phi(x)}. \quad (15)$$

Ginzburg-Landau theory (GLT) uses this “macroscopic” wavefunction to describe the superconducting, or ordered phase where $\psi \neq 0$ for temperatures below T_c and $\psi = 0$ otherwise. GLT starts with the idea that ψ represents some effective wavefunction of the superconducting electrons and the density of such electrons, in terms of the London parameter n_s , is given by the local relation [49]

$$n_s = |\psi(x)|^2. \quad (16)$$

Next, the free energy is expanded in powers of ψ and $\nabla\psi$, leading to a differential equation for ψ analogous to a Schrödinger equation for a free particle where a nonlinear term is included [49]

$$\frac{1}{2m^*} \left(\frac{\hbar}{i} \nabla - \frac{e^*}{c} \mathbf{A} \right)^2 \psi + \beta |\psi|^2 \psi = -\alpha(T) \psi, \quad (17)$$

where α and β are expansion coefficients, \mathbf{A} is the vector potential, and e^* and m^* are the particle effective charge and mass, respectively. The major significance of this result is that two features could be addressed that were previously unexplained by London theory, namely the spatial variation of the density of superconducting electrons n_s and the nonlinear effects of fields strong enough to change n_s .

Although λ and ξ are both dependent on the temperature, this mainly cancels out when we take the ratio of the two, $\kappa = \lambda/\xi$. This is the Ginzburg-Landau parameter, which is a key parameter in determining the nature of the behavior of a superconductor in the presence of a magnetic field.

When $\kappa \leq 1/\sqrt{2}$, the superconductor is known as Type-I. In Type-I superconductors, H_c is the critical field at which superconductivity is destroyed. ψ drops abruptly to zero in a first-order phase transition.

If, however, $\kappa \geq 1/\sqrt{2}$, an altogether different behavior is observed, as A. Abrikosov published in 1957 [56]. He referred to these as “Superconductors of the Second Group,” which we call Type-II superconductors today. What he found was that instead of the first-order, immediate breakdown of superconductivity, there was a continuous increase of magnetic field penetration into the material in the form of flux vortices. For this reason, in Type-II superconductors there are two critical magnetic fields H_{c1} and H_{c2} . After the first is reached, the magnetic field begins to penetrate the superconductor in the form of quantized flux vortices. These vortices increase in number as the external field is increased, until the second critical field has been reached. At this point, the superconductivity completely breaks down. The fields as a function of temperature, are illustrated in Fig. 5.

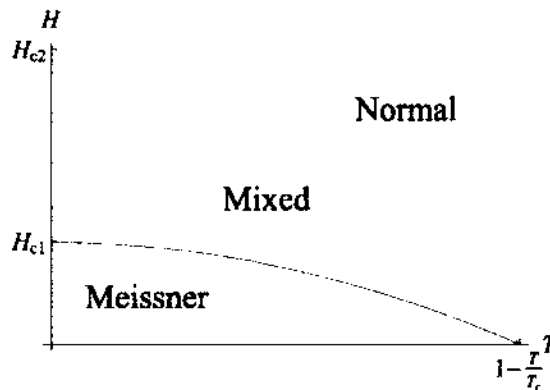


FIG. 5: Phase boundaries for Type-II superconductors.

As much of a milestone as GLT was, it still did not properly explain the third hallmark of superconductivity: the energy gap. Numerous experiments had established the existence of such a gap [57], and any microscopic theory of superconductivity had to explain the infinite conductivity, perfect diamagnetism, and the existence of an energy gap.

In 1955, John Bardeen argued that the modification of the London equations using the coherence length occurs naturally in a theory with an energy gap [58]. He started with the assumption that, in a superconducting state, a finite energy on the order of $k_B T_c$ is necessary to excite an electron from the surface of the Fermi sea. Additionally, these excited electrons should behave much like electrons in the normal state.

The following year, Leon Cooper utilized this idea to describe how electrons could overcome the Coulomb force, through interactions with lattice vibrations (phonons), to form weakly bound pairs [59]. In other words, for a system of many electrons at low T , any weak attraction, no matter how small, can bind two electrons together forming the so-called Cooper pair. This monumental work showed that due to the Fermi statistics of the electron, a paired state of electrons can actually have an energy less than that of the Fermi-energy of the material.

In 1957, Bardeen, Cooper, and Schrieffer developed a theory (BCS) based on the assumption that the supercurrent is not carried by single electrons but by these weakly bound Cooper pairs. All Cooper pairs occupy a single quantum state known as the BCS ground state. This is where the idea of the energy gap becomes important because the energy of the ground state is separated from the single electron states by this temperature dependent gap, $E_g = 2\Delta(T)$. The gap energy Δ is dependent on the temperature, and the critical temperature can be related to the zero temperature energy gap value by

$$1.76k_B T_c = \Delta(0). \quad (18)$$

There are a number of important results obtained by BCS theory, however for the purposes of this discussion, we will focus on the prediction made concerning the surface resistance.

In the presence of a direct current (DC) field, superconductors are free from energy dissipation, but as will be described in the following sections, for the applications of interest here, alternating currents (AC) are present. As was already pointed out, the alternating fields will penetrate the surface a distance λ , which then induces oscillations of the electrons which are not bound in Cooper pairs. It is the dissipation associated with these oscillations which significantly contributes to the overall surface resistance.

In order to arrive at an expression for the surface resistance in niobium ($\xi_0 \approx \lambda$

[60]), we first start with the normal and supercurrent. From Ohm's law

$$J_n = \sigma_n E_0 e^{-\omega t}, \quad (19)$$

which is the normal current density. The Cooper pairs will receive an acceleration $m_c a_c = -2eE_0 e^{-\omega t}$, which leads to a supercurrent density of

$$J_s = i \frac{2n_c e^2}{m_e \omega} E_0 e^{-\omega t}. \quad (20)$$

The total current density will be the sum of the two, which gives a complex conductivity of

$$\sigma = \sigma_n + i\sigma_s, \quad (21)$$

where, as in Eq. (20), $\sigma_s = (2n_c e^2)/(m_e \omega) = 1/(\mu_0 \lambda^2 \omega)$. The surface resistance is the real part of the complex surface impedance

$$R_s = \text{Re} \left[\frac{1}{\lambda(\sigma_n + i\sigma_s)} \right] = \frac{1}{\lambda} \cdot \frac{\sigma_n}{\sigma_n^2 + \sigma_s^2}. \quad (22)$$

For a normal metal, the Drude model provides an expression for the conductivity

$$\sigma_n = \frac{n_n e^2 \ell}{m_e v_F}, \quad (23)$$

where n_n is the density of normal, unpaired electrons. In an intrinsic semiconductor, the density of charge carriers is proportional to $e^{-E_g/2k_B T}$ [61]. Using the gap energy $E_g = 2\Delta(T)$, the normal conductivity can be written as

$$\sigma_n = \frac{e^{-\Delta(T)/k_B T} e^2 \ell}{m_e v_F}. \quad (24)$$

With the above expressions for σ_s and $\Delta(0)$ (Eq. 18), along with the fact that the resistance is the inverse of the conductivity, we arrive at a relationship for the BCS surface resistance

$$R_{BCS} \propto \lambda^3 \omega^2 \ell e^{-1.76T_c/T}. \quad (25)$$

This approximation is valid for $T < T_c/2$ [46]. What is most notable about Eq. (25) is that the BCS resistance increases as the square of the rf frequency and decreases exponentially with the temperature.

It is worth pointing out that in 1959, L. P. Gor'kov showed that GLT was equivalent to BCS for the special case when the temperature is near T_c [62]. Additionally, Gor'kov proved that the fundamental quantities in these two theories, namely the gap energy and the order parameter, are related by some proportionality constant and ψ can actually be thought of as the Cooper pair wave function in the center-of-mass frame.

2.2 EARLY CAVITY DEVELOPMENT

In the previous section, we introduced both the DC and AC characteristics of superconductivity. In particle accelerators, the superconducting cavity will be exposed to alternating currents at microwave frequencies from tens of MHz to several GHz, so this is where the focus will be henceforth.

When $0 < T < T_C$, AC currents will dissipate energy in the cavity walls [63–68]. This dissipated energy puts some practical limitations on superconducting cavities. Additionally, superconducting cavities must maintain a surface magnetic field below that of the superheating field, which is related to the penetration depth, coherence length, and critical field by $H_{sh} = (\lambda_L/\xi_0)^{-1/2}H_c$ [69]. Given these limitations, the strongest argument for using superconducting cavities can be made for accelerators operating either in continuous wave (cw) mode or pulsed with a high duty factor.

The practical limit to the performance of a superconducting cavity is the theoretical H_{sh} , which, for niobium, is around 230 mT [46]. While the ultimate limit to the achievable gradient that this field allows is 55 MV/m at $\beta_0 = 1$ and 30 MV/m for $\beta_0 < 1$ [46], the actual gradients will be geometry dependent, and typically lower than this.

Soon after the microscopic theory describing superconductivity was understood (BCS), proposals were being made to use such materials for cavities [70] and arrays of cavities [71] to accelerate particles.

The difficulty in exploiting such cavities for rf acceleration was quickly realized when two superconducting quarter-wave resonant lines, operating at 280 MHz, were fabricated and tested at CERN [72]. RF losses were found to be quite high and heavily dependent on the material purity and surface conditions [73, 74]. A few years later, electrons were accelerated for the first time by a superconducting lead coated structure at Stanford University [75].

In 1970, encouraging results were obtained at the High-Energy Physics Laboratory (HEPL) [76]. A pillbox cavity, made of reactor grade niobium, operating at 8.5 GHz and 1.25 K was able to achieve a peak electric field of 70 MV/m and a peak magnetic field of 108 mT. This result demonstrated the proof-of-principle for the high-gradient operation of Nb cavities. This early work led to the design and construction of the superconducting accelerator (SCA). This accelerator utilized standing-wave elliptical cavities.

Over the past four decades, many superconducting accelerators have been built. In addition to those that are still in operation, many more are under construction or in the advanced research and development phase because they have proven to be most valuable for both high-energy and nuclear physics experiments. In the following sections, we will introduce the fundamental properties of srf cavities.

2.3 THE PILLBOX CAVITY

To develop the relevant concepts relating to superconducting cavities, it is useful to start with a simple example. The pillbox cavity, shown in Fig. 6, provides such an example.

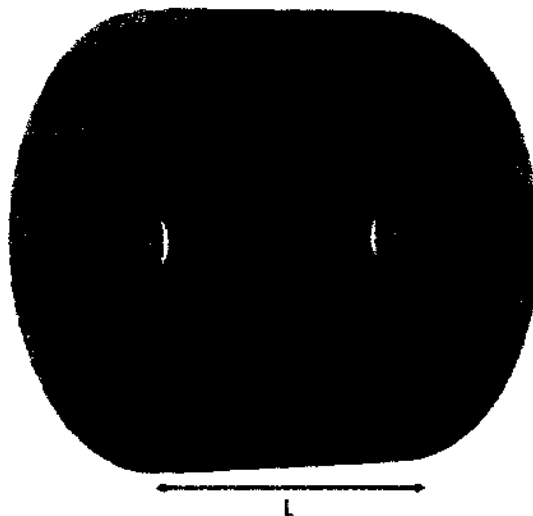


FIG. 6: Geometry of a pillbox cavity.

Before proceeding, it should be noted that adding the beam pipes to a standard pillbox cavity does change the field properties and frequency. The eigenmodes cannot be solved analytically since the addition of the holes change the boundary conditions

such that numerical simulation tools must be used to calculate them.

For a perfect electrical conductor (PEC), the boundary conditions placed upon the fields are

$$\hat{\mathbf{n}} \times \mathbf{E} = 0, \quad \hat{\mathbf{n}} \cdot \mathbf{H} = 0, \quad (26)$$

where $\hat{\mathbf{n}}$ is the unit vector normal to the surface. In order to find the fields, we start with Maxwell's equations in vacuum

$$\begin{aligned} \nabla \cdot \mathbf{E} &= 4\pi\rho & (a) \\ \nabla \times \mathbf{E} &= -\frac{1}{c} \frac{\partial \mathbf{B}}{\partial t} & (b) \\ \nabla \cdot \mathbf{B} &= 0 & (c) \\ \nabla \times \mathbf{B} &= \frac{4\pi}{c} \mathbf{J} + \frac{1}{c} \frac{\partial \mathbf{E}}{\partial t} & (d) \end{aligned} \quad (27)$$

where ρ is the charge density, c is the speed of light, and \mathbf{J} is the current density. Taking the curl of Eq. 27 (b) and inserting (d) for the curl of \mathbf{B} , we get the wave equation

$$\left[\nabla^2 - \frac{1}{c^2} \frac{\partial^2}{\partial t^2} \right] \cdot \begin{bmatrix} \mathbf{E} \\ \mathbf{B} \end{bmatrix} = 0 \quad (28)$$

where, in cylindrical coordinates,

$$\nabla^2 = \frac{1}{r} \frac{\partial}{\partial r} \left(r \frac{\partial}{\partial r} \right) + \frac{1}{r^2} \frac{\partial^2}{\partial \phi^2} + \frac{\partial^2}{\partial z^2}. \quad (29)$$

The solutions to Eq. (28) can be conveniently classified as transverse magnetic (TM) or transverse electric (TE). The former has a zero longitudinal (along the cylinder axis) magnetic field and the latter has a zero longitudinal electric field. While, for a pillbox cavity with beam pipe holes, the modes will actually be a superposition of TE and TM modes. However, these descriptions are still used as the convention for describing the modes in such a cavity.

If we assume a time dependence of the electric and magnetic fields of $e^{i\omega t}$, the field components of the TM modes can be described by [77]

$$\begin{aligned}
E_z &= Ak_r^2 J_m(k_r r) \cos m\phi \cos kz \\
E_r &= -Akk_r J'_m(k_r r) \cos m\phi \sin kz \\
E_\phi &= A(mk/r)J_m(k_r r) \sin m\phi \sin kz \\
B_z &= 0 \\
B_r &= -\iota A(m\omega/c^2 r)J_m(k_r r) \sin m\phi \cos kz \\
B_\phi &= -\iota A(\omega k_r/c^2)J'_m(k_r r) \cos m\phi \cos kz
\end{aligned} \tag{30}$$

where J_m is the m^{th} order Bessel function, k and k_r are the wave numbers in the longitudinal and radial modes, m is the azimuthal mode number, and $\omega/c = \sqrt{k^2 + k_r^2}$.

If the beginning and end of the cavity are at $z = 0$ and $z = \ell$, then, for the TM modes, the longitudinal wave number can be determined by the boundary condition that $E_r = 0$ and $E_\phi = 0$ at these two points. This leads to

$$k_p = \frac{p\pi}{\ell}, \quad p = 0, 1, 2, \dots \tag{31}$$

where p is the number of half cycles of variation in the z -direction.

If the radius of the cavity is R , the radial wave number can be determined by the boundary condition with $E_z = 0$ and $E_\phi = 0$ at $r = R$. This leads to

$$k_{r,mn} = \frac{x_{mn}}{R}, \tag{32}$$

where x_{mn} are the zeros of Bessel functions $J_m(x_{mn}) = 0$, m is the number of half cycles of variation in the r -direction, and n is the number of complete cycles of variation for $0 \leq \theta \leq 2\pi$.

The values of (m, n, p) are used to describe the modes, and the resonance wave number k for a given mode is

$$k_{mnp} = \sqrt{k_{r,mn}^2 + k_{z,p}^2} = \sqrt{\frac{x_{mn}^2}{R^2} + \frac{p^2\pi^2}{\ell^2}} = \frac{\omega_{mnp}}{c} = \frac{2\pi}{\lambda_{mnp}} \tag{33}$$

If the ratio of $R/\ell > 0.5$, the lowest order mode, or fundamental mode, of the pillbox cavity will be the TM_{010} mode. With the zero of the Bessel function being $x_{010} = 2.405$, the frequency of this mode reduces to

$$\omega_{010} = c \cdot \frac{2.405}{R}, \tag{34}$$

where $R = 0.766\lambda_{010}$. Because the wavelength is proportional to the inverse of the frequency, the diameter of a TM cavity is thus proportional to the rf wavelength. The fields for this mode are shown in Fig. 7.

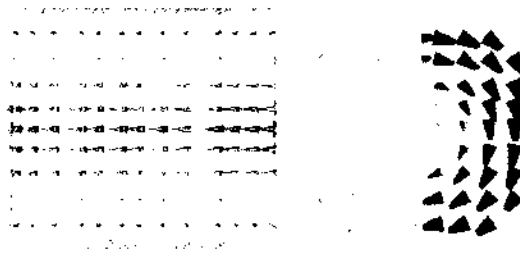


FIG. 7: Electric field (left) and magnetic field (right) of the TM_{010} mode of a pillbox cavity.

The TM_{010} is the mode used for acceleration in elliptical cavities, hence the term “TM-class” cavities.

2.3.1 MULTI-CELL CAVITIES

Multi-cell cavities are what is actually used in linacs because doing so increases the overall accelerating efficiency. Increasing the number of accelerating cells per cavity causes the ratio of active accelerating length to total length to improve. Standard pillbox cavities, strung together one after another, are not the design of choice, however, because their geometry is conducive to multipacting, which will be discussed in the next chapter. Instead, pillbox cavities with rounded outer edges are used. These are known as elliptical cavities.

To understand the properties of multi-cell cavities, it is useful to represent them as a system of coupled oscillators. This can be motivated by the fact that, like a mechanical system of coupled oscillators, this electromagnetic system will oscillate at some natural (resonant) frequencies where each cell “talks” to its neighboring cells via some coupling factor. Therefore, a series of elliptical cavities, connected by the beam tube, can be thought of as a system of coupled mechanical pendula, connected by a weak spring. When the pendula are swinging “out-of-phase,” the spring can disturb the oscillations, causing the mode frequency to increase. A simple two-cell elliptical cavity, for example, will exhibit the same behavior; the fields in adjacent cells will either be oriented in the same or opposite direction. In other words, the phase difference between the fields will be either 0° or 180° . This is why these modes

are called the 0 and π mode, respectively. The field patterns of these two modes are shown in Fig. 8.

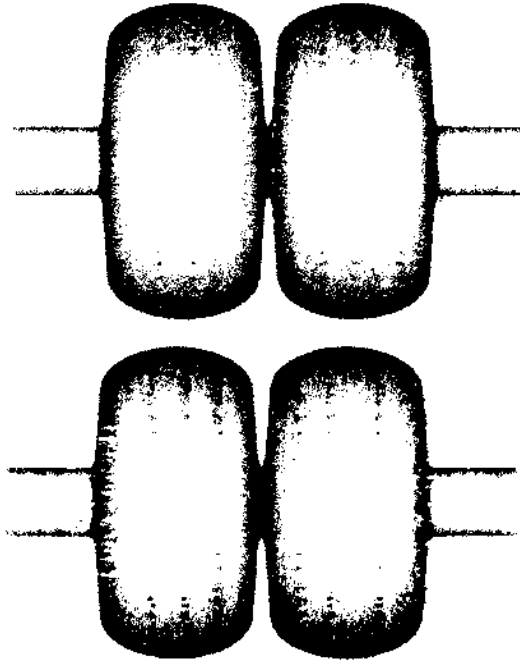


FIG. 8: Electric field profile of the 0 mode (top) and π mode (bottom) of a 2 cell elliptical cavity.

A system of $N + 1$ coupled oscillators will have a subset of $N + 1$ normal modes of oscillation. For example, a 7-cell cavity, such as the Jefferson Lab 12 GeV cavities, will have 7 modes of oscillation, where the 7th mode will be the π mode. Each mode will have a different cell-to-cell phase relation, in addition to increasing frequencies. The normal mode spectrum is given by [78]

$$\Omega_q = \frac{\omega_0}{\sqrt{1 + k \cos(\pi q/N)}} \quad (35)$$

where $q = 0, 1, \dots, N$ and k is what is known as the cell-to-cell coupling constant. More will be said about k later, but one thing that should be noted is that when k is large, the frequency separating the various modes is greater.

Figure 9 is an example of how the mode frequencies are related for a 7-cell elliptical cavity. Note that the accelerating mode is *not* the fundamental mode of a multi-cell elliptical cavity, but rather the highest frequency mode of this particular grouping

of frequencies (the pass band). As was mentioned previously, this is not the case for spoke cavities.

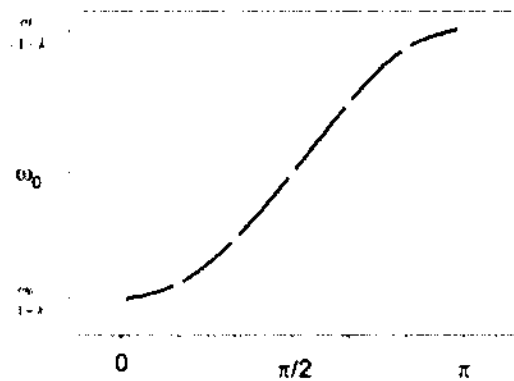


FIG. 9: Frequency relation for the normal modes of 7 coupled oscillators.

The cell to cell variation of the peak electric field on the beam axis is known as the “field flatness,” and is an important feature of multi-cell cavities. In elliptical cavities, the geometry of the end cells is often modified to compensate for the coupling to the beam pipe, which gives them a different resonance frequency than the center cells.

2.4 TEM-CLASS CAVITIES

In the previous section, we identified TM cavities as those that utilize a transverse magnetic mode for particle acceleration. Transverse electric (TE) modes also exist in these cavities, however they are not useful for acceleration unless the geometry is significantly altered, e.g. the so-called crossbar cavity [79]. There is another cavity type based on coaxial resonant lines, which utilize a transverse electromagnetic mode (TEM) for particle acceleration. These cavities are of particular interest because the spoke cavity falls into this category.

The term TEM-class cavity refers to the mode sustained along the inner conductor of a coaxial type resonator. The simplest example of this is the coaxial half-wave cavity. The electric and magnetic fields of a half-wave coaxial resonator are shown in Fig. 10.

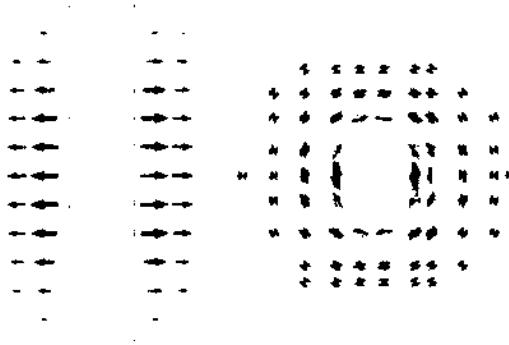


FIG. 10: Electric field (left) and magnetic field (right) of the fundamental TEM mode in a half-wave resonator.

TM-class cavities have electric walls (i.e. walls which are considered perfect electrical conductors) as boundary conditions for each cell. The frequency of such a cavity is related to the transverse dimensions, as Eq. (34) illustrated. The TEM mode frequency of a coaxial line is determined by the length (half an rf wavelength), rather than the transverse dimensions. Thus, we can imagine placing holes for the beam to pass through, as shown in Fig. 11, allowing for the coaxial half-wave resonator to be used for particle acceleration by way of the fundamental TEM mode. This results in a cavity with transverse dimensions roughly half that of a TM-type cavity of the same frequency.

From Fig. 1, it is clear that the spoke cavity is a variation of the half-wave coaxial resonator. Here, the spokes represent sections of short-circuited coaxial resonators. Therefore, as will be shown later, the field distribution in a spoke cavity is determined, to a great degree, by the geometry of the spokes themselves.

2.5 FIGURES OF MERIT

The performance of superconducting cavities, and what applications they are appropriate for, can often be characterized by a few important properties or parameters. This section gives a brief review of the cavity properties and parameters which will be reported on in the following sections.

The motion of a particle subjected to the electromagnetic fields within a resonant

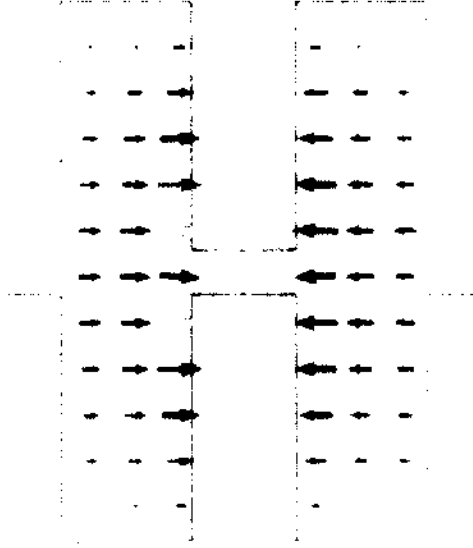


FIG. 11: Electric field of the fundamental TEM mode in a half-wave resonator with beam pipes and drift tube.

cavity is governed by the Lorentz force

$$\mathbf{F} = \frac{d(m\mathbf{v})}{dt} = q(\mathbf{E} + \mathbf{v} \times \mathbf{B}), \quad (36)$$

where $m = \gamma m_0$ is the relativistic mass of the particle with velocity \mathbf{v} and charge q . Because of the symmetry of the spoke cavity, the fundamental mode has no magnetic field on-axis and only a longitudinal electric field component, thus only acceleration takes place through the interaction with an electric field parallel to the velocity of the particle.

The energy (or voltage) gain acquired by the particle is the work done by the longitudinal electric field which, under the assumption that the velocity of the particle does not change in the cavity, is given by

$$V_{\text{acc}}(\beta, \varphi) = \int_{-\infty}^{\infty} E_z e^{i(\frac{\omega z}{c} + \varphi)} dz, \quad (37)$$

where ω is the rf frequency, φ is the phase between the particle and the rf field (where the fields are in rf cycle when the particle is at the center of the cavity), and z is the direction of particle propagation. The expression for voltage is expressed as a Fourier integral because the solution describing the electric and magnetic fields are proportional to $e^{i\omega t}$.

Under the assumption that the velocity does not change within the cavity, the voltage gain $V_{acc}(\beta, \varphi)$ has a sinusoidal dependence on the phase ϕ and will have a maximum V_0 for a certain particle velocity β_0 which will also be used to define the β of the cavity. V_0 can be divided by a reference length L to define the accelerating field at which the cavity is operating

$$E_{acc} = \frac{V_0}{L}. \quad (38)$$

While there is a consensus in the definition of the reference length L for TM cavities (given in Eq. 39 where N is the number of cells), there is no universally agreed upon definition for TEM cavities. In low-velocity TEM cavities, where the gaps are much less than the rf wavelength, the problem is treated as an electrostatic one, and the reference length can be defined as

$$L = N \frac{\beta_0 \lambda}{2}, \quad (39)$$

where N is the number of loading elements (features which provide a voltage difference), β_0 is the velocity of the particle that would acquire the maximum voltage from the cavity, and λ is the free-space wavelength corresponding to the frequency of the accelerating mode [80].

In TEM structures, with uniform loading elements, such as a spoke cavity with cylindrical spokes, the voltage acquired by the particle in the end gaps is about half the voltage gained in the central gaps, therefore, it is logical to use N as the number of loading elements. In an optimized cavity, as will be shown later, this is not the case. When the spoke becomes large and non-cylindrical, as is the case with the cavities presented here, the voltage gain is almost the same in the end gaps and the central gaps, therefore we find that in the present case, using N as the number of accelerating gaps rather than loading elements allows for a more accurate normalized field comparison between single- and multi-spoke cavities.

The energy stored in a cavity is given by,

$$U = \frac{1}{2} \epsilon_0 \int_V |\mathbf{E}|^2 dV = \frac{1}{2} \mu_0 \int_V |\mathbf{H}|^2 dV, \quad (40)$$

where the integration is taken over the entire volume of the cavity. The power dissipation is given by

$$P_d = \frac{R_s}{2} \int |\mathbf{H}|^2 dS, \quad (41)$$

where R_s is the surface resistance and the integral is taken over the inner surface of the cavity. The ratio of stored energy and the energy dissipated during one radian in the walls of the cavity is the quality factor

$$Q_0 = \frac{\omega_0 U}{P_d}. \quad (42)$$

There are other quality factors that will be discussed in detail, later, but it is appropriate to mention them now. First, there is an “external” quality factor Q_{ext} , which is given by

$$Q_{ext} = \frac{\omega_0 U}{P_{ext}}, \quad (43)$$

where P_{ext} is the power dissipated in all external loads attached to the cavity such as power couplers and pickup probes. Lastly, there is the “loaded” quality factor Q_L given by

$$\frac{1}{Q_L} = \frac{1}{Q_0} + \frac{1}{Q_{ext}}. \quad (44)$$

The geometrical factor, which is the product of the quality factor and the surface resistance, $G = R_s Q_0$ (in Ω), is independent of cavity size and material and depends only on the shape of the structure and the electromagnetic mode.

A measure of the power dissipation induced by the rf currents, and thus the efficiency of the structure in converting rf power to voltage gain, is the shunt impedance defined here as

$$R = \frac{V_0^2}{P_d}. \quad (45)$$

Since the power dissipation given in Eq. (41) is clearly dependent on the material, for a superconducting structure it has a direct impact on the requirements of the cryogenic system. A material-independent parameter which is often quoted and is more useful in assessing a particular cavity design is the product of the shunt impedance and the surface resistance, RR_s (in Ω^2).

The ratio of shunt impedance and quality factor $[R/Q]$, is another parameter that depends only on the shape and not on the cavity size or material. The parameter RR_s is obtained as the product of $[R/Q]$ and $G = QR_s$, and is often used (as we do here) in place of shunt impedance because it does not depend on material properties and operating frequency.

2.6 CAVITY PERFORMANCE LIMITATIONS

Superconducting radio frequency cavities are fundamentally limited by the theoretical peak magnetic and electric fields which the given material can sustain. The practical limits, however, often lead to a performance which is less than that of the ideal model. In this section, we detail some of the most common performance-limiting phenomenon. How each of these affect the cavity performance is shown in Fig. 12 [81].

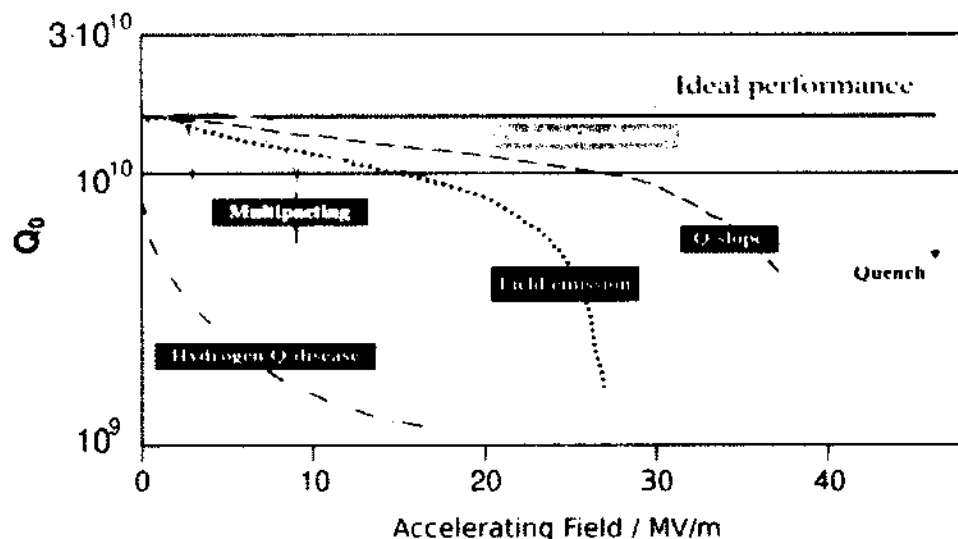


FIG. 12: SRF cavity limitations [81].

2.6.1 THERMAL BREAKDOWN

Thermal breakdown (TB) occurs when a portion of the cavity exceeds T_c . When this happens, that area is no longer superconducting, causing the stored energy of the cavity to suddenly decay. The time for this process to occur is typically a few milliseconds [82]. Once the energy has been dissipated, the cavity is able to regain the superconducting state and be filled with electromagnetic energy again. This process repeats without any intervention, which is why it is often characterized by a periodic, oscillatory behavior of the transmitted power. It should be noted that TB is most often the result of defects or particles already present in the material or incurred during fabrication, so unlike multipacting, no amount of in situ processing

will alleviate the negative consequences.

TB usually occurs in high magnetic field regions. The nature by which TB occurs does not necessitate any precursory events. In other words, there are no indications such as x-rays or a degradation of the quality factor, and the only way to overcome this problem often involves a costly disassembly, inspection, and re-processing of the cavity. This is why TB is perhaps the most undesirable limitation to encounter.

For a defect of radius R_d , the breakdown field can be estimated as [46]

$$H_{TB} = \sqrt{\frac{4\kappa_T(T_c - T_b)}{r_d R_d}}, \quad (46)$$

where κ_T is the average thermal conductivity of the niobium, T_c is the critical temperature of the niobium, T_b is the bath temperature, r_d is the radius of the defect, and R_d is the surface resistance of the defect [83].

2.6.2 FIELD EMISSION

There are a number of ways that parasitic electrons can be produced within a superconducting cavity, and here we detail one such way: field emission. What follows has been adapted from [84].

Fowler-Nordheim Theory

A potential barrier between the Fermi level and the vacuum level of a metal usually prevents electrons from escaping the surface. The vacuum level, however, exhibits a slope in the presence of an applied electric field, causing the barrier to become triangular. This is illustrated in Fig. 13 [84]. This barrier becomes more narrow with increasing field. When the field becomes large enough, the barrier becomes sufficiently thin and the probability for electron tunneling becomes non-negligible. The onset of field emission can occur at this point.

The height of the barrier shown in Fig. 13 as Φ is typically around 4-5 eV, depending on the metal, is known as the work function. In 1928, Fowler and Nordheim [85] were able to calculate the probability that electron tunneling through the barrier would occur. For a perfect metal with a Fermi-Dirac electron density, the following relationship was derived at 0 K,

$$J = \frac{AE^2}{\Phi} \cdot \exp\left(-B \frac{\Phi^{3/2}}{E}\right), \quad (47)$$

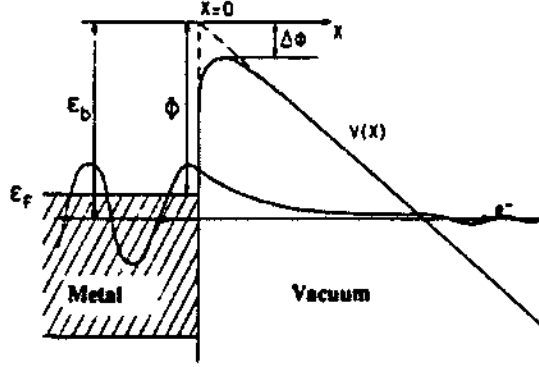


FIG. 13: Energy diagram of a metal-vacuum interface. ϵ_F is the energy at the top of the Fermi level, which is where conduction band electrons are found. When an electric field is applied, the potential barrier becomes triangular [84].

where J is the current density in A/m^2 , E is the applied electric field in V/m , Φ is the work function in eV, and A and B are given by,

$$A = \frac{e^3}{8\pi\hbar t^2(y)} \approx \frac{1.541 \times 10^{-6}}{t^2(y)} \quad (48)$$

$$B = \frac{4\sqrt{2m_0}}{3e\hbar} \cdot v(y) \approx 6.831 \times 10^9 v(y), \quad (49)$$

where $v(y)$ and $t(y)$ are tabulated dimensionless elliptical functions whose values can be found in, for example [86, 87], and the dimensionless parameter y is given by

$$y = \sqrt{\frac{e^3 E}{4\pi\epsilon_0 \Phi^2}} \approx \frac{3.795 \times 10^{-5} \sqrt{E}}{\Phi}. \quad (50)$$

It should be noted that Eq. (47) was obtained under conditions of a stationary field, but it is accepted that it also is applicable to rf fields up to several tens of GHz [88].

Equation (47) predicts a negligible current for fields in the MV/m range, which would be typical in an accelerating cavity. The reality is, a significant current can, and does, arise even when the surface electric fields are a few MV/m. This is because actual electrodes producing the emitted electrons do not have a well characterized surface, so the phenomenological description of the process is different [89].

Enhanced Field Emission

The enhanced field emission model assumes that the increased emission is due to microprotrusions and other defects of the emitter surface. These microprotrusions cause the surface to be far from ideal, which leads to local electric field enhancements by a factor β . The current emitted by one of the sites is given by

$$I = S \cdot \frac{A\beta^2 E^2}{\Phi} \exp\left(-B \frac{\Phi^{3/2}}{\beta E}\right), \quad (51)$$

where S is the surface area of the emitter. These emitters are not limited to defects in the material such as the microprotrusions, absorbed gas, surface roughness, scratches, or grain boundaries, but can also be introduced during cavity processing and assembly.

High pressure rinsing (1250 psi) with ultra-pure water along with judicious clean room assembly have proven to be the most effective preventative measures. In spite of this, contamination (e.g. metallic dust) can still be introduced. In this case, curative techniques such as rf and helium processing can prove beneficial.

2.6.3 MULTIPACTING

Multipacting will be discussed in more detail in Chapters 3 and 5, but we also mention it here because, historically, it has been a limitation of srf cavities. The phenomenon occurs when electrons emitted from the rf surface follow a trajectory such that their next encounter with the surface is an integral number of rf cycles after their emission. When the electron does impact the surface, there is a chance that multiple secondary electrons will be emitted, all of which can repeat the cycle leading to an avalanche effect. Eventually, all additional power added to the cavity goes into this process.

2.6.4 HYDROGEN Q-DISEASE

The niobium lattice has a large affinity for hydrogen [90]. Unfortunately, most fabrication and processing steps of a niobium cavity expose it to possible contamination. The Q degradation observed starting from $E_{acc} = 0$ is due to the creation of the niobium-hydrogen layer. The formation of these niobium hydrides happens during cooldown between 150-60 K. The concentration of hydrogen required in the surrounding gas is too high for a Nb-H layer to form at temperatures above 150 K,

and diffusion of hydrogen is too slow to accumulate at hydride centers below 60 K [46, 91].

There are typically two ways to address this problem. First, the bulk niobium can be outgassed through heating to temperatures of 600-900° C for several hours under high vacuum. Second, a rapid cooldown between 150-60 K decreases the likelihood hydrides will form. In fact, holding the cavity in this range is known as a Q -disease test. The idea is that if the cavity has an abundance of hydrogen, a noticeable drop in the quality factor should occur when cooled down to the operating temperature. If this happens, the cavity can then be warmed to above 150°, cooled quickly, and re-tested. If the Q has returned to a higher level, then the cavity is susceptible to Q -disease [92].

2.6.5 HIGH-FIELD Q SLOPE

As the name suggests, high-field Q slope is different than Q -disease in that its onset is at a specific gradient (higher than $E_{acc} = 0$). At this point, the intrinsic quality factor begins to decline with increasing field gradient. This can happen in the absence of x-rays (i.e. field emission). In contrast to TB, temperature maps have found that cavities suffering from Q slope experience a heating and therefore power dissipation throughout most of the cavity [93].

CHAPTER 3

CAVITY FUNDAMENTALS

In this chapter, we present a detailed discussion of the theoretical background needed to understand the various studies undertaken in this dissertation research. Further, the simulation tools used will also be elaborated on.

3.1 CAVITY MODES

In theory, a resonant cavity has an infinite number of modes that can be sustained within its boundaries. In a spoke cavity, we are primarily interested in the fundamental accelerating mode, although higher order modes are also of interest. As was mentioned previously, the fundamental mode of a spoke cavity is largely determined by the cavity radius ($\sim \lambda/2$), while the mode separation is determined by the cell-to-cell coupling. This gives us a rough idea of where to begin in order to obtain the proper operating mode frequency, but the actual mode spectrum and field patterns must be determined numerically.

CPU power for a desktop computer has increased so much over the last few decades that 3D electromagnetic simulation tools are now readily available. The majority of the frequency calculations and field patterns here have been done using Microwave Studio[®], which is one of several modules within the Computer Simulation Technology (CST[®]) software suite [94]. MWS uses a 3D Finite Integration Technique.

These simulation tools can give us great insight into the modes which are present in accelerator cavities. However, in order to corroborate these tools, extensive measurements must be carried out. The most common method for doing so is the bead-pulling technique. In this case, the bead, which is a small dielectric or conductor, is used to perturb the field along a given trajectory so that changes in amplitude or phase (of the perturbed field) can be measured for a given mode.

3.1.1 THE SLATER PERTURBATION METHOD

The insertion of a dielectric or conducting bead, with dimensions that are small compared to the rf wavelength, into the cavity results in a frequency change. The

magnitude of this shift gives us an understanding of the local electromagnetic field strength and direction. This interaction is known as the Slater perturbation method [95]. Moreover, this technique can be used to measure the aforementioned ratio of shunt impedance and quality factor $[R/Q]$ for *transverse* modes [96].

The introduction of a dielectric object in a volume where an electric field is present will result in a negative frequency shift while a metal object in the region of a magnetic field will lead to a positive frequency shift. When both fields are present, the frequency shift will depend on the relative strengths of each field. When the unperturbed field is uniform in an area larger than the radial dimensions of the object, the frequency shift is [97, 98]

$$\frac{\Delta f}{f} = \frac{\Delta U}{U} = -\frac{\pi r^3}{U} \left[\epsilon_0 \frac{\epsilon_r - 1}{\epsilon_r + 2} E_0^2 + \mu_0 \frac{\mu_r - 1}{\mu_r + 2} H_0^2 \right], \quad (52)$$

where r is the radius of the spherical bead, Δf is the frequency shift, f is the unperturbed frequency, E_0 is the electric field amplitude, H_0 is the magnetic field amplitude, ϵ_0 is the permittivity of vacuum, ϵ_r is the relative permittivity of the bead, μ_0 is the permeability of vacuum, μ_r is the relative permeability of the bead, U is the stored energy in the cavity, and ΔU is the change in stored energy. When measuring an accelerating mode where only the electric field exists on the beam axis, a dielectric bead can be used ($\mu_r = 1$), and Eq. (52) can be reduced to

$$\frac{\Delta f}{f} = -\frac{\pi r^3}{U} \left[\epsilon_0 \frac{\epsilon_r - 1}{\epsilon_r + 2} E_0^2 \right]. \quad (53)$$

3.2 MULTIPACTING

When the internal surface of a rf cavity is exposed to the high fields maintained in a superconducting cavity, electrons (known as primary electrons) can be emitted from the metal. The kinetic energy and trajectory of these electrons is determined by the electromagnetic fields, and in many cases, they will come in contact with another part of the surface with a certain amount of impact energy. If this energy falls within the secondary emission yield (SEY) range, then additional electrons, known as secondary electrons, will be ejected [99]. Figure 14 [100] shows a generic SEY curve. The parameters E_{oc}^I , and E_{oc}^{II} are known as the crossover energies for which $\delta = 1$. E_{om} marks the electron energy for which δ is maximum. These parameters can vary greatly between materials. Even for a given material, these parameters can

vary widely based on both the bulk properties and surface condition.

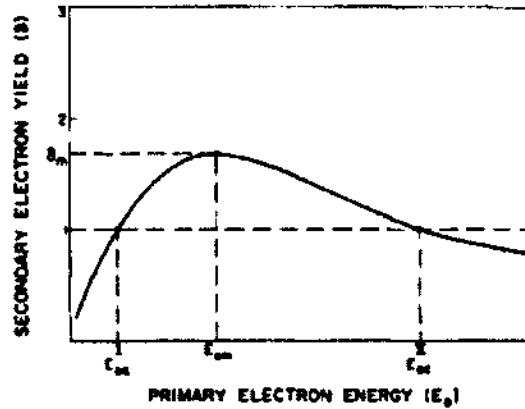


FIG. 14: Definition of secondary electron yield curve parameters [100].

When the SEY is greater than 1, just one electron can create many more. The multiplication factor Y after N impacts follows the relation

$$Y = \delta^N. \quad (54)$$

Therefore, at a typical operating frequency in the MHz range, a SEY of ~ 1.1 , after only 100 ns, the multiplication factor can be upwards of 10^4 .

For well prepared niobium cavities, the crossover energies in Fig. 14 are around 150 eV and 1050 eV, while E_{opt} is around 375 eV [46]. We have presented preliminary results for crossover energies of 150 eV and 2000 eV previously [101]. When secondary electrons are in resonant trajectories, and each impact energy is in the range for which $\delta > 1$, then a cascade can occur generating excessive heat, thus leading to thermal breakdown. These regions are commonly called barriers, and they are classified as either “soft” or “hard.” Soft barriers are those that can be conditioned through and thereby passed. It is believed conditioning occurs because multipacting electrons actually clean the surface to a point where the secondary emission yield is below unity [102]. Hard barriers are those which persist resulting in a limited achievable gradient and quenching.

By improving the quality of the surface, the soft barriers on the gradient can be eliminated. On the other hand, hard barriers can only be overcome by changing the cavity geometry in such a way as to avoid resonant trajectories altogether.

Multipacting is also characterized, most commonly, as either one-point or two-point. One-point multipacting occurs when the time of flight of the electron between two impacts is an integer number of rf cycles and that the electron's impact site is approximately the same as its ejection site. This condition can be described in terms of the cyclotron and rf frequencies as [103],

$$\frac{f}{n} = \frac{eB}{2\pi m}. \quad (55)$$

In the case of two-point multipacting, the time of flight is an odd number of half rf cycles and the impact site is not the same as the ejection site. The former condition can be described with the same parameters as Eq. (55) [104],

$$\frac{2f}{2n-1} = \frac{eB}{2\pi m}. \quad (56)$$

It is well-known that all cavities will experience some level of multipacting and that the most important factor in reducing its impact is to have optimal surface conditions. However, there are some geometric conditions that should be avoided as well. In order to determine what areas of the cavity are susceptible to sustained resonant electron trajectories, simulation tools are needed. We have chosen to use the Advanced Computational Electromagnetic 3P (ACE3P) code suite developed at SLAC [105].

There are several requirements for accurate multipacting simulations. First, we need the electromagnetic fields in the cavity to a high resolution. Second, a correct representation of the trajectory a particle will take when being emitted from a curved surface. Third, a realistic SEY curve to determine when electrons will be ejected from the surface, and finally, the ability to analyze the particle data to identify and record multipacting events [106].

We first solve for the fields in the cavity. This is done using a parallel eigenmode calculation code for accelerator cavities, Omega3P. This code utilizes a finite-element method to find the vector fields in the frequency domain [107]. The cavity volume is discretized into finite-element tetrahedrons, and Maxwell's equations, along with the PEC boundary conditions, are used to find the electric field around the perimeter of each element.

$$\nabla \times \left(\frac{1}{\mu} \nabla \times \mathbf{E} \right) - k^2 \epsilon \mathbf{E} = 0 \quad \text{on } \Omega, \quad (57)$$

where Ω is the surface of the computational domain and k is the wavenumber. When the electric field along the boundary has been found, the magnetic flux can be calculated by Eq. (27 b). Track3P is then used to calculate the particle trajectories and impact energy using

$$\frac{d\mathbf{p}}{dt} = e[\mathbf{E} + (\mathbf{v} \times \mathbf{B})], \quad (58)$$

and

$$\mathbf{p} = m\gamma\mathbf{v}, \quad \gamma = \frac{1}{\sqrt{1 - \frac{v^2}{c^2}}}. \quad (59)$$

Prior to beginning the Track3P simulations, a bounding box is created in which each tetrahedral mesh cell will emit 1 electron with an energy of 2 eV every 3.6° of the rf phase from the center of the internal face. After one rf cycle has elapsed, the particles are then tracked until the specified number of rf cycles is complete. In our case, we set the number of rf cycles to 50.

Particles impacting the surface with the right phase conditions will then emit another particle (with energy of 2 eV) perpendicular to that surface. This could present a problem, especially for confined spaces with many curved surfaces, since there is no accounting for emission angles. Even so, particles surviving a certain number of impacts will then be deemed “resonant,” and their initial and final position, phase with respect to the rf fields, and energy are recorded.

Track3P does not account for the number of secondary electrons emitted. Instead, a post-processing step can be taken using the enhancement counter function. At the end of the simulation, the enhancement counter function provides the total number of secondary electrons produced. Similar to Eq. (54), the enhancement counter can be described by

$$EC = \delta_1 \cdot \delta_2 \cdots \delta_m, \quad (60)$$

where $\delta_1, \delta_2 \cdots \delta_m$ are the number of secondary electrons generated at the first, second, m^{th} impacts determined by the SEY curve [108]. Clearly, if $EC > 1$, there is a potential for multipacting.

3.3 HIGHER ORDER MODES

Resonant accelerating cavities are designed for single mode operation. Higher Order Modes (HOMs) in electromagnetic cavities can be a source of beam instabilities; it is therefore necessary to identify the modes and their properties.

When characterizing the influence of HOMs, it is often useful to distinguish between “monopole” modes- those with a longitudinal electric field component E_z on the beam axis- and “multipole” modes with no E_z component. The monopole modes act to accelerate or decelerate the beam, while the multipole modes provide a transverse kick to the beam. Henceforth, the monopole modes will simply be referred to as accelerating modes while the multipole modes will be referred to as deflecting modes.

A common method for quantifying the influence a particular mode has is through what is called the *geometric shunt impedance*, or R/Q . While the definition of this quantity is somewhat different for accelerating and deflecting modes, it is a measure of how well the cavity can resonate with a particular mode.

For the accelerating mode $(R/Q)_0$ is given by [46]:

$$\left(\frac{R}{Q}\right)_0 = \frac{V_{acc}^2}{\omega_0 U}, \quad (61)$$

where V_{acc} is the accelerating voltage, ω_0 is the angular frequency of the fundamental mode, and U is the stored energy of the cavity.

To find the accelerating voltage V_{acc} , we consider that the rf electromagnetic fields within a cavity are subject to the boundary conditions given in Eq. (26). If, as before, we assume that the time and spatial dependence is sinusoidal, then the electric and magnetic fields have the form:

$$\mathbf{E}(z, t) = \mathbf{E}(z, \varphi)e^{\pm i(\omega t + \varphi)} \quad (62)$$

$$\mathbf{B}(z, t) = \mathbf{B}(z, \varphi)e^{\pm i(\omega t + \varphi + \frac{\pi}{2})}, \quad (63)$$

where ω is the angular frequency and z is the direction of propagation.

Furthermore, if we assume that the velocity does not change as the particle traverses the cavity, then the real part of the time dependence can be written as

$$e^{i(\omega t + \varphi)} \approx \cos\left(\frac{\omega z}{\beta c} + \varphi\right), \quad (64)$$

where $t = z/\beta c$. From the Lorentz force, and using the field descriptions above, we may define an accelerating (and deflecting) voltage, which is simply the maximum

energy gain a particle receives while traversing the cavity in the presence of the accelerating (or deflecting) electric and magnetic fields, divided by the particle's charge. The Lorentz force is

$$\mathbf{F} = q [\mathbf{E} + (\mathbf{v} \times \mathbf{B})] , \quad (65)$$

from which we can find the accelerating voltage, given by

$$V_{acc} = \left| \int_{-\infty}^{\infty} E_z(z, r=0) \cos \left(\frac{\omega z}{\beta c} + \varphi \right) dz \right|. \quad (66)$$

Thus, the accelerating electric field is

$$E_{acc} = \frac{V_{acc}}{L} , \quad (67)$$

where L is a reference length given in Eq. (39)

The longitudinal (R/Q) for accelerating modes where the direction of the electric field is along the z -axis, can be expressed as:

$$\left(\frac{R}{Q} \right)_n = \frac{\left| \int_{-\infty}^{+\infty} \vec{E}_z(z, r=0) e^{i \left(\frac{\omega_n z}{\beta c} + \varphi \right)} dz \right|^2}{\omega_n U} , \quad (68)$$

where ω_n is the angular frequency of mode n , βc is the particle velocity, and φ is an arbitrary phase that maximizes the coupling, defined with respect to the rf field.

For deflecting modes, we need to identify the 'transverse voltage' due to the presence of the transverse electric and magnetic fields. The transverse $(R/Q)_\perp$ can be calculated by direct integration:

$$\left(\frac{R}{Q} \right)_\perp = \frac{\left| \int_{-\infty}^{+\infty} \left(\vec{E}_\perp(z, r=0) + i(\vec{v}_z \times \vec{B}_\perp) \right) e^{i \left(\frac{\omega_n z}{\beta c} \right)} dz \right|^2}{\omega_n U} , \quad (69)$$

where the subscript \perp may refer to either the x or y direction; note however, that when discussing the transverse electric field $E_{x(y)}$ the relevant corresponding magnetic field is $B_{y(x)}$ as indicated by the i before the cross product.

Another way to calculate the coupling intensity of a deflecting mode in a resonant cavity is to use the Panofsky-Wenzel theorem [109, 110] to find $(R/Q)_\perp$. The Panofsky-Wenzel theorem relates the change in transverse momentum Δp_\perp of a fast

particle with charge e , propagating along the axis of a cavity, to the transverse gradient of the longitudinal component of the electric field (E_z) along the direction of propagation of the particle:

$$\Delta p_{\perp} = \left(\frac{e}{\omega}\right) \int_{-\infty}^{\infty} (-i) \nabla_{\perp} E_z dz. \quad (70)$$

where L is the length of the cavity and $\nabla_{\perp} = \frac{\partial}{\partial x} + \frac{\partial}{\partial y}$.

From this equation we may find an expression for the transverse voltage, such that:

$$\left(\frac{R}{Q}\right)_{\perp} = \lim_{a \rightarrow 0} \frac{\left| \int_{-\infty}^{+\infty} \left[\vec{E}_z(z, r = a) - \vec{E}_z(z, r = 0) \right] e^{i\left(\frac{\omega_n z}{\beta c} + \varphi\right)} dz \right|^2}{(k_n a)^2 \omega_n U} \quad (71)$$

where $k_n = \omega_n/c$, and a is the transverse offset from the beam axis.

3.4 BEAM INTERACTION WITH HIGHER ORDER MODES

The purpose of the accelerating cavity is to provide a way to transfer energy from an rf generator to a beam of charged particles. A particle bunch traversing the cavity is able to excite all resonant modes of the particular structure. As was previously mentioned, the consequences of this are an additional heat load on the cryogenic system and possible beam instability issues.

In the following sections, we will address these interactions. The increased demands on the cryogenic system are determined by the level of beam loading a cavity experiences from the particular beam traversing it. In this case, the induced voltage and associated power dissipation are calculated. These properties depend on the characteristics of the HOMs, and can be estimated by using an idealized point charge, i.e. independent of the beam properties. A more detailed analysis can then be done allowing for specific beam properties to be incorporated.

Instabilities introduced by the interaction of the beam with the HOMs will then be discussed. By first introducing the concept of wake fields, we will then be able to explore how these beam-produced fields interact with a single bunch as well as multiple bunches. Single bunch effects simply refer to how a bunch interacts with itself. The effects one bunch has on another, known as coupled-bunch effects, will be developed by closely following the derivations given in [78, 111–113].

3.4.1 POINT CHARGE BEAM LOADING

Each mode has an associated voltage that a point charge moving at some fixed velocity can induce, which is given by

$$\Delta V_{q,n} = -q \frac{\omega_n}{2} \left(\frac{R}{Q} \right)_n, \quad (72)$$

where ω_n is the angular frequency of mode n , and $(R/Q)_n$ is as defined in Eq. (68) and (69). This is known as the *fundamental theorem of beam loading* [114].

Each cavity mode also has an associated loss parameter k_n , which is a measure of how well the beam is able to deliver energy to the cavity at that mode's particular frequency. Expressing k_n with parameters which we can easily evaluate, such as angular frequency and geometric shunt impedance (R/Q)

$$k = \frac{\omega_n R_n}{4 Q_0}. \quad (73)$$

We introduce the energy loss of a point charge q into an otherwise empty cavity as

$$U = \alpha V_b^2 = \frac{q^2}{4\alpha} = kq^2, \quad (74)$$

where α is a constant of proportionality. The voltage induced by the point charge in the cavity mode

$$V_b = 2kq, \quad (75)$$

and the voltage induced in that mode that the charge sees

$$V_q = kq. \quad (76)$$

Using these definitions, we can express the cavity stored energy induced by a point charge as $U = V_b^2/4k$. Thus the loss parameter becomes $k = V_b^2/4U$.

The voltage induced by a charge q traversing the cavity is $V_{bn} = 2k_n q$ for each mode n . Because the modes of a cavity are orthogonal, we can sum the voltages induced, and hence power absorbed, for each mode. Thus, we can define the total beam-induced voltage V_{bT} as the sum of the fundamental mode voltage plus that of all the higher order modes

$$V_{bT} = \sum_{n=0} V_{bn} = V_{b0} \sum_{n=0} \frac{V_{bn}}{V_{b0}} = V_{b0} \sum_{n=0} \frac{k_n}{k_0}. \quad (77)$$

The total energy deposited in the cavity, after the passage of the charge is thus

$$U_T = q^2 \sum_{n=0}^{\infty} k_n = k_0 q^2 \sum_{n=0}^{\infty} \frac{k_n}{k_0}. \quad (78)$$

Note that the sum is taken over all modes because the point charge loses energy to all of them, when the cavity is initially empty. The loss in beam-energy due to the excitation of HOMs is given by

$$U_{HOM} = U_T - U_0 = k_0 q^2 (B - 1), \quad (79)$$

where $B = \sum_{n=0}^{\infty} k_n/k_0$ is the higher order mode enhancement factor. This leads to an additional power loss in the cavity of

$$\Delta P_{HOM} = \sum_{n>0} \frac{\omega_n U_n}{Q_{0n}} = q^2 \sum_{n>0} \frac{\omega_n k_n}{Q_{0n}}. \quad (80)$$

3.4.2 BEAM LOADED POWER DISSIPATION

Picking up from Eq. (80), the dissipated power for a mode n at time t can be written in terms of the cavity voltage, geometric shunt impedance, and quality factor

$$P_{c,n}(t) = \frac{|V_n(t)|^2}{(R/Q)_n Q_{0,n}}. \quad (81)$$

This dissipated power can be assumed to be constant in cw operation. Ideally, only a small portion of this power would be dissipated in the cavity walls, but instead it would be extracted via higher order mode couplers. These couplers will act as a load and couple to the given mode fields as $\beta = Q_0/Q_{ext}$. Here we have included the *external* quality factor Q_{ext} , and β is known as the coupling constant.

3.4.3 BUNCH EXCITATION OF ACCELERATING MODES

In the previous section, we discussed the idealized case of a point charge exciting HOMs, however, in actual accelerators, the charged particles are delivered in packets known as bunches. The distribution of charges in these bunches can often be approximated as Gaussian.

$$\lambda(z) = \frac{1}{\sigma_z \sqrt{2\pi}} \exp \left[-\frac{(z - z_0)^2}{2\sigma_z^2} \right], \quad (82)$$

where σ_z is the characteristic length along the propagation direction z . It should be noted that the excitation of *only* accelerating modes is accomplished by a bunch traversing the cavity exactly along the beam axis. Because the eigenmodes are orthogonal, this mode excitation can be calculated through the superposition of voltages,

$$d\tilde{V} = 2k_n dq e^{i\omega_n t_q}, \quad (83)$$

induced by individual charges dq comprising the bunch traversing the cavity in time t_q . Now, because we are dealing with bunches traveling through sinusoidally varying fields, we must also account for the phase advance of these fields,

$$\tilde{V} = 2k_n \int e^{i\omega_n t_q} dq = 2k_n \int_{-\infty}^{\infty} I(t) e^{i\omega_n t} dt, \quad (84)$$

to get the voltage induced by the entire Gaussian bunch. $I(t)$ is the time-dependent current through the cavity,

$$I(t) = \frac{Q_b}{\sqrt{2\pi}\sigma_t} \exp\left[-\frac{t^2}{2\sigma_t^2}\right], \quad (85)$$

where Q_b is the total charge of the Gaussian bunch and $\sigma_t = \sigma_z/c$ is the standard deviation of the bunch in time.

Taking the integral in Eq. (84), the bunch induced voltage is given by

$$\tilde{V} = 2k_n Q_b \exp\left[-\frac{\omega_n^2 \sigma_z^2}{2c^2}\right]. \quad (86)$$

This is the voltage induced by a single bunch. However, in reality, bunches will be traversing the cavity in succession, separated in time by T_b . Each excited mode will have a characteristic decay time of T_d , which is related to the external quality factor Q_{ext} by $T_d = 2Q_{ext}/\omega_n$. After a time t , the voltage remaining in the cavity after the passage of a single bunch will be

$$V_q \exp(i\omega_n t) \exp\left(-\frac{t}{T_d}\right). \quad (87)$$

After a second bunch passes, the instantaneous voltage is

$$V_q \left[1 + \exp(i\omega_n T_b) \exp\left(-\frac{T_b}{T_d}\right) \right]. \quad (88)$$

For a cw beam, in steady state, the beam-induced voltage can be obtained by summing an infinite number of voltages

$$\tilde{V}_b = V_q \sum_{k=0}^{\infty} \exp(ik\omega_n T_b) \exp\left(-k\frac{T_b}{T_d}\right), \quad (89)$$

where the time dependence $\exp(i\omega_n T_b)$ has been left out because we are dealing with the steady state of a single time structure bunch [46]. Taking the sum over k , we obtain

$$\tilde{V}_b = \frac{V_q}{1 - \exp(-T_b/T_d) \exp(i\omega_n T_b)}. \quad (90)$$

We are interested in determining the power dissipated due to the induced voltage, which is why it is necessary to separate the real and imaginary parts of Eq. (90). Doing so, we find

$$\begin{aligned} \tilde{V}_b &= \frac{V_q}{[1 - \exp(-T_b/T_d) \cos(\omega_n T_b)]^2 + \exp(-2T_b/T_d) \sin^2(\omega_n T_b)} \\ &\quad - \frac{V_q \exp(-T_b/T_d) \cos(\omega_n T_b)}{[1 - \exp(-T_b/T_d) \cos(\omega_n T_b)]^2 + \exp(-2T_b/T_d) \sin^2(\omega_n T_b)} \\ &\quad + i \frac{V_q \exp(-T_b/T_d) \sin(\omega_n T_b)}{[1 - \exp(-T_b/T_d) \cos(\omega_n T_b)]^2 + \exp(-2T_b/T_d) \sin^2(\omega_n T_b)}, \end{aligned}$$

and simplifying the real part $\Re(V_b)$

$$\Re(\tilde{V}_b) = 1 + \frac{\exp(-T_b/T_d) \cos(\omega_n T_b) - 1}{1 + \exp(2T_b/T_d) - 2 \exp(T_b/T_d) \cos(\omega_n T_b)}. \quad (91)$$

Therefore, the power dissipated by the beam in a given mode is

$$P_b = I_0 \Re(\tilde{V}_b), \quad (92)$$

where I_0 is the average beam current.

3.4.4 BUNCH EXCITATION OF DEFLECTING MODES

Using the Panofsky-Wenzel Theorem as given in Eq. (70) and the associated transverse $(R/Q)_\perp$ given in Eq. (71), we can calculate the transverse voltage induced by a bunch as

$$V_\perp = \frac{1}{2} i a q \frac{\omega_n^2}{c} \left(\frac{R}{Q} \right)_{\perp, n}. \quad (93)$$

As before, for a pulse consisting of several bunches, the sum of individual voltages can be taken as long as the phase relationship and their exponential decay is taken into account, and the offset a from the beam axis is constant.

The formulas in this section provide a good first estimate of the voltage and associated power dissipation that should be expected from the beam excitation of HOMs.

Another thing to consider is HOMs whose frequency falls close to what are known as *machine lines*. The term machine line refers to frequencies that are multiples of the bunch frequency and the frequency of any bunch substructures. For example, a machine operating with a repetition rate (lowest cavity frequency / bunch frequency $\times 100\%$) of 100%, where the bunches are injected at 162.5 MHz will have machine lines at $n \cdot 162.5$ MHz with $n = 1, 2, 3, \dots$

3.5 WAKE FIELDS

Before discussing how beam-excited HOMs can go beyond generating additional power dissipation, and cause instabilities in the beam itself, we must introduce the concept of wake fields. Relativistic charged particles traveling through a cavity will interact with the surrounding environment. If, for example, there are variations in the cavity profile, material, or material properties, wake fields will be generated which can create a wake potential on trailing particles. This results in beam instabilities. As we have seen in the previous sections, the modes excited through this interaction between the beam and the cavity will be dissipated in the cavity walls, thus leading to an additional heat load.

3.5.1 WAKE FIELD GENERATION

Consider a leading particle q_L that is moving in the z direction with velocity $v \approx c$ a distance r_1 from the z axis. A trailing particle q_t is a distance s behind q_L and offset r_2 from the z axis. This second particle travels at the same velocity v as the first. The position at time t of the leading charge is then $z = ct$ while the trailing charge position is $s = ct - z$. The situation is depicted in Fig. 15.

If the particles are traveling in, for example, a perfectly conducting beam pipe, there would be no force on the trailing particle. This is because the fields produced by the leading particle are Lorentz contracted into a thin disk perpendicular to the direction of motion and opening at an angle on the order of $1/\gamma$, where γ is the usual

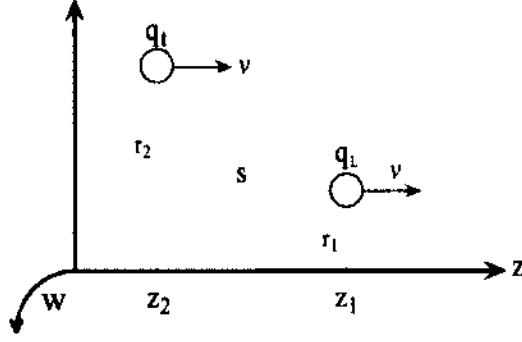


FIG. 15: A point charge q_t trailing another q_L . Both are traveling at $v \approx c$.

relativistic factor given in Eq. (59). However, if the situation is even slightly different than this idealized case, there will be an interaction between the particles.

This interaction can be described by solving Maxwell's equations to find the fields generated by the leading particle and how these fields affect the momentum of the trailing particle. When the fields are known, the momentum change can be calculated from the Lorentz force,

$$\Delta p(r_1, r_2, s) = q_t \int_{-\infty}^{\infty} [\mathbf{E}(r_1, r_2, z, t) + c\hat{z} \times \mathbf{B}(r_1, r_2, z, t)]_{t=(z+s)/c} dz. \quad (94)$$

The beam dynamics will be different in the longitudinal (z) and transverse (x and y) directions. Because of this, the change in momentum is normally separated into a longitudinal component Δp_z and a transverse component $\Delta \mathbf{p}_\perp$. At this point, the longitudinal and transverse wake function can be introduced as

$$w_z(r_1, r_2, s) = \frac{\Delta p_z c}{q_L q_t} = \frac{1}{q_L} \int_{-\infty}^{\infty} [E_z]_{t=(z+s)/c} dz, \quad (95)$$

$$\mathbf{w}_\perp(r_1, r_2, s) = \frac{\Delta \mathbf{p}_\perp c}{q_L q_t} = \frac{1}{q_L} \int_{-\infty}^{\infty} [\mathbf{E}_\perp + c\hat{z} \times \mathbf{B}]_{t=(z+s)/c} dz. \quad (96)$$

Thus, we have two effects on the trailing particle: one changes the energy while the other deflects its trajectory. The bunch size is much less than the beam pipe, meaning that $r_1, r_2 \ll \text{beam aperture}$. This allows for the longitudinal wake function to be approximated as $w(s) = w(0, 0, s)$ [115]. For the transverse wake function, the small values of r_1 and r_2 make it possible to expand $\mathbf{w}_\perp(r_1, r_2, s)$ and keep only the low order linear terms, of which, the dipole term is dominant [115].

We are interested in finding how the wake fields produced by the lead particle cause either a loss in the voltage or transverse kick to the trailing particle. As Fig. 15 illustrated, the trailing particle is a distance s from the lead particle. In the case of a bunch with a longitudinal charge distribution $\rho(s)$, the longitudinal wake potential can be defined as

$$W_z(s) = \int_0^\infty w_z(s)\lambda(s-s_0)ds, \quad (97)$$

where s is the test particle position and the integral is taken over all such particles and λ is the line density of charge. Similarly, the transverse wake potential is given by

$$W_\perp(s) = \int_0^\infty w_\perp(s)\lambda(s-s_0)ds. \quad (98)$$

Equation (97) gives the voltage lost by a test particle at position s while Eq. (98) is the transverse kick for a test particle at that same position. For our purposes, we would like to find the impedance, which is the Fourier transform of the wake function:

$$Z(k) = \frac{1}{c} \int_{-\infty}^\infty w_z(s)e^{-iks} ds \quad (99)$$

$$Z_\perp(k) = \frac{1}{c} \int_{-\infty}^\infty w_\perp(s)e^{-iks} ds. \quad (100)$$

The wakes, and thus the associated impedance, can persist for the duration of a single bunch or last longer then the time between bunches. The former are known as short-range wake fields and the latter are long-range wake fields.

3.6 BEAM INSTABILITIES DUE TO HIGHER-ORDER MODE EXCITATION

In addition to understanding what the excitation of higher order modes will add to the cryogenic requirements of a machine, it is essential to look at what the voltage induced by the beam, on the beam, will do to the overall beam quality. Even if the power dissipated in the cavity walls is negligible, if small transverse kicks to the beam cause undesirable effects at the end of the linac, higher order mode damping may still be necessary.

There are two scenarios which need to be considered. The first is on a time scale representative of a single-bunch, single-pass effects. The second is on a larger time

scale, where the modes excited by one bunch remain long enough to interact with subsequent bunches. The latter are referred to as coupled bunch effects.

3.6.1 SINGLE-BUNCH EFFECTS

As we have seen, short-range wake fields act over the time period of the bunch length. This is typically in the picosecond to nanosecond range. With this short time period, these short range wakes do not depend on the Q_0 of the particular HOM because they are often on the order of 10^9 and thus decay on a much longer time scale. Instead, these wakes depend only on the geometric shunt impedance of the mode, R/Q_0 , which is only dependent on the cavity geometry. Longitudinal wakes decrease as the square of the beam aperture. So from a beam dynamics point of view, a larger beam aperture can be desirable [46].

The effects of longitudinal wake fields can result in an energy loss at the tail of the bunch caused by the head of the bunch. This can lead to harmful energy spread. In the case of a linear accelerator, which we are primarily concerned with, this energy spread can degrade the final focus of the beam which makes a small spot size difficult to achieve. The energy spread induced by wake fields can be estimated as

$$\frac{\delta E_b}{E_b} = \frac{2qk_{\parallel}}{E_{acc}}, \quad (101)$$

where E_b is the beam energy and k_{\parallel} is the total structure loss factor.

The short-range transverse wake fields can deflect the tail of the bunch which leads to emittance growth and beam halo. Emittance, in this case, just refers to the focusing or defocusing of the particle bunch by the rf fields. It is proportional to the area made by the beam in phase space. A detailed description of beam halo can be found in [78]. Because of emittance growth, the overall effect of transverse wakes is to reduce the charge per bunch. Transverse wakes decrease as the cube of the aperture [46]. So again, a larger beam aperture is desirable from a beam dynamics standpoint.

3.6.2 COUPLED-BUNCH EFFECTS

As was mentioned in the previous section, if the wake field remains longer than the spacing of the bunches, the subsequent bunches can be affected. These are called coupled bunch instabilities. We previously saw that the value of R/Q_0 can be used

to describe how well a single pass of a beam bunch can excite a given mode. A train of bunches, on the other hand, can excite a mode for a time on the order of Q_L/ω_n , and as such, the quantity $R/Q \times Q_L$ is used to describe the coherent summation of multiple excitations over the filling time of a given mode.

3.6.3 SINGLE-PASS EFFECTS

In a previous section, we saw that for a deflecting mode to be excited by a particle bunch, the particles need to be slightly off-axis. Dipole HOMs have the effect of pushing the particles into areas of higher longitudinal field. This longitudinal field can accelerate or decelerate the beam, depending on the sign of

$$\Delta W = e \int_0^L \left(\frac{\partial E_z}{\partial x} \right) x dz, \quad (102)$$

where x is the transverse displacement relative to the axis, E_z is the longitudinal electric component of the deflecting mode, and L is the length of the cavity. If the value is negative, the particle gives energy to the deflecting mode. In turn, the now stronger deflecting field on-axis further deflects the beam. This feedback loop is known as ‘‘Regenerative Beam Breakup.’’ The fact that this is a collective effect suggests that there is a beam current, below which the effect is negligible. This is known as the threshold current and is given by [78]

$$I_{th} \approx \left(\frac{\pi}{L} \right)^2 \frac{\lambda_D V_b}{4Q(\tau_{\perp}/Q)} F_a(x), \quad (103)$$

where λ_D is the wavelength of the HOM, V_b is the beam-induced voltage, L is the length of the cavity and τ_{\perp} is the transverse shunt impedance per unit length. This threshold current is defined by the condition that the power delivered from the beam into the field is equal to the power losses of the mode in the structure [116]. $F_a(p_f/p_i)$ is a correction factor to account for acceleration from p_i to p_f ,

$$F_z(x) = \frac{(x-1)^3}{6x[(x-1)^2/2 + x - 1 - x \ln x]}. \quad (104)$$

For negligible acceleration (i.e. $p_f/p_i = x \approx 1$), F_a goes to 1, while for large arguments, F_a goes to 1/3 [117]. For superconducting cavities, the L^2 dependence of Eq. (103) is not that important since they generally have fewer cells. However, for low-energy beams, modes with a high Q_L could pose a significant problem.

If single-bunch effects are not a concern, it is still possible for a bunch passing through the cavity, offset from the beam axis, to excite a deflecting mode. This mode can then cause deflection in subsequent bunches. The level of additional excitation, by subsequent bunches, depends on the relative frequencies of the bunch train and the excited HOM. As in the previous section, when HOMs are near harmonics of the bunch frequency, like the machine lines, resonance conditions can occur and cause an even greater amplification. Even when this is not the case, it is possible for a series of cavities to produce an amplification of the initial offset when the first bunch entered the first cavity. This effect is known as “cumulative beam breakup.”

3.7 MULTIPOLE COMPONENTS OF THE ACCELERATING FIELD

There are no srf cavities with a pure TM mode, even a pillbox cavity with beam pipes will have small deviations from the ideal case. An increasing complexity of the structure, especially in the area of the beam, introduces additional higher order multipole components to the accelerating field. In order to accurately describe the motion of particles traversing a linear accelerator, it is necessary to account for these additional components and work toward minimizing them, if needed.

The following treatment of the multipole component derivation for magnets is based on that given in [118]. Beginning with Maxwell's equations, Eq. (27), we see that they are linear,

$$\nabla \cdot (\mathbf{B}_1 + \mathbf{B}_2) = \nabla \cdot \mathbf{B}_1 + \nabla \cdot \mathbf{B}_2, \quad (105)$$

and

$$\nabla \times (\mathbf{H}_1 + \mathbf{H}_2) = \nabla \times \mathbf{H}_1 + \nabla \times \mathbf{H}_2, \quad (106)$$

where $\mathbf{H} = (1/\mu)\mathbf{B}$. This means that if two fields \mathbf{B}_1 and \mathbf{B}_2 satisfy Maxwell's equations, so does their sum $\mathbf{B}_1 + \mathbf{B}_2$. As a result, the principle of superposition can be used to construct complicated magnetic and electric fields by adding together a set of simpler fields.

We are interested in the fields that satisfy Maxwell's equations in free space, e.g. the interior of an accelerator cavity with no charges present. In that case, $\mathbf{J} = 0$ and thus

$$\begin{aligned}\nabla \cdot \mathbf{B} &= 0 \\ \nabla \times \mathbf{B} &= 0.\end{aligned}\tag{107}$$

If we consider a field given by $B_z = \text{constant}$, and

$$B_y + \imath B_x = C_n (x + \imath y)^{n-1},\tag{108}$$

where n is a positive integer and C_n is a complex number. It should be noted that the field components B_x , B_y , and B_z are all real but the complex notation is used simply for convenience. To see that Eq. (108) is a solution to Maxwell's equations, consider the operator

$$\frac{\partial}{\partial x} + \imath \frac{\partial}{\partial y}.\tag{109}$$

When we apply this to the left side of Eq. (108), we find

$$\left(\frac{\partial}{\partial x} + \imath \frac{\partial}{\partial y}\right)(B_y + \imath B_x) = \left(\frac{\partial B_y}{\partial x} - \frac{\partial B_x}{\partial y}\right) + \imath \left(\frac{\partial B_x}{\partial x} + \frac{\partial B_y}{\partial y}\right) = [\nabla \times \mathbf{B}]_z + \imath \nabla \cdot \mathbf{B}.\tag{110}$$

Further, from Eq. (108), we see that B_x and B_y are independent of z and therefore the x and y components of $\nabla \times \mathbf{B}$ vanish. If we now apply Eq. (109) to the right side of Eq. (108),

$$\left(\frac{\partial}{\partial x} + \imath \frac{\partial}{\partial y}\right)(x + \imath y)^{n-1} = (n-1)(x + \imath y)^{n-2} + \imath^2(n-1)(x + \imath y)^{n-2} = 0.\tag{111}$$

Hence, Eq. (108) is a solution to Maxwell's equations for a magnetostatic system in free space. Fields given by Eq. (108) are called *multipole fields*, and because of the linearity of Maxwell's equations, any number of these multipole fields can be superposed and still remain valid solutions to Maxwell's equations.

Eq. (108) can also be written in the more conventional notation of Ref. [111], which we will use here as,

$$B_y + \imath B_x = B_{ref} \sum_{n=1}^{\infty} (b_n + \imath a_n) \left(\frac{x + \imath y}{R_{ref}}\right)^{n-1}.\tag{112}$$

where the b_n are known as the normal multipole coefficients and a_n are the skew multipole coefficients. B_{ref} is the magnetic field value at some reference radius R_{ref} .

It is useful to consider a few examples to aid in interpreting the impact of multipole components. Consider the fields on the beam axis ($y = 0$).

$$B_y = B_{ref} \sum_{n=1}^{\infty} b_n \left(\frac{x}{R_{ref}} \right)^{n-1} \quad (113)$$

$$B_x = B_{ref} \sum_{n=1}^{\infty} a_n \left(\frac{x}{R_{ref}} \right)^{n-1} . \quad (114)$$

A multipole component where $n = 1$ (a dipole) would have field components $B_y = b_1 B_{ref}$ and $B_x = a_1 B_{ref}$, which are constant. A component with $n = 2$ is a quadrupole and the fields are given by

$$B_y = b_2 B_{ref} \frac{x}{R_{ref}} \quad (115)$$

$$B_x = b_2 B_{ref} \frac{x}{R_{ref}} , \quad (116)$$

which shows that both B_x and B_y vary linearly with x . A sextupole ($n = 3$) would vary as x^2 , octupole ($n = 4$) as x^3 and so forth.

Figure 16 [118] shows the field patterns of common multipoles with their skew components.

The higher order multipole components are analyzed using the method given in [119]. We start with the accelerating gradient,

$$E_{acc}(r, \phi, z) = E_z(r, \phi, z) \cdot e^{i \frac{\omega z}{c}} , \quad (117)$$

and using the multipole expansion,

$$E_{acc}(r, \phi, z) = \sum_n E_{acc}^{(n)} r^n e^{in\phi} = \sum_n E_z^{(n)} r^n [\cos n\phi + i \sin n\phi] , \quad (118)$$

where n is the multipole order, r is the radius at which the field is evaluated, and ϕ is the angle from the transverse axis. The multipole field components $E_z^{(n)}(z)$ can be calculated by using the Fourier series expansion of $E_z(r, \phi, z)$, which is given by,

$$E_z^{(n)}(z) = \frac{1}{r^n} \int_0^{2\pi} E_z(r, \phi, z) [\cos n\phi + i \sin n\phi] d\phi , \quad (119)$$

with the time-dependent multipole field component given by $E_{acc}^{(n)}(z) = E_z^{(n)}(z)e^{i\omega t}$.

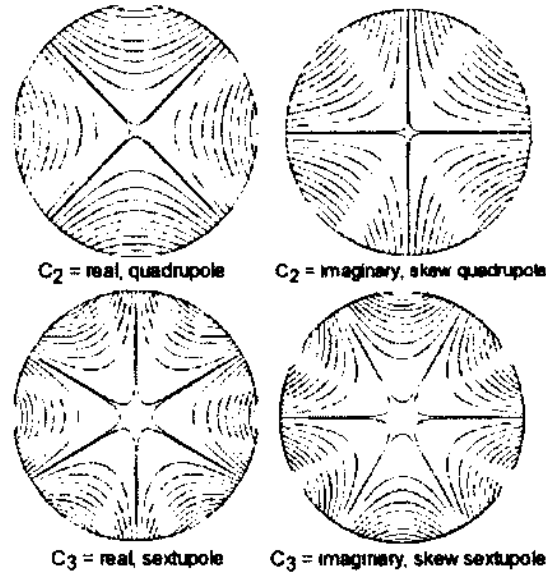


FIG. 16: Examples of common multipole field patterns.

The multipole components b_n are defined using the standard definition for magnets [119], and can be calculated by equating a magnetic kick to the transverse rf-kick strength,

$$b_n = \int_{-\infty}^{\infty} B^{(n)}(z) dz \quad [\text{T/m}^{n-2}] , \quad (120)$$

where $B^{(n)}(z)$ is given by

$$B^{(n)}(z) = \frac{1}{qc} F_t^{(n)}(z) = i \frac{n}{\omega} E_{acc}^{(n)}(z) \quad [\text{T/m}^{n-1}] . \quad (121)$$

3.8 MECHANICAL PROPERTIES

For high quality, reliable beams, it is essential that the frequency of a cavity can be reliably maintained within some bandwidth, usually several Hz. Therefore, it is imperative that we estimate how much the frequency varies from external pressure, radiation pressure, and mechanical vibrations. In addition to the beam quality issues associated with frequency shifts, there is also extra rf power required to prevent detuning, which can add to capital and operational costs.

To minimize the effort needed to stabilize the frequency, some sort of tuner is usually employed which will allow for a controllable rf frequency perturbation that can then be used to compensate for the “natural” frequency detuning [120]. A detailed tuner design is beyond the scope of this dissertation, however, a detailed analysis of methods for minimizing the detuning effects will be presented.

3.8.1 PRESSURE SENSITIVITY

When the cavity is under vacuum, the walls will experience external pressure, from either atmospheric pressure or liquid helium, which will change the internal volume and cause stress on the cavity surface. The change in internal volume results in a frequency shift and should be accounted for in order to achieve the target frequency during cryogenic testing and operation.

How sensitive a cavity is to He pressure must be considered when designing a cavity intended to be placed in a helium vessel and cryomodule. In addition to the deformations, micro-oscillations can lead to additional frequency instabilities [121]. All of these perturbations to the cavity volume, and the accompanying frequency shifts, can be described by the Slater perturbation theorem [122]. The theory tells us that the first-order shift $\delta\omega$ in the angular frequency ω is given by

$$\frac{\delta\omega}{\omega} = \frac{\int(\mu H^2 - \epsilon E^2)d\tau}{4U}, \quad (122)$$

where H is the magnetic field, E is the electric field, and U is the stored energy of the unperturbed cavity mode while ϵ and μ are the permittivity and permeability, respectively. The integral is taken over the *perturbed* volume of the cavity [123]. From Eq. (122), it is clear that the frequency increases if H is large where the walls are pushed in and decreases if E is large there.

3.8.2 MECHANICAL MODES

Mechanical vibrations from the environment can couple to the cavity, causing it to oscillate. This motion can cause a frequency variation of the accelerating mode, which can lead to amplitude and phase modulation of the electromagnetic field.

When a cavity has couplers attached to it, we use the loaded quality factor Q_L , defined previously as

$$Q_L = \frac{\omega U}{P_{total}}, \quad (123)$$

where U is the stored energy and P_{total} is the total power dissipation, including that from the cavity walls and that which leaks out of all couplers. The loaded quality factor determines the bandwidth of the cavity, which, in turn, determines the frequency stability requirements. The bandwidth is given by,

$$\Delta\omega = \frac{\omega_0}{Q_L}, \quad (124)$$

where, as before, ω_0 is the angular frequency of the fundamental mode.

For some applications, such as Rare Isotope Accelerators and Energy Recovery Linacs, a Q_L of greater than 10^7 is desirable [124]. This means that we would like to have as low a P_{total} as possible. With the fairly low gradient for these applications, much of the rf power requirement will be determined by the phase and amplitude control rather than what is needed for the beam [125]. With all things being equal, there is a one-to-one relationship between the available rf power that has to be supplied to the cavity and the amount of frequency compensation that can be achieved [125]. This is why, especially for the applications we are concerned with, the power needed for frequency stabilization is of great importance.

3.8.3 LORENTZ FORCE DETUNING

In addition to the frequency instabilities caused by mechanical vibrations, there are also deformations to the cavity walls due to radiation pressure from the fields, which are also described by Eq. (122). This mechanical deformation is appropriately known as Lorentz Force Detuning (LFD). In Fig. 17, we can see an exaggerated view of the deformation taking place in an elliptical cavity due to the Lorentz force.

In an elliptical cavity, the regions that experience the greatest deformation are also the areas that cause the largest change in frequency. The magnetic field tends to increase the radius, as you move from the center to the iris, while the electric field tends to decrease the cell length. Thus, both the magnetic and electric field tend to decrease the frequency. In addition, at the point where the Lorentz force changes signs, the frequency shift due to each of the fields also changes signs (magnetic field would increase cell length and electric field would decrease radius). This results in

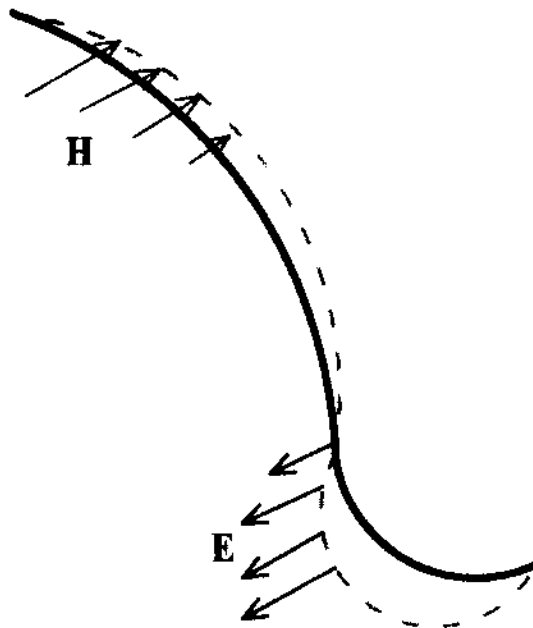


FIG. 17: Effect of the Lorentz force on the cell shape of an elliptical cavity.

an inability to compensate for the total frequency shift through pure geometric optimization [46]. As will be seen in Chapter 7, through judicious mechanical stiffening, the frequency shift due to LFD can almost be completely eliminated in spoke cavities.

While these cavities are intended to operate continuous wave (cw), it is important to understand the sensitivity to LFD for when considering overall frequency tuning requirements. LFD results in a change in the rf eigenfrequency, which is described by

$$P = \frac{1}{4}(\mu_0 H^2 - \epsilon_0 E^2), \quad (125)$$

while the resultant change in frequency will be

$$\Delta f = -k_L E_{acc}^2, \quad (126)$$

where k_L is Lorentz force detuning coefficient. A typical coefficient is a few Hz/(MV/m)².

CHAPTER 4

ELECTROMAGNETIC OPTIMIZATION

As was mentioned in Chapter 3, many of the simulations, particularly those for electromagnetic design, were performed using CST Microwave Studio[®] [94]. The primary source of error within such software comes from the discretization of the mesh. This is typically small compared to that introduced during the fabrication process. Therefore, rather than focusing on errors in individual data points, we determine how a parameter such as frequency changes with finer and finer mesh. This will give us an idea of how fine a mesh we must have in order to get acceptably accurate results. Figure 18 shows the convergence of the frequency on a value as the mesh number increases. Symmetry planes were used so that only one quarter of the cavity had to be meshed.

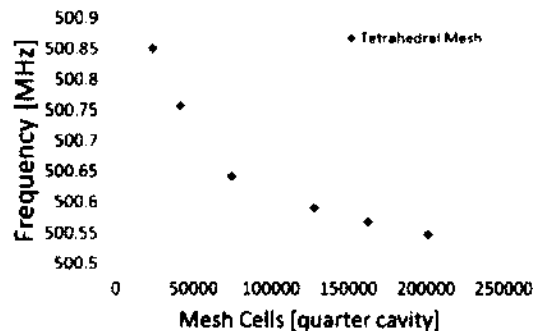


FIG. 18: Convergence of the frequency as the number of mesh cells are increased.

4.1 DESIGN GOALS

High surface fields in superconducting cavities are highly undesirable because of the detrimental effects on performance. At high surface magnetic fields, quenching can occur, and high surface electric fields can cause field emission. When comparing the performance of cavities, normalized surface fields are often discussed. These fields are E_p/E_{acc} and B_p/E_{acc} , where E_p is the peak surface electric field, B_p is

the peak surface magnetic field and E_{acc} is the accelerating electric field defined in Eq. (67). Minimizing these fields is one of the goals in cavity design. Note that, for all the cavities that we have investigated, the inside length of the cavity (iris-to-iris) is always substantially less than that given by Eq. (39) when N is the number of gaps. Therefore, if we had chosen the inside length as the reference length to define E_{acc} , the quoted ratios of peak fields to accelerating field would have been lower. The disadvantage of that choice is that the inside length, even at constant frequency and β_0 , is not constant but depends on the details of the cavity geometry, and therefore makes it difficult to compare different designs. Our choice for the reference length is independent of the particularities of a design, once the frequency, β_0 , and number of spokes are chosen, and makes comparison easier.

It is important to note that there is no such thing as an “optimal” design for all applications. Each application will have specific design considerations; what may constitute an optimized design for one project may in fact be undesirable for another. An optimized design, however, is more than just minimization of normalized fields since, at some point in the design, both peak surface electric field and peak surface magnetic field cannot be reduced anymore and the reduction of one often leads to the increase of the other. It is then important for the normalized surface fields to be balanced in the sense that the current technical limits or application-specific demands are achieved simultaneously. In other words, if a peak surface electric field of 40 MV/m and a peak surface magnetic field of 80 mT can be routinely reached with the same probability, then a cavity with a ratio of $B_p/E_p \simeq 2$ mT/(MV/m) would indicate that the normalized fields are properly balanced. Obviously, this “optimized” ratio is very much dependent on the state of the art, and has changed over time. It is also dependent on the application and the intended operational conditions, such as temperature. For this work we have used as a design goal a ratio of $\simeq 2$ mT/(MV/m).

In some applications, maximization of the shunt impedance is more important than minimization of the surface fields and the designs that maximize the former can be different from the ones that minimize the latter. In other words, there is not a single best optimized design, and what we have attempted here is to show how various design choices (dimensions, shapes) can affect the electromagnetic properties (fields, shunt impedance).

The design environment within CST allows for a multitude of structures to be

simulated and a variety of calculations to be performed. The electromagnetic simulations are accomplished using the Finite Integration Technique [94]. From these simulations, the frequencies and field properties of a desired number of cavity modes can be determined. In addition, the cavity properties described in the previous section can be evaluated.

4.2 DESIGN STRATEGY

The basic geometry of a spoke cavity consists of an outer conductor, usually either cylindrical or rectangular, with one or more “spokes,” which are conductors that run radially, through the longitudinal symmetry axis. A number of strategies can be used for the optimization process; here we will provide a detailed description of those presented in [126]. Alternatively, advanced methods such as combining a simulation code with a multi-objective genetic algorithm have been used [31]. Multi-objective optimization can rapidly lead to an optimized design but makes it more difficult to separate the impact of each parameter on the cavity properties. Here we have chosen a more systematic approach which results in consistent optimization outcomes to those obtained with a multi-objective approach.

Any optimization strategy will quickly reveal that the geometry of the spokes themselves often has the greatest impact on the peak surface fields. Spokes can be broken into two areas in terms of both their physical location and field (electric or magnetic) that they primarily affect. The region which intersects the wall of the outer conductor is referred to as the spoke base, while the region intersecting the beam line is referred to as the spoke aperture. The base or aperture regions are often referred to as having elliptical, racetrack, or cylindrical geometries. Figure 19 shows the main parameters of spokes with a racetrack geometry. It should be noted that the same definitions apply to elliptical spoke geometries.

Performing a sweep of the parameters identified in Fig. 19, whether the spoke aperture and base are of the elliptical or racetrack variety, can be done by decoupling the size from the shape. By doing so, desirable shapes can be found and the best sizes of those can be determined. Alternatively, both the size and shape can be varied simultaneously.

In order to identify a shape which effectively minimizes the surface fields, several different values for spoke base (aperture) area or circumference can be chosen and a sweep of two parameters can be done while maintaining that area or circumference.

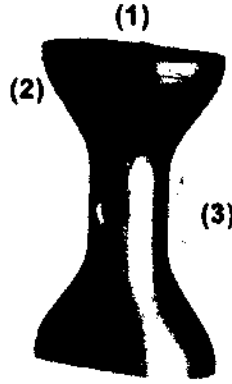


FIG. 19: CST Microwave Studio[®] (MWS) view of a racetrack-shaped spoke. (1) base or aperture width, (2) base or aperture length, (3) aperture height.

For example, the base width and length can be varied while maintaining a constant circumference. This has the effect of changing the base shape while keeping the overall surface area in contact with the fields unchanged. Doing so allows us to distinguish shapes that are more desirable than others. With a variety of preferred shapes identified, the optimal sizes of these shapes can be obtained and compared by scaling the dimensions while maintaining the shape.

In addition to the geometries explored, it is important to investigate the orientation of the spokes relative to the beam line. We define a spoke base or aperture region as being longitudinal if the longest dimension (either racetrack or elliptical geometries) is parallel to the beam line and transverse otherwise. More will be said about this in the next section.

4.3 DEPENDENCE OF RF PROPERTIES ON GEOMETRIC PARAMETERS

In this section, we analyze dependencies that the peak surface fields and shunt impedance have on various cavity dimensions. It should be understood that what is described here are general trends; the actual magnitudes of variations will depend greatly on the values of the cavity parameters which remain fixed.

The cavity radius and iris-to-iris length are approximately determined by the operating frequency and desired β_0 . The peak surface fields depend greatly on the shape and dimensions of both the spoke base and the spoke aperture region. All

data presented have been acquired under conditions of constant frequency and β_0 , meaning that the cavity radius and iris-to-iris length were varied along with the parameters under consideration in order to maintain constant frequency and design velocity.

As was already mentioned, a reference length given by Eq. (39), where N is the number of full accelerating gaps, is used here. For high-velocity spoke cavities, we found that, if a single-spoke cavity is assumed to have two accelerating gaps and a two-spoke cavity has three full accelerating gaps, then, for identical spoke and end-cap geometries, normalized surface fields and shunt impedance are consistent and can be accurately compared. Figure 20 shows an example of the dependence of the normalized magnetic field on the spoke base length. The cavities are the same in all respects except iris-to-iris length and outer conductor diameter.

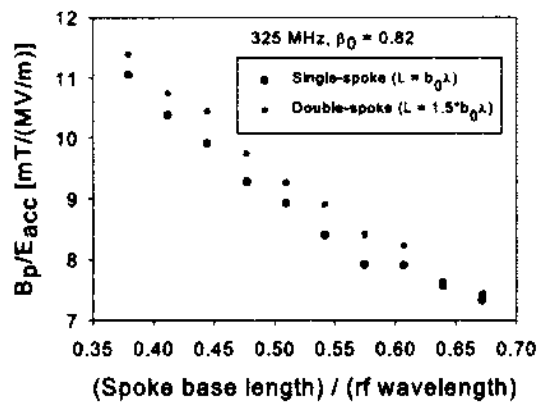


FIG. 20: Dependence of the normalized magnetic field on the spoke base length for a single- and double-spoke cavity with the same spoke and end cap geometries.

Figure 21 shows some additional cavity parameters discussed here. Both the spoke base and aperture region have been investigated with elliptical, cylindrical, and racetrack geometries. The parameters in Figs. 19 and 21 will be discussed in terms of how they influence the normalized fields, shunt impedance, energy content, and frequency. There are no significant differences in terms of peak surface fields and shunt impedance achievable with elliptical or racetrack geometries, so here we have chosen to present the optimization results for a racetrack spoke base geometry.

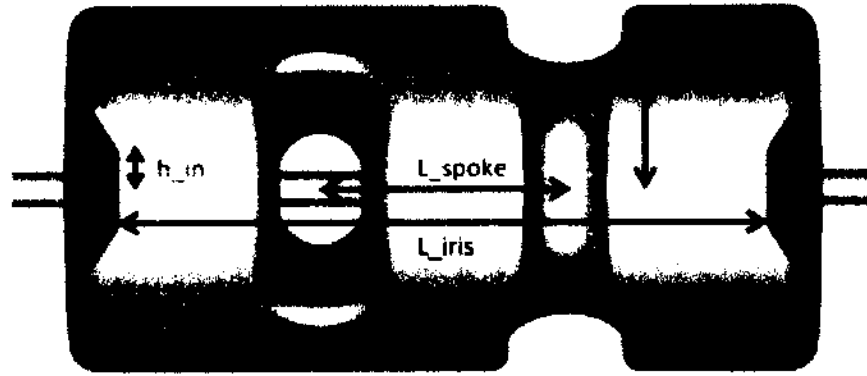


FIG. 21: Cut-away view of a two-spoke 500 MHz, $\beta_0 = 1$ cavity.

4.3.1 SPOKE BASE

The magnetic field of the fundamental accelerating mode in a spoke cavity is more concentrated near the surface of the outer conductor and encircles the spokes; the size and shape of the spoke base region thus has a strong effect on the peak surface magnetic field and a lesser effect of the peak surface electric field.

A comparison of the normalized magnetic fields that longitudinal and transverse spoke base orientations provide, in a double-spoke cavity, is presented in Figs. 22-24. Note that for the longitudinal orientation, the ratio of (base length) / (rf wavelength) is limited to around 0.5. This is because the length of the cavity constrains this dimension in a way the diameter does not constrain the transverse orientation.

The dependence of the normalized field on the longest base dimension (which we call the length) is similar, at smaller dimensions, for both orientations; however, a lower normalized field can be obtained with a larger transverse base. The difference, for this given cavity's other fixed dimensions, is about 25% for the normalized magnetic field, which is significant. An even greater difference can be seen in Fig. 23. A transverse spoke base can provide a shunt impedance which far exceeds that of a longitudinal base. At a value of spoke base length to rf wavelength of 0.45, for example, a transverse spoke base can provide a shunt impedance on the order of 2 times higher than a longitudinally oriented spoke base. In a small machine, intended to operate at 4 K, this difference in shunt impedance would have a dramatic impact on the power dissipation and thus the cooling requirements.

Additionally, the energy content in a longitudinal orientation can be close to 50% higher than its transverse counterpart. This is illustrated in Fig. 24. In terms of microphonics control, the higher energy content of a longitudinally oriented spoke base could be much more problematic [125].

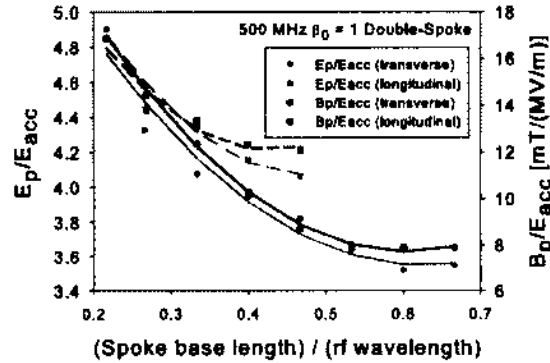


FIG. 22: Dependence of the normalized magnetic and electric fields on the spoke base length and orientation.

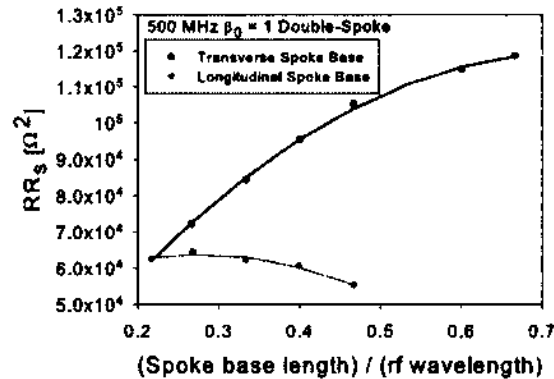


FIG. 23: Dependence of the geometric shunt impedance on the spoke base length and orientation.

For the two orientations, the difference in the achievable normalized electric field is not as much as for the other rf properties. Figure 22 shows this difference to be just a few percent. It must be stressed, however, that these results by no means suggest that a longitudinal orientation should not be considered. As will be shown later, the longitudinal base results in a smaller cavity diameter for a given frequency

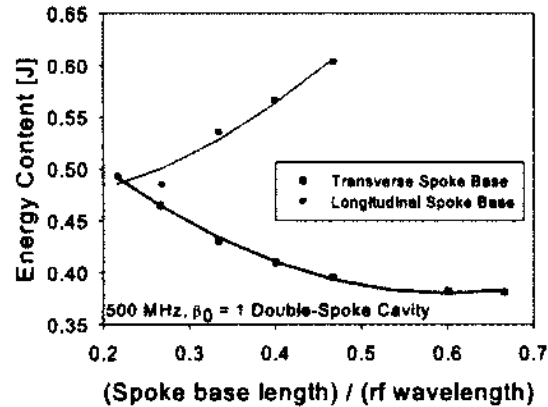


FIG. 24: Dependence of the energy content (at 1 MV/m) on the spoke base length and orientation.

and a stronger cell-to-cell coupling (i.e. increased mode separation). For applications where shunt impedance is not critical, but size and large mode separation are, the longitudinal orientation may be preferable.

In Fig. 25, the dependence of the normalized fields on the spoke base length is shown for a single-spoke cavity. Note that the trends are the same as for a double-spoke cavity, but the range of achievable values is much narrower.

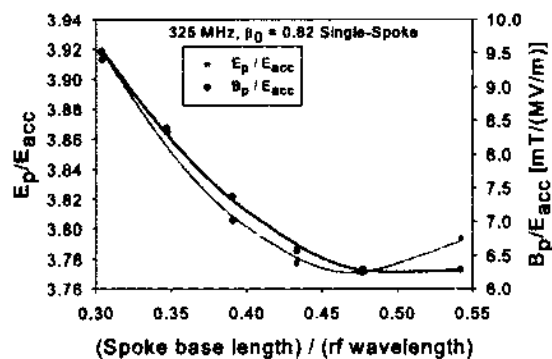


FIG. 25: Dependence of the normalized magnetic and electric fields on the spoke base length (for a transverse orientation).

Before proceeding with any optimization strategy, it is important to first understand how each of the individual parameters affect the cavity's rf properties. Figures

22 - 25 have already shown the dependence that several cavity properties have on the spoke base length. Figure 26 shows a parameter sweep of the spoke base width (transverse and longitudinal racetrack geometry) to show how the normalized magnetic and electric fields are affected, while Fig. 27 shows how the shunt impedance and energy content change. Note that in Figs. 26 and 27, the spoke base approaches a cylinder, which would be located far to the right on the plots, but never actually becomes cylindrical. This is because at this base length, a cylindrical base would be impractical and thus not relevant.

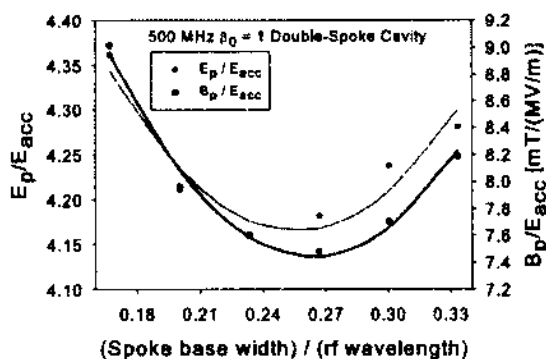


FIG. 26: Dependence of the normalized magnetic and electric fields on the spoke base width (for a transverse orientation).

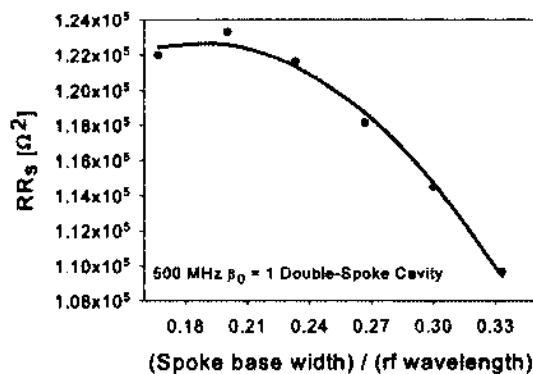


FIG. 27: Dependence of the geometric shunt impedance on the spoke base width (for a transverse orientation).

Figure 26 illustrates that the base width orientation can only improve the normalized electric field by about 5%, while the impact on the magnetic field is higher.

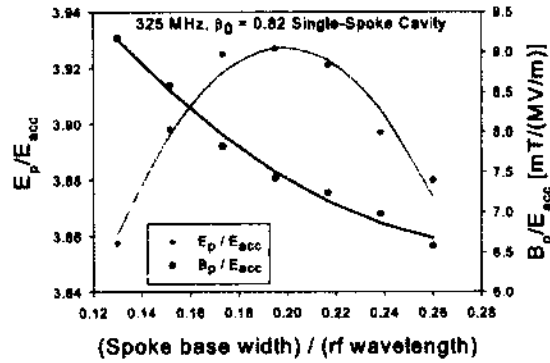


FIG. 28: Dependence of the normalized magnetic and electric fields on the spoke base width (for a transverse orientation).

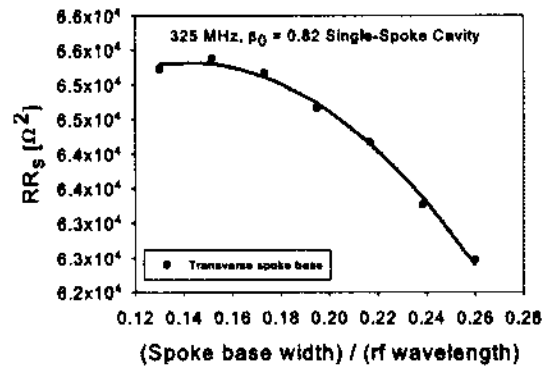


FIG. 29: Dependence of the geometric shunt impedance on the spoke base width (for a transverse orientation).

Figure 27 shows that increasing the spoke base width can have a positive effect on the shunt impedance for both orientations, but more so for the longitudinal base. This is consistent with Fig. 23, which showed that a longitudinal base has a higher shunt impedance for a more cylindrical shape. In Fig. 27, the energy content decreases for a wider longitudinal base, and increases for the transverse orientation. Again, this is consistent with what was illustrated in Fig. 24 which showed that a more cylindrical shape provides a lower energy content than a longitudinal base.

4.3.2 SPOKE APERTURE

The electric field of the fundamental accelerating mode of a spoke cavity is concentrated at the accelerating gaps along the beam path. The shape and dimensions of the spoke aperture region thus have a great impact on the peak surface electric field. Because the field is concentrated in this region, achieving a uniform distribution along the surface of the spoke aperture is important for realizing a low peak surface electric field.

A similar approach has been used in optimizing the aperture region to that used in optimizing the base. We first begin by analyzing how individual parameters influence the fields and shunt impedance, then study different aperture shapes and determine the optimal size of those shapes. For this optimization, we have looked at elliptical, racetrack, and cylindrical shapes. The elliptical cross-section and the racetrack are similar enough that we need not present results for both.

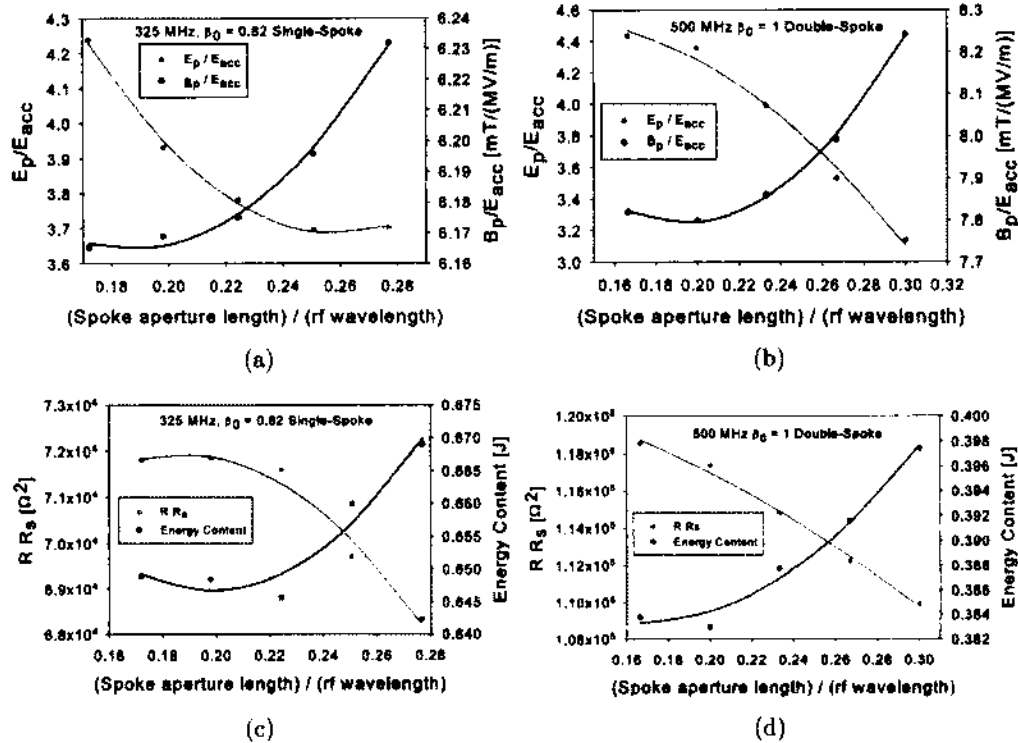


FIG. 30: Dependence of the normalized electric and magnetic fields, shunt impedance, and energy content on the aperture length for the single-spoke (a, c) and double-spoke (b,d) cavities.

Figure 30 is an example of how the normalized electric and magnetic fields behave with respect to the spoke aperture length (both have a transverse orientation). In both cases, increasing the aperture length decreases the normalized electric field and increases the normalized magnetic field. The amount that the normalized magnetic field increases is at most a few percent. The normalized electric field can be changed by 25% or more. The effects are more dramatic for the smaller, 500 MHz double-spoke cavity.

Figure 30 (c) and (d) shows the dependence of RR_s and the energy content for the same aperture dimensions. The shunt impedance is decreased (increasing the power dissipation) by 3%-5% while the energy content is increased by a similar amount. Both of these results have a negative impact on the cavity performance. However, from Fig. 30, at an aperture length to rf wavelength ratio of around 0.22 for the single-spoke and 0.26 for the double-spoke, the normalized electric field is at a minimum while the adverse effects on the other rf parameters are minimal.

The dependence of these same properties on the spoke aperture width are examined in Fig. 31.

The aperture width seems to have a greater effect on the rf properties than the length. When the width of the aperture increases, the length of each accelerating gap decreases. This has the effect of increasing the electric field for a given voltage. By doing so, the peak surface field will begin to increase, which is what is observed in Fig. 31 (a, b). Both normalized fields can be changed significantly, while the shunt impedance peaks and the energy content decreases.

Interestingly, the aperture height has more of an influence on the peak surface magnetic field than the electric field. This is evident in Fig. 32, as the normalized electric field changes by only a few percent while the magnetic field can increase by 20% or more as the height gets larger.

4.3.3 SPOKE SEPARATION

In low- β_0 structures made with several loading elements (multi-spoke, split-ring or twin-quarter-wave for example) the side gaps are approximately half the size of the central gap and the energy gained in the side gaps is approximately half that gained in the central gaps. As was already noted, the distance between the centers of the side-gaps, to a large degree, determines the β_0 of a spoke cavity. Therefore, for high- β_0 cavities at the frequencies discussed here, the cavity length becomes greater

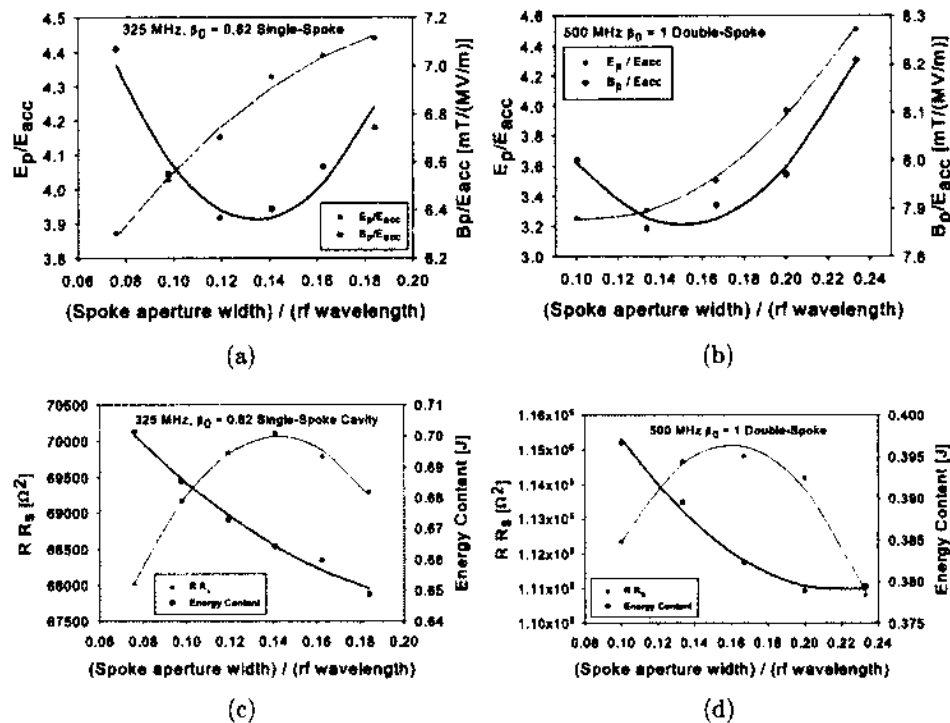


FIG. 31: Dependence of the normalized electric and magnetic fields, shunt impedance, and energy content on the aperture width for the single-spoke (a, c) and double-spoke (b, d) cavities.

than a meter. This large size can add some additional challenges, however there are some advantages to be gained. This longer cavity provides a great deal of flexibility in the spoke base dimensions.

Figure 33 shows what is referred to here as the spoke angle ϕ , which is a measure of the difference between the transversely oriented spoke aperture and base length and height. This angle not only has a strong effect on the surface fields, but also on the spoke separation. Balancing the fields in the accelerating gaps of a multi-spoke resonator is not paramount, however E_p/E_{acc} will be approximately minimized when the electric field is homogeneously distributed on the spoke surfaces. If, during a sweep of the parameter ϕ , the spoke separation remains constant along with β_0 and frequency, the distribution of the electric field on the beam line will become severely inhomogeneous, causing the normalized electric field to increase. If the length of the spoke aperture region is on the order of those in Fig. 33 ($\sim 0.10\beta_0\lambda$), then

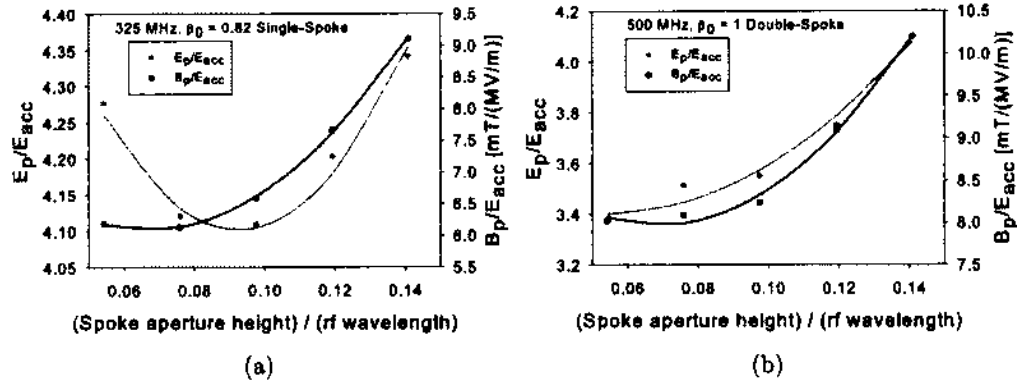


FIG. 32: Dependence of the normalized electric and magnetic fields on the aperture height for the single-spoke (a) and double-spoke (b) cavities.

for a small ϕ , the spoke separation is very close to one-half of the total iris-to-iris distance. On the other hand, as ϕ becomes larger for a transversely oriented spoke base, the structure begins to resemble a disk-loaded waveguide, and as such, the spoke separation required to balance the fields in each cell becomes close to the distance between each spoke and the end walls (one-third of the iris-to-iris length). Figure 34 shows how the electric field profiles change for different values of ϕ if the electric fields in each cell are equalized by changing the spoke separation. For the small spoke angle (20.5°), the center gap is approximately $\beta_0\lambda/2$ whereas for $\phi = 44.4^\circ$, the gaps are roughly the same size.

- (i) The normalized electric field is approximately minimized when the field is distributed homogeneously on the spoke surface in the accelerating region.
- (ii) The optimal spoke separation depends greatly on ϕ . For fixed aperture dimensions, as ϕ increases, the spoke separation needed to minimize the normalized electric field decreases.
- (iii) Increasing the spoke separation beyond the point at which the magnitude of the electric field is equal in each accelerating gap reduces the velocity acceptance of the cavity.

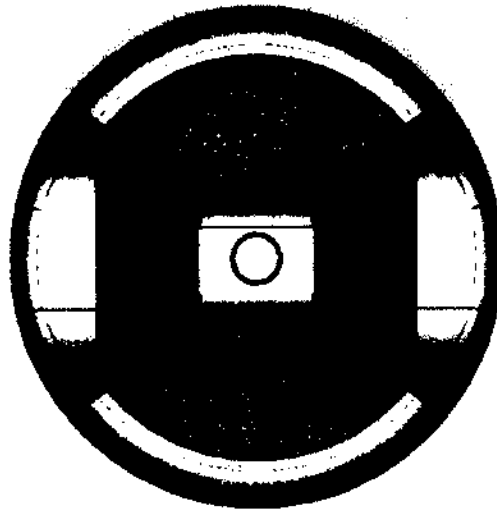


FIG. 33: End view of a single spoke showing the spoke angle ϕ .

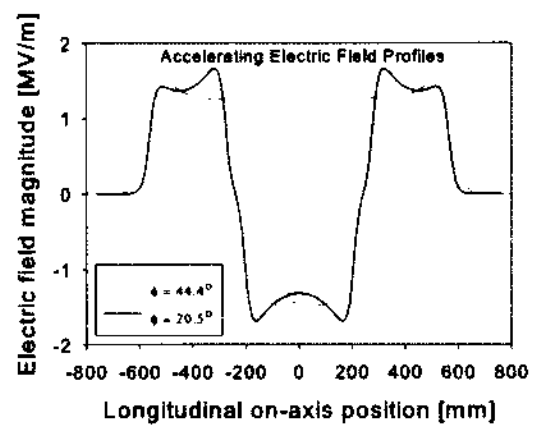


FIG. 34: On-axis electric field profiles (at 1 J) for different spoke angle ϕ .

4.3.4 REENTRANT PARAMETERS

Referring to Fig. 21, h_{out} can be used to minimize the peak surface magnetic field, h_{in} can be used to minimize the peak surface electric field, and H will strongly influence both. As with optimization of any parameter with respect to the peak surface fields, it is important to also consider maximizing the shunt impedance. In the case of parameters such as these, which do not impact the surface fields as greatly as the spoke parameters, we find that there can be a small gain in shunt impedance while obtaining a mild reduction in peak surface fields. Figure 35 shows how h_{out} impacts both the normalized magnetic field and RR_s .

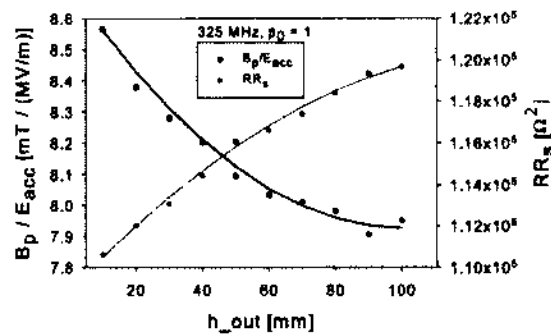


FIG. 35: Dependence of the normalized magnetic field and RR_s on the parameter h_{out} .

It is clear that increasing h_{out} has positive effects on the normalized magnetic field by increasing the volume for which the field has to encircle the spokes. This also results in a decreased power dissipation which leads to a higher shunt impedance.

H is a parameter, as can be seen in Fig. 21, which has an effect on both the normalized magnetic and electric fields. Figure 36 shows how the normalized magnetic field and shunt impedance change for a varying H , while Fig. 37 shows how the normalized electric field and shunt impedance change.

The parameter H changes the overall length of the cavity, but does not change the iris-to-iris distance. In Fig. 36 it is clear that as this parameter increases, the normalized surface magnetic field decreases. The opposite is actually true for the normalized electric field as can be seen in Fig. 37. Thus, in the cavities examined here, there is no single value of H that can minimize either of the fields while simultaneously maximizing the shunt impedance, but from Figs. 36 and 37, a value of around 100

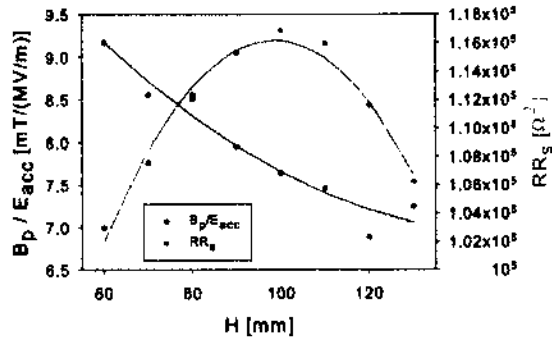


FIG. 36: Dependence of the normalized magnetic field and RR_s on the parameter H.

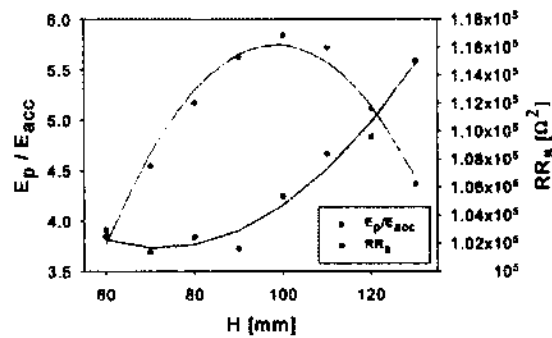


FIG. 37: Dependence of the normalized electric field and RR_s on the parameter H.

mm, for this 325 MHz, $\beta_0 = 1$ double-spoke cavity, sufficiently minimizes both fields while maximizing the shunt impedance.

Finally, since h_{in} is a parameter which is close to the beam line, it can be used to optimize the normalized electric field. Figure 38 shows how the normalized electric field and shunt impedance change with varying h_{in} .

4.3.5 CURVE ROUNDING

Another consideration with regard to field optimization is the rounding radius applied to otherwise sharp edges formed when designing the cavity. There are a few areas of the cavity where the rounding radius can have a significant effect on the fields, two of which are discussed here and shown in Fig. 39.

In Fig. 40, we can see how the normalized magnetic field changes for a wide

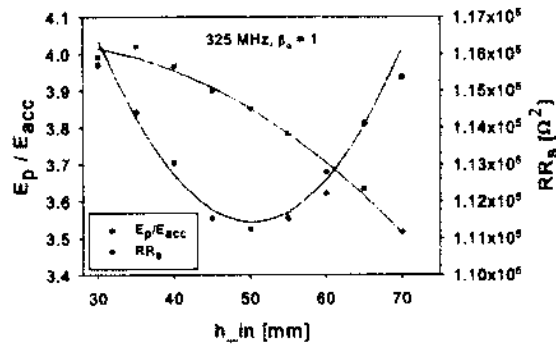


FIG. 38: Dependence of the normalized electric field and RR_s on the parameter h_{in} .



FIG. 39: Cavity with no rounding at (1) the outer conductor edges and (2) the spoke base.

range of outer conductor edge rounding. There is almost a 10% difference in the two extremes.

The spoke base rounding radius (identified as “2” in Fig. 39) also has a strong influence on the peak surface magnetic field, as Fig. 41 illustrates.

Increasing the spoke base rounding radius decreases the normalized magnetic field, while there is a large range of outer conductor rounding radii for which the peak magnetic field is virtually unchanged.

When determining an optimal rounding, the impact on multipacting should be considered, as will be seen in Chapter 5. While the effect cannot be eliminated completely because it is much more dependent on the cavity surface conditions and ability to provide adjustable levels of power to the susceptible regions of the cavity, we have found that it can be reduced through simple modifications to the geometry.

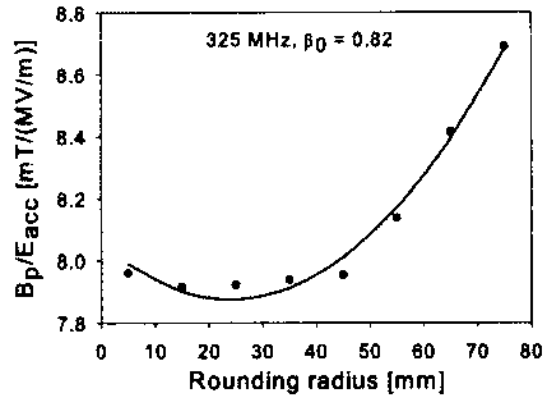


FIG. 40: Dependence of B_p/E_{acc} on the outer conductor edge rounding.

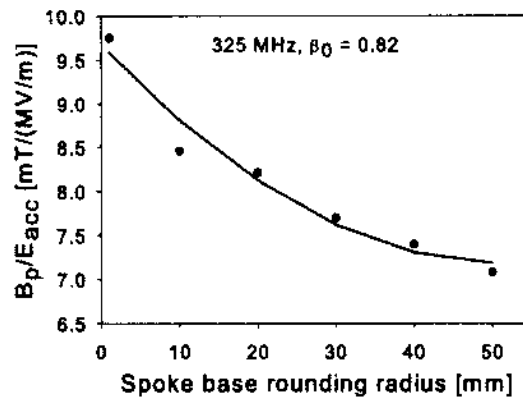


FIG. 41: Dependence of B_p/E_{acc} on the spoke base rounding radius.

4.4 COUPLER PLACEMENT

In order to transfer power from a source to the cavity, a fundamental power coupler (FPC) is needed. They can come in multiple varieties, but fall into two main categories: waveguide or coaxial. While waveguide couplers are mechanically simple, coaxial couplers have the advantage of being able to change the impedance by providing variable matching conditions.

The coaxial couplers also come in three varieties: magnetic field coupling, electric field coupling, and a combination of the electric/magnetic field coupling. To couple to the magnetic field, a current loop is used, where the coupling strength can be

varied by changing the area of the loop and/or its orientation with respect to the magnetic field. To couple to the electric field, a voltage probe is used, the length and diameter of which can be adjusted to vary the coupling strength. The third type of structure, which couples to both fields is a “hook.” In this case, varying the orientation and size allows for adjustable coupling strength.

The frequency at which FPCs are intended to operate at is that of the cavity, with some adjustability to compensate for temperature, pressure, or tuning variations in that frequency. For our purposes, the FPC must be able to deliver several hundred watts, transmitted either cw or pulsed. With no beam present, nearly all the power is reflected back through the coupler. A standing wave is created by this reflected power, which has twice the voltage and current [127]. Thus, by Eq. (41), the FPC must be able to handle four times the forward power.

There are two situations we must consider when determining the coupling requirements. The first is for cryogenic testing of a proof-of-principle cavity, which is what is being done in this work. The second is for an operational cavity within a specific machine. This coupling condition will also be described below, and the importance as it relates to higher order mode damping requirements will be discussed in 6.

Pickup couplers are used to extract power from the cavity in order to measure the transmitted power. Large amounts of power are not intended to be removed by the pick-up coupler, therefore they are typically very weakly coupled. Together, the cavity, pick-up, and the FPC make up a coupled system where, ideally, no rf power is reflected, i.e. all power is transmitted to the beam.

In this section, we will discuss some of the basic considerations when determining the placement and dimensions of a coaxial FPC and pickup probe.

4.4.1 COUPLING STRENGTH

When the cavity has one or more couplers attached, they make up a system which can be characterized by certain parameters. First, there is external quality factor Q_{ext} , which is given by

$$Q_{ext} = \frac{\omega_0 U_0}{P_{ext}}, \quad (127)$$

where P_{ext} is the average dissipated power in the source load. Thus, as we have already introduced, the *loaded quality factor* Q_L is that of the system and is given by

$$\frac{1}{Q_L} = \frac{1}{Q_{ext}} + \frac{1}{Q_0}, \quad (128)$$

or, in terms of the total dissipated power P_{total} , $Q_L = \omega_0 U / P_{total}$. We can now define a coupling parameter β as

$$\beta \equiv \frac{Q_0}{Q_{ext}}. \quad (129)$$

Therefore, the loaded quality factor can be written as

$$\frac{1}{Q_L} = \frac{(1 + \beta)}{Q_0}. \quad (130)$$

This tells us how strongly the couplers interact with the cavity. A large value of β implies that the power leaking out of the coupler is large compared to the ohmic losses in the cavity wall. When a cavity is “critically coupled,” the value of β is 1. Because the quality factor of the cavity depends on the temperature (through the BCS resistance), we would like for the external quality factor to be adjustable. The value of Q_{ext} is, in fact, adjustable and is determined by the penetration of the inner conductor into the volume of the cavity.

In addition to the beam ports, both the 325 MHz single-spoke and 500 MHz double-spoke cavities have two additional ports on the end cap which are necessary for chemical processing. In the case of the proof-of-principal single-spoke cavity, the only options for coupling and pick up ports are on the end caps, although, ports on the outer conductor would be preferable for an operational cavity.

For the 500 MHz double-spoke cavity, there are multiple options for where the input and pickup couplers could be placed. Figure 42 shows these options.

Both cavities have been fabricated with cleaning ports on the end caps and no ports on the outer conductor. In the case of coupling at the end caps, there is no choice of where to place the ports because they need to be 90° from the spoke base in order to not increase the peak surface magnetic field.

For these simulations, we use a standard rod with a diameter of 4.74 mm because this is what we typically use for cryogenic testing at Jefferson Lab. In this case, we are not concerned with having an impedance mismatch. To determine the appropriate length, we first must determine the Q_0 of the cavity. Using the relation between the geometry factor and surface resistance, the quality factor can be determined as

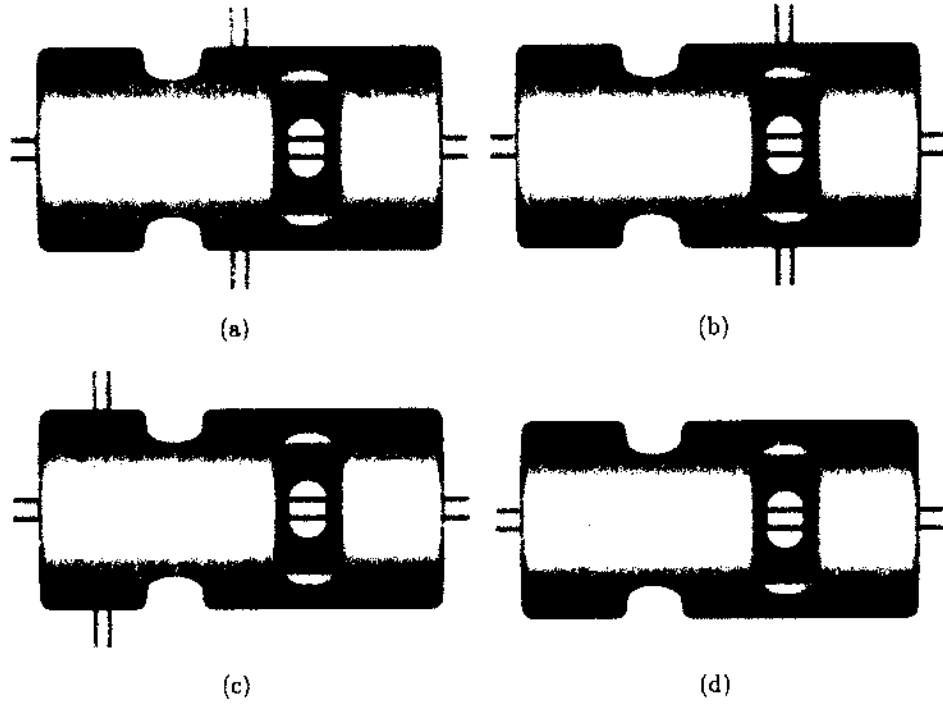


FIG. 42: Location of coupling ports (a) cavity center, (b) spoke plane, (c) end cell, and (d) end cell perpendicular to the spoke.

$$Q_0 = \frac{G}{R_s}. \quad (131)$$

R_s is the surface resistance which is comprised of a BCS component and a residual one. At 500 MHz, the BCS resistance is around 105 n Ω at 4 K and 2 n Ω at 2 K. We will also assume a modest residual resistance of 10 n Ω . Using these values, we find that the Q_0 should be around 1.5×10^9 at 4 K and 1.5×10^{10} at 2 K.

We can now determine what the external quality factor should be for the 500 MHz double-spoke cavity in the presence of an electron beam with the parameters of the ODU Inverse Compton Source. First, we look at the situation where the input power is at ω_0 and the particles are on-crest. The reflected power is given by

$$P_r = P_g \left(\frac{\beta - 1}{\beta + 1} - \frac{I_b \sqrt{R_s \beta}}{(\beta + 1) \sqrt{P_g}} \right)^2, \quad (132)$$

where P_g is the generator power, I_b is the average beam current (1 mA, in this case),

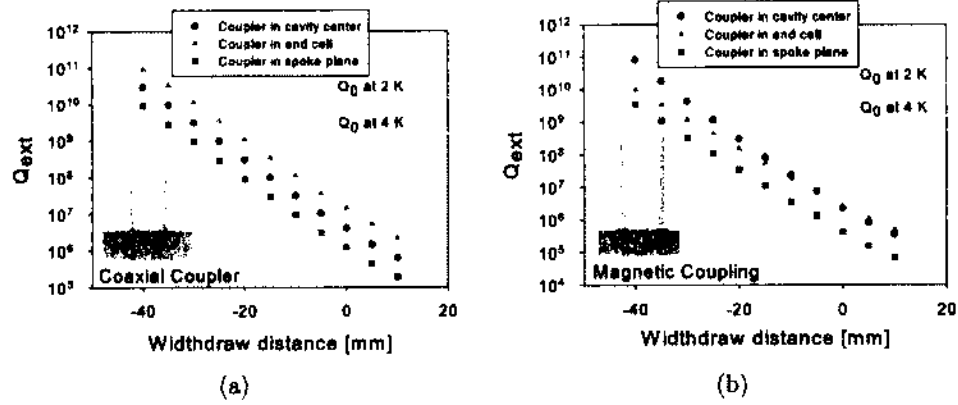


FIG. 43: Fundamental power coupling using (a) a standard coaxial rod and (b) a hooked rod for various port positions.

and R_s is the shunt impedance of the accelerating mode. The power delivered to the cavity is

$$P_c = \frac{4\beta}{(1+\beta)^2} P_g. \quad (133)$$

The optimal external quality factor is then,

$$Q_{ext} = \frac{Q_0}{\beta} = \frac{Q_0}{1 + \frac{R_s}{P_c}}, \quad (134)$$

where $P_b = I_b V_{acc}$ is the beam power. For the case of $I_b = 0$, the beam power is also zero, and this reduces to the case of cryogenic testing where we want $Q_{ext} = Q_0$.

For a real situation, we have a beam as well as frequency fluctuations. The rf requirements for a constant gradient are

$$P_g = \frac{1+\beta}{4\beta} \frac{V_{acc}^2}{\frac{R}{Q} \cdot Q_L} \left[\left(1 + \frac{R}{Q} \cdot Q_L \frac{I_b}{V_{acc}} \cos \varphi \right)^2 + \left(2Q_L \frac{\omega - \omega_0}{\omega_0} - \frac{R}{Q} Q_L \frac{I_b}{V_{acc}} \sin \varphi \right)^2 \right],$$

where φ is the angle between the particle and the rf field and $(\omega - \omega_0)$ is the detuning from the cavity frequency. The optimal detuning is given by

$$\omega - \omega_0 = -\omega_0 \frac{R}{Q} \cdot Q_L \frac{I_b}{V_{acc}} \sin \varphi, \quad (135)$$

and the optimal loaded quality factor Q_L is

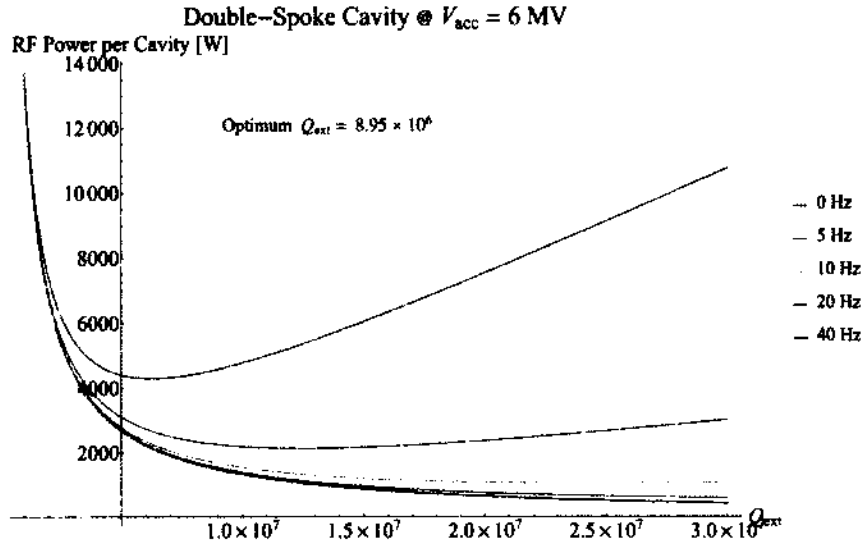


FIG. 44: RF power per cavity for the Q_{ext} resulting from various frequency shifts.

$$Q_L = \frac{V_{acc}}{\frac{R}{Q} \cdot I_b \cos \varphi} \quad (136)$$

These optimal detuning and Q_L values mean that all power is transferred to the beam, i.e. there is no reflected power.

If we use the beam parameter of the ODU Inverse Compton Source and the 500 MHz, $\beta_0 = 1$ double-spoke cavity, we have the following: $V_{acc} = 6$ MV, $R/Q = 670$ Ω , $I_b = 1$ mA, and $\varphi = 0$ (on-crest), we obtain an optimal loaded quality factor of 8.95×10^6 . This is illustrated in Fig. 44, where the power per cavity is shown for various values of $(\omega - \omega_0)$ as well as the optimal value.

4.4.2 PORT LOSSES

If the port flanges are made of stainless steel, as they are for these cavities, it is very important to make sure that the port length is long enough such that the magnetic field will not cause any significant losses at the steel flange. If the losses at the flanges are high (leading to a low Q for the port), the Q_0 of the entire cavity will be limited. If the calculated Q of each port is higher than the Q_0 of the cavity when considering only BCS resistance, then it is acceptable.

To determine the Q of a particular port, we start with the following,

TABLE 1: 500 MHz, $\beta_0 = 1$ Port Losses

Port	Length/number	Total Q_0
Beam Port	117 mm / 2	1.9×10^{15}
End Cap	60 mm / 4	2.7×10^{10}
End Cap	70 mm / 4	3.3×10^{11}
Outer Conductor	60 mm / 2	1.5×10^{14}

$R_{BCS} = 2 \text{ n}\Omega$ for a 2 K $Q_0 = 1.1 \times 10^{10}$

$$Q_0 = \frac{\omega U}{P_d},$$

where ω is the frequency, U is the energy content (1 J), and P_d is the dissipated power on the flange, which can be defined as

$$P_d = \frac{R_s}{2} \int |\mathbf{H}|^2 dA,$$

where R_s is the surface resistance of steel,

$$R_s = \sqrt{\frac{\mu_0 \omega}{2\sigma}}, \quad (137)$$

with $\sigma = 1.45 \times 10^6$ for steel. This leads to,

$$Q_0 = \frac{2\omega}{R_s \int \mathbf{H}^2 dA}. \quad (138)$$

This is accomplished by calculating the field values $H(r, \phi)$ at the end of the port (where the steel flange connects) and integrating along r and ϕ .

From the results in Table 1, the ports on the end caps are by far the most lossy. If the end cap cleaning/coupling ports were in fact 60 mm, the Q_0 of the cavity would indeed be limited by these losses. After trimming and braising, the ports are in excess of 90 mm.

4.5 RESULTS

The results are broken into two parts, depending on the application. First, in applications where the highest available gradient is needed, lowering the surface fields is more important than increasing the shunt impedance. In the second, if only

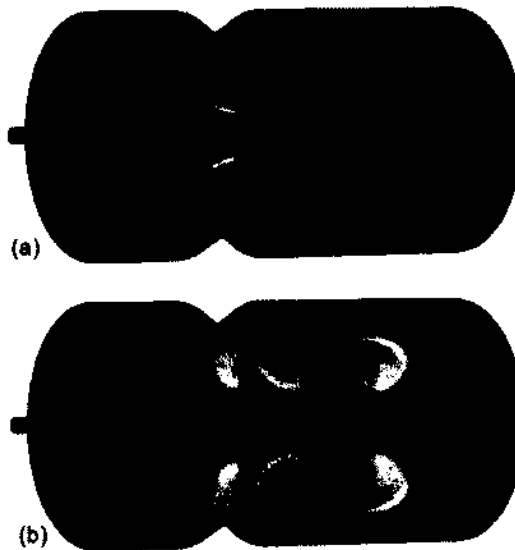


FIG. 45: CST MWS[®] cut-away view showing the surface (a) electric and (b) magnetic fields of the fundamental mode of the optimized 325 MHz, $\beta_0 = 0.82$ cavity.

modest gradients are needed and the dissipated power is the limiting factor, the shunt impedance is maximized which causes the peak surface fields to be higher.

These specific optimizations were done for cavities we developed prior to deciding on which ones to move forward with. The lessons learned were then applied to the 325 MHz single-spoke cavity and the 500 MHz double-spoke cavity. The former was optimized for lower surface fields while the latter was optimized for higher shunt impedance. The geometric and rf properties of these two are given at the end of the chapter in Tabs. 8 and 9.

4.5.1 FIELD OPTIMIZATION

The $\beta_0 = 0.82$ models that have been designed and are targeted more toward high-energy protons and ions, and as such, the most important optimization consideration is to reduce the peak surface magnetic and electric fields. The preceding sections provide a detailed discussion of how the most influential parameters affect the fields and shunt impedance, and in this section we present the results of field minimization optimizations.

Before doing so, there is another consideration to be made, namely the placement

TABLE 2: Cavity Parameters, 352 MHz, $\beta_0 = 0.82$ and $\beta_0 = 1$

Parameter	$\beta_0 = 0.82$	$\beta_0 = 1$	Units
Frequency of accelerating mode	352	352	MHz
Frequency of nearest mode	360	358	MHz
Cavity diameter	560	585	mm
Iris-to-iris length	859	1061	mm
Cavity length	1042	1226	mm
Reference length $[(3/2)\beta_0\lambda]$	1048	1278	mm
Aperture diameter	50	50	mm

of the coupler ports. One advantage of spoke cavities, which was mentioned previously, is that couplers can be placed on the outer conductor. Although not reported here, we have included a fundamental power coupler port, cleaning ports (shown in Fig. 1), and HOM damping ports in simulations of the final design, and have found that through judicious placement, the electromagnetic properties are not negatively affected.

Figure 45 shows the surface electric and magnetic fields for the optimized 325 MHz, $\beta_0 = 0.82$ cavity. Tables 2 - 5 provide the cavity parameters and rf properties of four high- β_0 cavities that have been optimized to date. The aperture diameter was fixed at 60 mm for the 325 MHz cavities and 50 mm for the 352 MHz cavities. The actual cavities which will be built and tested may be somewhat different based on fabrication and ease of cleaning considerations.

4.5.2 SHUNT IMPEDANCE OPTIMIZATION

One of the motivations for spoke cavity development is that they are generally compact enough to operate at lower frequencies such that they need only be cooled to 4.2 K. For applications which require relatively small machines, especially those intended to run in cw mode, operating at 2 K may not be feasible, therefore interest in spoke cavities operating at $\beta_0 = 1$ is growing. The optimization considerations for these velocity-of-light cavities intended to be used in compact accelerators are somewhat different than that of cavities to be used in more conventional machines. In the former, power dissipation is perhaps more important, therefore maximizing the shunt impedance is the highest priority.

TABLE 3: RF Properties, 352 MHz, $\beta_0 = 0.82$ and $\beta_0 = 1$

Parameter	$\beta_0 = 0.82$	$\beta_0 = 1$	Units
Energy Gain at β_0^*	1048	1278	kV
R/Q	642	715	Ω
QR_s	158	175	Ω
$(R/Q) \cdot QR_s$	1.01×10^5	1.25×10^5	Ω^2
E_p/E_{acc}	3.64	3.69	-
B_p/E_{acc}	7.06	7.06	mT/(MV/m)
B_p/E_p	1.94	1.91	mT/(MV/m)
Energy Content*	0.77	1.03	J
Power Dissipation*†	0.79	0.92	W

*At $E_{acc} = 1$ MV/m and reference length $(3/2)\beta_0\lambda$ † $R_s = 73$ n Ω TABLE 4: Cavity Parameters, 325 MHz, $\beta_0 = 0.82$ and $\beta_0 = 1$

Parameter	$\beta_0 = 0.82$	$\beta_0 = 1$	Units
Frequency of accelerating mode	325	325	MHz
Frequency of nearest mode	332	331	MHz
Cavity diameter	606	626	mm
Iris-to-iris length	932	1135	mm
Cavity length	1132	1315	mm
Reference length $[(3/2)\beta_0\lambda]$	1135	1384	mm
Aperture diameter	60	60	mm

TABLE 5: RF Properties, 325 MHz, $\beta_0 = 0.82$ and $\beta_0 = 1$

Parameter	$\beta_0 = 0.82$	$\beta_0 = 1$	Units
Energy Gain at β_0^*	1135	1384	kV
R/Q	634	737	Ω
QR_s	158	173	Ω
$(R/Q) \cdot QR_s$	1.00×10^5	1.28×10^5	Ω^2
E_p/E_{acc}	3.69	3.67	-
B_p/E_{acc}	7.06	7.06	mT/(MV/m)
B_p/E_p	1.91	1.92	mT/(MV/m)
Energy Content*	0.99	1.27	J
Power Dissipation*†	0.88	1.02	W

*At $E_{acc} = 1$ MV/m and reference length $(3/2)\beta_0\lambda$ † $R_s = 68$ n Ω

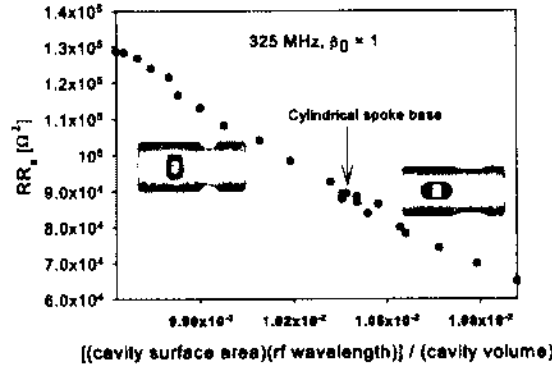


FIG. 46: Dependence of RR_s on the ratio of cavity surface area to volume.

From Eq. (45), it is clear that the shunt impedance is a measure of how much accelerating voltage can be gained for a given dissipation. Increasing the shunt impedance, therefore, is how the dissipation can be decreased. The power dissipation can be written as,

$$P_d = \frac{V_0^2}{(R/Q) \times G} \times R_s, \quad (139)$$

where the voltage, here, is normalized to an accelerating gradient of 1 MV/m, reference length $(3/2)\beta_0\lambda$ (for a double-spoke cavity), and the surface resistance is fixed for a given frequency. Thus, to decrease the power dissipation, the product of R/Q and G should be increased. Again, both of these parameters are determined solely by the geometry of the cavity and not by the size or material properties.

In elliptical cavities, optimizing the geometry of the outer walls to maximize Q_0 often leads to a spherical shape because this corresponds to the smallest surface area for a given volume [78]. We find a similar argument can be made in the case of these particular geometries, as is illustrated in Fig. 46, where the dependence of RR_s on the ratio of total surface area to volume (multiplied by rf wavelength to eliminate units) is shown. At this point, we cannot argue that this is universally true, only that there appears to be a correlation present.

In Tabs. 6 and 7, we present the rf properties for all four cavities given in the previous section, however, here the focus of optimization was to achieve a higher shunt impedance while still maintaining reasonable surface fields.

TABLE 6: RF Properties, 352 MHz, $\beta_0 = 0.82$ and $\beta_0 = 1$ cavities optimized for higher shunt impedance

Parameter	$\beta_0 = 0.82$	$\beta_0 = 1$	Units
Energy Gain at β_0^*	1048	1278	kV
R/Q	647	757	Ω
QR_s	173	180	Ω
$(R/Q) \cdot QR_s$	1.12×10^5	1.36×10^5	Ω^2
E_p/E_{acc}	4.30	4.05	-
B_p/E_{acc}	7.81	7.58	mT/(MV/m)
B_p/E_p	1.82	1.87	mT/(MV/m)
Energy Content*	0.76	0.97	J
Power Dissipation*†	0.72	0.88	W

*At $E_{acc} = 1$ MV/m and reference length $(3/2)\beta_0\lambda$

† $R_s = 73$ n Ω

TABLE 7: RF Properties, 325 MHz, $\beta_0 = 0.82$ and $\beta_0 = 1$ cavities optimized for higher shunt impedance

Parameter	$\beta_0 = 0.82$	$\beta_0 = 1$	Units
Energy Gain at β_0^*	1135	1384	kV
R/Q	640	743	Ω
QR_s	171	183	Ω
$(R/Q) \cdot QR_s$	1.09×10^5	1.36×10^5	Ω^2
E_p/E_{acc}	4.13	4.11	-
B_p/E_{acc}	7.54	7.77	mT/(MV/m)
B_p/E_p	1.83	1.89	mT/(MV/m)
Energy Content*	1.01	1.25	J
Power Dissipation*†	0.80	0.96	W

*At $E_{acc} = 1$ MV/m and reference length $(3/2)\beta_0\lambda$

† $R_s = 68$ n Ω

TABLE 8: Cavity Parameters, 325 MHz, $\beta_0 = 0.82$ Single-Spoke and 500 MHz, $\beta_0 = 1$ Double-Spoke Cavities

Parameter	$\beta_0 = 0.82$	$\beta_0 = 1$	Units
Frequency of accelerating mode	325	500	MHz
Frequency of nearest mode	337	509	MHz
Cavity diameter	609	416	mm
Iris-to-iris length	539	744	mm
Cavity length	717	841	mm
Reference length	756*	900†	mm
Aperture diameter	60	50	mm

* $\beta_0\lambda$

† $(3/2)\beta_0\lambda$

4.5.3 CAVITIES UNDER DISCUSSION

As was mentioned previously, the cavities which were fabricated used the optimization results discussed in this chapter to make the 325 MHz single-spoke cavity have lower surface fields and the 500 MHz double-spoke cavity have a higher shunt impedance. This is an important distinction and the reasons are related to the application envisioned for each. Table 8 show the geometric properties for each and Table 9 lists the rf properties.

TABLE 9: RF Properties, 325 MHz, $\beta_0 = 0.82$ Single-Spoke and 500 MHz, $\beta_0 = 1$ Double-Spoke Cavities

Parameter	$\beta_0 = 0.82$	$\beta_0 = 1$	Units
Energy Gain at β_0	757*	900 [†]	kV
R/Q	449	675	Ω
QR_s	175	174	Ω
$(R/Q) \cdot QR_s$	7.86×10^4	1.2×10^5	Ω^2
E_p/E_{acc}	3.6	3.7	-
B_p/E_{acc}	6.0	7.6	mT/(MV/m)
B_p/E_p	1.7	2.1	mT/(MV/m)
Energy Content	0.61*	0.38 [†]	J
Power Dissipation	0.48 [‡]	0.87 [§]	W

*At $E_{acc} = 1$ MV/m and reference length $\beta_0\lambda$

[†]At $E_{acc} = 1$ MV/m and reference length $(3/2)\beta_0\lambda$

[‡] $R_s = 68$ n Ω

[§] $R_s = 105$ n Ω

CHAPTER 5

MULTIPACTING ANALYSIS

In this chapter, we detail the simulations undertaken to identify and minimize multipacting activity in the cavities under investigation. What we have discovered is that there are commonalities all these cavities share regardless of the design velocity, frequency, or number of spokes. There are three distinct gradient regions, defined by the cavity frequency, which can be used to determine the locations of resonant multipacting electrons.

5.1 SIMULATION PARAMETERS

The following multipacting simulations were performed with Track3P within the ACE3P code suite [105], as described in Chapter 3. The SEY curve used for the enhancement counter was for niobium baked at 300° C. Figure 47 shows this curve.

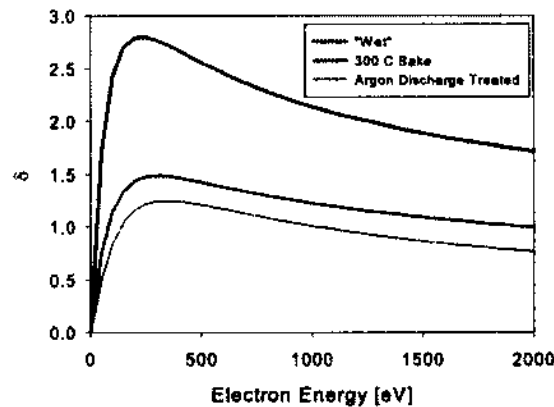


FIG. 47: Secondary emission yield of niobium for various surface treatments.

The cavity was divided in half longitudinally, parallel to the spoke. This plane defined the symmetry of the cavity and served as a magnetic boundary, i.e. $B_T = 0$. To expedite the computation time, the half-cavity was divided into slices which would contain the emitting sites. These slices were taken for the radius of the cavity



FIG. 48: 500 MHz, $\beta_0 = 1$ cavity divided into slices along z for multipacting simulations.

TABLE 10: Multipacting Simulation Parameters.

Parameter	Value	Units
Gradient Scanned	0.1-15.0	MV/m
RF Cycles	50	-
SEY ≥ 1	50-2000	eV
z-length of slice	150	mm
Symmetry factor	2	-
Mesh Cells (single-spoke)	119,263	-
Mesh Cells (double-spoke)	253,546	-

and extended some distance in z (the longitudinal direction). Figure 48 depicts the emitting domains.

Each tetrahedron in a given slice served as an emitting site while the entire cavity was a 'secondary.' Therefore, if the electron's trajectory took them out of the slice under investigation, it would still be able to produce secondaries which would continue to be tracked.

5.2 EMITTING SITES AND RESONANT LOCATIONS

In addition to knowing where the resonant locations are as a function of the electric field gradient, it is also useful to know where these multipactors originate. In Figs. 49 and 50, the emitting sites and resonant locations are shown for each cavity. The coloring of the multipactors is determined by the electric field gradient at which they appear. For example, in Fig. 49 (a), the multipactors colored red are

emitted from the sites shown and those same multipactors find resonant trajectories, also shown in red in Fig. 49 (b).

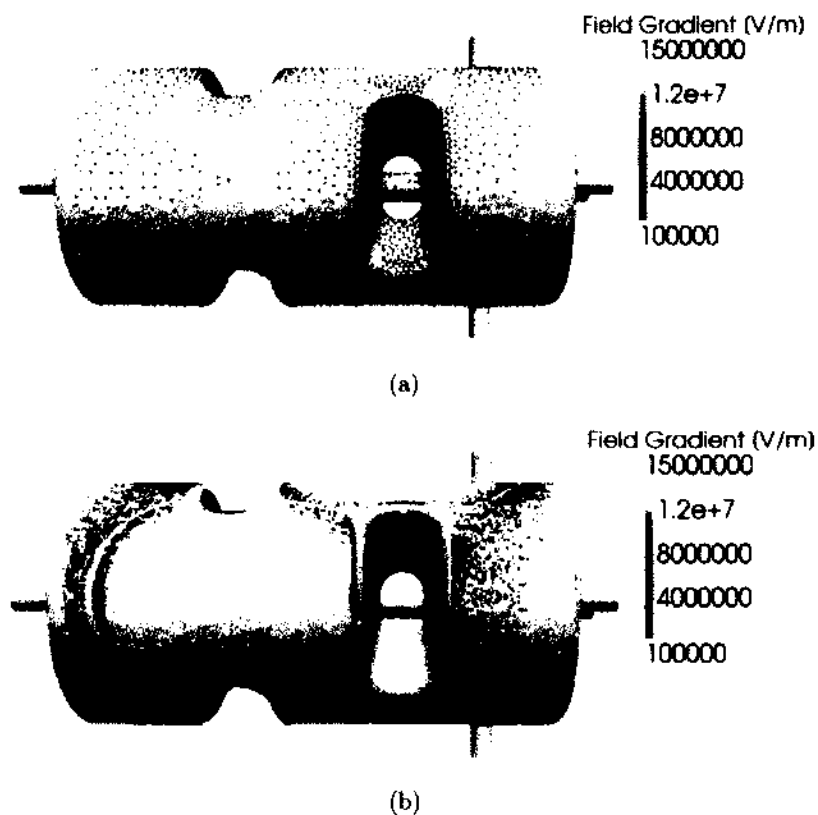


FIG. 49: (a) Emitting sites and (b) resonant locations by accelerating field gradient.

In the case of the 500 MHz double-spoke cavity, the multipacting electrons present at low gradient (colored in blue, 100 kV/m - 4.5 MV/m) start out on the outer conductor, spoke base, and spoke surfaces which are perpendicular to the beam line. These electrons find resonant trajectories which cover the outer conductor in the areas of the accelerating gaps. The medium gradient multipactors (dark blue and red, 4.5 MV/m - 8 MV/m) are emitted mostly the spoke surface (both parallel and perpendicular to the beam line) and end up on the outer conductor and spoke base rounding radius. Finally, the high gradient multipactors (orange and yellow, > 8 MV/m) start out mostly from the end caps and less so from the spoke surfaces.

For the 325 MHz single-spoke cavity, the multipacting electrons present at low gradient (light blue and blue, 100 kV/m - 2.5 MV/m) also emanate from the outer

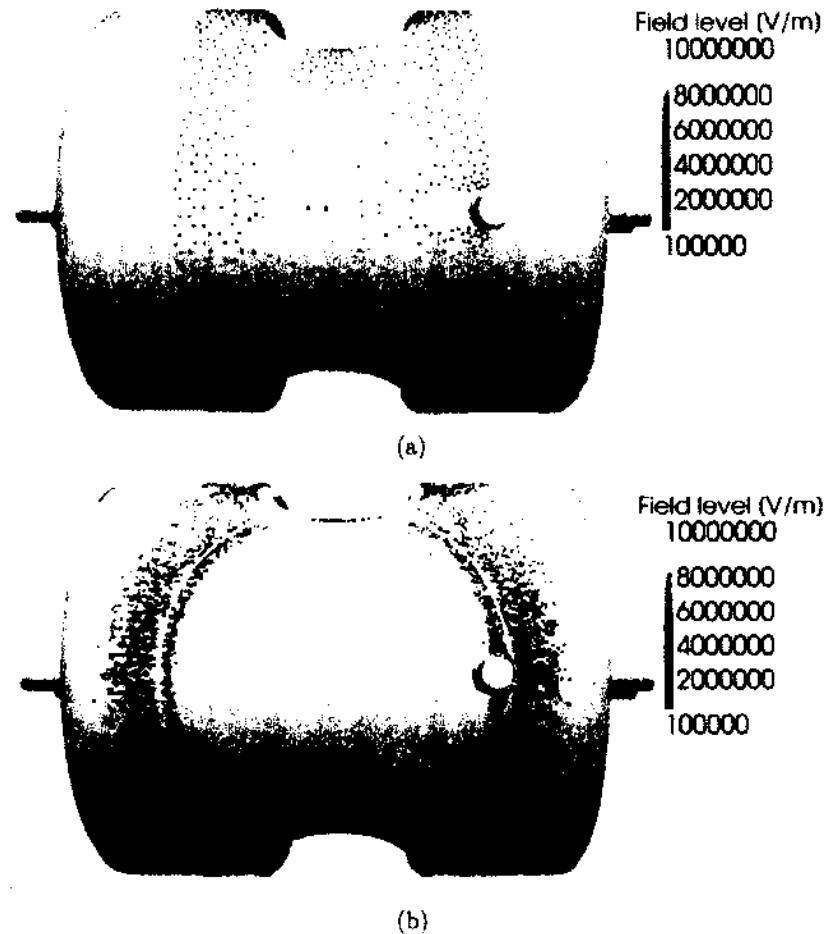


FIG. 50: (a) Emitting sites and (b) resonant locations by accelerating field gradient.

cylinder, mostly along where the spoke base meets the outer conductor. In the medium gradient regime (dark blue, 3 MV/m - 5.0 MV/m), multipactors start on the outer conductor, many from the spoke rounding radius region, and end up on the outer conductor as well as in the same spoke rounding radius. Finally, the high gradient region (red, orange, and yellow, > 5 MV/m) start mainly on the end caps and surrounding outer conductor but end up localized to the end cap rounding radius.

Another illustration of this is shown in Fig. 51, where the resonant electrons for various field gradients are shown as a function of longitudinal position. The electric field gradient has been divided into three distinct ranges listed above; a low, medium, and high gradient. Doing so allows us to then divide the cavity into areas where only

TABLE 11: Location of Multipactors for Various Electric Field Gradients.

Range	325 MHz Singl-Spoke	500 MHz Double-Spoke	Location
Low	0.1-2.5	0.1-4.5 MV/m	Accelerating Gaps
Medium	3.0-5 MV/m	4.5-8 MV/m	Drift Region
High	5.0-10 MV/m	8-15 MV/m	End Caps

multipactors within those gradient ranges are stable.

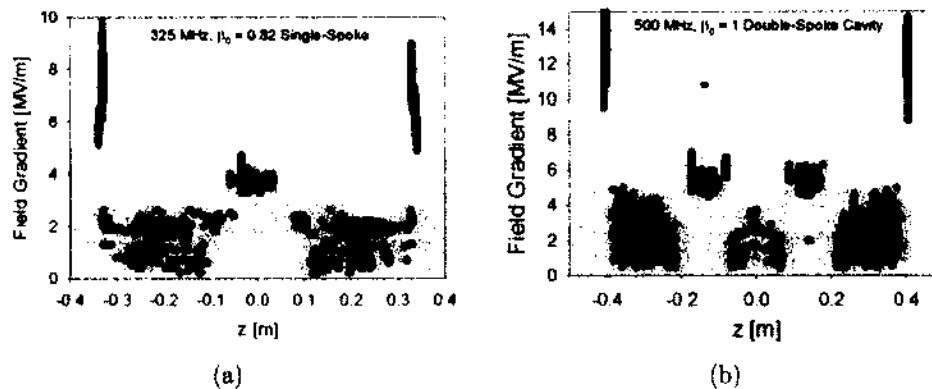


FIG. 51: Field gradient at which resonant electrons appear as a function of longitudinal position for the (a) 325 MHz single-spoke cavity and (b) 500 MHz double-spoke cavity.

While these ranges differ for each cavity, the location of stable multipactors within these ranges is the same for both. What is immediately noticeable is that the lower frequency, single-spoke cavity has a much smaller gradient range which supports higher order multipactors than the 500 MHz double-spoke cavity. An example of an electron trajectory resonant in the end cap rounding radius (present at high gradient but with low impact energy) is shown in Fig. 52.

5.3 IMPACT ENERGIES

The high energy multipactors present at “low” gradients are located on the outer conductor along the accelerating gaps. For this reason, perhaps the most important factor in reducing any limits they may present is having a well prepared surface or ability to vary the coupling of the fundamental power coupler. The medium and high



FIG. 52: Two-point resonant electron trajectory in the end cap of the cavity.

gradient resonant electrons mostly exist as two-point, first order multipactors in the rounding radius of the end cap and spoke base. This suggests that if we can change the geometry in some way, we may be able to disrupt their trajectories or affect their impact energy.

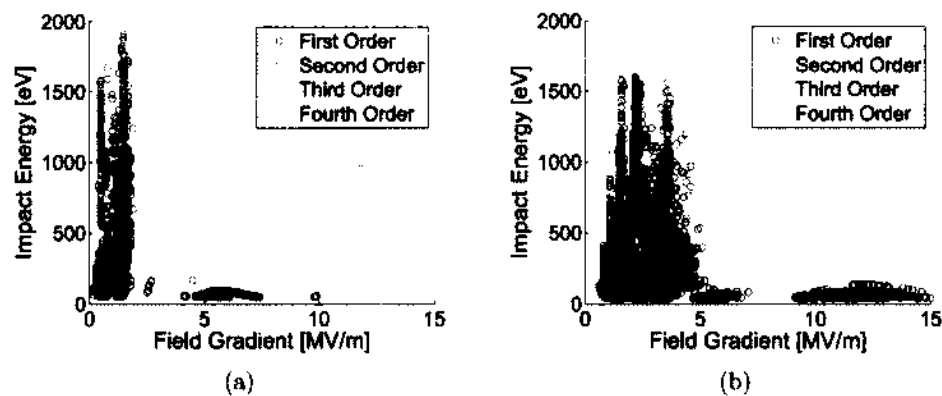


FIG. 53: Dependence of resonant electron energy on electric field gradient for the (a) 325 MHz single-spoke cavity and (b) 500 MHz double-spoke cavity.

In Fig. 53, we show the resonant electrons for field gradient levels from 100 kV/m to 10 MV/m in both an optimized 325 MHz, $\beta_0 = 0.82$ single-spoke cavity and a 500 MHz, $\beta_0 = 1$ double-spoke cavity. The most important feature of both plots is the obvious distinction between what happens at low gradient vs. what happens closer to the operating gradient. For the single-spoke cavity, we can define the “low gradient” region as being below 2.5 MV/m while that of the double-spoke cavity is below 4.5 MV/m. While the first order multipactors cover most of the gradient range, the low

TABLE 12: Electric field gradient range for multipactors of order 1-4.

Order	Range (Single-Spoke)	Range (Double-Spoke)
1	0.6-10 MV/m	1.5-10 MV/m
2	0.4-2.7 MV/m	1.1-5.0 MV/m
3	0.4-1.0 MV/m	0.7-1.8 MV/m
4	0.3-1.4 MV/m	0.6-2.7 MV/m

gradient area contains all higher order multipactors as well. In Table 12 the gradient ranges for the different order multipactors are listed.

While there is no way of determining if these barriers will be limiting just from the simulations, it appears that the higher the cavity frequency, the wider the expanse of the higher order multipactors. It should also be noted that a high resonant electron energy does not necessarily indicate a barrier of some sort since the SEY curve tends to peak at around 300 eV.

5.3.1 ENHANCEMENT

In order to get an understanding for how these multipactors may contribute to the avalanche effect described previously, a post-processing step can be taken using the enhancement counter function, as outlined in Chapter 3. We will look at the enhancement counter for both longitudinal position z and as a function of the accelerating electric field gradient.

In the single-spoke cavity, the gradient for which strong multipacting is expected to occur is generally below 2.5 MV/m, as was observed in Fig. 53 (a). Figure 54 (a) shows that a strong enhancement below 2 MV/m and a very small enhancement above that.

Figure 54 (b) shows the location in z where the enhancement happens. Notice that most takes place on the outer body in the region of the accelerating gaps and not in the end caps.

The 500 MHz double-spoke cavity is a very different situation. From Fig. 53 (b), it would be expected that strong multipacting activity should take place below ~ 5 MV/m. Figure 55 (a) confirms this but also suggests that high levels of multipacting are likely to take place well above this. Whether the enhancement at low field is a hard barrier or not will be discussed in Chapter 11, but from the simulation alone,

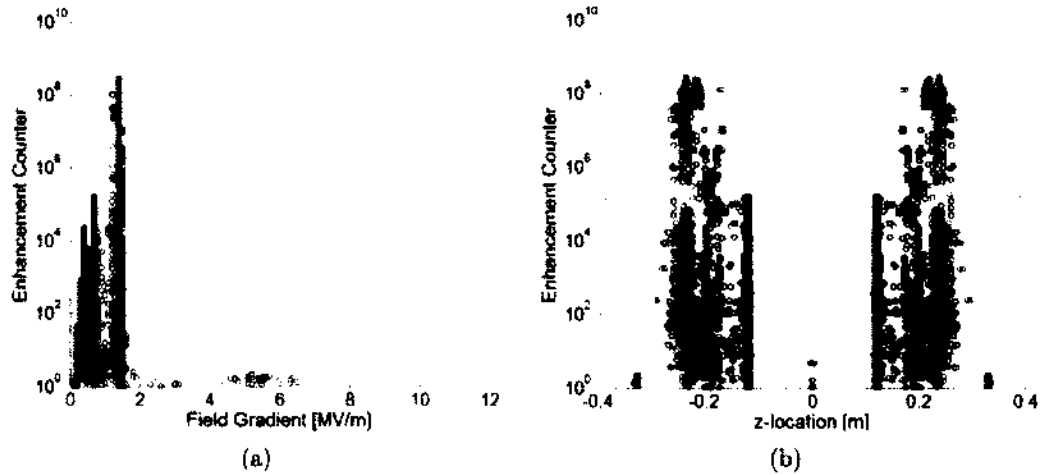


FIG. 54: 325 MHz cavity enhancement counter by (a) field gradient and (b) longitudinal location.

it certainly could be. The medium gradient region (4.5-8 MV/m), also has some strong enhancement, as does the high gradient region of 8-15 MV/m. Between 7 and 9 MV/m, there is almost no enhancement, which would make this a good operating region, assuming the strong multipacting levels below 5 MV/m could be processed.

The dependence of the enhancement on the z position is also shown in Fig. 55 (b). It is not surprising that the strongest enhancement occurs on the outer cylinder in the accelerating gap regions, primarily the end cells. Unlike the single-spoke cavity, it does appear that there is also some strong enhancement in the rounding radius of the end caps.

5.4 COUPLERS

Two couplers are presented: a simple coaxial fundamental power coupler and a higher order mode coupler. The former was discussed in Chapter 4 and the latter will be discussed in more detail in Chapter 6.

The dimensions of the fundamental power coupler for our purposes here are determined only by the required impedance of 50Ω . This means that the only variables will be the inner and outer conductor diameters. These values will then be fixed throughout the simulation, and are determined by

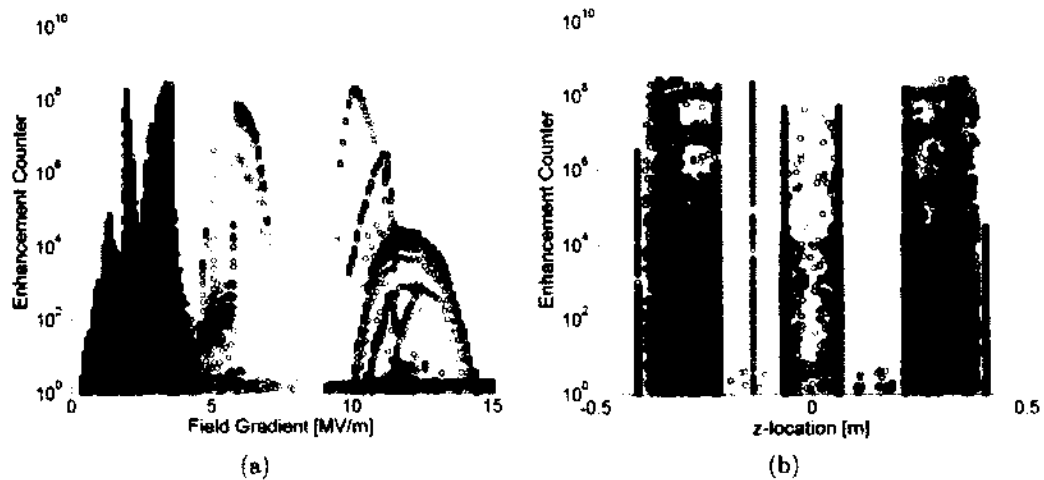


FIG. 55: 500 MHz cavity enhancement counter by (a) field gradient and (b) longitudinal location.

$$Z_c = \sqrt{\frac{L}{C}} = \frac{138}{\sqrt{\epsilon_r}} \log\left(\frac{D}{d}\right) (\Omega), \quad (140)$$

where L and C are the inductance and capacitance while D is the diameter of the outer conductor and d is the diameter of the inner conductor. The cavities fabricated here have a port diameter of 40 mm which sets the coaxial rod diameter to 17.3 mm for these simulations.

The location of the FPC can also be changed, as we observed in Fig. 42. When the coupler is in the plane of the spoke, and perpendicular to it, the strongest coupling occurs (see Fig. 43). As will be seen in Chapter 6, this is perhaps not the best location when trying to damp both polarizations of the deflecting modes. For this analysis, the FPC is placed in one of the end cells, parallel to the spoke.

Figure 57 (a) shows the surface electric field of the fundamental mode. As would be expected, electrons emanating from the tip of the probe get caught in the magnetic field and become distributed on the surface of the cavity outer conductor. Those emanating from higher up on the probe become trapped between the outer conductor of the coaxial cable and the probe.

The probe of the FPC is assumed to be made of copper, the SEY curve of which is shown in Fig. 56. The range of energy where $\delta > 1$ is roughly 300 eV to 2300 eV.

The impact energies and enhancement counter for the FPC are shown in Fig. 57

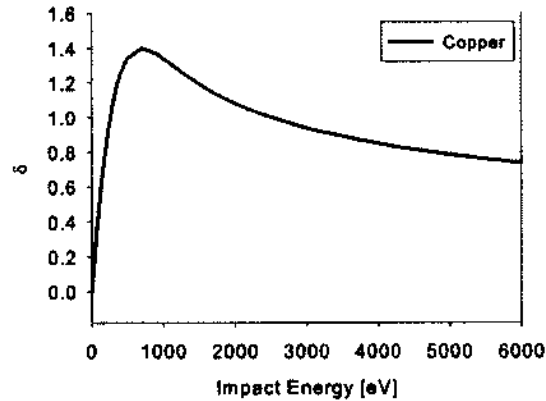


FIG. 56: Secondary emission yield of copper.

(b, c). The high energy multipactors present at low electric field gradient emanate from where the copper probe is closest to the cavity volume. As the field gradient increases, the resonant locations are located higher and higher up on the probe.

Figure 58 shows the same for the HOM coupler. The behavior is similar to the FPC in that the electrons emitted from the tip of the probe spread out along the surface of the cavity. Those emitted in the high-field region around the middle of the coupler end up being trapped in the horizontal power extraction port.

The HOM coupler seems to only have a possible problem area at around 3.5 MV/m. This is consistent with previous studies of similar HOM couplers [128]. Even though the impact energy covers a wide range, as seen in Fig. 58 (b), the enhancement in the range (c) is not that dramatic.

We should be cautious not to draw too many conclusions from the results of these studies for couplers. The reason for this is that Track3P releases electrons perpendicular to the emitting surface. When discussing highly curved surfaces in close proximity to each other, this may not be reliable.

5.5 MULTIPACTING REDUCTION

The most important factor in reducing multipacting is the quality of the cavity surface. However, we have investigated what modifications to the geometry can be made in order to reduce the effect as well. This work was carried out on a 325 MHz $\beta_0 = 0.82$ double-spoke cavity, and the lessons were applied to both cavities discussed

thus far.

Other than changing the actual field pattern in the cavity, there is little that can be done to affect the multipactor trajectories aside from changing the geometry where the particles are resonant. The high resonant electron energy stable multipactors are mostly located on the cylindrical outer conductor with some being around the spoke base. This curvature can thus be changed in an attempt to disrupt these trajectories. Similarly, there are low energy resonant multipactors that reside in the curvature of the end caps. Figure 59 the resonant electron energies and electric field gradient for an end cell (a) and the middle cell (b).

The rounding radius of the end cap and spoke base can in fact influence multipacting, at least the low energy, high gradient multipactors. By changing these two rounding radii, we can see in Fig. 60 that at high gradients, there are resonant multipactors with a low resonant energy.

A slight decrease of the resonant energy through rounding the end cap further while the spoke base rounding appears to have a greater impact.

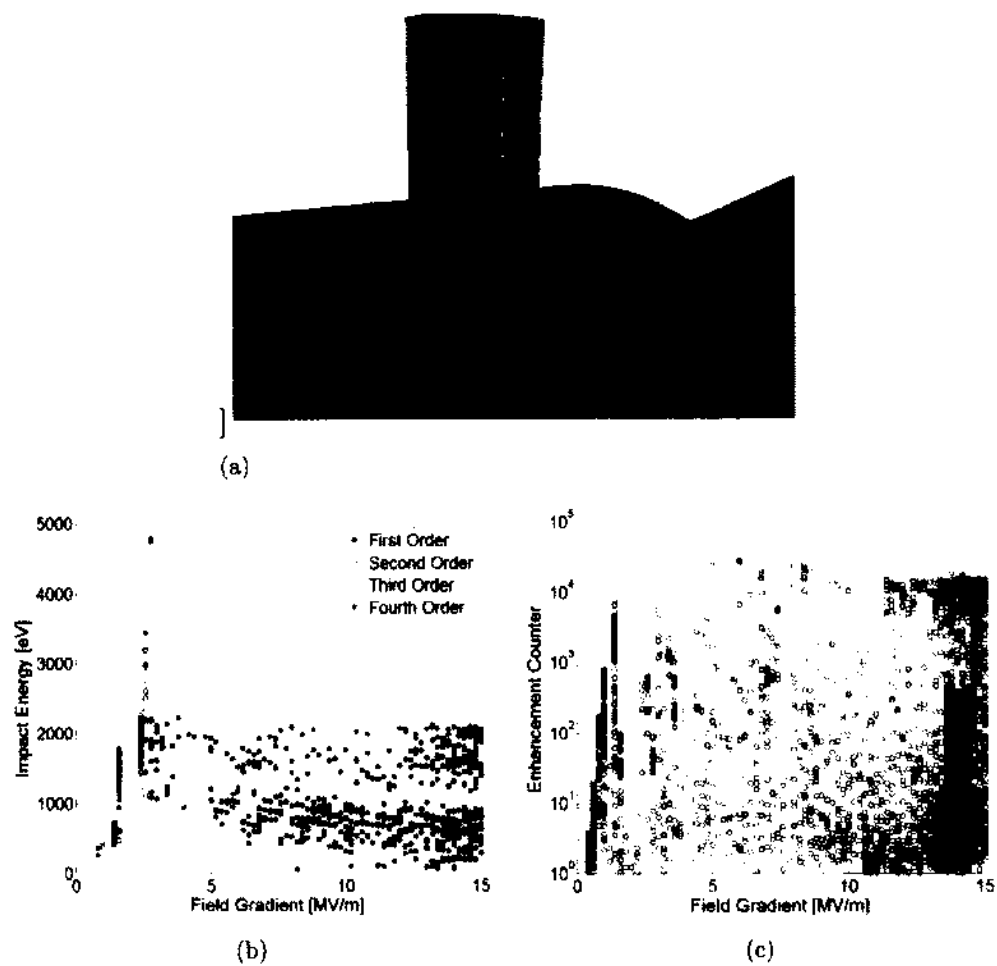


FIG. 57: (a) Electric field distribution of the fundamental mode within the FPC and location of resonant electrons, (b) impact energy of multipacting electrons emanating from the coupler, and (c) enhancement factor.

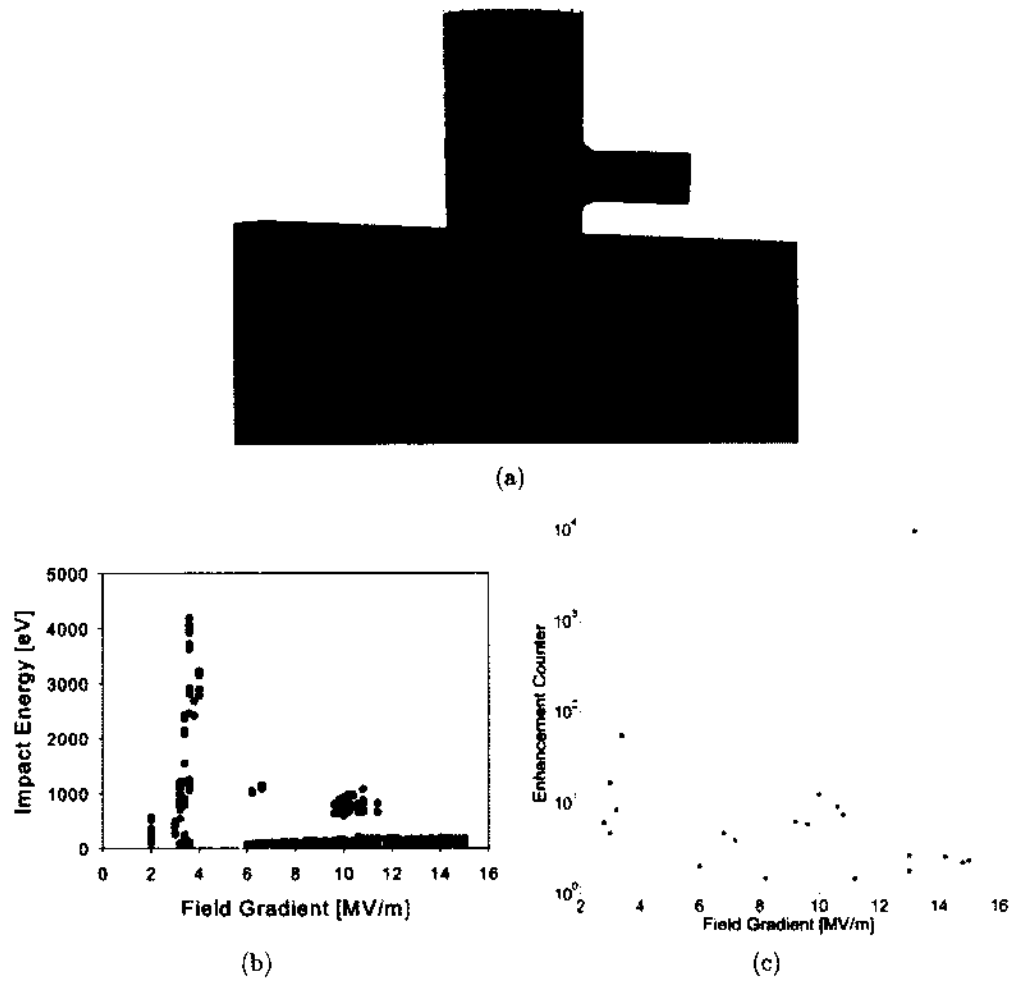


FIG. 58: (a) Electric field distribution of the fundamental mode within the HOM coupler and location of resonant electrons, (b) impact energy of multipacting electrons emanating from the coupler, and (c) enhancement factor.

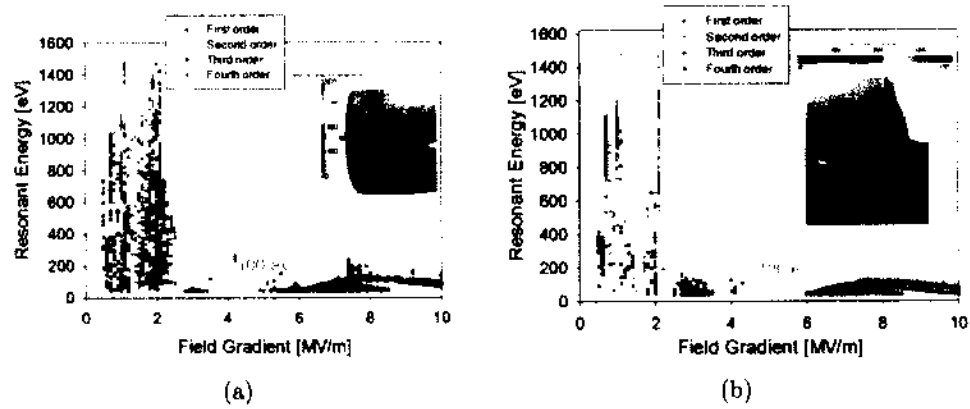


FIG. 59: Dependence of resonant electron energy on electric field gradient for (a) the end cells (region 1) and (b) the center cell (region 2) of a 325 MHz $\beta_0 = 0.82$ double-spoke cavity.

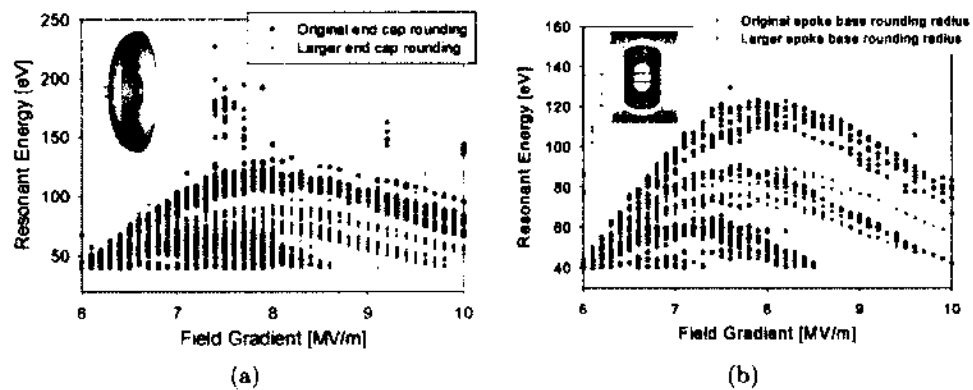


FIG. 60: Influence of the rounding radius of the (a) end cap and (b) spoke base on the resonant energy of stable high gradient multipactors.

CHAPTER 6

HIGHER ORDER MODE ANALYSIS

6.1 IDENTIFICATION OF MODE TYPES

The frequency spectrum of the multi-spoke cavity is broad. The first three modes for a two-spoke cavity are accelerating modes. Figure 61 presents the electric field profiles of these modes.

Due to the lack of cylindrical symmetry in multi-spoke cavities, we cannot classify the HOMs into monopole and multipole modes, as is usual for elliptical cavities. Instead, modes with a large electric field and negligible magnetic field along the beam axis can be categorized based on the main orientation of the electric field with respect to the beam axis as longitudinal (along the z axis) or transverse (along the x and/or y axes). These modes can therefore be described in terms of their resulting voltage as accelerating or deflecting. Modes with a large longitudinal magnetic field can be categorized as TE-type (characterized by a large magnetic field component along the beam axis and a negligible electric field along the direction of propagation) or hybrids (non-negligible electric and magnetic fields along the direction of beam propagation). The hybrid modes can actually have a very significant electric field in multiple directions. As can be seen in Fig. 62 (b), there is a hybrid mode at $f = 3081$ MHz in the 500 MHz double-spoke cavity. The magnitude of the E_z and E_x components reaches the MV/m range.

The geometry of a double-spoke cavity is such that most deflecting modes are two-fold degenerate. The degenerate modes are separate modes with the same frequency, and similar electromagnetic fields under some symmetry inversion. The transverse fields can be described as a superposition of fields in the x and y directions, but since the modes are degenerate any orthogonal linear combination of eigenvectors can be used and will be a solution at ω_n . For this reason, the field profiles of deflecting modes are not unique. To illustrate this point, the transverse electric field profiles of the fourth and fifth modes (M4 and M5) in the 500 MHz, $\beta_0 = 1$ cavity are presented in Fig. 62 (c, d); for this cavity these are the first deflecting modes. There may be

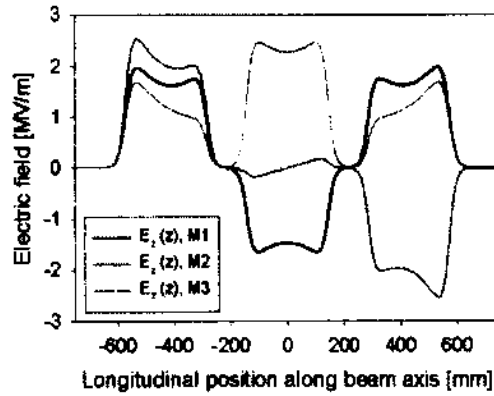


FIG. 61: On-axis field profiles for the first three accelerating modes of the 500 MHz, $\beta_0 = 1$ double-spoke cavity.

some orientations in which the field profiles of the degenerate fields may be more symmetric, however this will have no effect on the (R/Q) values of the modes.

The degeneracy of the deflecting modes does complicate the spectrum; however, in an actual cavity the polarizations will be fixed by the placement of input, pickup, and HOM couplers. In the following sections, it will be shown how the introduction of a fundamental power coupler can force a certain polarization of some modes thereby simplifying the job of HOM damping.

Using CST MWS and Omega3P (within the SLAC ACE3P code suite) [105], we have analyzed HOMs in the range between the fundamental accelerating mode, f_0 , and the cut-off frequencies of the beam pipe f_c . The cut-off frequency is given by

$$f_c(TE_{11}) = \frac{J'_{11}c}{2\pi r} \quad (141)$$

$$f_c(TM_{01}) = \frac{J_{01}c}{2\pi r}, \quad (142)$$

where r is the beam pipe radius, J_{01} and J'_{11} are the first zeros of the Bessel function of $J_n(x)$, $J'_n(x)$ of first order, and c is the speed of light. Which of these equations we use depends on the ratio of beam pipe radius to length. If this ratio is greater than 0.5, the TM_{01} is the lowest, otherwise the TE_{11} is used.

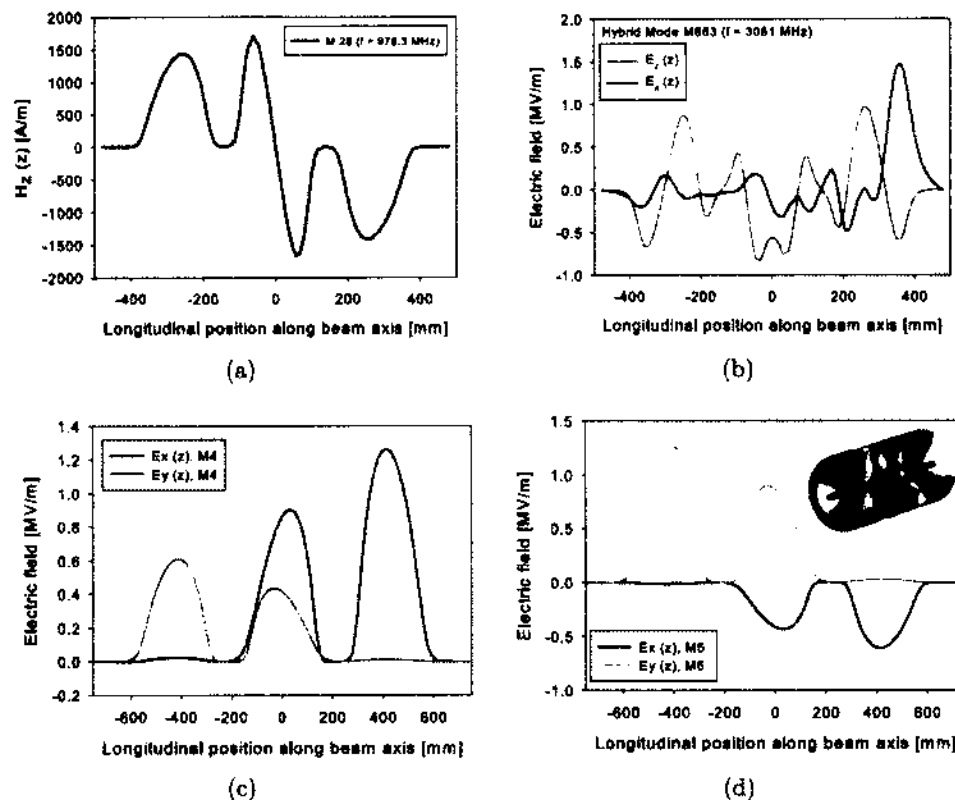


FIG. 62: On-axis field profiles for (a) TE-type, (b) hybrid modes, and (c,d) a pair of degenerate deflecting modes of the 500 MHz, $\beta_0 = 1$ double-spoke cavity.

The frequencies for both cavities are shown in Table 13. The beam pipe is generally longer than the radius of aperture, so the TE_{11} cut-off frequency of 2.93 GHz and 3.52 GHz will be used throughout.

In the case of the double-spoke cavities, the deflecting modes do not necessarily deflect along one of the cartesian axes, meaning that there are separate $(R/Q)_{y,x}$ values to be calculated for the x and y -directions; the magnitude of which will be presented as simply (R/Q) .

For a single-spoke cavity, the HOM spectrum is simpler. As with multi-spoke cavities, modes can be characterized as accelerating, deflecting, or TE-type. Because of the symmetry, the deflecting modes are not degenerate (the spoke forces only one

TABLE 13: Cut-off frequencies of the single-spoke and double-spoke cavities.

Cavity	Aperture radius	f_c (TE ₁₁₁)	f_c (TM ₀₁₀)
325 MHz single-spoke	30 mm	2.93 GHz	3.83 GHz
500 MHz double-spoke	25 mm	3.52 GHz	4.59 GHz

polarization). A deflecting mode comprised of E_x and H_y components, for example, is not just a mode with E_y and H_x components translated by some angle. These are in fact separate modes altogether. Figure 63 shows the on-axis electric field for the fundamental mode as well as the on-axis electric and magnetic fields for the first deflecting mode.

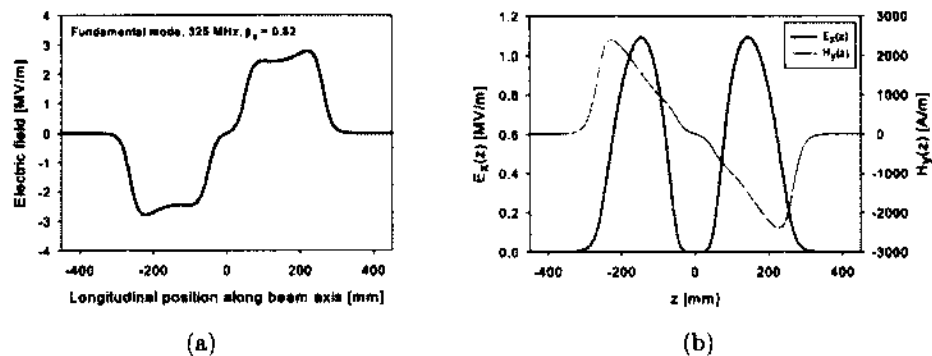


FIG. 63: On-axis field profiles for (a) the fundamental mode and (b) the first deflecting mode of the 325 MHz, $\beta_0 = 0.82$ single-spoke cavity.

6.2 GEOMETRIC SHUNT IMPEDANCE (R/Q)

The coupling strength of each electromagnetic mode with charged particles within the cavity is characterized by the ratio of the mode's shunt impedance to the cavity's quality factor, (R/Q). This is a convenient way to characterize modes since (R/Q) is a function of the accelerating (deflecting) voltage in Eqs. (66, 69), the power dissipated in the cavity walls, the rf frequency, and the energy content of the cavity. This quantity is useful when comparing cavities, in part, because it does not depend on the cavity size or material.

We define the z -axis as the direction of propagation of the beam, or longitudinal

direction. We have chosen to align the spokes respectively along the x - and y - axes, transverse to the direction of beam propagation. Since double-spoke cavities do not exhibit cylindrical symmetry, deflection may occur in any transverse direction, such that for a single mode, particles may experience deflecting voltages simultaneously along the x and y directions.

Usually the phase φ that maximizes the coupling of the particle with the cavity mode can be determined by inspection. In the case of multi-spokes cavities, however, this may not be true, and so we have used MATLAB to find φ in our calculations, by solving the optimization equations

$$\frac{dV_x(z)}{d\varphi} = 0, \quad (143)$$

$$\frac{dV_y(z)}{d\varphi} = 0. \quad (144)$$

Starting with the definition of $V_y(z)$

$$V_y(z) = \int [E_y \sin(\alpha + \varphi_y) - H_x \cos(\alpha + \varphi_y)] dz, \quad (145)$$

where $\alpha = \omega z / \beta_0 c$. Then

$$\frac{dV_y(z)}{d\varphi} = \int \{E_y [\cos \alpha \cos \varphi_y - \sin \alpha \sin \varphi_y] + H_x [\sin \alpha \sin \varphi_y + \cos \alpha \cos \varphi_y]\} dz = 0. \quad (146)$$

Dividing by $\cos \varphi_y$, rearranging and solving for φ_y we get

$$\varphi_{max,y} = \arctan \left[\frac{\int E_y \cos \alpha dz + \int H_x \sin \alpha dz}{\int E_y \sin \alpha dz - \int H_x \cos \alpha dz} \right]. \quad (147)$$

Similarly, for $V_x(z)$

$$\varphi_{max,x} = \arctan \left[\frac{\int E_x \cos \alpha dz - \int H_y \sin \alpha dz}{\int E_x \sin \alpha dz + \int H_y \cos \alpha dz} \right]. \quad (148)$$

Of course, this method could just as easily find a minimum but since we are only interested in the absolute value, that point is not relevant. In this way, we are quickly able to identify the phase between the particle and rf fields which imparts the highest transverse voltage. This value is then used to calculate $(R/Q)_\perp$, which is compared to that obtained from Panofsky-Wenzel, i.e. Eq. (69).

The HOM spectrum for both cavities (at the design velocity) are presented in Fig. 64. For the single-spoke cavity, we are able to identify a direction for the deflection while for the double-spoke cavity, we just generalize all transverse modes as deflecting. In both cases, (R/Q) of the fundamental mode is many times higher than that of the next highest value. The trends are also the same; as the frequency increases, the geometric shunt impedance decreases and the density of modes increases.

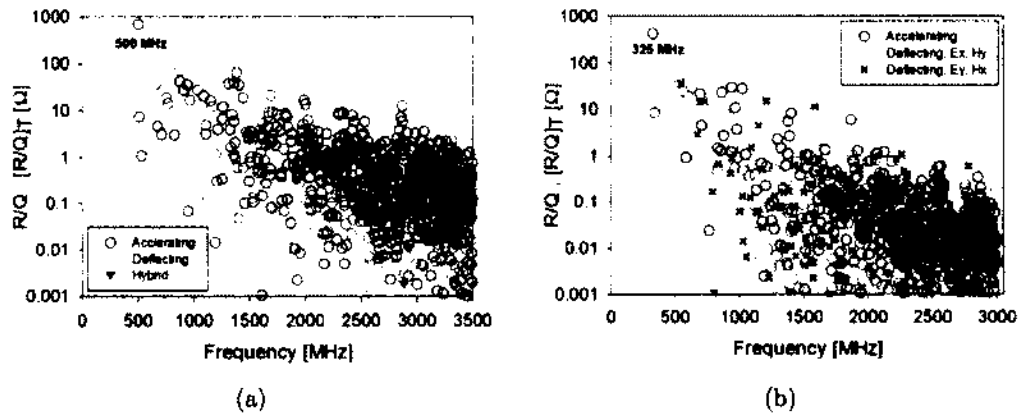


FIG. 64: Geometric shunt impedance vs. frequency for (a) the 500 MHz double-spoke cavity and (b) the 325 MHz single-spoke cavity.

6.3 VELOCITY DEPENDENCE

As mentioned previously, one of the most appealing features of a spoke cavity is its large velocity acceptance; for this reason it becomes necessary to understand the dependence of (R/Q) on $\beta = v/c$, over a wide range of β (0.6 to 1) for the fundamental mode and HOMs. Furthermore, we need to consider that the phase φ that maximizes the mode coupling with beam particles will be velocity-dependent as well. Thus, for each β we have used the method described in the previous section to identify a corresponding φ that yields a maximum $(R/Q)_{\perp}$ for the relevant mode (identifying worst-case scenarios).

When considering the velocity dependence of (R/Q) for the different cavities, the application should be considered to analyze a meaningful range of particle energies. The 325 MHz, $\beta_0 = 0.82$ cavity, for example, is intended for high energy protons/ions while the 500 MHz, $\beta_0 = 1$ double-spoke cavity is intended to accelerate electrons from 1.5 MeV to 25 MeV. In either case, we can find the particle velocity by first

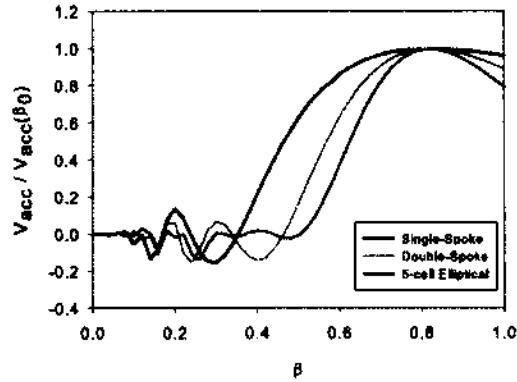


FIG. 65: Velocity acceptance of a single- and double-spoke cavities compared to a 5-cell elliptical cavity.

determining γ with

$$E = K + m_0c^2 - \gamma m_0c^2, \quad (149)$$

then solving for v to get

$$v = \sqrt{1 - \frac{1}{\gamma^2}} \cdot c. \quad (150)$$

For accelerating an electron from 1.5 MeV to 25 MeV (as in the ODU light source), this corresponds to $0.967 \leq \beta \leq 1$. Therefore, for our purposes it is not necessary to consider the β -dependence of (R/Q) for electron acceleration. As an illustration, we will consider both single- and double-spoke cavities designed for $\beta_0 = 0.82$ operating at 325 MHz [101].

To determine the useful velocity range of such cavities, consider the velocity acceptance shown in Fig. 65. The single-spoke cavity is greater than 96% efficient in accelerating particles between $0.7 \leq \beta \leq 1$. This corresponds to protons with energies between 380 MeV and greater than 1.5 GeV. The double-spoke cavity has a 96% efficiency between $0.74 \leq \beta \leq 0.92$ (460 MeV and 1.5 GeV). For comparison, the velocity acceptance of a 5-cell elliptical cavity is also shown to have a similar efficiency between $0.76c$ and $0.88c$.

These velocity ranges are relevant, for example, to the European Spallation Source (ESS) linac [129, 130], where the high-velocity section uses 5-cell elliptical cavities

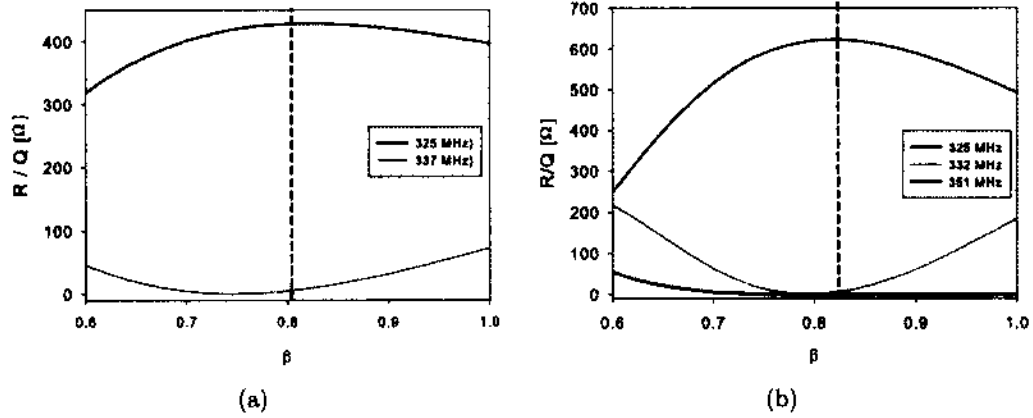


FIG. 66: Dependence of geometric shunt impedance on particle velocity for the first pass band of the (a) 325 MHz, $\beta_0 = 0.82$ single-spoke cavity and (b) 325 MHz, $\beta_0 = 0.82$ double-spoke cavity.

(704.42 MHz, $\beta_0 = 0.86$) to accelerate protons from 561 MeV to 2 GeV ($0.78 \leq \beta_0 \leq 0.95$).

Figure 66 shows the β -dependence of the first 2 and 3 modes for the single- and double-spoke cavities, respectively. As one would expect, the highest (R/Q) of the fundamental mode is at the design β . The effects that the number of gaps has is also clearly observed. Just as with the velocity acceptance, the (R/Q) of the single-spoke cavity is much flatter across the entire range shown.

The velocity dependence of other higher order modes, both accelerating and deflecting, are shown in Fig. 67. The modes were selected based on the maximum geometric shunt impedance but there is nothing particularly special about them other than that. An interesting feature of the single-spoke HOMs is that most of them have the highest (R/Q) value at higher β . This is generally the case for the double-spoke as well, especially for the deflecting modes.

As was mentioned in the previous section, the deflecting modes of the double-spoke cavity are degenerate. Unlike the single-spoke cavity, the deflection does not necessarily occur either parallel or perpendicular to one of the spokes, rather, the net deflection may be directed at some angle with respect the spokes. In this sense, each member of a deflecting mode pair has a direction-specific $(R/Q)_\perp$ value, which we will label either x or y .

In order to calculate the $(R/Q)_{x,y}$, an associated $\varphi_{max,x,y}$ must first be found for

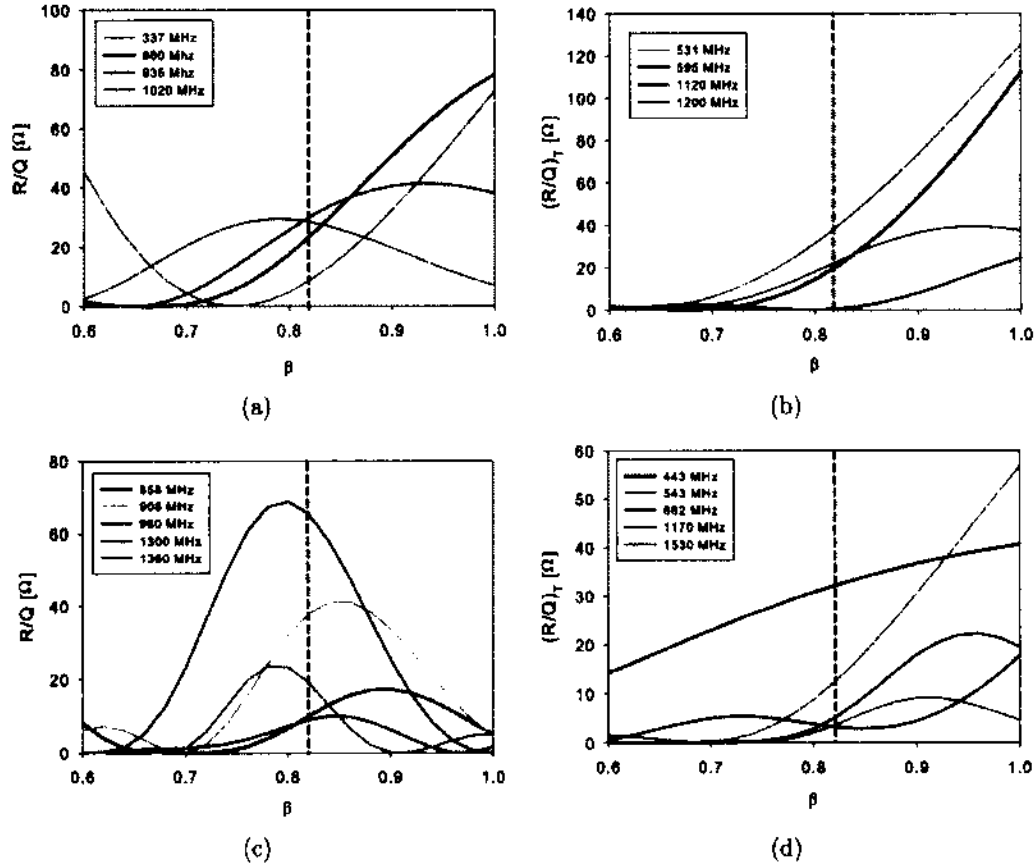


FIG. 67: Velocity dependence of selected (a) accelerating and (b) deflecting modes of the single-spoke cavity and (c) accelerating and (d) deflecting modes of the double-spoke cavity.

each β under investigation. Figure 68 shows how $(R/Q)_x$ and $(R/Q)_y$ are related to each other for one pair of deflecting modes. As would be expected, $(R/Q)_x$ of one mode is the same as the $(R/Q)_y$ of the other. It should be noted that for each pair, $\varphi_{max,x} \neq \varphi_{max,y}$, for a given β . In other words, the phase between the fields and the particle required to achieve a maximum deflecting voltage for each direction is different. It is interesting to observe, however, that for some value of β , this phase will be the same. In some cases, there are even multiple values of β for which this is the case. For example, the modes shown in Fig. 68 at 727 MHz have the same value of φ_{max} at $\beta = 0.66, 0.82,$ and 0.90 .

Finally, the $(R/Q)_\perp$ values reported in the Appendix are the vector magnitude

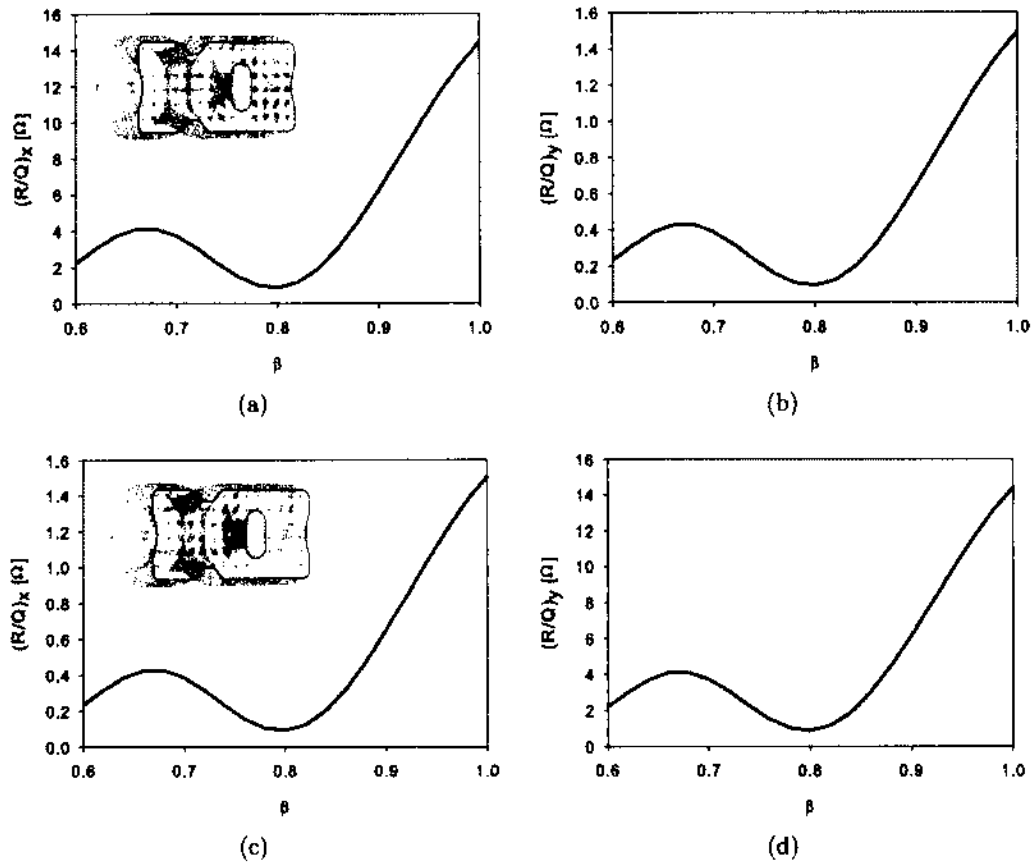


FIG. 68: Direction specific velocity dependence of $(R/Q)_{x,y}$ for a degenerate pair of deflecting modes in the 325 MHz double-spoke cavity. (a) and (b) are for one mode and (c) and (d) are for the other.

using $(R/Q)_x$ and $(R/Q)_y$ as the components. We can also determine the overall direction of $|(R/Q)_\perp|$ using these components. Because $R/Q \propto V^2$, this also gives us information about the direction of deflection, while the actual direction can occur in any quadrant (not just between 0 and π). Surprisingly, many fall along one of the Cartesian axes. For each pair of degenerate modes, if the angle of deflection for one is along the x -axis, the angle of the other mode will be 90° from that (along the y -axis).

Some modes do not behave in this way and cause a net deflection at some angle from the x -axis. However, the angle between the deflection of each member of a degenerate pair will be 90° . In Table 14, a few examples of this behavior are shown.

TABLE 14: Deflection Angle of Degenerate Deflecting Mode Pairs.

Frequency	θ_1	θ_2	Difference
700 MHz	-2.01°	88.0°	90.0°
727 MHz	-5.97°	83.9°	89.9°
770 MHz	38.9°	-50.1°	89.0°

TABLE 15: Beam Parameters: ODU Inverse Compton Source

Parameter	Value	Units
Bunch Charge	10	pC
Rep. Rate	100	MHz
f_{rf}	500	MHz
Beam Current	1	mA
Bunch Length	0.9 (3)	mm (psec)
Cavity Voltage V_{acc}	6	MV
Quality Factor Q_0	1.5×10^9	-

θ_1 and θ_2 are the deflecting angle of the first and second member of a mode pair, respectively. The difference shows that the angle between the deflection directions of the two modes is roughly 90°.

6.4 BEAM LOADING

In this section, the beam loading calculations are reported for the ODU Inverse Compton Source. In addition, a generic calculation is performed for the 325 MHz single-spoke cavity to give us a sense of the potential power dissipated from HOMs, and thus the possible need for damping.

In order to find the loaded quality factor of the cavity, in the presence of the beam, we first need to find the impedance R_b . Starting with the beam power

$$P_b = I_c V_{acc} \cos \phi_0, \quad (151)$$

where ϕ_0 is the phase of the beam with respect to the cavity rf fields. Electron linacs typically operate on crest ($\phi_0 = 0$), since the energy deviation does not lead

to time-of-flight variations, as would be the case for heavier particles such as ions or protons. In this case, the beam power is

$$P_b = 1 \text{ mA}(6 \text{ MV}) \cos 0 = 6 \text{ kW}.$$

The impedance of the beam is given by

$$R_b = \frac{V_{acc}^2}{2P_b} = \frac{36 \times 10^{12} \text{ V}^2}{2(6 \text{ kW})} = 3 \times 10^6 \Omega.$$

To find the power dissipation as described in Eq. (80), we first need to determine the loss factor, k_{loss} for each individual HOM. This loss factor does not take into account the interaction of the bunches with their wakes. Using the geometric shunt impedance and frequency values given in the Appendix, the loss factor is shown in Fig. 69.

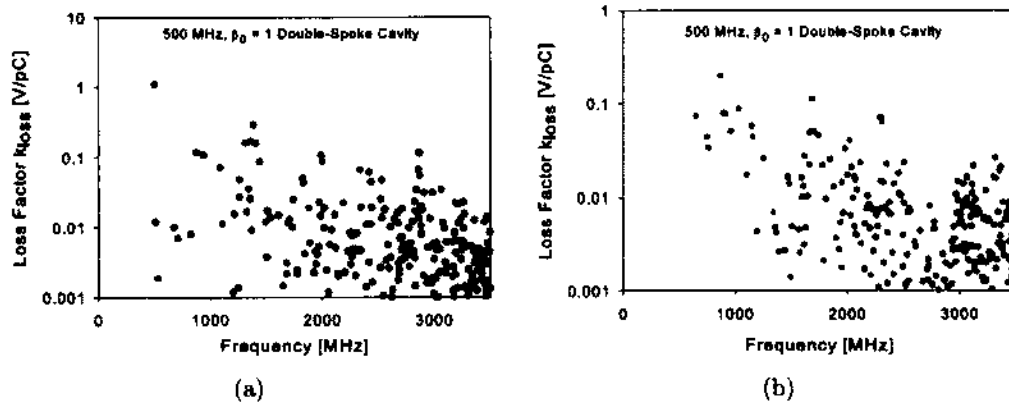


FIG. 69: Loss factor of (a) accelerating modes and (b) deflecting modes for the 500 MHz double-spoke cavity.

We can see that, other than for the fundamental mode, the loss factor is on the same order for both accelerating and deflecting modes. The loss factor of the 325 MHz single-spoke cavity (for a 60 pC proton beam) is shown in Fig. 70. In this case, the particle velocity also needs to be considered since $k_{loss} \propto (R/Q)(\beta)$.

An interesting effect occurs when we plot the sum of the loss factors for all accelerating modes while also looking at the contribution from only the fundamental. Figure 71 shows the total loss factor (normalized) along with the fundamental mode and accelerating HOMs as a function of β .

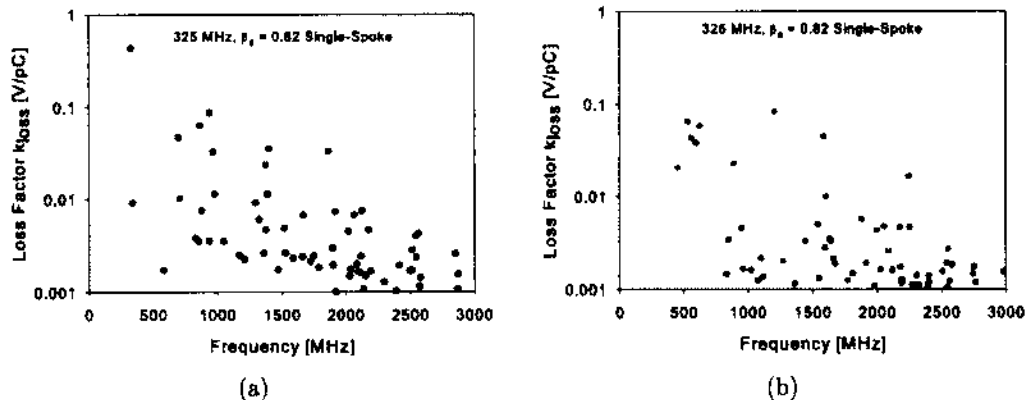


FIG. 70: Loss factor of (a) accelerating modes and (b) deflecting modes for the 325 MHz single-spoke cavity.

The contribution of the accelerating modes is less than that of the fundamental mode below about $\beta = 0.75$. Above that, the contributions diverge such that at $\beta = 1$, the other accelerating modes contribute several times that of the fundamental mode to the total loss factor.

From Eq. (86), the voltage that a single bunch induces on the cavity can be calculated. The individual voltages can then be integrated for frequencies up to the beam pipe cut off frequency. In Fig. 72, the integrated voltage due to accelerating and deflecting modes are shown separately. Notice that below ~ 1000 MHz, the deflecting modes are responsible for a greater induced voltage. This is expected because, as shown in the Appendix, the low-frequency geometric shunt impedances are much higher for the deflecting modes.

From the voltage, we can then get the power dissipation with

$$P_b = I_0 \Re(\tilde{V}_b),$$

where I_0 is the average beam current. In the case of the ODU Inverse Compton Source, the nominal current is 1 mA. In Fig. 73, we can see that the power dissipated is in the mW range for both the nominal current and a current which is a factor of 10 higher. Even at 100 mA, the dissipated power would be about 5 W per cavity, or roughly 20 W total for the linac. This is close to 10% of the expected power dissipated in the operating mode.

We can also look at an application of the 325 MHz single-spoke cavity. This

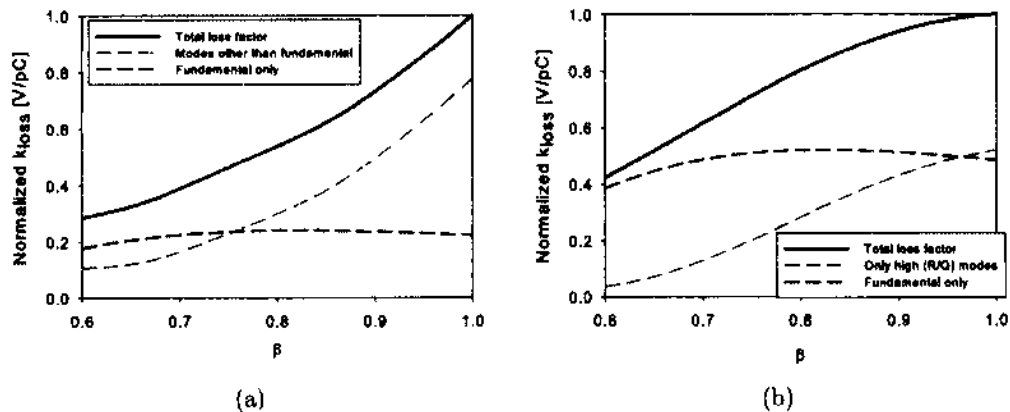


FIG. 71: (a) Loss factor of all accelerating modes (black solid) (a), only high (R/Q) modes (b) and the contribution from the fundamental mode (blue dashed) and that of all other accelerating modes considered (red dashed).

TABLE 16: Specifications of the required proton beam for C-ADS

Parameter	Value	Units
Energy	1.5	GeV
Current	10	mA
Beam power	15	MW
rf frequency	162.5/325/650	MHz
Duty factor	100	%
Bunch charge	60	pC
Bunch length	3	mm

design is not for a specific machine, but is intended for high-velocity protons/ions such as those proposed for Accelerator Driven Systems (ADS). As an example, the linac for the Chinese ADS (C-ADS) consists of a low-velocity portion with half-wave resonators operating at 162.5 MHz and single-spoke cavities, a medium-velocity region with additional spoke cavities and elliptical cavities operating at 325 MHz, and a high-velocity region with 650 MHz elliptical cavities [131].

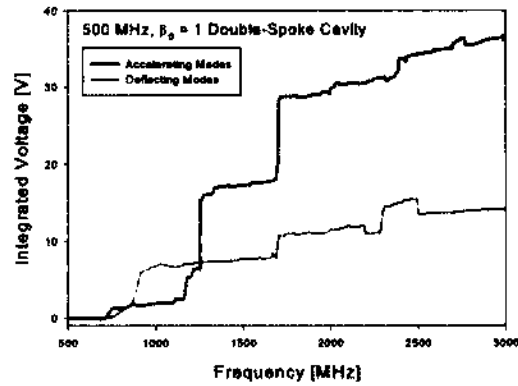


FIG. 72: Accumulated induced voltage due to HOM excitation.

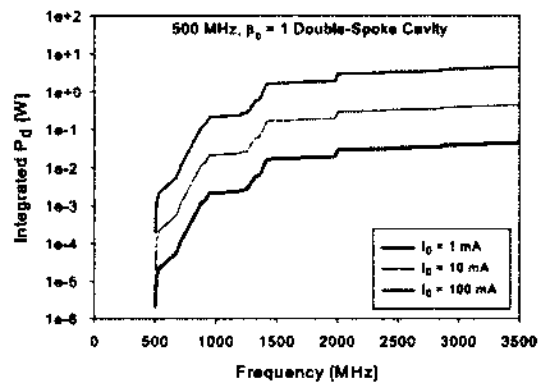


FIG. 73: Integrated power dissipated in the cavity walls due to HOM excitation.

6.5 REGENERATIVE BEAM BREAKUP

Unlike cumulative beam breakup, regenerative BBU is confined to a single structure. In this case, the deflecting mode excitation is carried from cell to cell via the strong electromagnetic coupling. An off-axis beam entering the initial cell of the structure is deflected by the magnetic field and acquires a larger transverse displacement. One-quarter period later, the off-axis beam in the back part of the structure encounters the linearly increasing longitudinal electric field of the excited deflecting mode. This decelerates this part of the beam, causing the beam to dump energy back into the deflecting mode. This effect is quickly distributed throughout the cavity due to the high level of cell-to-cell coupling. If the beam induced growth rate exceeds the ohmic loss rate in the cavity walls, the field and beam displacement run away exponentially, resulting in a loss of the beam within the linac. This can only happen beyond a starting, or threshold current given by Eq. (103), or, in terms of transverse impedance

$$I_{th} = \frac{\pi^3 E k}{2 Z'' L^2}, \quad (152)$$

where E is the beam energy, k is the wavenumber of the HOM, L is the reference length of the cavity, and Z'' is the transverse impedance per unit length squared (Ω/m^2) [132].

For this preliminary study, the beam parameters given in Tabs. 15 and 16 can be used along with the HOM properties given in the Appendix. What we wish to do is first estimate the impedance limit which would be given if the threshold current is the beam current. We can then compare the undamped mode impedance with this "threshold" impedance.

Figure 74, shows the impedance above which regenerative BBU would occur for a 1 mA electron beam (double-spoke) and a 10 mA proton beam (single-spoke). Also, the impedance calculated as $(R/Q) * Q_0$ which represents the impedance of a completely undamped mode. The beam energy difference is so great that for the proton beam (b), the undamped impedance for each mode is insignificant. For the ODU inverse Compton source, an electron beam at 25 MeV has a relatively low threshold for mode impedance as many undamped modes would exceed this value. With this being the case, we can now look at what level of damping would be necessary to suppress the HOMs sufficiently enough such that the threshold current

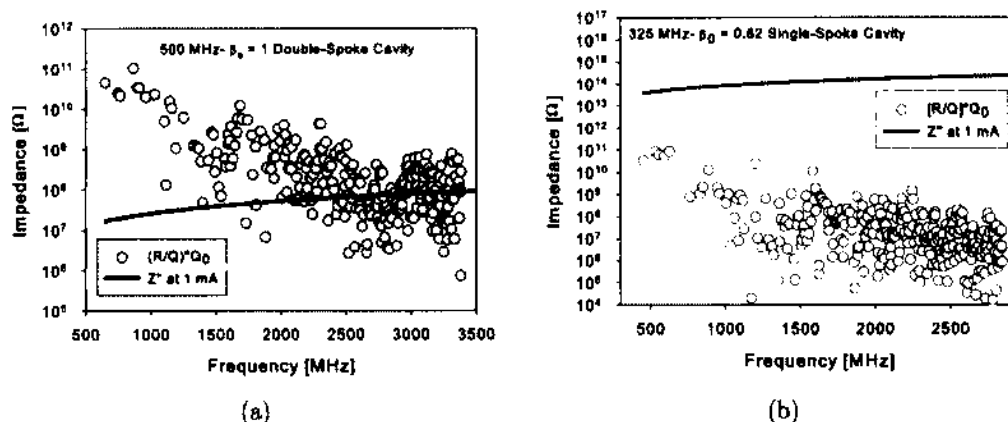


FIG. 74: Impedance for undamped deflecting HOMs and the impedance of each mode at $I_{th} = 1$ mA for the 500 MHz double-spoke (a) and $I_{th} = 10$ mA for the 325 MHz single-spoke (b).

is not breached.

In Fig. 75, the threshold current is shown for three levels of HOM damping. The horizontal lines represent the nominal current of 1 mA and a 10 mA safety margin current. We consider $Q_L = 10^8$ to be that of virtually undamped modes, perhaps only damped by the fundamental power coupler. For 1 mA, very few modes have a threshold current below this, even on an undamped cavity. However, if we build in a $10\times$ safety margin, several deflecting modes have a threshold current below this level. We would be most concerned with modes falling at or near an integer number of repetition rate of 100 MHz (shown by the vertical lines). If all modes are damped to at or below 10^7 , none have a threshold current below the operating and very few are below 10 mA.

What can be concluded from this is that moderate level of damping is going to be necessary. In the next sections, what level can be achieved will be discussed as well as if those levels are acceptable.

6.6 HIGHER ORDER MODE COUPLERS

In Chapter 3, and the previous sections, the undesirable consequences associated with HOMs were described. Namely, HOM excitation places an additional burden on the cryogenic system as well as causes beam instabilities. There is some level

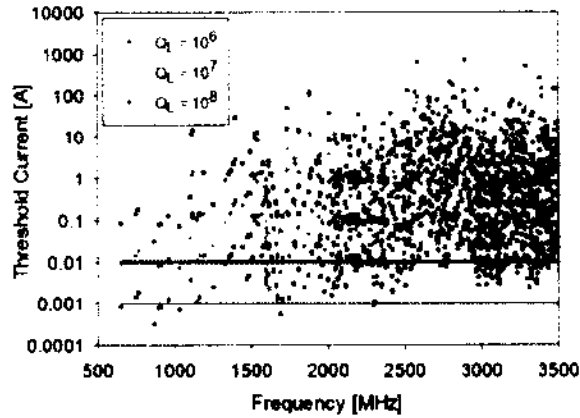


FIG. 75: Threshold current for all higher order deflecting modes at various levels of damping.

of geometric manipulation that can be done to affect the HOM spectrum, such as introducing symmetry-breaking components/features that eliminate degeneracy or improve mode separation. In fact, as was mentioned in Chapter 1, the reason the spokes are arranged perpendicular to each other in a multi-spoke cavity is to improve the separation between the fundamental mode and the nearest neighbor mode(s). However, clever choices in the cavity geometry cannot eliminate all dangerous HOMs, thus, there is often a need to extract the power generated by HOMs and deposit it in a higher temperature environment.

We saw in Chapter 1 that the energy deposited by a single charge q passing through the cavity is given by

$$U_q = k_n q^2, \quad (153)$$

where k_n is the loss factor

$$k_n = \frac{\omega_n R}{2 Q_0}. \quad (154)$$

Equations (153) and (154) apply to a single point charge moving through a PEC cavity, where the total power transferred to the cavity by a bunch depends on the beam current [133]. In either case, it is clear that the goal of any HOM coupler design must be to strongly couple to modes that are found to be problematic as defined in the previous sections.

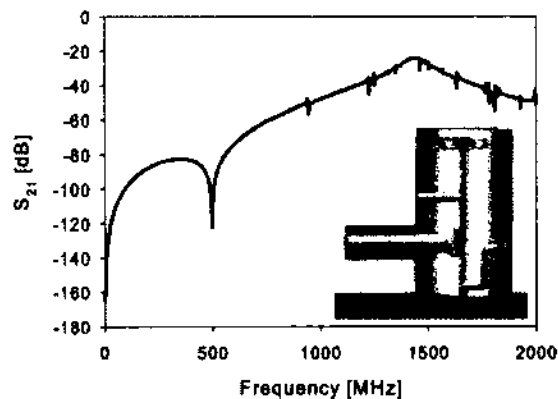


FIG. 76: Transmission curve of a notch filter.

There are three primary HOM coupler designs: 1) antenna/loop couplers, 2) waveguide couplers, and 3) beam pipe couplers with absorbers [133]. In order to retain the longitudinal compactness spoke cavities provide, we are not interested in the third option. Waveguide couplers are generally used in high frequency cavities, but for the low frequencies we are using, they would not be compact, so we will not focus on those either. This leaves the antenna/loop couplers, which will now be discussed.

6.6.1 COAXIAL HIGH-PASS NOTCH FILTERS

A higher order mode coupler which rejects only a narrow frequency is often referred to as a notch filter. The transmission curve of such a filter (shown in Fig. 76) resembles that of the high-pass filter, however there is strong rejection (the notch) at a particular frequency. In this case, the notch is at 500 MHz, with an increasing damping above that.

The design presented in Fig. 76 is a modified version of the HERA and TESLA HOM coupler [134–136]. The notch filter consists of a coaxial line antenna, a 50 Ω extraction line, multiple inductive stubs and capacitive gaps including the notch for frequency adjustment. One drawback of the notch filter is its complexity as compared to the simple design from the previous section.

The frequency of the notch filter we have designed for the damping requirements

described in the next section can be roughly estimated by considering the circuit diagram shown in Fig. 77 (a).

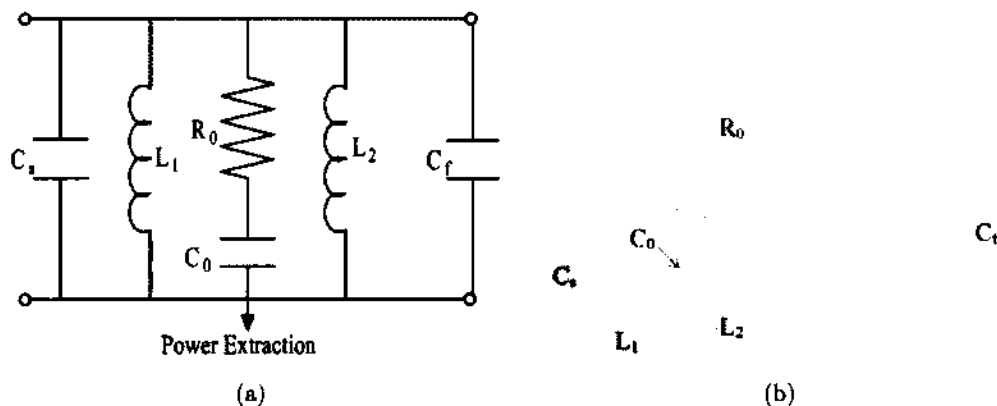


FIG. 77: (a) Circuit diagram [137] and (b) schematic of the notch filter used for mode damping on the 500 MHz double-spoke cavity.

6.7 HIGHER ORDER MODE DAMPING

Using a combination of high-pass notch filters as described in the previous section, it is possible to damp the higher order modes to both minimize the additional cryogenic load and prevent beam instabilities. This combination is not always straightforward; it depends on what modes are dangerous and how they are polarized in the case of deflecting modes.

There are different reasons why a mode could be dangerous. For the accelerating modes, the main concern is power dissipation into the cavity walls. If the frequency of the mode is the same, or within a half-width to a harmonic of the beam frequency, this is an even greater problem. Beam breakup and emittance growth are the primary concern for deflecting modes. In either case, it is necessary to determine a reasonable criteria to estimate the impact individual modes can have and determine what level of damping is needed to avoid any unwanted consequences.

In Chapter 4, it was shown that the loaded quality factor of the 500 MHz cavity fundamental power coupler should be 9×10^6 . Since this value is much lower than the Q_0 of the majority of HOMs, the level of damping by the FPC must be considered before determining any additional damping requirements.

In Figure 78 the external quality factor is shown for a range of accelerating and deflecting modes of the 500 MHz, double-spoke cavity. The FPC is located in an end

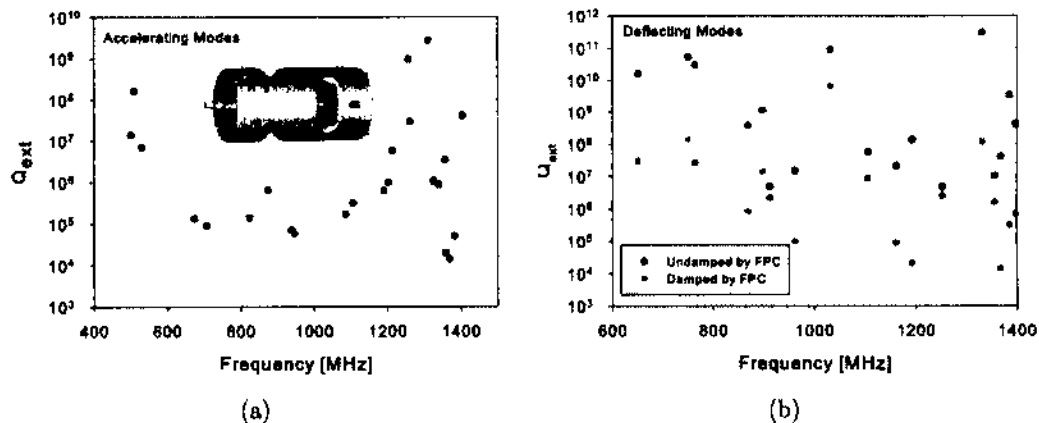


FIG. 78: (a) Accelerating and (b) deflecting modes damped by the FPC alone. Note that only one deflecting mode polarization is damped.

cell, oriented parallel to the spoke (shown in red). As would be expected, the FPC can only couple to one polarization of each deflecting pair. Note that a high Q_{ext} only means that the mode does not couple to the FPC and is therefore undamped. In this case, any calculation involving Q_{ext} would be replaced with Q_0 .

The various polarizations of the deflecting modes determine the placement of the HOM couplers more than the accelerating modes so it is natural to begin there. Referring to Fig. 74 (a), it is clear that many, if not most deflecting modes in the 500 MHz double-spoke cavity would have to be damped even for the nominal current of 1 mA. In addition, from Fig. 78 (b), that a number of the deflecting modes do get damped by the FPC while some do not.

Normally, a minimum of two HOM couplers are needed to couple each polarization of a mode (usually referred to as vertical and horizontal). This is true in multi-spoke cavities as well. What needs to be determined is if more than two HOM couplers are needed. There are a number of options for coupler placement, but only those placed in areas where a mode's electromagnetic fields are present will be effective. In Fig. 79 the surface fields are shown for two pairs of degenerate deflecting modes along with two HOM couplers and the FPC in a particular configuration.

The location of the HOM couplers are determined by the surface fields of the deflecting modes, examples of which are shown in Fig. 79. Which modes should be determinant depends on the beam spectrum as well as the $(R/Q)_\perp$. Figure 74

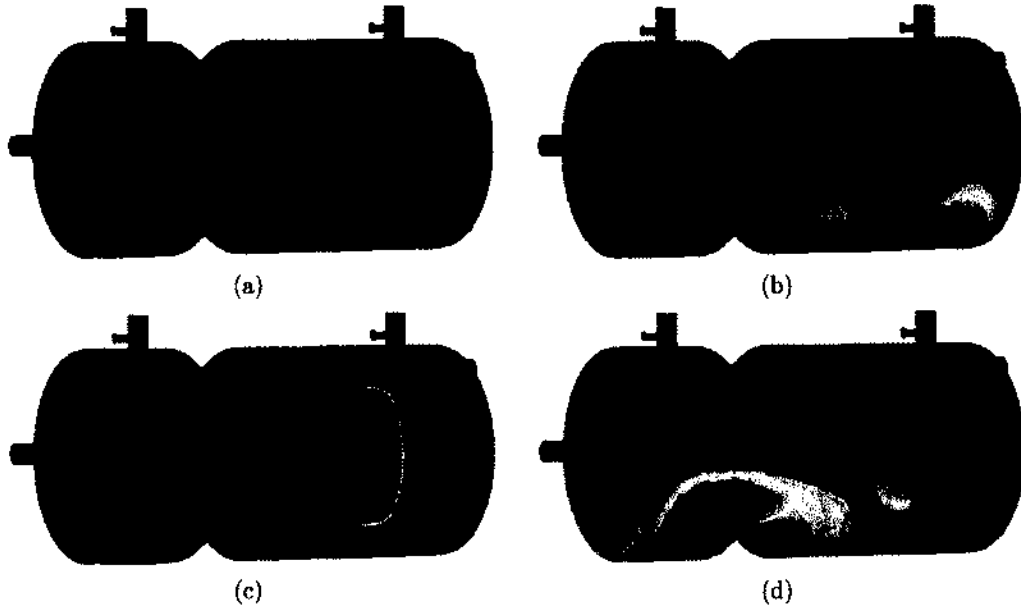


FIG. 79: Surface electric field of two pairs of deflecting modes. (a) and (b) are at 650 MHz while (c) and (d) are at 897 MHz.

(a) does not tell much other than most deflecting modes would need to be damped. However, which mode configurations are important can be narrowed down when considering Fig. 75 with the undamped Q s given in the Appendix.

To determine which accelerating modes pose a problem in terms of cryogenic load, we will first focus on determining what coupling is necessary to keep the power to less than 1 W, even if it is a mode which is resonant with a bunch frequency (i.e. machine line). This constitutes a worst case scenario where the particles are exactly on-crest ($\varphi = 0$ as would be the case for electrons) and the bunch spacing is much less than the decay time of a mode. In this situation, the power dissipated for each mode would be

$$P_c = \frac{R_s I_0^2}{(1 + \beta)^2}, \quad (155)$$

where β is the coupling coefficient (Q_0/Q_{ext}), R_s is the mode's shunt impedance, and I_0 is the average beam current. In this way, we can solve for what the external quality factor must be in order to have less than 1 W dissipated into the cavity walls for each mode, even if it is resonant with a machine line.

Figure 80 (a) shows the Q_{ext} necessary to have no more than 1 W of dissipated power even if the mode is resonant with a machine line (red) and the actual Q_{ext} achieved from the configuration shown in Fig. 79. While there may be a few modes at the low frequency end that may need more damping if they were in fact resonant with a machine line, the vast majority of modes are very well damped.

For the same configuration of couplers, we can also determine if the requirements to avoid breaching the threshold current are met. Figure 80 (b) shows the impedance budget (as determined by the threshold current of 1 mA) as well the damped mode impedance. As we can see, most of the modes are in fact damped sufficiently.

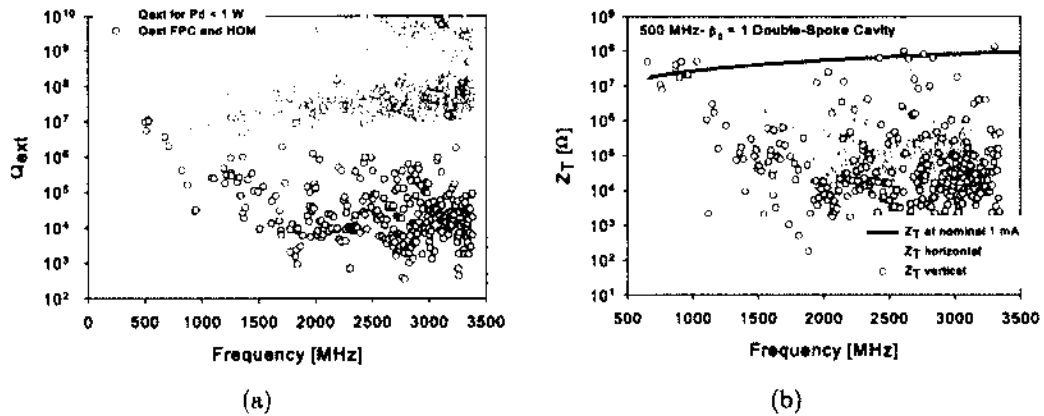


FIG. 80: (a) Q_{ext} needed for less than 1 W dissipated power and the actual Q_{ext} provided by the FPC and HOM couplers and (b) Mode impedance after damping. The line plot represents the impedance budget at a nominal current of 1 mA.

CHAPTER 7

MECHANICAL ANALYSIS

Any mechanical study must take into account the intended operating conditions specific to the particular cavity. In this case, both cavities must withstand 1 atm external pressure at room temperature during the leak check and 1.4 atm during the vertical dewar testing. Additionally, a cavity must not yield or rupture under 2.2 atm external pressure during cool-down in a cryo-module. Simulation boundary conditions will be similar to those that would be realized in the case that the cavity is loaded into a machine-type cryo-module.

Some of the quantities which will be discussed are stress and strain. The stress is defined as the ratio of force to original area of cross-section of the material while strain is the ratio of change in length to the original length. A typical stress/strain curve is shown in Fig. 81.

When stress is placed on the material, initially the relationship with strain is linear. Up to a certain point identified at (2) in Fig. 81, the material will return to its original shape when the load placed on it is released. In other words, the deformation is elastic in nature. After that point, known as the “yield” or plastic deformation limit, the material will be permanently deformed and the relation between stress and strain becomes non-linear. In addition, once the material has been plastically

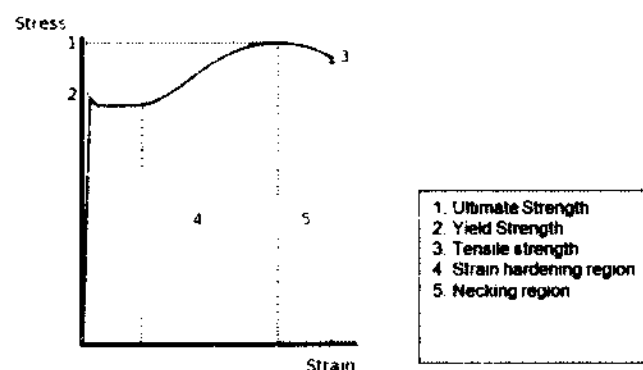


FIG. 81: Stress/strain curve for a typical metal.

deformed, it will experience strain hardening thus making it increasing difficult to repair. This is what we wish to avoid.

7.1 PRESSURE SENSITIVITY

The criteria that this analysis is intended to meet are:

- (i) retain the design shape by identifying and strengthening the areas of the cavity which may experience plastic deformation, and
- (ii) identify what combinations of stiffening techniques can be used to minimize the change in frequency under operating conditions

The deformation and associated von-Mises stress on the cavity due to the atmospheric pressure are found using ANSYS®. We examined the conditions a cavity will encounter once it is fabricated and ultimately tested in the VTA. These are 1 atm vacuum load at 300 K and 1.4 atm vacuum load at 4.2 K. It is not necessary to consider a vacuum load at 2 K as the pressure due to liquid helium is much less than atmospheric (23 Torr). To do this, we calculate the maximum von-Mises stress on the cavity to see if it exceeds the limit for plastic deformation at room temperature and at 4.2 K which are about 50 MPa and 300 MPa, respectively [138].

There are two boundary conditions which are used for this investigation. The first is for a completely free cavity meaning that all surfaces are able to move due to the force placed on them by the vacuum. The second has the beam pipe ends fixed as would be the case when in a cryo-module or some other restrictive structure.

Figure 82 shows the area of maximum stress for the 325 MHz single-spoke cavity under these two conditions. In both cases the end cap experiences the greatest amount of stress, however, when the cavity is unrestrained, the location is near the cleaning ports while for the case of a fixed beam port, the maximum occurs where the beam pipe meets the end cap.

With no support fixture, the 325 MHz single-spoke cavity experiences 323 MPa equivalent stress (at 300 K), which is at the upper limit of what is acceptable. With the beam pipe fixed, this value is reduced to 52 MPa which is within the acceptable range for 300 K vacuum measurements. However, Fig. 82 (c) and (d) show the same conditions at 1.4 atm. In this case, the unrestrained model has a maximum equivalent stress of 438 MPa, which is localized. However, there are large areas

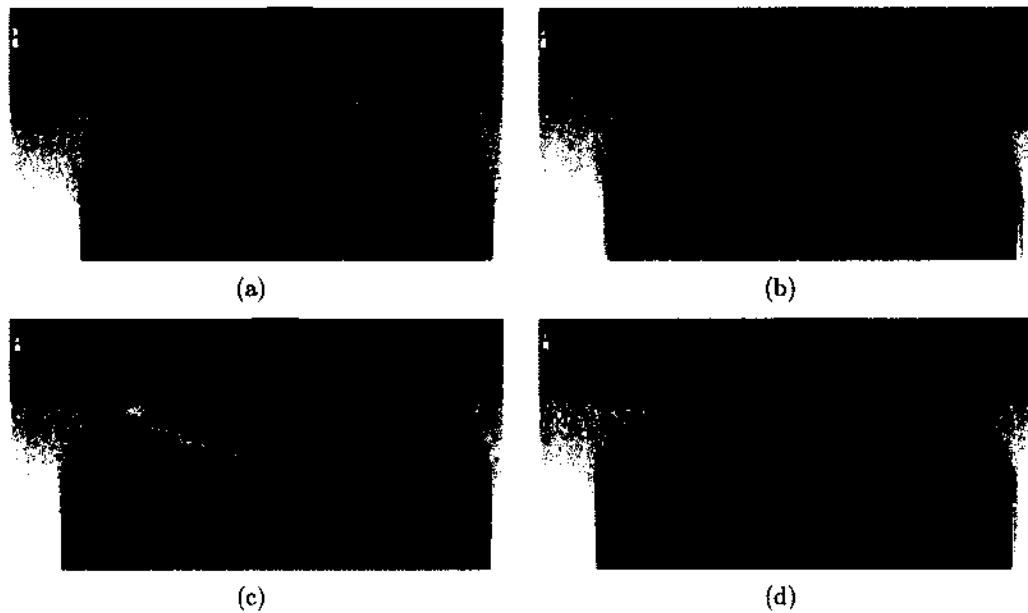


FIG. 82: von-Mises stress under 1 and 1.4 atm, on the bare, 3 mm thick cavity, with (a, c) the beam pipe free and (b, d) with it fixed.

which experience more than 100 MPa. Even the restrained model has areas with 60-90 MPa equivalent stress. We can conclude that fixing the beam pipe is insufficient for cryogenic testing in the VTA. As a solution, an external support structure was constructed and is attached where the beam pipe meets the end cap reentrant cone, as shown in Fig. 83. The stress on the end cap is now less than 50 MPa, while the maximum of 65 MPa is on the spoke. The fact that a 3 mm spoke experiences 65 MPa at 1.4 atm is the reason we made them 4 mm thick.

The 500 MHz cavity was originally intended to be mounted in a helium jacket and cryo-module, which gives us an idea of the boundary conditions to use throughout the simulation. The bare, 3 mm thick quarter-cavity with 4 mm thick spokes, is fixed at the beam pipes. The real situation, however, is somewhere between having fixed supports and a free cavity, but closer to fixed than free.

The material properties used are [139]

- (i) Nb density = 8580 kg/m^3
- (ii) Young's modulus at room temperature: 82700 MPa



FIG. 83: von-Mises stress at 1.4 atm on the 325 MHz single-spoke cavity with the external support structure attached.

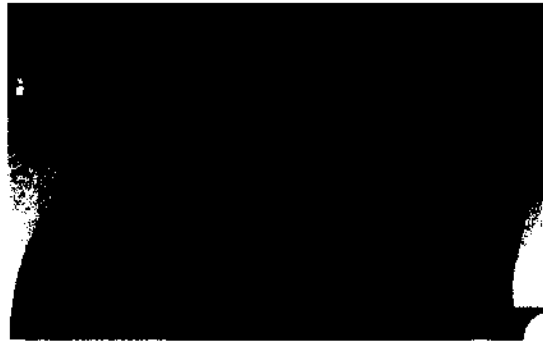


FIG. 84: von-Mises stress of the 500 MHz cavity under 2.2 atm, on the bare, 3 mm thick cavity, 4 mm spokes, with the beam pipes fixed.

(iii) Young's modulus at 4 K: 123000 MPa

(iv) Poisson ration = 0.38

The areas that experience the greatest stress (shown in Fig. 84), for the bare cavity, are where the beam pipes meet the reentrant end caps and the spoke body. Because of this, a stiffening mechanism(s) must be imposed in those areas.

We have explored previously proposed stiffening mechanisms such as ribs [11, 140] and rings [11, 17]. At 2.2 atm, both the end caps and spokes need to be either stiffened or thickened. We have found that 4 mm thick spokes allow them to withstand this pressure, so this is the solution chosen here.

In order to meet the criteria previously mentioned, it is important to first understand what effect deformations of different parts of the cavity have on the frequency.

To do this, a script written by Gary Cheng of Jefferson Lab was used to calculate the frequency of the undeformed and deformed cavity. The approach taken here has been to divide the cavity into the outer conductor, the end caps, and the spokes. 1 atm external pressure was then applied to each of those surfaces, individually, while leaving all other surfaces free from pressure and free to move. Table 17 summarizes the results of this analysis.

TABLE 17: Pressure Sensitivity by area. A 1 atm vacuum load was applied only to each of the three areas, individually, and the frequency shift was calculated.




Area	Δf (kHz)	$\Delta f/\Delta P$ (Hz/Torr)
	14	18
	-88	-120
	-0.91	-1.2



FIG. 85: 3 mm cavity with 4 mm thick spokes and end cap stiffening ribs.

The data given in Table 17 provides a starting point, but does not account for how individual areas affect each other when taken as a whole. Given that any stiffening solution must meet the first criteria above, it allows us to understand the degree of stiffening these areas should receive in order to minimize the 4 K, 1 atm vacuum load frequency shift. For example, a completely rigid outer cylinder would not be able to balance the frequency shift due to weakly stiffened end caps. However, as Fig. 132

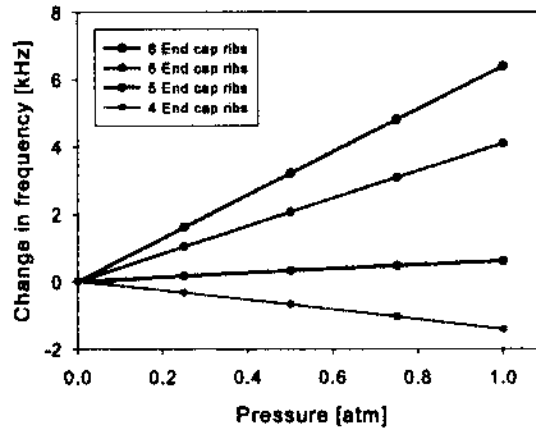


FIG. 86: Change in frequency (from 500 MHz) for varying numbers of end cap stiffening ribs.

illustrates, varying the stiffness of the end caps, by changing the number of stiffening ribs, one can greatly reduce the frequency shift at 4 K. In Table 18, we show how changing the number of end cap ribs can change the frequency shift due to *only* the end caps, under 4 K conditions.

TABLE 18: Pressure sensitivity by number of end cap ribs. A 1 atm vacuum load was applied only to both end caps, and the frequency shift was calculated.

Number of ribs	Δf (kHz)	$\Delta f/\Delta P$ (Hz/Torr)
8	-3.04	-4.00
6	-5.63	-7.41
5	-8.09	-10.6
4	-11.9	-15.7

What we have attempted to show here is that stiffening a spoke cavity such that it is able to withstand 2.2 atm external pressure, is straightforward. Balancing the frequency shifts incurred by deformations from various parts of the cavity requires a judicious placement of stiffening structures, after the stress limits have been achieved. Another consideration, however, is that decreasing the number of end cap stiffening ribs does lessen the area for which the stress is distributed. So while 5 stiffening ribs on each end cap may provide a minimal frequency shift, it does bring the stress on each rib closer to the plastic deformation limit.

7.2 MECHANICAL MODES

Figure 87 shows the cavity deformation due to the first six mechanical modes. The first one, at 86 Hz, is a concern because the frequency is so low. Extending the stiffening ribs or adding a ring to the end cap should reduce this motion. Modes 4 and 5 are just small oscillations in the spoke body, which we have already seen in Table 17, do not disturb the frequency much. Modes 2, 3, and 6 do have the potential to seriously distort the cavity volume, however the frequency is quite high, so it is unlikely we will add stiffening ribs on the outer conductor in order to dampen these modes.

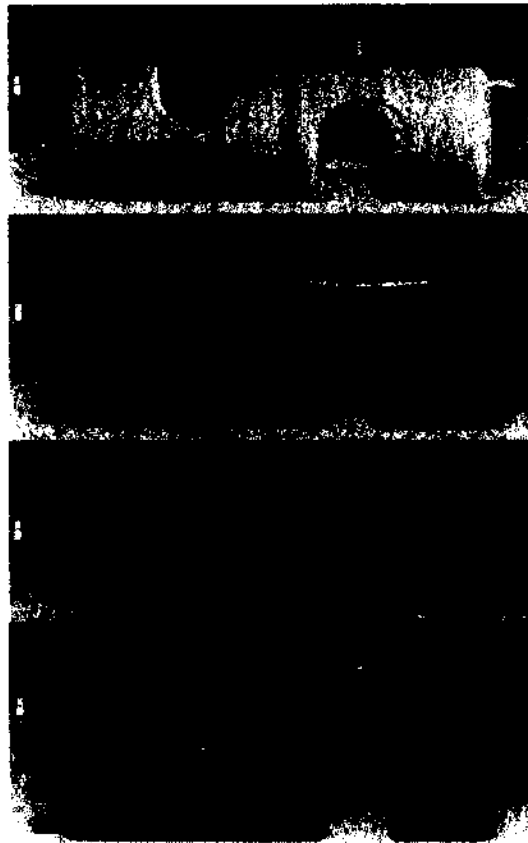


FIG. 87: 500 MHz, $\beta_0 = 1$ cavity deformation due to the first six mechanical modes.

CHAPTER 8

MULTIPOLE ANALYSIS

The method presented in Chapter 3 has been used to calculate the multipole components of the cavities presented here. In order to practically calculate these components, we must extract the field values $E_z(z)$ at various values of r , ϕ , and z , then perform the integration in Eq. (119) in order to find the values of $B^{(n)}(z)$. These are then integrated as in Eq. (120). To get the field values, virtual cylinders are created that run the full length of the cavity. These cylinders are of varying radii, centered on the beam axis, as shown in Fig. 88.

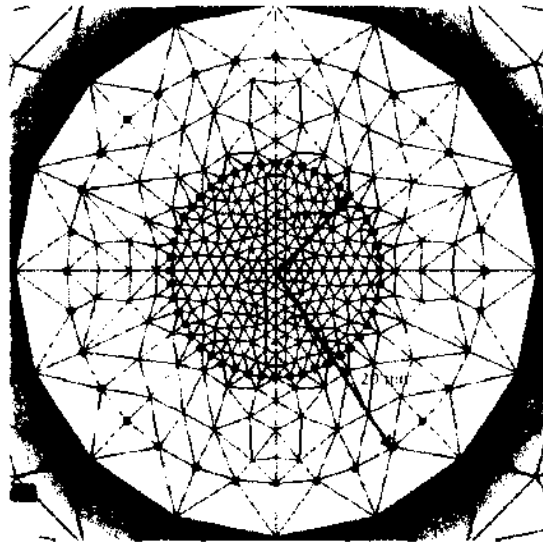


FIG. 88: Transverse cross-section of the mesh at the beam pipe showing the points to be analyzed for two different radii.

Before calculating the multipole components and associated strengths, it can be useful to explore the transverse voltage particles will encounter as their distance from the beam axis changes. This gives us an understanding of the field quality that results in non-uniformities of the transverse deflecting voltage. In a spoke cavity, whether single or multiple, the loading elements introduce these non-uniformities in

TABLE 19: Components of the Transverse Deflecting Voltage

Cavity	Direction	V_{\perp} Components
Single-Spoke	x	$E_x(z) \sin\left(\frac{\omega z}{\beta c}\right) - H_y(z) \cos\left(\frac{\omega z}{\beta c}\right)$
Single-Spoke	y	$E_y(z) \sin\left(\frac{\omega z}{\beta c}\right) + H_x(z) \cos\left(\frac{\omega z}{\beta c}\right)$
Double-Spoke	x	$E_x(z) \cos\left(\frac{\omega z}{\beta c}\right) + H_y(z) \sin\left(\frac{\omega z}{\beta c}\right)$
Double-Spoke	y	$E_y(z) \cos\left(\frac{\omega z}{\beta c}\right) - H_x(z) \sin\left(\frac{\omega z}{\beta c}\right)$

the transverse fields even within the cross section of the beam aperture. Therefore, this will be the starting point for the analysis of both cavities. Like the accelerating voltage, the transverse voltage is determined by the Lorentz force

$$V_{\perp} = \left| \int_{-\infty}^{+\infty} [\mathbf{E}_{\perp}(z, r=0) + i(\mathbf{v}_z \times \mathbf{B}_{\perp})] e^{i\left(\frac{\omega n z}{\beta c}\right)} dz \right|, \quad (156)$$

where the directions are taken to be horizontal (x) or vertical (y). It should be noted that the phase φ is determined by the on-crest particles traveling on the beam axis. The on-axis electric field for a single-spoke cavity behaves as $E_x(z) \sin\left(\frac{\omega n z}{\beta c}\right)$, while that of the double-spoke cavity can be described by $E_x(z) \cos\left(\frac{\omega n z}{\beta c}\right)$. The deflecting voltages are then calculated using the components given in Table 19.

For the purposes of these calculations, it is assumed that the phase of the offset particles is the same as those on the beam axis, whether the transverse fields can be described in the same way as the accelerating field or not.

After identifying what we will call the field non-uniformity, the specific multipole components will be characterized. We will then explore how the geometry of the spoke, specifically at or near the beam path, can be used to affect these components. Finally, a comparison of the performance, from a beam optics point of view, will be presented for one of the specific applications we are considering.

8.1 500 MHZ DOUBLE-SPOKE CAVITY

The accelerating field of the double-spoke cavity is an even function in z , however the transverse electric fields (x and y) are odd, as Fig. 89 shows. This means that the particles receiving the largest transverse kick would be those which are 90° out of phase with those getting the maximum accelerating voltage.

Figure 90 shows the transverse voltage (in the x and y directions) as a function of transverse offset from the beam line. It is clear that there is a linear increase in the voltage imparted on a particle as it moves away from the beam axis. Additionally, a negatively charged electron, for example, moving away from the design path in the positive y -direction will experience a positive voltage (force in the negative y direction) and a negative voltage (positively directed force) when moving in the negative y -direction. On the other hand, the opposite would be true when the electron moves in the x -direction. In other words, there is a vertical focusing and a horizontal defocusing. This behavior is characteristic of a quadrupole magnet.

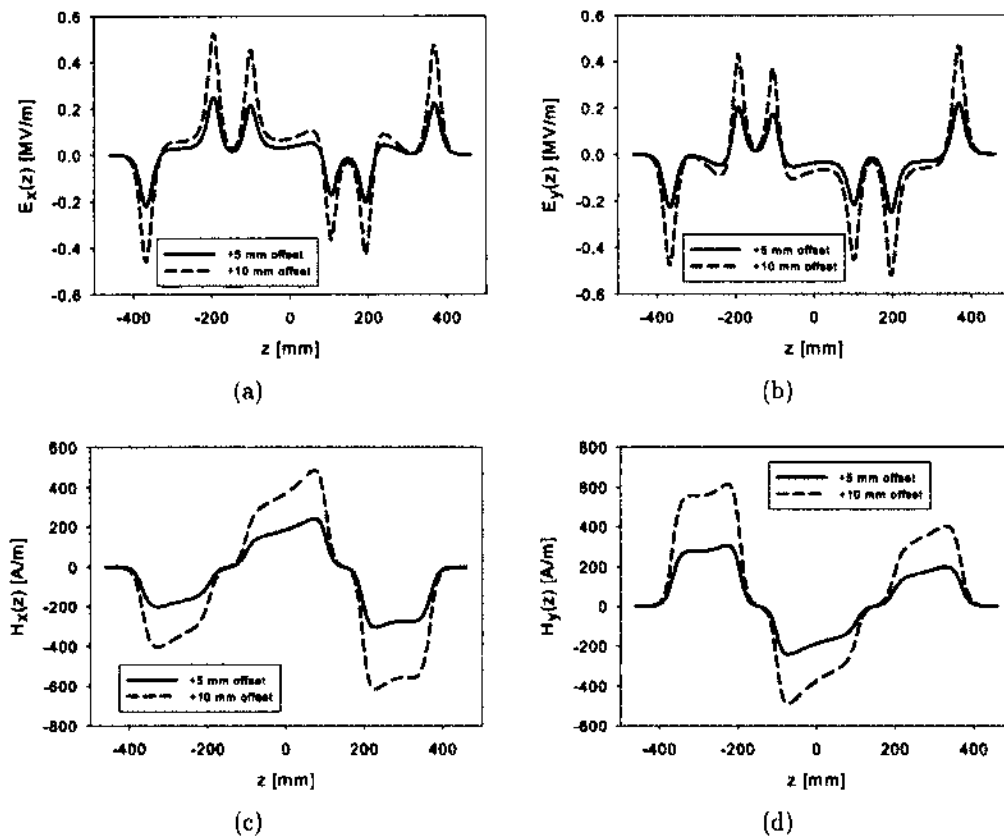


FIG. 89: Components of the transverse fields as a function of z at +5 mm and +10 mm from the beam axis.

So just by looking at the field non-uniformity, we can determine that the fundamental accelerating mode contains a quadrupole ($n = 2$) component. We can now determine the relative strength of this component, given by Eq. (120), by first finding

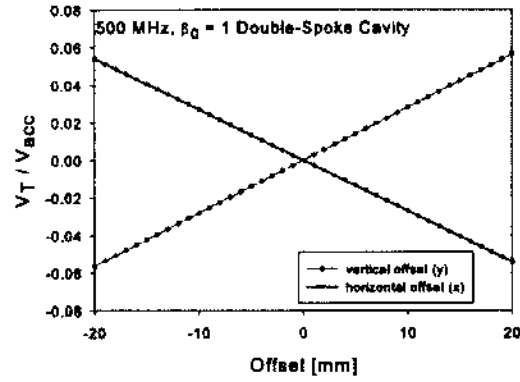


FIG. 90: Dependence of normalized transverse voltage on offset position from the beam symmetry axis.

$E_z^{(n)}$, in Eq. (119). Figure 91 shows $E_z^{(2)}$, which is the quadrupole component.

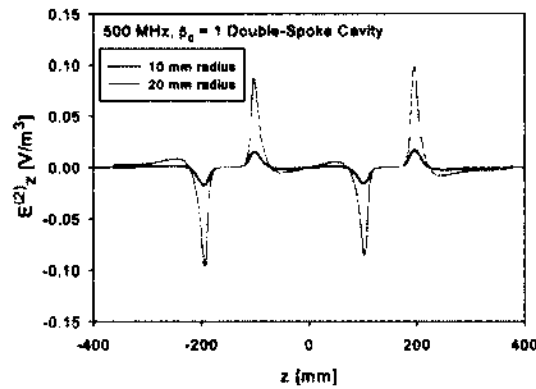


FIG. 91: Quadrupole ($E_z^{(2)}$) component of the 500 MHz double-spoke cavity.

It is clear that there is a well-defined quadrupole component, which confirms the obvious conclusion drawn from a simple non-uniformity analysis. This process can be continued to identify the other higher order multipole components. Figure 92 shows $E_z^{(n)}$ for $n = 4$ and 6 for a cavity with a racetrack aperture.

In Fig. 92, the $n = 4$ and $n = 6$ components are shown. The odd-numbered poles ($n = 1, 3,$ and 5) are left out because they are negligible. This provides a good illustration of the limits of this method. We can see that the octupole field is clear, with a maximum of 0.02 V/m^3 , and the dodecapole ($n = 6$) component is almost

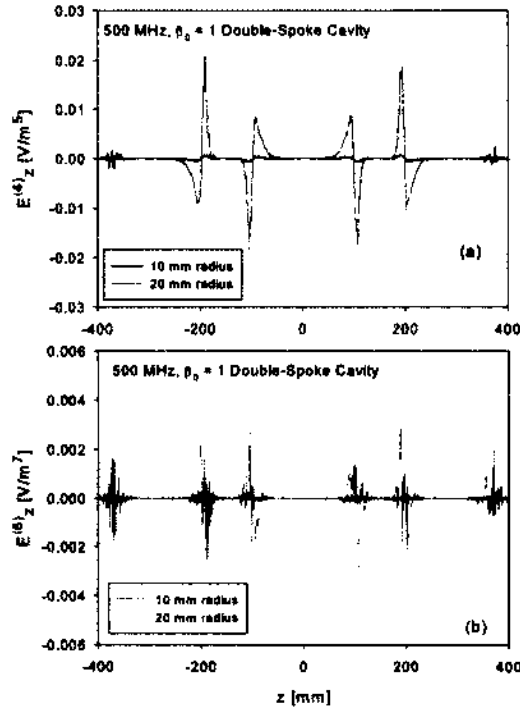


FIG. 92: (a) $E_z^{(4)}$ and (b) $E_z^{(6)}$ components of the 500 MHz double-spoke cavity fundamental accelerating mode.

completely obscured by noise. However, when we integrate $E_z^{(n)}$, as in Eq. (120), it would appear that there is a dodecapole component, but this is unreliable.

From Table 20 and Fig. 92 it is obvious that the values of b_n are only reliable up to b_4 .

Various cavities were considered for fabrication, and the field non-uniformity for each of these cavities is shown in Fig. 94. The difference in the models essentially comes down to the shape of the spoke aperture region. A standard racetrack is preferred because of the rf properties, but a rounded square, ring [141], and elliptical aperture have also been studied, and are shown in Fig. 93.

These geometries have varying degrees of symmetry. The ring and racetrack apertures, for similar cavities, have been studied and presented elsewhere [142]. Additional optimization of apertures (c) and (d) is necessary. However, it is likely that some compromise would have to be made, in terms of increased peak surface fields, in order to decrease the multipole components. Figure 98 shows the $E_z^{(2)}$ and $E_z^{(4)}$

TABLE 20: Normal Multipole Coefficients of the 500 MHz Double-Spoke Cavity with a Racetrack Aperture

b_2	b_4	b_6
$0.37 + 0.0006i \text{ V/m}^3$	$-3.8 + 730i \text{ V/m}^5$	$-1 \times 10^6 + 6 \times 10^5 i \text{ V/m}^7$

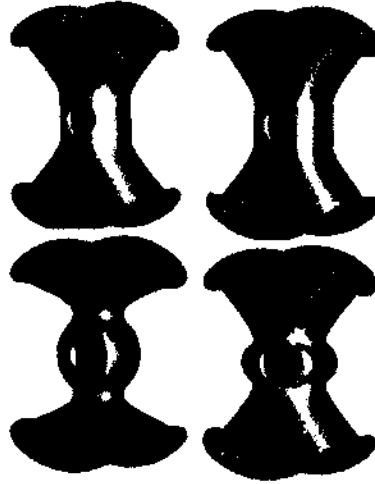


FIG. 93: Various spoke aperture geometries studied. (a) racetrack, (b) rounded square, (c) ring, and (d) elliptical.

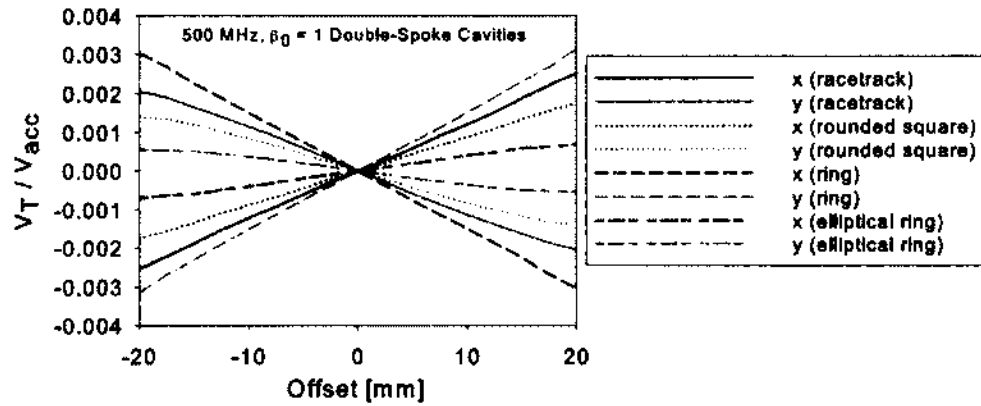


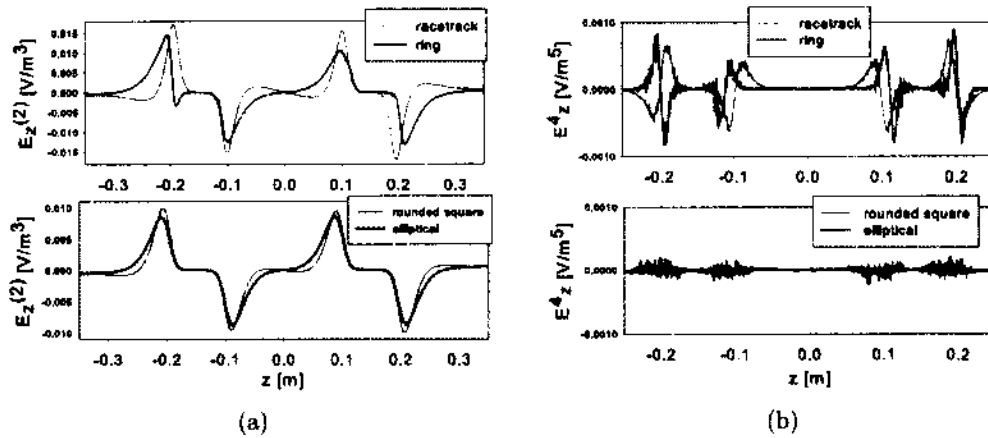
FIG. 94: Dependence of transverse voltage (normalized to V_{acc}) on transverse offset for the aperture geometries presented in Fig. 93.

TABLE 21: Multipole Components, 500 MHz, $\beta_0 = 1$

Aperture Geometry	b_2 [mT]	b_4 [mT/m ²]
Racetrack	$0.37 + 0.006z$	$-3.9 + 720z$
Rounded Square	$0.25 - 0.001z$	N/A
Ring	$-0.45 - 0.07z$	$141 - 264z$
Elliptical	$-0.1 - 0.001z$	N/A

components as a function of position. All the cavities have the same mesh, and similar $E_z^{(2)}$ components, however there is a clear difference in the $E_z^{(4)}$ components. With the square and elliptical aperture, the octupole component is small enough to be obscured by noise.

While there are some similarities with the studies done by [141] and [143] on HWRs and single-spoke cavities, the geometry of the spokes presented here (other than the actual aperture region) is vastly different, which makes a direct comparison difficult.

FIG. 95: (a) $E_z^{(2)}$ and (b) $E_z^{(4)}$ for various aperture geometries.

8.2 325 MHz SINGLE-SPOKE CAVITY

The on-axis accelerating field of a single-spoke cavity is an odd function of z while the transverse electric fields (x and y) are even as Fig. 96 shows. So to preserve the phase of the on-axis particles, this implies that the functions used to calculate the

transverse voltage, given in Table 19, will actually give the smallest value.

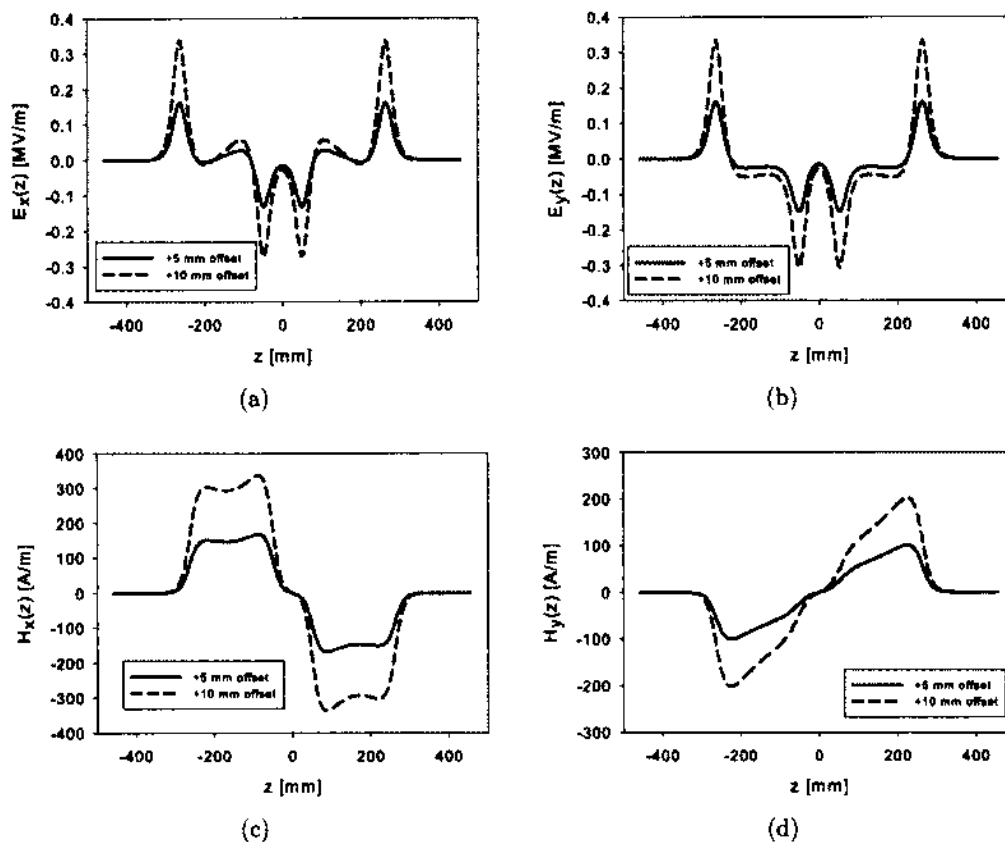


FIG. 96: Components of the transverse fields as a function of z at +5 mm and +10 mm from the beam axis.

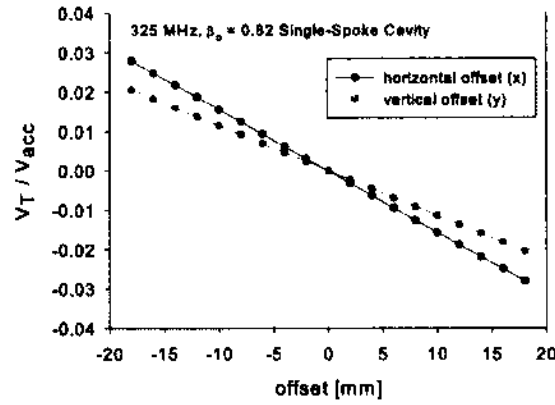


FIG. 97: Dependence of normalized transverse voltage on offset position from the beam symmetry axis.

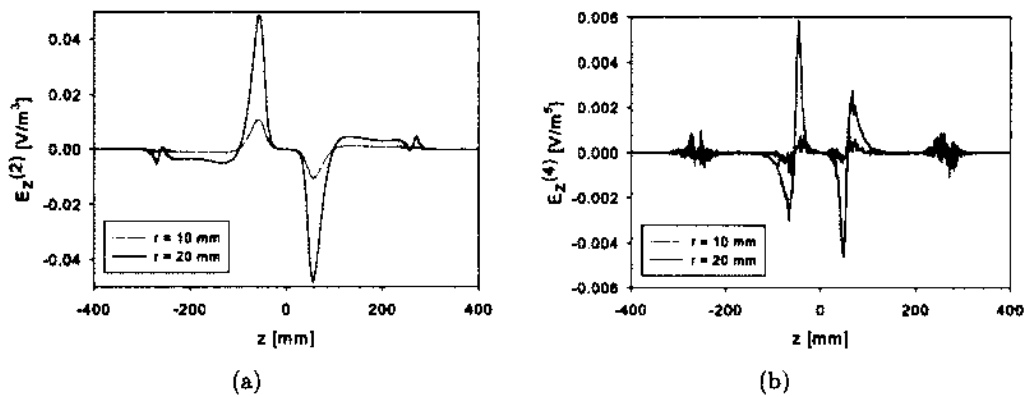


FIG. 98: Time independent multipole field components of (a) $E_z^{(2)}(z)$ and (b) $E_z^{(4)}(z)$ for the 325 MHz single-spoke cavity at radii of 10 and 20 mm.

CHAPTER 9

FABRICATION

Rotationally symmetric cavities, such as the TM-class discussed previously, are typically fabricated with die formed niobium sheets by either deep-drawing or hydroforming. The niobium is of high purity, meaning that the residual resistivity ratio ($RRR = R_{res}(293K)/R_{res}(4.2K)$) greater than 250 [144]. A large RRR means that the material has a high electrical and thermal conductivity at low temperature. These formed parts are then welded together in an electron beam (EB) welder under vacuum [145]. The spoke cavity is clearly far more complex, however, with a judicious fabrication plan, these same techniques can be used to form several individual parts which can then be EB welded together.

The 325 MHz, $\beta_0 = 0.82$ single-spoke cavity was fabricated and chemically etched at Niowave, Inc. in Lansing, MI [146], while the 500 MHz, $\beta_0 = 1$ double-spoke cavity was fabricated, processed, and tested at Jefferson Lab [147]. Many of the fabrication techniques are the same, but there are some differences, as will be shown in the following section.

Throughout the process of fabrication, processing, and ultimately cryogenic testing, a superconducting cavity will experience several changes to the geometry which will affect the frequency. All of these changes must be taken into account when considering the so-called room temperature design. Therefore, after the cavity has been completely fabricated, i.e. the final welds are complete, there should be a frequency achieved that accounts for further changes in the geometry which will occur during chemical etching, evacuation, and cooling.

9.1 SPOKE FORMING

The spoke of the 325 MHz single-spoke cavity was fabricated in the following way: dies were created for the base, two identical halves were deep-drawn in these dies which were then EB welded together. This so-called “clam shell” was then EB welded to the spoke aperture region, which was machined from a solid Nb block. Figure 99 shows the conceptual design, individual parts, and completed spoke.

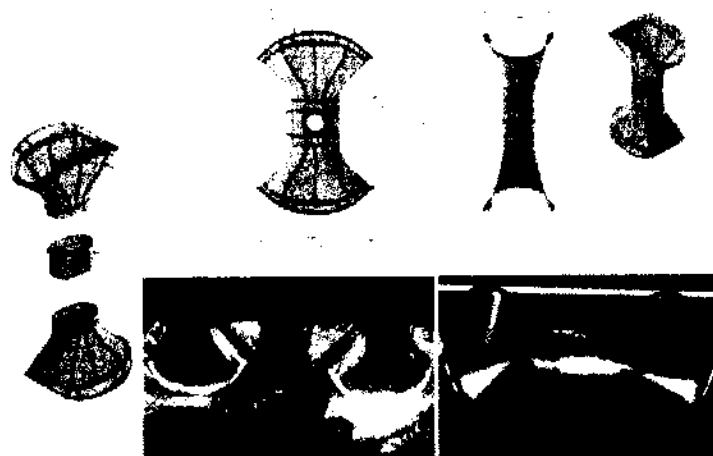


FIG. 99: Engineering drawing, welded parts, and assembled spoke for the 325 MHz single-spoke cavity.

In the case of the 500 MHz double-spoke cavity, we had a different approach to forming the spokes. A die was made to form two identical halves of the entire spoke, those halves would be trimmed and EB welded down the center. At the time of welding, the drift tube section would also be put in place.

Jefferson Lab had no prior experience forming this type of complicated structure, so a half-scale model was made to perfect the process on aluminum blanks (AL1100) before trying to form the full-scale niobium spokes.

Once the half-scale spokes could be formed consistently, a full-scale die was machined and the spoke halves were fabricated, trimmed, prepared and welded. Figure 100 shows the die in the press and the final welded spoke.

After the full-sized niobium spoke halves were trimmed and welded along with a beam pipe to form a spoke subassembly, they were measured using the Coordinate Measuring Machine (CMM) at Jefferson Lab. A maximum of 152 points were measured and a best fit model was constructed which could then be compared to the simulation.

Figure 101 shows a welded and trimmed spoke on the CMM machine next to a rendering produced by the machine. To compare with simulation, a coordinate system is set up around the fabricated spoke such that the deviation of the points can be measured. As seen in Table 22, the more points used in the alignment, the

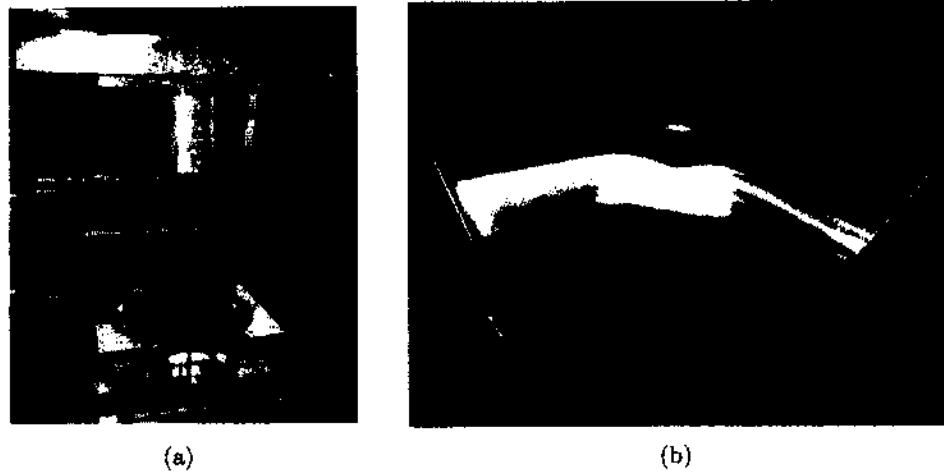


FIG. 100: (a) Full spoke die in the press and (b) fully formed and welded spoke.

TABLE 22: CMM measurements of the deviation in the fabricated spoke subassembly.

Deviation Threshold (mm)	Surface Profile (mm)	Number of Points
0.635	3.07	102
1.27	2.90	144
1.91	2.82	152

less total deviation is found.

9.2 OUTER CONDUCTOR

For both cavities, but especially for the 325 MHz cavity, the outer conductor is large enough that it presents some challenges to standard rolling techniques. The 325 MHz single-spoke cavity outer conductor is so large that Niowave opted to fabricate it out of four quarter-cylinders and EB weld them together to make the completed outer cylinder. Figure 102 (a) - (c) shows the evolution of the 325 MHz single-spoke cavity outer conductor.

The 500 MHz double-spoke cavity is a bit longer than the single-spoke, but the diameter is roughly 30% smaller, so the outer shell could be formed from two halves

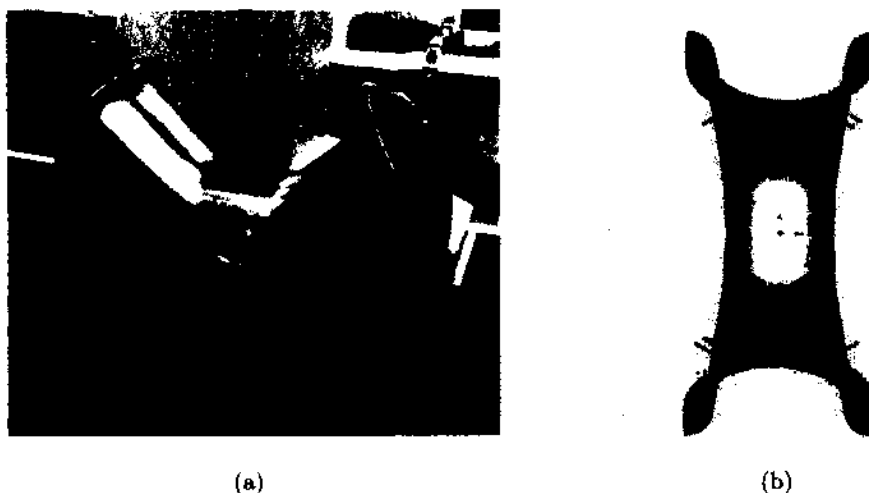


FIG. 101: (a) Welded spoke and (b) CMM results showing deviations from the cavity model.

that would enclose each spoke (shown in Fig. 102 (d)). Each half can then be welded together along the transverse mid-plane.

9.3 TRIM-TUNING AND THE BEAD-PULL

Before the spoke cavity receives the final electron beam weld, which completes the fabrication, the end of either the outer conductor or the end caps can be trimmed to compensate for any machining inaccuracies which have resulted in an offset in the fundamental mode frequency. This process is known as trim-tuning. Just measuring the frequency can be done using a network analyzer alone. However, for multi-cell cavities this provides an opportunity to adjust the relative strength of the electric field in each cell, i.e. the field flatness. In this case, it is necessary to know the field profile along the beam axis in addition to the mode frequency. This is where bead-pulling, as described in Chapter 3, is used.

In the case of the single-spoke cavity, this process was done at Niowave, Inc. Whether the cavity outer conductor is trimmed from one side only (which is done to achieve field flatness) or equally from both sides, simulations predict that the frequency should decrease by ~ 68 kHz/mm. Figure 103 shows the data collected at Niowave. We can see that there is a discrepancy between simulation and experiment. The data reveals a frequency shift of ~ 50 kHz/mm, which is 18 kHz/mm less than

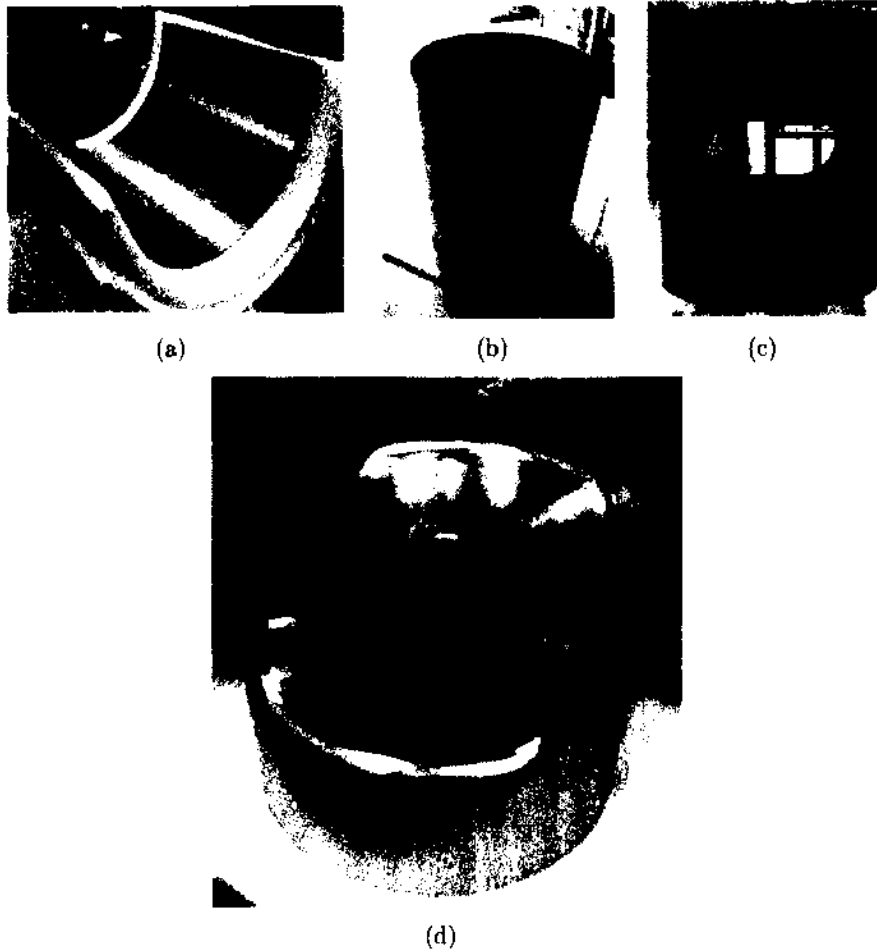


FIG. 102: 325 MHz outer conductor: (a) Two quarters together, (b) all 4 quarters together, and (c) outer conductor with holes for spoke.

expected, or roughly 25%. The origin of the discrepancy is unclear.

From Eq. 53, we can solve for the shift in frequency from the unperturbed value as

$$\Delta f = -\frac{\pi r^3}{U} \left[\epsilon_0 \frac{\epsilon_r - 1}{\epsilon_r + 2} E_0^2 \right] f, \quad (157)$$

where the teflon bead used had a 12.62 mm diameter and $\epsilon_r = 2.05$ while the room temperature unperturbed frequency was 321.9985 MHz. In a bead-pull, what is actually measured is Δf , while the simulation solves for E_0^2 as a function of position for a given value of U (1 J). This allows us to calculate the expected frequency shift

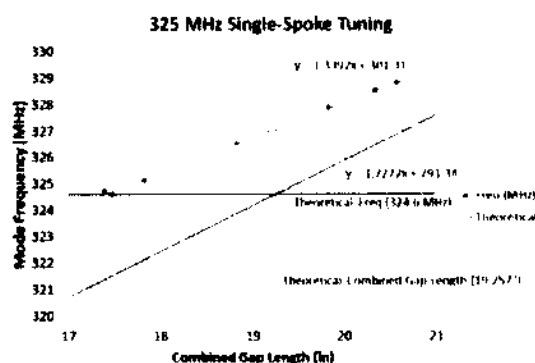


FIG. 103: Frequency changes due to trimming the outer conductor of the 325 MHz single-spoke cavity.

and compare it to the actual shift, as is done in Fig. 103.

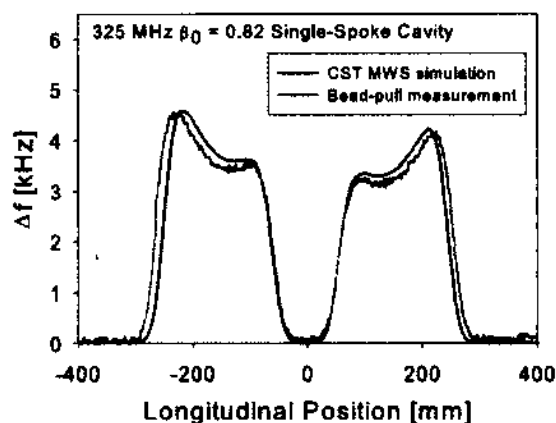


FIG. 104: Simulated (a) and measured (b) field profile of the 325 MHz single-spoke cavity.

The bead-pull data presented in Fig. 104 is after an initial leak check was performed on the bare cavity. This resulted in a permanent deformation to the end caps, which is shown in Fig. 105. The deformation was not uniform; one end cap sunk in more than the other resulting in different length accelerating gaps. Note that the cleaning ports are now angled toward each other. The effect of a vacuum load on the unsupported cavity was discussed in Chapter 7. In addition to the experimental bead-pull data, a simulation is also shown which attempts to duplicate the

TABLE 23: 325 MHz Single-Spoke Cavity Field Flatness.

Step	Frequency (MHz)	Field Flatness (%)
After Welding	324.740	0.1
After Leak Check	321.880	12
After Straightening	322.685	3

field profile based on the gap length measured by Niowave. There is a fairly good agreement, where the small discrepancy may be due to inaccuracies in the gap length measurement.

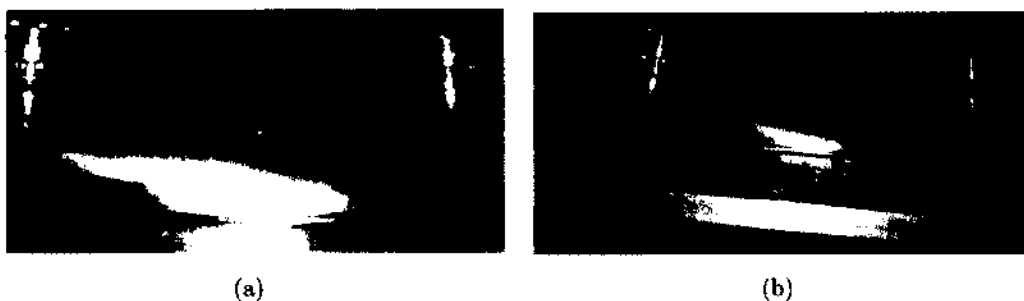


FIG. 105: End caps of the 325 MHz single-spoke cavity after plastic deformation occurred during a leak check.

In an attempt to correct this problem, the cavity was mechanically straightened. This involved pulling on one of the beam pipes so as to increase the accelerating gap that was reduced the most. The frequency and field flatness for each of these steps is shown in Table 23. After the mechanical straightening of the cavity, the field flatness was improved from 12% to just 3%.

The trim-tuning of the 500 MHz double-spoke cavity was performed at Jefferson Lab as the last step before the end caps were to be welded to the outer conductor, thereby sealing the cavity. The cavity frequency is decreased by trimming the outer conductor, so in order to fine tune the frequency without the risk of going too low, it was intentionally made slightly longer than was required. Figure 106 shows data taken after each of 3 successive trimmings along with the simulated frequency shift. Before trimming, the frequency was much higher than expected (503.206 MHz) so the initial amount taken off was 40 mm. The next two steps took off 7.5 mm from

one side and 5 mm from the other.

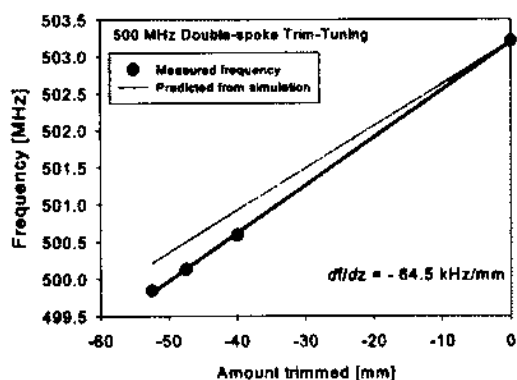


FIG. 106: Frequency changes due to trimming the outer conductor of the 500 MHz double-spoke cavity.

From the measurements, we find that the frequency change is -63.4 kHz/mm. Simulations were used to estimate this amount and predicted -57 kHz/mm, a difference of 11%. It is interesting to note, however, that the value of -63.4 kHz/mm is after all the trimming was completed; if we look at each step individually, it was -64.2 kHz/mm after 40 mm, -60.7 kHz/mm after 7.5 mm, and -57.6 kHz/mm after trimming just 5 mm.

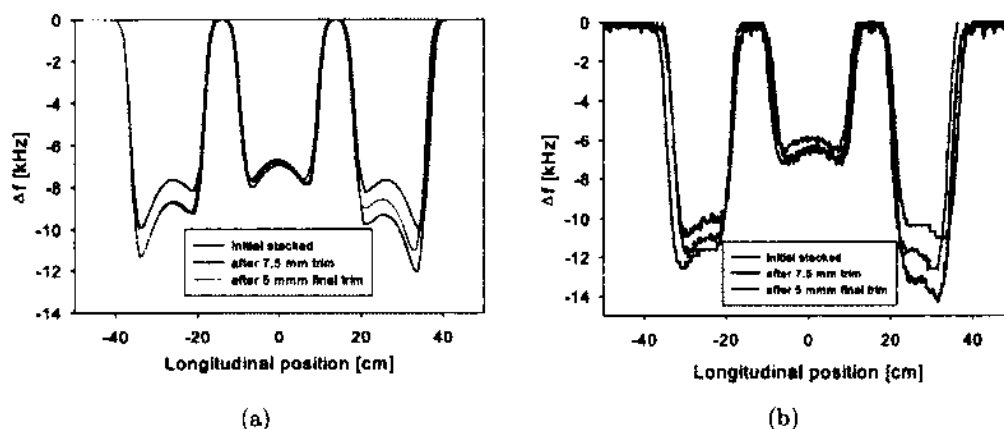


FIG. 107: Simulated (a) and measured (b) field flatness changes by trimming the outer conductor.

The amounts removed for each step in the trim-tuning were not chosen arbitrarily. In Chapter 10 we will see how each process step changes the frequency leading us

TABLE 24: Simulated and Measured Geometric Shunt Impedance.

Cavity	Simulated	Measured	Difference (%)
325 MHz single-spoke	449	531	18
500 MHz double-spoke	675	613	9

to a room temperature, after final weld goal. This gives us a limit for the maximum amount we could take off during the trimming while the field flatness dictates which end cell to cut. The desired frequency at room temperature after the final weld was 499.7 MHz, while the pre-trimmed cavity frequency was 503.206 MHz. At a simulated df/dz of -57 kHz/mm, we decided to trim 20 mm from each end cell expecting to arrive at a new frequency of 500.926 MHz. After the 40 mm total trimming, the field profile is shown in Fig. 107 as the purple line in both simulated (a) and measured (b).

The next trim of 7.5 mm from one side was done in order to correct the difference in field values between the two end cells. This can be seen in Fig. 107 (b). The initial bead-pull showed that the frequency shift in one end cell was -12 kHz while the other was -11 kHz. 7.5 mm was then cut from the -11 kHz side. The result is shown in blue. We can see that this was too much as the field imbalance was actually overcompensated. 5 mm was then cut from the other side which balanced the fields in the end cells to within a 2.5 percent.

Finally, the information obtained during bead-pull measurements can also be used to calculate the cavity's geometric shunt impedance, (R/Q) given in Eq. (68). We are measuring $\Delta f/f$, which is proportional to E_0^2/U , as shown in Eq. (157), and with the relationship

$$\frac{R}{Q} = \frac{|V|^2}{\omega U}, \quad (158)$$

we can integrate the measured E_0^2/U and multiply by the constants to find (R/Q) . Since the geometric shunt impedance is strictly dependent on the geometry of the cavity, we can expect this value to be sensitive to fabrication defects which cause the cavity to be significantly different from the ideal simulation.

Table 24 shows the simulated and measured values of (R/Q) along with the difference. For the 500 MHz double-spoke cavity, the values differ by less than

10%. This is reasonable considering the challenges in fabrication and the significant deviations from the simulated model. Also, the bead-pull was done before the cavity was ever under vacuum, which also caused some deformations in the end cells, as we will see in the upcoming chapters. On the other hand, the 325 MHz single-spoke cavity bead-pull was performed after the cavity had suffered deformations due to the vacuum load, and this may explain why the difference is more significant.

9.4 FINAL ROOM TEMPERATURE CAVITY

After the trim tuning has been completed, the end caps are welded, sealing the cavity. Figure 108 shows both cavities after the fabrication process is complete.



FIG. 108: Fabricated (a) 325 MHz single-spoke (b) 500 MHz double-spoke cavities. Note that the 325 MHz cavity is equipped with the stiffening structure.

Chapter 10 will discuss the processing steps in detail, but for these purposes we are interested in how each step will affect the cavity frequency so that we can compare the final welded cavity frequency goal with the actual frequency.

The first processing step which will impact the frequency is the bulk chemical etching. This will remove material from the inner surface resulting in an increase in the volume and decrease in frequency. After the etching, the cavity will be cleaned, assembled, and placed under vacuum. The frequency shift associated with the vacuum load is not straightforward to predict because the pressure applied to different areas of the cavity can result in either positive or negative shifts in the frequency. This is actually not that important for these purposes because when the cavity is operating at 2 K, the external pressure is not significant. Finally, when the cavity is cooled, the niobium will shrink according to the linear thermal expansion coefficient

$$\alpha_L = \frac{1}{L} \frac{dL}{dT}, \quad (159)$$

TABLE 25: Frequency Changes by Process.

Process	Shift (kHz)
500 MHz Double-Spoke	
BCP	-326
Cooling	+663
Net Change	+337
325 MHz Single-Spoke	
BCP	-207
Cooling	+151
Net Change	-56

where L is the initial length and T is the temperature. At 300 K, $\alpha_L = 0.7 \times 10^{-5} \text{ K}^{-1}$. The shrinkage is approximately linear down to ~ 10 K, and zero below this [148]. We can then relate the length of the material at room temperature with that at cryogenic temperatures as

$$\frac{L_{300K} - L_{2K}}{L_{300K}} = 143 \times 10^{-5}. \quad (160)$$

If we scale the model by this amount, we can get an estimate for the frequency shift due to the cavity being cooled and adjust the room temperature target frequency accordingly. Table 25 shows the simulated results for each major process to be performed after the final welding.

Based on the results presented in Table 25, the room temperature, welded cavity frequency targets should be 499.67 MHz for the double-spoke and 324.95 MHz for the single-spoke.

CHAPTER 10

CAVITY PROCESSING

In order to get the optimal performance from a superconducting niobium cavity, a number of steps are taken after fabrication is complete but before cryogenic testing commences. In this chapter we will introduce some of the processing steps that the cavities went through and discuss how they were done.

10.1 BULK CHEMICAL ETCHING

Most of the cavity parts were formed by stamping, as was outlined in Chapter 9. This process damages a surface layer approximately 100-200 μm thick [149]. This layer is most commonly removed with a bulk chemistry process known as buffered chemical polishing (BCP).

The BCP mixture is the traditional 1:1:2 ratio of Hydrofluoric acid (49%), Nitric acid (69.5%), and Phosphoric acid (85%), which effectively etches away the surface layer mentioned above. The chemical process responsible for this etching involves the reaction of the nitric acid with the niobium to form a niobium pent-oxide (Nb_2O_5) which, in turn, reacts with the Hydrofluoric acid to form a hydro-soluble Niobium-Fluoride (NbF_5), which is then swept out of the cavity as the acid is circulated from bottom-to-top [150]. Serving as a buffer, the Phosphoric acid stabilizes the reaction rate as does the temperature of the acid and quantity of dissolved Nb present in the solution [151].

10.1.1 325 MHZ SINGLE-SPOKE CAVITY

When the 325 MHz cavity was in its individual components/assemblies prior to electron beam welding, each part/assembly was cleaned with acetone and methanol, then run through 2 cycles in an ultrasonic cleaner (first with a Micro-90 degreaser/ultra-pure water (UPW) solution, then with just UPW). This cleaning was done prior to etching the components.

The ultrasonic cleaners at Niowave, are not large enough to fit the entire 325 MHz cavity inside, so prior to the full cavity etch. it was "hand-cleaned" with Micro-90, acetone, and methanol.

One of the stipulations we put on the fabrication of this cavity is that the spoke was to be formed from 4 mm thick niobium while the outer conductor and ports could be made from 3.175 mm (1/8") niobium. The actual initial thickness was not measured by Niowave, Inc. so we cannot determine the exact amount of etching the cavity received.

The BCP (both bulk and light) was intended to remove 120 μm from the entire inner surface. The thickness was measured at Jefferson Lab, after all processing was performed. It was found that the maximum thickness was 3.958 mm (at one of the spokes) while the minimum thickness was 3.06 mm (at one of the end caps). Even if it is assumed that the material could be thicker than required, at certain points, this implies that the maximum etch was most likely $\sim 100 \mu\text{m}$ but that the average could be less than that.

10.1.2 500 MHZ DOUBLE-SPOKE CAVITY

The bulk chemical etching is intended to remove 150 μm in two stages, with 75 μm being removed followed by a 180° rotation and another 75 μm removal. The reason for this rotation is to minimize the differences in removal rates caused by different acid flow patterns at the top and bottom of the cavity.

TABLE 26: 500 MHz Chemical Etching

Before Etching		
Parameter	Value [mm]	Position
maximum thickness	3.2	Bottom end cap
minimum thickness	2.63	Reentrant top end cap
Average	3.06	N/A
Std Dev	0.14	N/A
After Bulk BCP		
maximum thickness	3.17	Bottom end cap
minimum thickness	2.34	Reentrant top end cap
Average	2.87	N/A
Std Dev	0.16	N/A
Maximum Etch	0.30	End Cells
Minimum Etch	0.03	End cap port
Average Etch	0.20	N/A

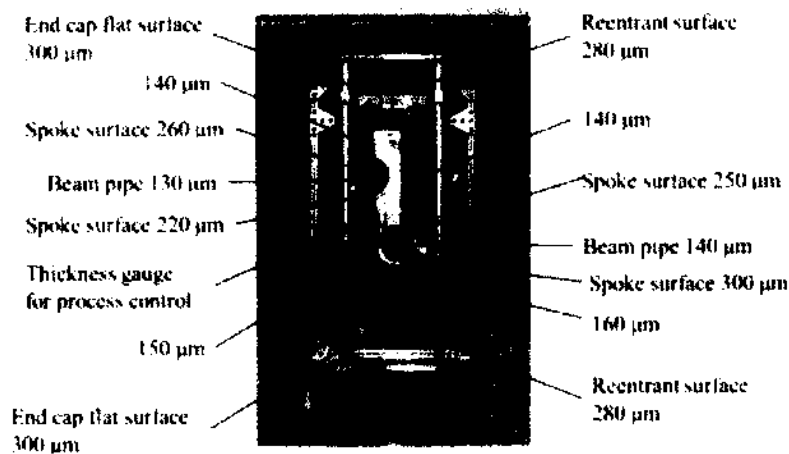


FIG. 109: Bulk BCP removal amounts at the measured locations on the 500 MHz double-spoke cavity [147].

In Table 26 and Fig. 109 [147], we can see that the average niobium thickness, before processing, was ~ 3 mm. The minimum thickness of 2.63 mm is located where the beam pipe meets the end cap. In addition to having a weld joint, the end cap is formed from a circular blank. During pressing, a radius of curvature is formed where the beam pipe will be welded into place. This results in the stretching of the formed part.

Generally speaking, surfaces which were perpendicular to the vertical acid flow had much more material removed than those parallel to it. For a more uniform removal, future treatments could possibly be done with the cavity placed horizontally and being rotated.

10.2 HEAT TREATMENT

When fabricating superconducting rf cavities from bulk niobium, one of the fabrication steps is often a high temperature heat treatment in an ultra-high vacuum (UHV) furnace. This has the positive effect of removal of hydrogen from the bulk through outgassing. During cool-down for cryogenic testing, precipitation of this hydrogen in the niobium can lead to a reduction of the quality factor, known as *Q*-disease. Removal of hydrogen reduces the chances that a cavity will suffer from *Q*-disease.

Another benefit is grain growth. Although at the temperatures we are using,

the grain growth is very small [133]. Larger grains help to reduce the number of grain boundaries which are potential field emitters and sources of additional surface resistance.

10.2.1 325 MHZ SINGLE-SPOKE CAVITY

The dimensions of this cavity prevented Jefferson Lab from performing the heat treatment in their furnace. Fermi National Accelerator Laboratory (Fermilab), however, does have a furnace and the technical expertise to perform the heat treatment. After the 150 μm chemical etching was performed at Niowave, Inc. it was shipped to Allan Rowe's group at Fermilab.

The baking recipe is as follows:

- (i) Rate of rise test
- (ii) Temperature ramp rate 3° C per minute
- (iii) Hold 100° C for 30 minutes
- (iv) Temperature ramp rate 3° per minute
- (v) Hold at 350° C for 12 hours to remove all the water in the cavity and outgassing of heavy molecules
- (vi) Temperature ramp rate 3° C per minute
- (vii) Hold at 600° C for 10 hours
- (viii) Cooldown

Figure 110 shows the temperature and pressure reading for the baking process listed above. The first pressure peak represents the leak rate test and the second peak at $\approx 2 \times 10^{-6}$ Torr corresponds to the beginning of the 350 °C soak where all the water and heavy molecules ($\text{amu} \leq 50$) are outgassing.

Figure 111 shows the total and partial pressure of some relevant molecules during the heat treatment. The gap in the RGA data corresponds to the loss in system air. The RGA starts acquiring data again when the cooldown has already started and this explains the different slope in the partial pressures in the last part of the plot.

Figure 112 shows the spectrum at the beginning and end of the two soaks. Notice the high partial pressure and wide spectrum of heavy molecules coming out at the

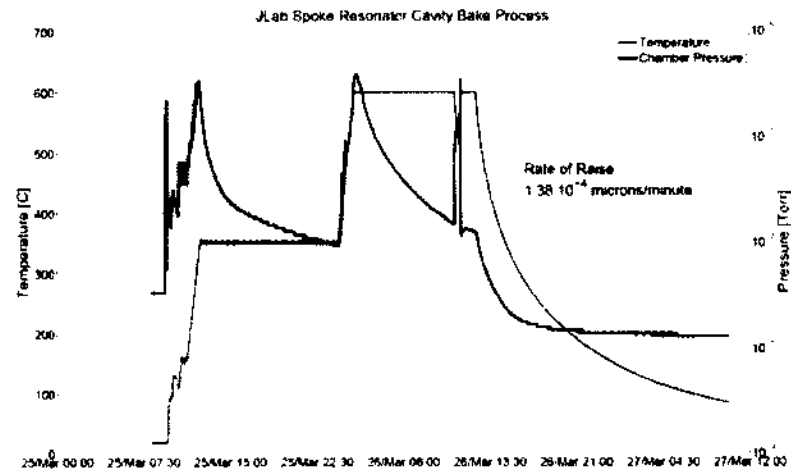


FIG. 110: Bake process for the single-spoke resonator. 12 hours at 350 °C and 10 hours at 600 °C.

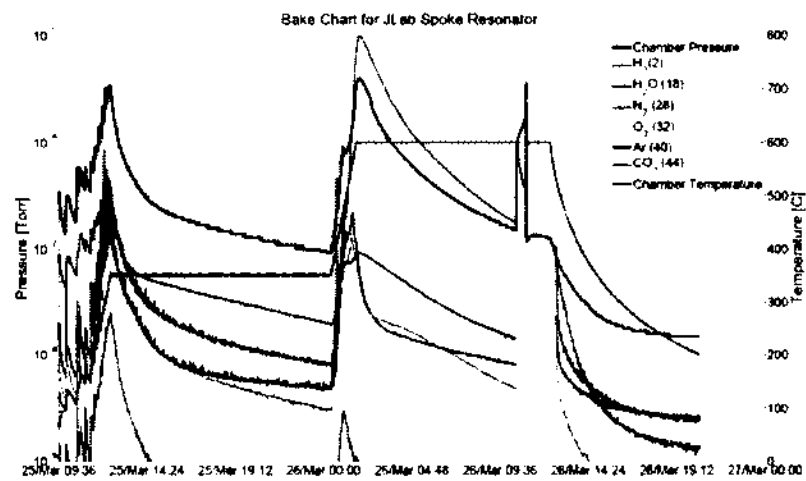


FIG. 111: RGA data collected during the baking process.

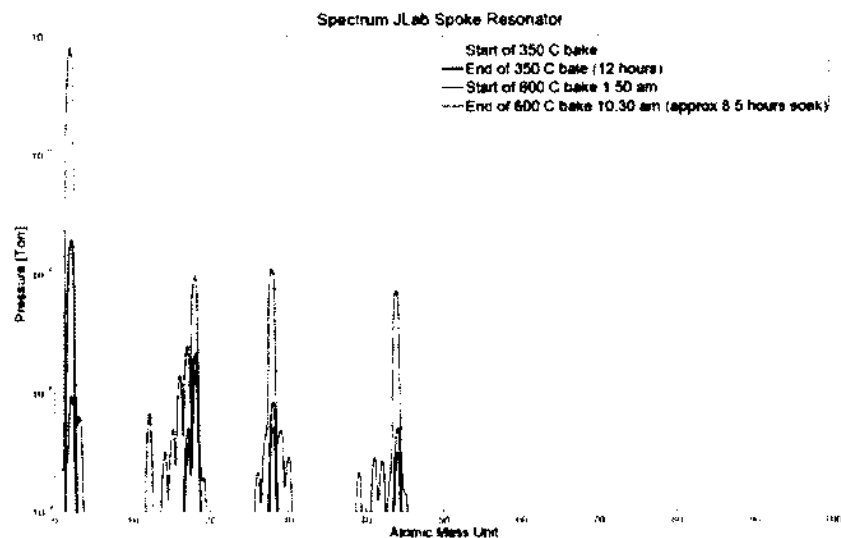


FIG. 112: Spectrum at the beginning and end of the two soaks, 350 °C and 600 °C respectively.

beginning of the 350 °C soak which are eliminated at the end of the 12 hours. This indicates that despite the ultrasonic cleaning and preparation that was performed both at Niowave, Inc. and Fermilab, the cavity was still contaminated.

10.2.2 500 MHZ DOUBLE-SPOKE CAVITY

As with the single-spoke cavity, the 500 MHz double-spoke cavity received a 600° C heat treatment for roughly 10 hours. As is expected, Fig. 113 shows a high outgassing of H₂. During the high temperature stage, the hydrogen partial pressure decreased by close to two orders of magnitude.

When the H₂ partial pressures are compared for the single- and double-spoke cavities, there are significant differences. In both cases, hydrogen has the most abundant outgassing, but there is roughly an order of magnitude difference in both the maximum and minimum (at 600° C). Now, there are multiple factors which could account for this. The most obvious is that the etching of the double-spoke cavity was much greater than that of the single-spoke, thus leading to more exposure and absorption of hydrogen.

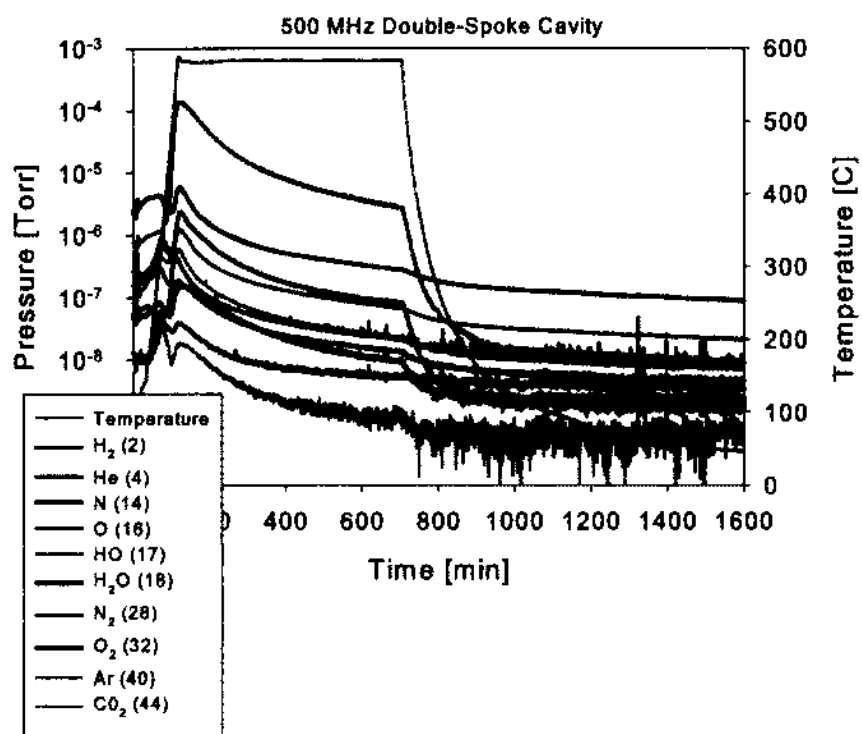


FIG. 113: RGA data collected during the 10 hour, 600 °C bake of the 500 MHz double-spoke cavity.

10.3 LIGHT CHEMICAL ETCHING

In an effort to remove any contamination of the niobium that may have been picked up after the heat treatment, a 10-30 μm removal of material was performed on both cavities. This is accomplished with buffered chemical polishing in the same volume ratio as the bulk etch (1:1:2).

After an initial round of testing, an additional light BCP was performed at Niowave. Now that the thickness had been measured, we could determine how much material was removed during this final step. Four locations were measured on each end cap and three locations were measured from each side of the spoke for a total of fourteen points. The amount of removal ranged from 11 μm near one of the end cap ports to 49 μm on one of the spokes.

In the 500 MHz cavity, the amount of removal during the bulk etching was large enough that we decided to do only a minimal amount of light etching. Removal of 10 microns as measured at the cavity center leads to a 20 micron maximum at the flat surfaces of the end caps.

10.4 HIGH PRESSURE RINSING

After the light chemical etching, there is always a possibility that microparticle contamination can occur before the cavity is assembled for cryogenic testing. This contamination has been identified to be a leading cause of field emission. High-pressure rinsing the inside surfaces of the cavity with ultrapure water has proven to be one of the most effective ways to remove these microparticles and therefore reduce field emission [152, 153]. A schematic of the HPR system at Jefferson Lab is shown in Fig. 114.

As has been stated, the chemical processing of the 325 MHz single-spoke cavity was done at Niowave, Inc. Upon arrival at Jefferson Lab, the cavity was visually inspected, which revealed a white residue on the internal surface of the cavity. Figure 115 shows 2 views of the streaks that appear to be caused from insufficient rinsing of the cavity after the light etching.

In order to rinse the 325 MHz cavity at Jefferson Lab, special accommodations had to be made. The size of the HPR cabinet is such that the rinsing nozzle, which only can move up and down, can accommodate the cavity only for rinsing through the beam pipe opening. Rinsing through the side ports, however, is the only way

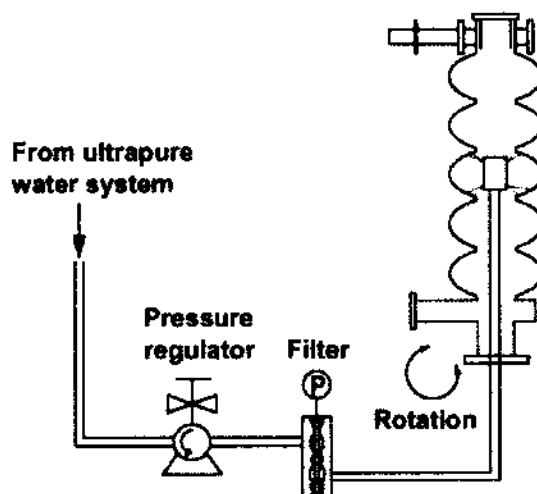


FIG. 114: Schematic view of the Jefferson Lab high pressure rinsing cabinet.

to reach certain parts of the inner surface of the spoke, as can be seen in Fig. 116. In order to reach the sides of the spoke, a manual hand wand was connected to a pressure washing system (supplied with di-water) in the wet-chemistry area.

The disadvantages of using such a system are that it is not in the clean room and the DI-water runs through the pressure washing machine which is not designed for such applications. This leads to the possibility that, while some contaminants are removed, others may be introduced.

Similar challenges were encountered with the 500 MHz double-spoke cavity. It is smaller in diameter, which made it easier to handle. However, now the 'blind spots' of the HPR nozzle are even more numerous. The same approach was taken—manually rinse the cavity through the 4 cleaning ports in the wet-chemistry area, then immediately transfer the cavity to the clean room and proceed with the production-quality high pressure rinsing.

10.5 LOW TEMPERATURE HEATING

After rinsing with ultra-pure water and drying for ~ 24 hours in the Jefferson Lab class 100 clean room, the cavity is assembled and moved to the Vertical Staging Area (VSA). In order to expel as much water from the surface as possible, a low temperature ($120\text{ }^{\circ}\text{C}$), 48 hour "in situ" baking under ultra-high vacuum was performed

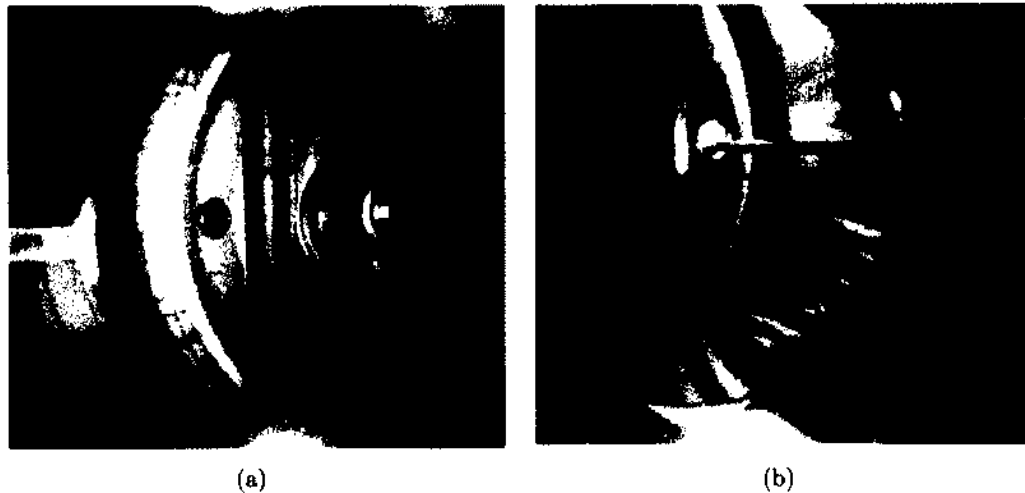


FIG. 115: Acid residue still present in the 325 MHz single-spoke cavity upon arrival at Jefferson Lab.



FIG. 116: Schematic of the HPR nozzle in the single-spoke cavity.

as a final step in the preparation. Several laboratories have reported benefits of this type of low temperature baking which include an improvement in the cavity quality factor (through a reduction in R_{BCS}) and recovery from high-field “ Q -drop.” [154]. These benefits have been related to oxygen diffusion into the niobium which causes nanometer-scale changes in the structure of the niobium/oxide interface.

The 325 MHz cavity was too large for the standard “bake boxes” at Jefferson Lab, so it had to be wrapped in layers of aluminum foil, silicone heat tape, and more aluminum. Thermocouples were inserted at 8 locations to monitor the temperature and check for uniformity. The range in measured temperatures was 90 °C to 148 °C,

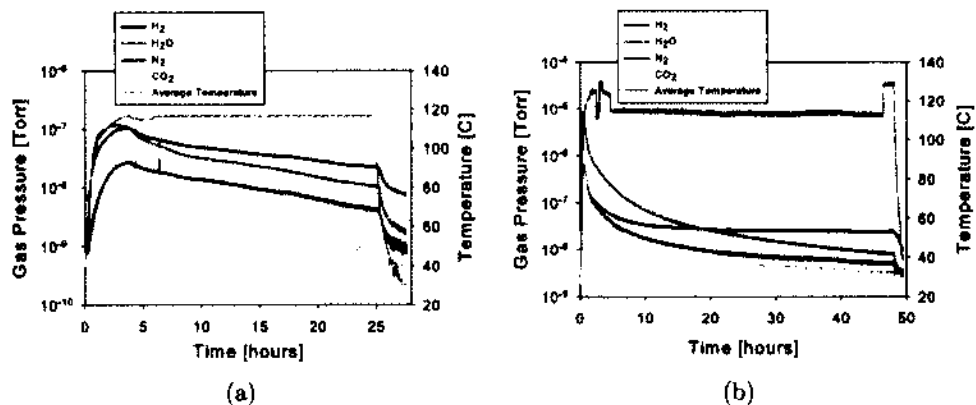


FIG. 117: Gas pressure and temperature during the first (a) and second (b) 120° C bake of the 325 MHz single-spoke cavity.

with the average being 116 °C for the first test bake (25 hours) and 113 °C for the second bake (49 hours).

One thing that is immediately clear in Fig. 117, is that the order of magnitude of the partial pressures was significantly higher for the second baking.

The 500 MHz double-spoke cavity was able to fit in the bake box at Jefferson Lab. Baking is this way allows for a much more uniform temperature distribution. This cavity was baked for 48 hours at 120 °C.

CHAPTER 11

CRYOGENIC TESTING RESULTS

This chapter reports on the results obtained through 2 cryogenic rounds of testing for the 325 MHz single-spoke and 500 MHz double-spoke cavities. The most pertinent results are those of the achievable accelerating gradient and intrinsic quality factor. The measurement of the surface resistance gives us an idea of the material quality and effectiveness of our processing techniques. While somewhat less important, the pressure sensitivity was also measured.

11.1 VERTICAL TEST AREA AT JEFFERSON LAB

The cryogenic testing of both cavities was carried out at Jefferson Lab which houses the Vertical Test Area (VTA). The cavities are installed in a custom cage assembly, this assembly is then attached to a test stand where the vacuum system is connected to a relief valve on the cavity, and the entire apparatus is finally loaded into one of the cryogenic testing dewars. A schematic is shown in Fig. 118.

Each test dewar is housed in a radiation shielded pit which is enclosed under a lead cover. The VTA dewars each have liquid Helium (LHe) supply lines and sensors, pressure sensors, and thermometers. The dewars are supplied with 4 K LHe at a rate of around 250-300 L/hr, which can then be pumped down further to reach temperatures as low as 1.9 K [155].

Once the cavity is in the dewar, under vacuum, and at temperature, the losses in the cables are determined using a 1 W amplifier. Some sections of the cables are located within the vacuum vessel, meaning they are only accessible from one end. In order to obtain the losses in these cables, a two-way loss measurement is carried out using a calibrated network analyzer as a source, a power meter, and a circulator [156].

During the high power testing, a 500 W amplifier and a 50 to 1300 MHz Self-Excited Loop (SEL) system were used. A SEL, similar to that shown in Fig. 119 but without the external phase set point, uses a cavity resonant frequency the way an oscillator uses a tank circuit [157, 158]. The cavity frequency can be tracked in this

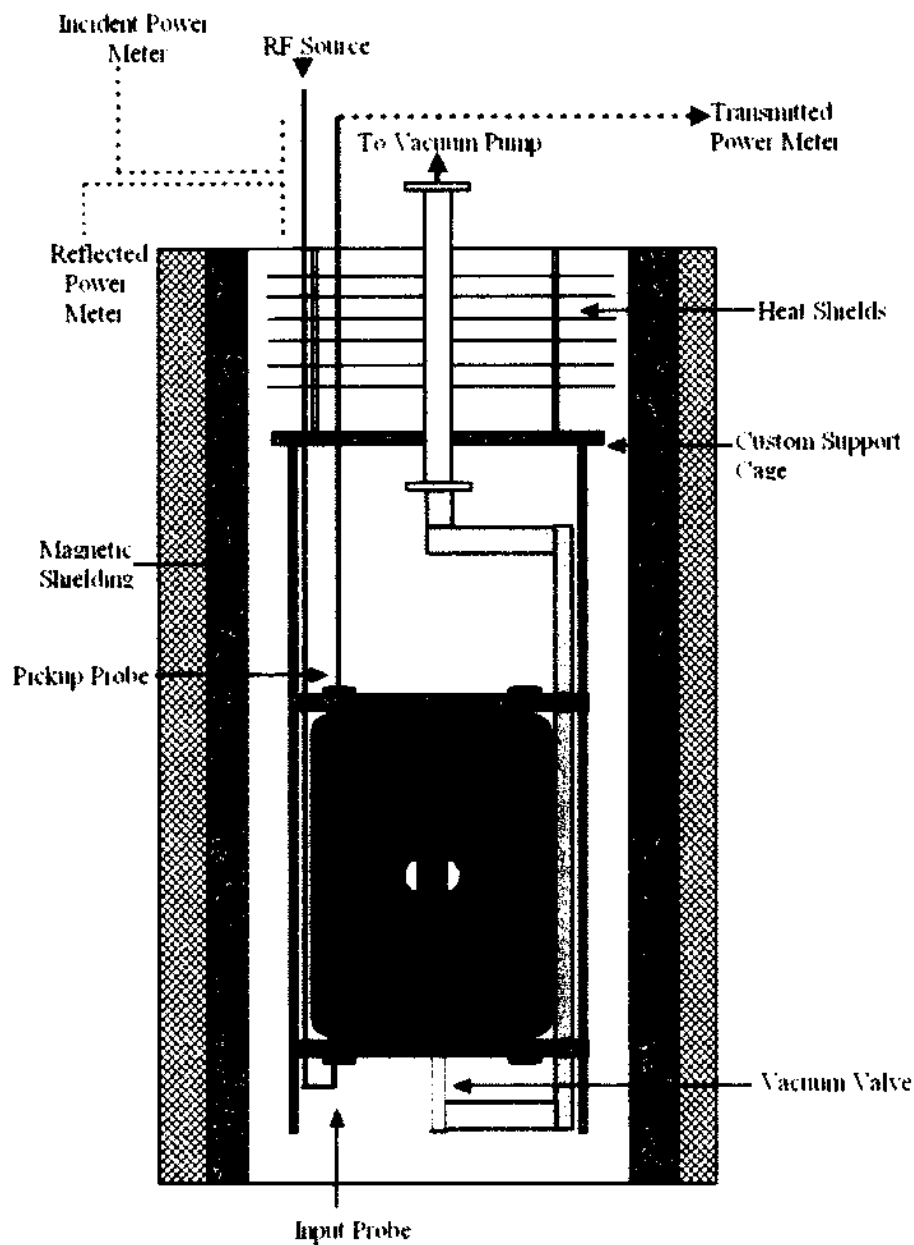


FIG. 118: Schematic view of the 325 MHz single-spoke cavity in the vertical test cryostat of the VTA.

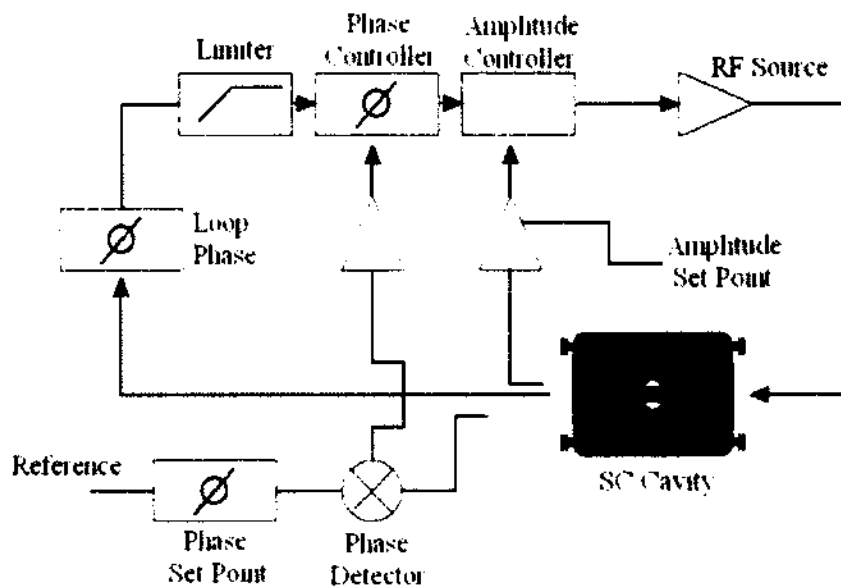


FIG. 119: SEL block diagram.

way. Limiting feedback is used to control the amplitude which can then provide an external set point which can be compared to the signal from the cavity. By comparing the cavity signal to a reference, the circuit (shown in Fig. 119) is phase-locked to a reference, which is near the cavity frequency.

11.2 CALIBRATION OF INPUT AND PICKUP PROBES

As was mentioned in Chapter 4, the effectiveness of the power coupler and pickup probes is determined, in part, by their placement on the cavity body. For these proof-of-principle cavities, there were no ports located on the outer conductor so the power coupling was done via the cleaning ports located on the end caps. For the cryogenic testing, we refer to the external quality factor of the input coupler and pickup probe as Q_{ext1} and Q_{ext2} , respectively. The testing of both cavities was done with a fixed-length input coupler.

The goal is to have as little delivered power reflected at the lowest cryogenic temperature we plan to test at which was 2 K in both cases. This requires that the length of the input probe be such that it is critically coupled at 2 K, i.e. the coupling constant $\beta = 1$, or $Q_{ext1} \sim Q_0$. For the pickup, also referred to as the “field probe,”

we want as little coupling to the fundamental mode as possible to ensure that neither heating nor an unnecessary sink of otherwise usable power occurs. Therefore, $Q_{ext2} \gg Q_0$.

The calibration of both probes is done prior to the cavity processing. To accomplish this, we place an auxiliary antenna at one of the other ports, excite the fundamental mode, and measure the signal transmitted through either probe under investigation using a network analyzer (NWA). Measuring the S-parameter S_{21} gives the loaded quality factor

$$\frac{1}{Q_L} = \frac{1}{Q_{ext1}} + \frac{1}{Q_{ext2}}. \quad (161)$$

In order to get the β , we use the resonant and detuned amplitudes of the signal probe, measured through S_{11} , to find the reflection coefficient

$$\Gamma = \frac{S_{11}(resonant)}{S_{11}(detuned)}, \quad (162)$$

which allows us to calculate β

$$\beta = \frac{1 - \Gamma}{1 + \Gamma}. \quad (163)$$

The intrinsic quality factor is then

$$Q_0 = (1 + \beta) \cdot Q_L. \quad (164)$$

Finally, the external quality factor of the probe being calibrated is

$$Q_{ext} = \frac{4\beta Q_L}{(1 + \beta)} \cdot 10^{|S_{21}[dB]|/10}. \quad (165)$$

By successively measuring and trimming the length of the copper probes, we can achieve the desired result, as shown in Table 27.

What is called the “required” result for Q_{ext1} in Tab. 27 is the Q_0 of the cavity at 2 K based on an assumed value of R_s , which is subjective. For example, the Q_{ext1} of 7.8×10^9 is based on a R_{BCS} (which can be calculated using Eq. (25)) of 1 n Ω and R_{res} of 20 n Ω . The estimate of residual resistance turned out to be quite high, as will be seen in the following sections.

We perform both 4 K and 2 K tests, so the goal is to be coupled well enough to the cavity such that the rf source requirements do not exceed more than a few hundred watts. Hence, we wish to be critically coupled at 2 K.

TABLE 27: Calibrated and measured external quality factors of the input and pickup probes compared to value required for critical coupling.

	325 MHz Single-Spoke		500 MHz Double-Spoke	
	Q_{ext1}	Q_{ext2}	Q_{ext1}	Q_{ext2}
Required	7.8×10^9	2×10^{11}	1.5×10^{10}	2×10^{11}
Calibrated	6×10^9	2×10^{11}	1.15×10^{10}	2.5×10^{11}
Measured	5×10^9	1.75×10^{11}	9.5×10^9	1.83×10^{11}

11.3 GRADIENT MEASUREMENTS

Perhaps the most cited metric of cavity performance is the measure of the intrinsic quality factor Q_0 as a function of the accelerating gradient E_{acc} . One limiting factor to cavity performance occurs when features on the surface produce an intense, directed electric field which can cause electrons to be emitted. These electrons can in turn impact on the cavity surface and produce heat. This is known as field emission and leads to a degradation of Q_0 . Another typical limiting factor is cavity quenching. This occurs when the surface magnetic field rises enough to create normal conducting areas which leads to a drastic drop in Q_0 . Both of these situations can be minimized, if not eliminated altogether, by proper treatment of the cavity surface.

What we are interested in measuring is E_{acc} , Q_0 , and Q_{ext2} . To initially determine these values, after the losses in the cables have been accounted for in the measurement software, what is known as a decay measurement is carried out. This is usually done in pulsed operation with a width long enough to allow the energy to completely empty out of the cavity. The decay time is calculated as

$$\tau = \frac{Q_L}{\omega_0}, \quad (166)$$

where ω_0 is the cavity frequency. Calculating τ then allows us to determine the value of Q_L . During these pulsed decay measurements, the coupling of the input probe Q_{ext1} is also determined by viewing the crystal detector reading of the reflected power on an oscilloscope. Examples of this are shown in Fig. 120.

The topmost trace is how the forward, or incident power would appear in pulsed operation. Below that we show how the reflected power would behave during such a pulse if the input probe were critically coupled to the cavity, i.e. $\beta = 1$. The reflected

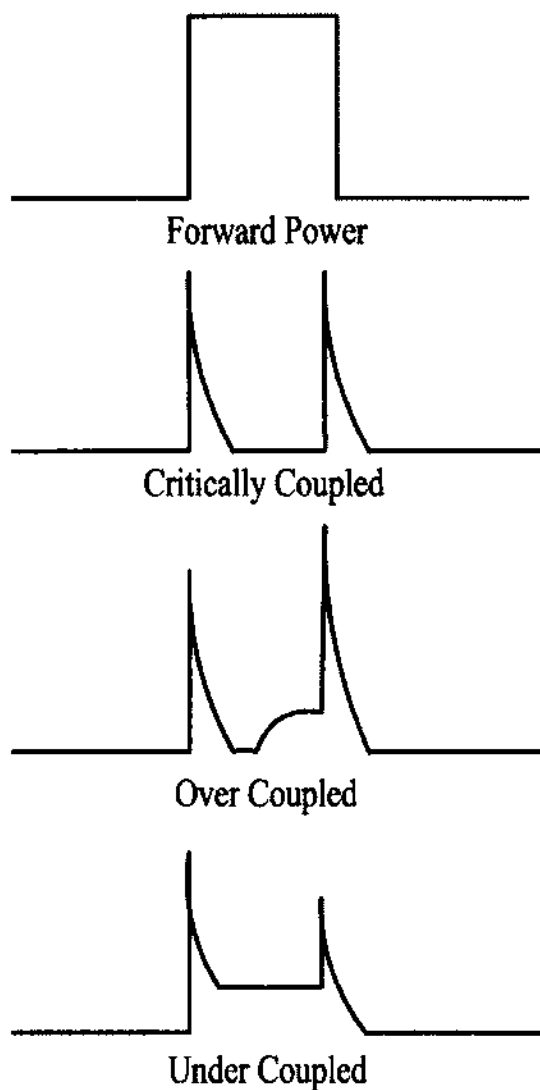


FIG. 120: Various coupling schemes. The top shows the forward power during pulsed operation. Below are examples of how the reflected power reading would look when the input probe is critically coupled, over coupled, and under coupled.

power can be described by [159]

$$P_r(t) = P_i \left(1 - \frac{4\beta}{(1+\beta)^2} (1 - \exp^{-t/2\tau})^2 - \frac{4\beta}{(1+\beta)} (1 - \exp^{-t/2\tau}) \exp^{-t/2\tau} \right), \quad (167)$$

where τ is the decay time given in Eq. (166), β is the coupling coefficient, and t is elapsed time. Equation (167) describes the behavior of the various curves in Fig. 120 quite nicely. If we focus on the initial decay, we find that the different couplings appear as shown in Fig. 121.

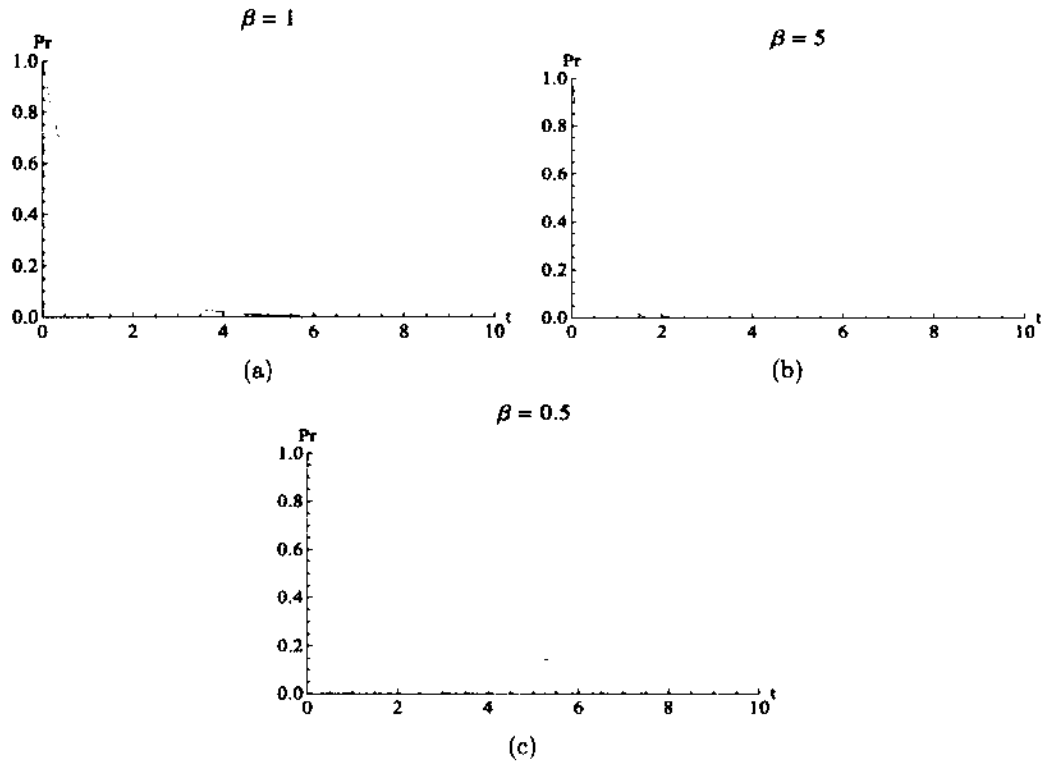


FIG. 121: Reflected power as a function of time for (a) critically coupled, (b) over-coupled, and (c) undercoupled.

Once the decay time has been used to determine the Q_L and the coupling β of the input probe, this can be combined with the crystal detector values of the forward, reflected, and transmitted power to calculate Q_0 . The accelerating electric field then follows from

$$E_{acc} = \sqrt{P_{loss} Q_0 \frac{(\tau/Q)}{L}}, \quad (168)$$

where L is the reference length ($(3/2)\beta_0\lambda$ for a double-spoke and $\beta_0\lambda$ for a single-spoke), and (r/Q) is the geometric shunt impedance per unit reference length. Finally, Q_{ext2} is found to be

$$Q_{ext2} = E^2 P_t \frac{L}{(r/Q)}. \quad (169)$$

With Q_{ext} determined in pulse mode operation, the test can be carried out in continuous wave (cw) mode and the calculation of E and Q_0 become more straightforward,

$$E_{acc} = \sqrt{P_{trans} Q_{ext2} \frac{(r/Q)}{L}} \quad (170)$$

$$Q_0 = E_{acc}^2 P_{loss} \frac{L}{(r/Q)}. \quad (171)$$

11.3.1 325 MHZ SINGLE-SPOKE CAVITY

The initial tests of the 325 MHz single-spoke cavity exhibited soft multipacting barriers which were predicted quite accurately by Track3P (within the SLAC ACE3P code suite [105]). Below 2.5 MV/m, abundant multipacting activity was expected and it was indeed observed, as shown in Fig. 122. In addition, we can see small dips in the Q_0 at 4 K around 4 and 6 MV/m. These agree with simulations. After a relatively short amount of processing, it was found that these barriers could be eliminated.

The single-spoke cavity suffered from abundant field emission, which limited the gradient to roughly 8 MV/m at 2 K, corresponding to $E_p \approx 30$ MV/m and $B_p \approx 50$ mT.

Helium processing is a technique which has been shown to help reduce field emission, although the exact mechanism is still not completely clear [160]. Helium is inside a cavity under vacuum. The pressure is then raised to just below that suitable for rf discharge, where the cavity is then operated at high power.

It is thought that this produces such a high local current that the helium is ionized and forms a plasma which heats and melts the source, provides microscopically directed helium ion bombardment of the source, or enhances the local field to the point of drawing out current densities sufficient to explode the emitter [161].

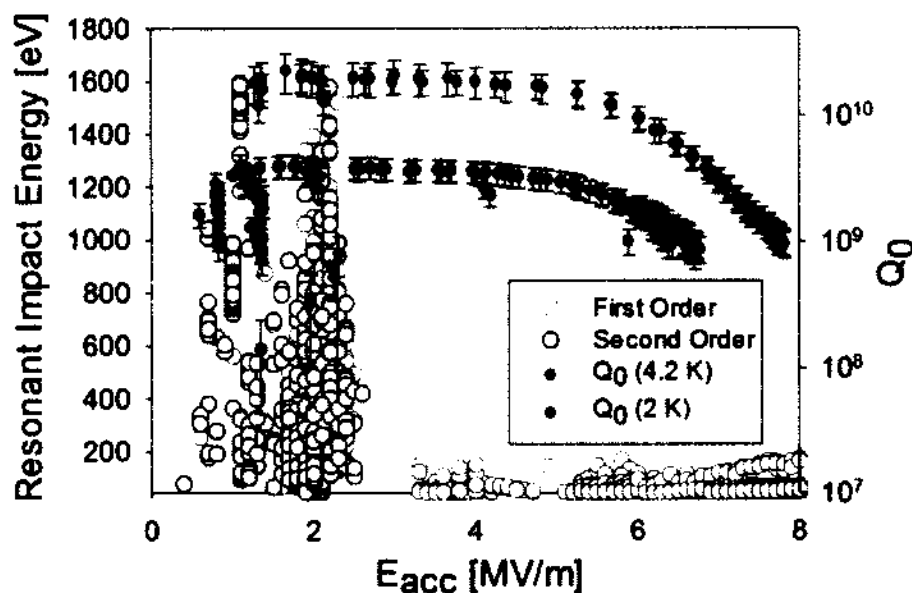


FIG. 122: 325 MHz single-spoke cavity initial test results showing simulated multi-pacting events.

To accomplish the helium processing, the following method was used. The gas was supplied to the cavity by first isolating the vacuum of the cavity/teststand system. A tee was inserted above the dewar lid with one end going to the helium gas, one to the roughing pump, and the third going to an isolation valve on the dewar lid. A Residual Gas Analyzer (RGA) was at the location of the roughing pump (with one vacuum pressure gauge) and another gauge was monitoring the pressure of the cavity/teststand below the isolation valve. The helium used was from a standard tank (not high-purity) so a filter was used between the tank and a needle valve. Figure 123 shows the setup.

The He pressure desired was 10^{-6} - 10^{-5} Torr, which is below the discharge level. On the first attempt, the pressure reached was higher ($\sim 10^{-4}$), which caused the gas to discharge at the input coupler such that no power could be delivered to the cavity. The cavity was then pumped down overnight. Once the pressure was within range, rf power was applied. The next step is to operate the cavity at the highest field possible, which is typically in the heavy field emission regime. The duty cycle

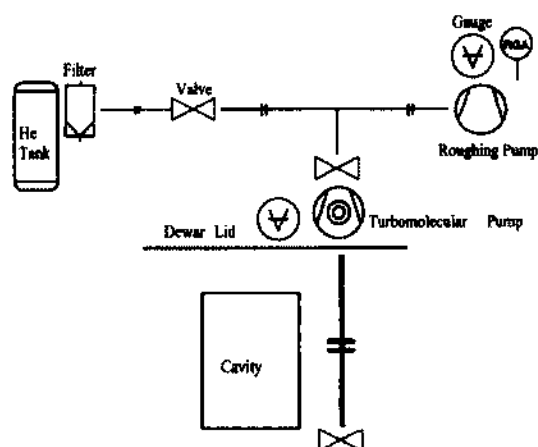


FIG. 123: Schematic diagram of the setup used for helium processing.

is then adjusted so that thermal stability can be maintained. What follows is that field emitted electrons will ionize the helium gas, these ions will then stream back to the emitting sites, thus bombarding the emitter(s).

In Fig. 124, it is clear that the achievable gradient improved. There appears to be a slight degradation of the 2 K Q_0 at low field, which would imply that the surface resistance increased. This effect is hardly noticeable at 4 K, where the surface resistance is dominated by R_{BCS} so that a change of a few $n\Omega$ would only contribute to a few percent increase/decrease in Q_0 .

One possible contributor is that the surface of the cavity had a number of stains (possibly from insufficient rinsing after chemical etching) which could not be eliminated through high pressure rinsing alone. Also, because of the large size of the cavity, a production-quality HPR could only be done through the beam pipes. The parts of the spoke and outer conductor that could not be reached, therefore, had to be rinsed manually through the cleaning ports.

After the initial tests, the cavity was shipped back to Niowave to receive additional etching in hopes that the residue could be removed. Most was removed, however, there was still at least one stain that we could see. For this second round of testing, the cavity received an ultrasonic cleaning, HPR, and 48 hour 120° C bake.

When the cavity was cooled to 4.2 K, we noticed that the Q_0 was much lower than in the previous test. In Fig. 125, we can see that the 4.2 K Q_0 is less than one third the previous value (9×10^8 vs. 3×10^9). The cavity was then cooled to 2 K

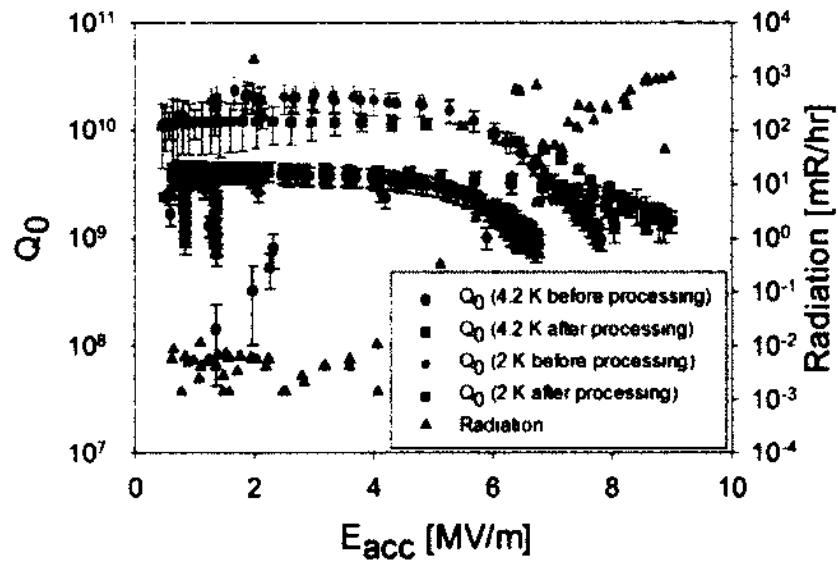


FIG. 124: 325 MHz single-spoke cavity test results before and after helium processing.

and tested again. As can be seen by the red dots in Fig. 125, the Q_0 barely changed (1×10^9). It can also be seen that the errors in Q_0 measurements are larger than in the previous test. This is because the Q_0 was substantially lower than the values of Q_{ext1} and Q_{ext2} , which led to errors of roughly 25%.

Even at 7 MV/m, we were not limited by field emission. Instead, the necessary input power was so high because the coupler was significantly undercoupled. This led to the reflected power being high enough to risk damaging the cables, so the test was halted.

After the tests were complete and the cavity was removed from the dewar, it was discovered that the magnetic field compensation coil was not functioning properly. The contribution to the residual resistance due to the external magnetic field is

$$R_{mag} = \left(\frac{B_{ext}}{2B_{c2}} \right) R_n, \quad (172)$$

where B_{ext} is the external magnetic field, B_{c2} is the critical magnetic field, and R_n is the surface resistance in the normal state. An estimate for niobium with $RRR = 300$ and $R_n \approx 1.5\text{m}\Omega$ at 1 GHz is given in [46] as

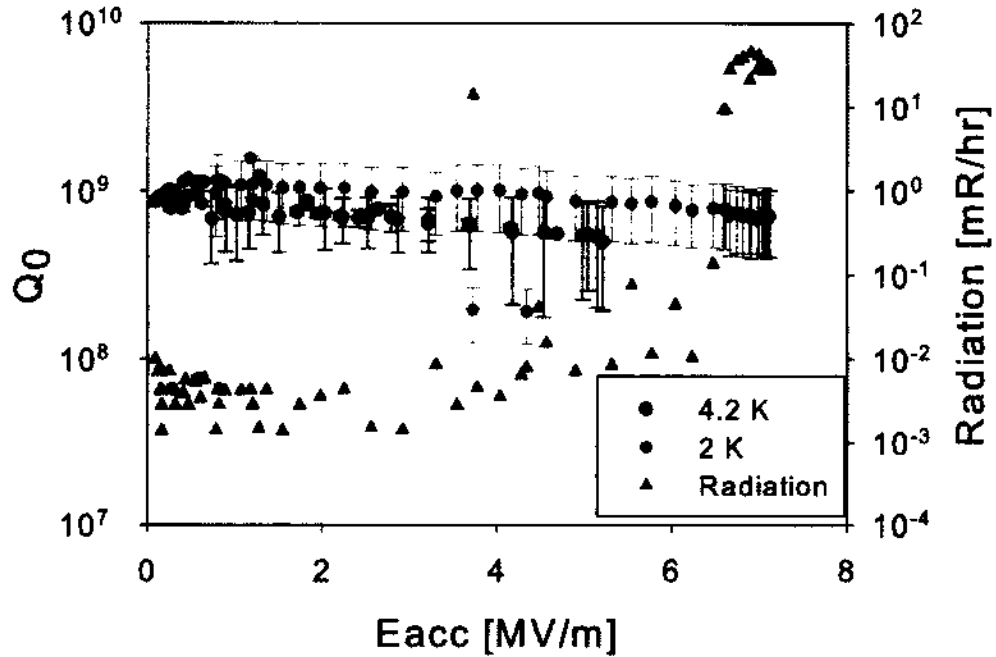


FIG. 125: 325 MHz single-spoke cavity test results after the second light etching done at Niowave.

$$R_{mag} = 0.3(n\Omega)B_{ext}(mOe)\sqrt{f(GHz)}. \quad (173)$$

With this in mind, we then measured the magnetic field in the dewar over the area where the cavity sits. Figure 126 shows that the uncompensated field ranges between 1350 mG and 460 mG. Also, when the field was compensated according to the standard setting at Jefferson Lab for dewar 5, the field in that region was between 16 and 27 mG. We then adjusted the current to the compensation coil and achieved a field of less than 3 mG throughout the cavity region.

With the Q_0 value in Fig. 125 of 10^9 , we can estimate the surface resistance to be roughly $182 \text{ n}\Omega$. Further, with the average uncompensated magnetic field given in Fig. 126 of 1 G, we can estimate the additional residual resistivity to be $171 \text{ n}\Omega$. This leaves $11 \text{ n}\Omega$ of surface resistance, 0.7 of which is from R_{BCS} at this temperature and frequency. The improvements we made to the external magnetic field can be estimated to reduce the residual resistance by roughly $4 \text{ n}\Omega$.

After the compensation coil was working properly and the field was reduced, the

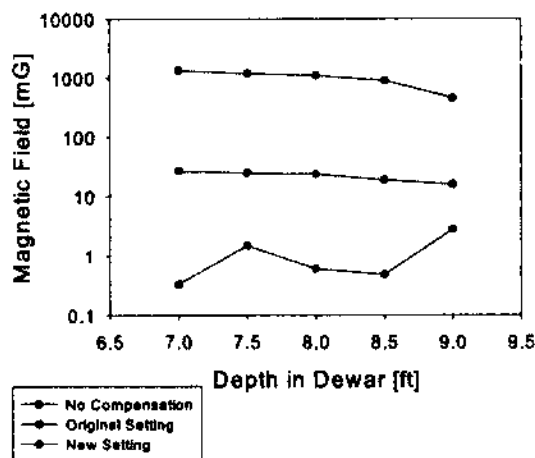


FIG. 126: Magnetic field in the region of the dewar where the cavity sits.

cavity was tested again. We can see in Fig. 127 that Q_0 improved a great deal from previous tests. However, it is also clear that field emission was still a problem which severely limits the achievable gradient. Two rounds of helium processing were employed which yielded substantial improvement of 42%.

11.3.2 500 MHZ DOUBLE-SPOKE CAVITY

The gradient measurements of the 500 MHz, $\beta_0 = 1$ double-spoke cavity are shown in Fig. 128. The low-field Q_0 of this cavity are 2.5×10^9 and 1.1×10^{10} for 4.2 K and 2.3 K, respectively. A cold leak appeared when the cavity was cooled. Because of this, the cavity vacuum was in the 10^{-7} range and prevented cooling to 2 K. A great deal of multipacting between 1 and 4 MV/m had to be processed, which is consistent with the Track3P simulations.

A gradient of 4 MV/m (4.2 K) and 3.7 MV/m (2.3 K) marked the onset of oscillatory behavior. The inset of Fig. 128 (b) shows the decay time of the transmitted power during such an oscillation. After tens of milliseconds, the transmitted power goes to zero, signalling a loss of superconductivity.

The breakdown of superconductivity happens when the surface magnetic field exceeds the critical field. A defect on the surface, e.g. an impurity in the niobium or a flatness imperfection, has a thermal conductivity which is different than that within the bulk niobium. If the thermal conductivity between the defect and bulk

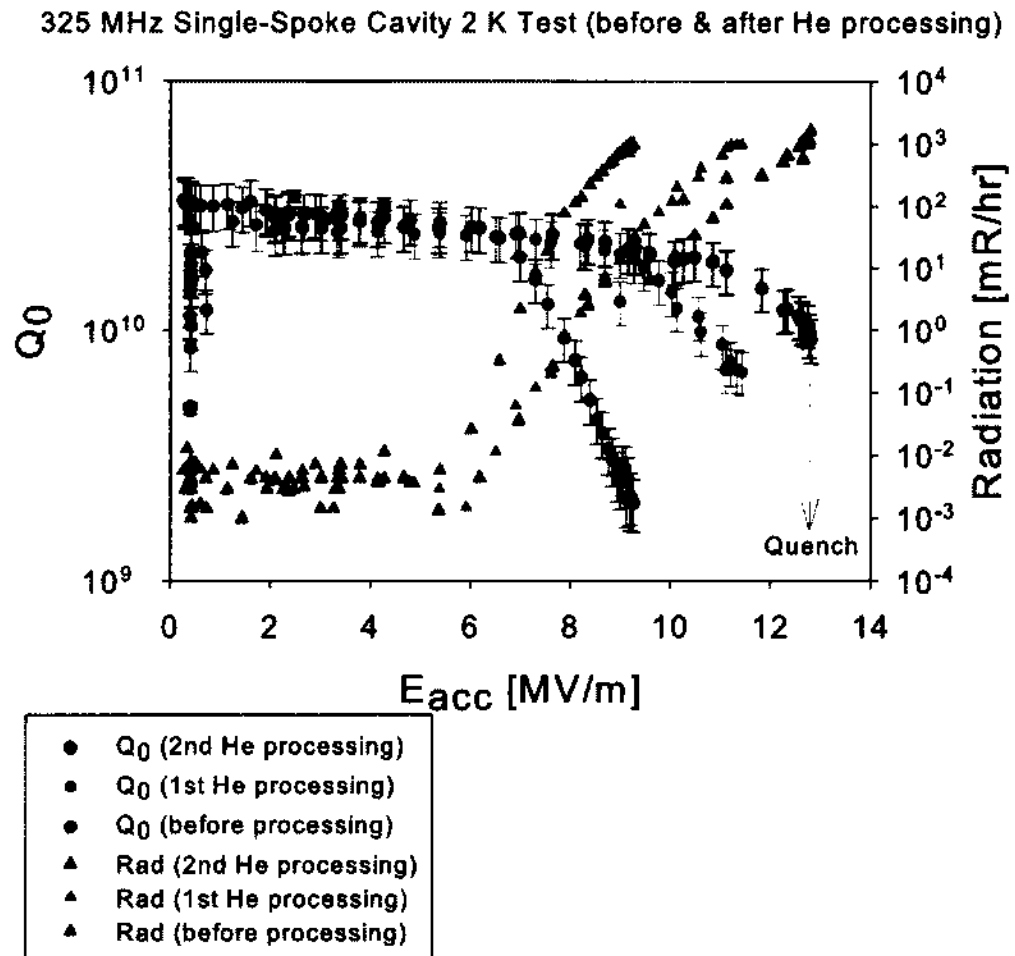


FIG. 127: Comparison of 2 K tests before and after helium processing.

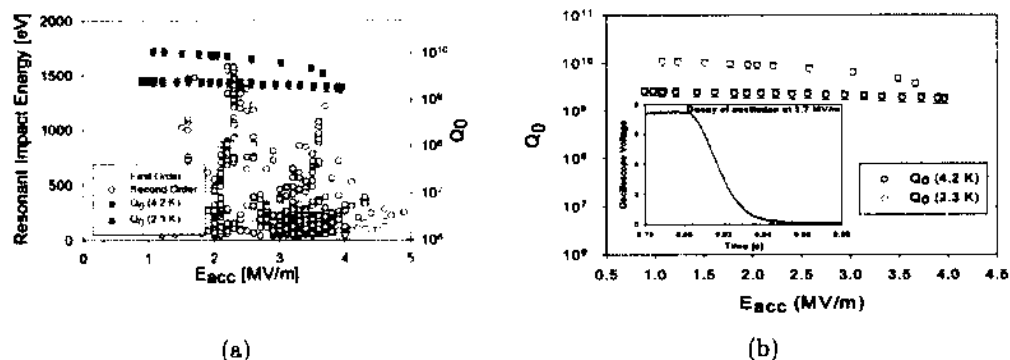


FIG. 128: 500 MHz double-spoke cavity gradient measurements (a) with multipacting region shown and (b) without. The inset of (b) shows an oscilloscope trace of the transmitted power at 2.3 K and 3.7 MV/m.

material is good, the heat generated at the site of the defect can be dissipated in the surrounding niobium, thus increasing the local temperature. As long as the temperature stays below T_c , superconductivity is preserved and a quench will be avoided. If and when the temperature of the defect and the surrounding bulk niobium exceeds T_c , superconductivity will be lost and the now normal conducting niobium will dissipate several joules (~ 10 at 4 MV/m) of energy stored in the cavity causing thermal breakdown. Since the electromagnetic field stored in the cavity is dissipated as ohmic heating, the location of the defect can cool very quickly. Superconductivity will be restored, the defect and the surrounding bulk niobium will begin to heat, and the quench process starts again.

Multipacting, as discussed in Chapter 3, does cause heating which can lead to thermal breakdown. In addition to the heating, the electrons liberated through this process consume any additional power being delivered to the cavity. Both of these effects are consistent with observations and simulations show that the field levels for which these oscillations begin are within the predicted range. However, a great deal of multipacting happened below 4 MV/m (as predicted by simulation) which was processed. Unlike the other multipacting levels, this one showed no measurable sign of improvement even after spending several hours at this field level. While multipacting cannot be completely ruled out, the observations suggest that it is unlikely.

The leak in the cavity vacuum was traced to staining on a port flange. All the

flanges were polished, the pickup probe feed through was replaced, and the cavity was prepared for re-testing without additional chemical processing. The Q_{ext} of the input and pickup probes were now measured to be 1×10^{10} and 1.5×10^{10} , respectively.

On the second 4 K test a great deal of multipacting was encountered which was persistent and difficult to process. The levels were found at the following gradients (in MV/m): 0.57, 0.71, 0.91, 1.03, 1.29, 2.7, 3.09, 3.25, and 4.5. The low gradient levels (0.57 MV/m-1.29 MV/m) were difficult to process because when more power was delivered to the cavity, the gradient would just jump to a higher level instead of transferring that power to the electrons resonant at that level. Also, to process the multipacting, more and more incident power is required. This will cause the gradient to oscillate between different multipacting levels. At the higher levels (3.09 MV/m-4.5 MV/m), the amount of incident power required to continue processing is so high (~ 200 W) that the cavity will quench.

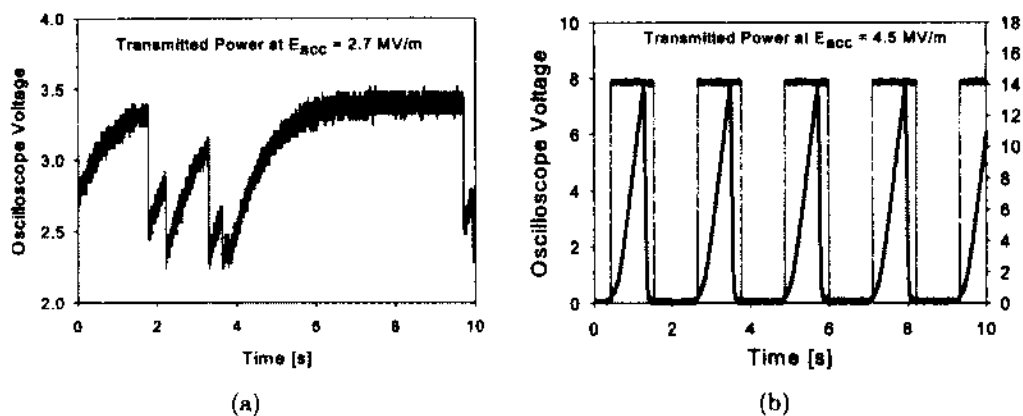


FIG. 129: (a) Typical transmitted power P_t during a multipacting event compared to (b) an actual quench where the black curve is P_t while the red curve is the pulsed incident power P_{inc} .

In Fig. 129, the transmitted power P_t as read by the oscilloscope is shown for two different events. At 2.7 MV/m, we observe multipacting where P_t oscillates between multiple levels. Note that some processing is happening when P_t remains at a constant level before dropping to some other multipacting level. In contrast, Fig. 129 (b) shows what appears to be an actual quench event. This occurs at a gradient of 4.5 MV/m and we note that P_t drops to zero, which implies that a large fraction of the cavity has become normal conducting. The incident power P_{inc} is being pulsed,

but the pulse width is greater than the time it takes for P_t to rise and fall.

The gradient measurements for this second, and final 4 K test are shown in Fig. 130 (a) along with the previous results. What we find is that the intrinsic quality factor Q_0 is slightly higher than before, but within the error of the previous measurements. The test on October 9, 2014 also shows a few of the multipacting levels.

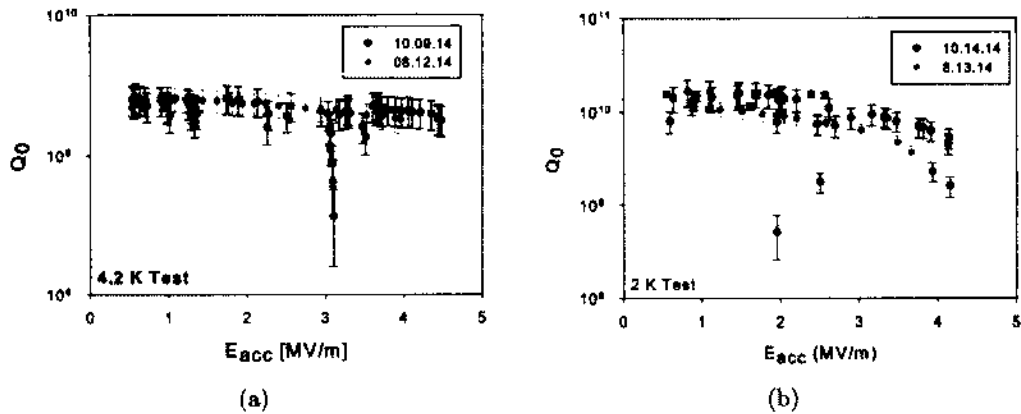


FIG. 130: Gradient measurements of the 500 MHz double-spoke cavity taken at (a) 4.2 K and (b) 2 K.

After the 4 K tests were completed, the cavity was then cooled to 2 K (possible now because there was no leak). As is usual, during the cool-down the Q_0 and frequency were periodically recorded for R_{res} estimates. Figure 130 (b) shows the results of this test alongside the previous results.

For all of the tests, both before and after repairing the leak, the radiation was quite low. The maximum radiation monitored was only in the 10^{-2} mR/hr range, which is much lower than that measured with the 325 MHz single-spoke cavity. For this reason, we have not plotted it in Figs. 128 and 130.

11.4 SURFACE RESISTANCE MEASUREMENTS

The surface resistance of a superconducting cavity can be described using BCS theory as $R_s = R_{BCS} + R_{res}$, where R_{BCS} is temperature and frequency dependent, while R_{res} depends on the quality of the surface [67]. The geometry factor $G = Q_0 R_s$ is known (given in Tab. 9) and R_{BCS} can be calculated with Eq. (25). As the cavity is cooled, periodic measurements of Q_0 , frequency, and temperature are recorded.

These are then used to fit with the following

$$R_s[n\Omega] = \frac{a}{T[K]} \exp\left[-\frac{b}{T[K]}\right] + R_{res}, \quad (174)$$

where a and b are constants. For each measurement, the electric field gradient must be held as close to constant as possible. As the temperature decreases, Q_0 increases. This results in a higher electric field gradient for a given input power. Therefore, for each measurement, the power should be adjusted such that the electric field gradient is maintained at a constant level. This drifting of the gradient, when not properly compensated, can provide a source of error.

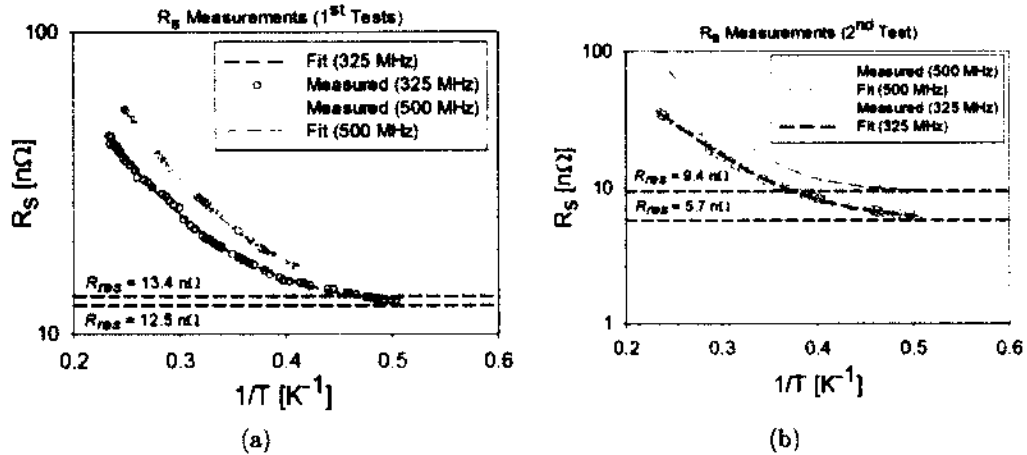


FIG. 131: Surface resistance measurements and fitting for both cavities during the (a) first tests and (b) second tests.

Perhaps the most important precaution needed is to ensure that the cavity is not sitting in a multipacting level when the data collection is to take place. If this happens the Q_0 value will be artificially low, resulting in an overestimate of the residual resistance.

The surface resistance vs. $1/T$ for both cavities is shown in Fig. 131. The residual resistance of the 325 MHz single-spoke cavity is 12.5 nΩ. The 500 MHz double-spoke cavity was more difficult to estimate in this way because the cold leak only allowed for cooling to a safe temperature of 2.3 K. It is clear in Fig. 131 that the 500 MHz cavity R_s curve does not go to a high enough $1/T$ value to get a reliable estimate for R_{res} . The value obtained, while on the high side, gives $R_{res} = 13.4$ nΩ.

Prior to the second test, the 500 MHz double-spoke cavity was not chemically processed any further. The leak was fixed, it received both the manual and production quality HPR, low temperature baking, and clean room assembly. We would expect that without exposing a “new” surface, R_s should be relatively close between successive tests. However, as we saw in Fig. 131 (a), the fit was not a good estimate given that the temperature could not be brought to 2 K. In this second test, we found the residual resistance to be 9.4 n Ω for the 500 MHz cavity and 5.5 n Ω for the 325 MHz cavity.

11.5 PRESSURE SENSITIVITY

Both of the cavities discussed here were intended to only be tested in the VTA, and therefore only need to withstand a vacuum load of 1.1 atm. The 325 MHz single-spoke cavity is unable to withstand this pressure without some form of external reinforcement. A simple structure was designed and fabricated by Niowave, Inc. to stiffen the cavity sufficiently for testing (shown in Fig. 132).

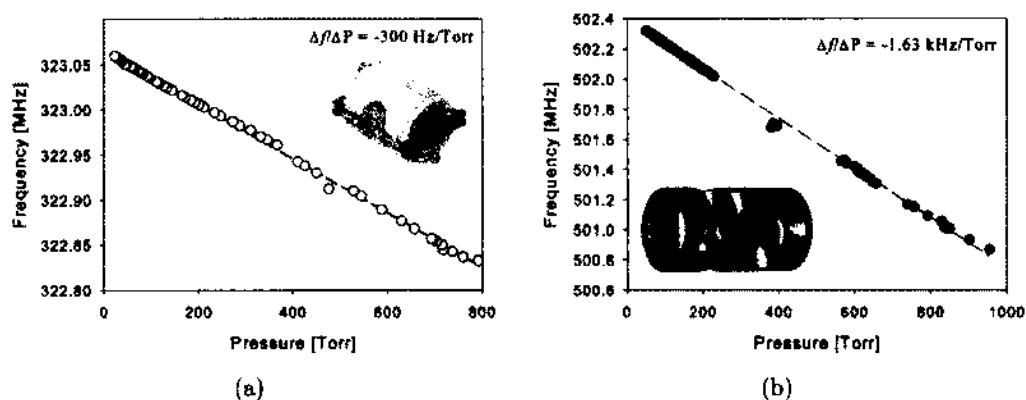


FIG. 132: Pressure sensitivity of the (a) 325 MHz single-spoke cavity and the (b) 500 MHz double-spoke cavity.

The 500 MHz double-spoke cavity reaction to various pressures was simulated as outlined in Chapter 7. It was known that stiffening would be necessary at 2.2 atm, but at the pressure required to test in the VTA (1.1 atm), this should not have been required. However, there were factors not included in the simulations. The first is the stretching of the niobium as the end caps were formed. This stretching caused the material to be thinner in the reentrant region of the end caps (as noted in Tab.

26). The second is that the bulk etching was far from uniform which resulted in the end cap reentrant areas have more material removed. Both of these factors led to the areas of the cavity most susceptible to plastic deformation to also be the thinnest.

CHAPTER 12

CONCLUSION

High-velocity spoke cavities can be optimized to provide low power dissipation (high shunt impedance) and surface fields which allow for reasonable accelerating gradients. The minimization of the surface fields by increasing the dimensions of the spoke base causes the cavity to lose some of its compactness, but still maintains transverse dimensions of at least 20% less than that of a TM cavity at the same frequency. Depending on the application (e.g. if only low gradients are required) a cylindrical or longitudinally oriented spoke can be used to regain the full compactness advantage.

These cavities also have a more complicated geometry than their TM counterparts, and as such, have a large number of variable parameters that allow for customization for a variety of applications. This makes it difficult to determine a few simple rules for optimization, but here we have identified the most influential parameters and how they can be used to reduce the peak surface fields and increase the shunt impedance. If the fields are to maintain a proper balance, for the geometries studied here, it was found that the trade-off between normalized fields and shunt impedance are at least 10%. In other words, the shunt impedance of a cavity can be increased by at least 10% at the expense of increasing the normalized electric and magnetic fields by 10%.

The optimized multi-spoke geometries presented here led to all accelerating gaps being of similar length because the transversely oriented spoke base is large enough to decrease the cell-to-cell coupling. If we define this coupling as in [46],

$$k = \frac{\frac{1}{2} [(f^{(N)})^2 - (f^{(1)})^2]}{2(f^1)^2 - (f^N)^2 [1 - \cos[\pi/N]]}, \quad (175)$$

where f^1 is the frequency of the fundamental mode and f^N is the frequency of the nearest mode ($N = 2$). Figure 133 is an example of how the cell-to-cell coupling k decreases as the transverse dimension of the spoke base increase, and stays relatively the same as the base dimensions of a longitudinally oriented spoke increase. This is an important point that should be emphasized again. A longitudinal spoke base

orientation allows for a much larger mode separation and slightly smaller diameter, which is why, for some applications, they may be preferable to the transverse geometries presented here.

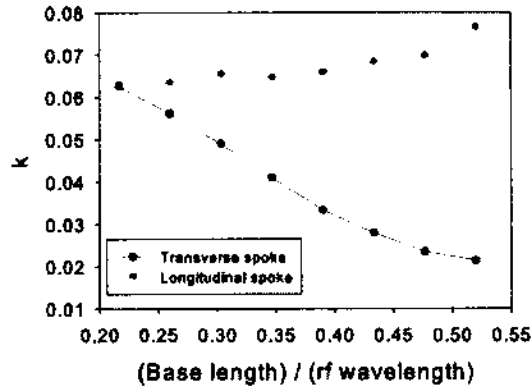


FIG. 133: Coupling k between cells of an optimized $\beta_0 = 0.82$, 325 MHz two-spoke cavity. The left-most point is common to both curves since it represents a cylindrical spoke base.

This decreased cell-to-cell coupling accompanying an optimized spoke design would suggest that perhaps tuning to achieve field profile balance could become important, as it is in TM cavities. However, even with only a few percent coupling, the tolerance to manufacturing inaccuracies is quite high. Figure 134 (a) shows that with a 3% coupling, a 5 mm imbalance in the length of the end cells leads to a 10% difference in the on-axis electric field while for as much as a 1 cm imbalance, there is only a 16% difference in the fields.

By comparison, with a cylindrical spoke geometry, the tolerance to manufacturing inaccuracies is even higher, as would be expected. Figure 134 (b) shows how the on-axis longitudinal electric field changes in each cell when one of the end cells is reduced in length by 5 mm and 10 mm. As opposed to the field profiles in Fig. 134 (a), where the voltage acquired in each cell is roughly equal, it is clear, as was previously mentioned, the voltage gained in the center cell of the cylindrical spoke cavity (Fig. 134 (b)) is roughly twice that of the end cells. The cell-to-cell coupling in this cavity, by Eq. 175, is 6%. The imbalance of the fields is now 3.8% and 7.3% for a cell length difference of 5 mm and 10 mm, respectively.

What can be concluded from the design and optimization procedure is that spoke cavities are highly customizable. Optimizing them for low peak surface fields and high

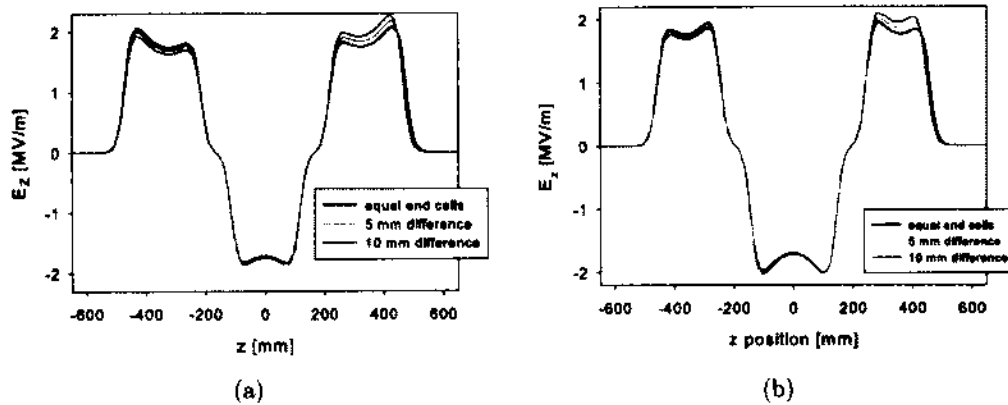


FIG. 134: On-axis electric field profile for equal end cell lengths and an imbalance of 5 and 10 mm, for (a) an optimized 325 MHz, double spoke cavity and (b) for a double-spoke cavity with cylindrical spokes, operating at 325 MHz. The imbalances are created by adding length to one end cell while keeping the spokes fixed.

shunt impedance does lessen some of their advantages outlined previously—their transverse size increases and the separation between the fundamental and nearest modes decreases—however those advantages are still present, and can be quite significant depending on the application.

Until now, there has been very little examination of higher order modes in superconducting spoke cavities of any velocity regime [20]. Here we have developed the tools necessary for characterizing these modes and evaluating their potential to increase power dissipation and cause beam instabilities. Specifically, the effects within a compact machine such as a light source have been investigated and it has been determined that a moderate damping will be necessary.

These are some of the first high-velocity superconducting spoke cavities fabricated and tested. Both the $\beta_0 = 1$ and 0.82 cavities reached a high Q_0 and were found to have a reasonable residual resistance. Multipacting was encountered, but easily processed. The single-spoke cavity was initially limited by field emission while the double-spoke may be experiencing some sort of thermal breakdown. Each of the limitations are not fundamental to the design.

The multipacting simulations presented here are the most detailed, to date. Not only have we identified the emitting and resonant locations for various field gradients, we have found a correlation between the cavity frequency and the possible difficulty

in processing the low gradient multipactors. Also, we have found geometric parameters which can lessen the energy, and hence secondary emission yield, of resonant multipactors.

In all of the cryogenic tests, multipacting was encountered in roughly the same gradient ranges predicted by simulation. The 325 MHz single-spoke cavity processing was accomplished in a fairly short time. The 500 MHz double-spoke cavity was more difficult, as would be expected from the severe enhancement shown in simulation at gradients up to 4.5 MV/m. While it took several hours, we were able to process away these low gradient multipacting levels. This implies that, at least for these frequencies, multipacting is unlikely to be a limiting factor.

The studies undertaken here have demonstrated that both single- and multi-spoke cavities are indeed feasible options for specific applications. In fact, various programs are now aggressively pursuing projects using high-velocity spoke cavities [162–164].

BIBLIOGRAPHY

- [1] M. Kuntze, in *Proc. of the 1973 Particle Accelerator Conference* (San Francisco, CA, USA, March, 1973) p. 49.
- [2] I. Ben-Zvi and J. M. Brennan, *Nucl. Instrm. Meth.* **212**, 73 (1983).
- [3] J. R. Delayen, *Nucl. Instrm. Meth.* **B40/41**, 892 (1989).
- [4] J. R. Delayen, C. L. Bohn, and C. T. Roche, *Nucl. Instrm. Meth.* **B56/57**, 1025 (1991).
- [5] J. R. Delayen and C. L. Bohn, in *Proc. 4th Workshop on RF Superconductivity* (Tsukuba, Japan, August, 1989) p. 427.
- [6] J. R. Delayen, W. L. Kennedy, and C. T. Roche, in *Proc. of the 1992 Linear Accelerator Conference* (Ottawa, Canada, August, 1992) p. 695.
- [7] K. W. Shepard, P. N. Ostroumov, and J. R. Delayen, *Phys. Rev. ST Accel. Beams* **6**, 080101 (2003).
- [8] J. R. Delayen, in *Proc. 10th Workshop on RF Superconductivity* (Tsukuba, Japan, September, 2001) pp. 152–161.
- [9] M. Kelly, in *13th International Workshop on RF Superconductivity* (Beijing, China, 2007) p. WE302.
- [10] S. Belomestnykh and V. Shemelin, in *Proc. of the 12th International Workshop on RF Superconductivity* (Ithaca, NY, USA, July, 2005) pp. 060424–03.
- [11] Z. Conway, K. W. Shepard, M. P. Kelly, J. D. Fuerst, and M. Kedzie, in *Proc. of the 12th Workshop on RF Superconductivity* (Ithaca, NY, USA, 2005).
- [12] Z. Conway, M. P. Kelly, S. I. Sharamentov, K. W. Shepard, G. K. Davis, J. R. Delayen, and L. R. Doolittle, in *Proc. of the 13th Workshop on RF Superconductivity* (Beijing, China, 2007) p. WEP67.
- [13] M. P. Kelly, K. W. Shepard, and M. Kedzie, in *Proc. of the 10th Workshop on RF Superconductivity* (Tsukuba, Japan, September, 2001) p. PT017.

- [14] M. Kelly, in *Proc. of the 2006 Linear Accelerator Conference* (Knoxville, TN, USA, 2006) p. MO3002.
- [15] J. R. Delayen, in *Proc. of the 2010 Linear Accelerator Conference* (Tsukuba, Japan, 2010).
- [16] E. Zaplatin, in *Proc. of the 12th International Workshop on RF Superconductivity* (Ithaca, NY, USA, July, 2005) p. TUP41.
- [17] F. L. Krawczyk, K. C. D. Chan, R. C. Gentzlinger, W. B. Haynes, J. P. Kelley, D. I. Montoya, E. N. Schmierer, D. L. Schrange, and T. Tajima, in *Proc. of the 8th European Particle Accelerator Conference* (Paris, France, June 3-7, 2002) pp. 272-274.
- [18] K. W. Shepard, Z. A. Conway, J. D. Fuerst, M. P. Kelly, G. J. Waldschmidt, and A. M. Porcellato, in *Proc. of the 2007 Particle Accelerator Conference* (Abuquerque, New Mexico, USA, June 25-29, 2007) p. WEPMN087.
- [19] E. Rampnoux, L. Berthelot, P. Blanche, S. Bousson, J. Lesrel, L. Lukovac, and G. Olry, in *Proc. of the 2009 Particle Accelerator Conference* (Vancouver, BC, Canada, May 4-8, 2009) p. WE5PFP029.
- [20] Xiao Yong-Chaun et al, *Chinese Phys. C* **35**, 188 (2011).
- [21] K. W. Shepard, M. P. Kelly, J. D. Fuerst, M. Kedzie, and Z. A. Conway, in *Proc. of the 2005 Particle Accelerator Conference* (Knoxville, TN, USA, 2005) p. 4338.
- [22] J. D. Fuerst, M. Kedzie, M. P. Kelly, and K. W. Shepard, in *Proc. of the 2003 Particle Accelerator Conference* (Portland, Oregon, 2003) p. TPAB044.
- [23] T. Tajima et al, in *Proc. of the 2003 Particle Accelerator Conference* (Portland, Oregon, May 12-16, 2003) p. TPAB063.
- [24] G. Olry et al, in *Proc. of the 12th International Workshop on RF Superconductivity* (Ithaca, NY, USA, July 2006) p. TuP38.
- [25] G. Olry et al, in *Proc. of 11th Workshop on RF Superconductivity* (Lubeck/Travemunder, Germany, September 8-12, 2003) p. TUP55.

- [26] I. Gonin et al, in *Proc. of the 2008 Linear Accelerator Conference* (Victoria, BC, Canada, 2008) p. THP030.
- [27] L. Ristori et al, in *Proc. of the 14th International Conference on RF Superconductivity* (Berlin, Germany, September, 2009) p. THPPO011.
- [28] W. S. Graves, W. Brown, F. X. Kaertner, and D. E. Moncton, *NIM A* **608**, S103 (2009).
- [29] T. Satogata, K. Deitrick, J. R. Delayen, B. R. P. Gamage, K. Hernandez-Chahin, C. S. Hopper, G. Krafft, and R. G. Olave, in *Proc. of the 4th International Particle Accelerator Conference* (Shanghai, China, May 12-17, 2013) pp. 2292–2294.
- [30] T. Hayakawa, N. Kikuzawa, R. Hajima, T. Shizuma, N. Nishimori, M. Fujiwara, and M. Seya, *NIM A* **621**, 695 (2010).
- [31] M. Sawamura, R. Hajima, R. Nagai, and N. Nishimori, in *Proc. of the 15th International Conference on RF Superconductivity* (Chicago, IL, USA, July, 2011) p. MOPO036.
- [32] P. Ostroumov, in *Presentation at the 4th Meeting of the ESSS Linac Reference Group* (2009).
- [33] C. S. Hopper and J. R. Delayen, *Phys. Rev. ST Accel. Beams* **16**, 102001 (2013).
- [34] E. O. Lawrence and M. S. Livingston, *Phys. Rev.* **40**, 19 (1932).
- [35] D. Sloan and E. Lawrence, *Phys. Rev.* **38**, 2021 (1931).
- [36] E. L. Hubbard et. al., *Rev. Sci. Instrum.* **32**, 621 (1961).
- [37] D. A. Bromley, *Nucl. Instrum. Methods* **122**, 1 (1974).
- [38] R. Middleton, *Nucl. Instrum. Methods* **122**, 35 (1974).
- [39] M. V. Isaila et. al., *Int. Conf. Heavy Ion Sources* **19**, 207 (1972).
- [40] H. A. Grunder and G. R. Lambertson, in *Proc. of the 8th International Conference on High Energy Accelerators* (Geneva, 1971).

- [41] M. R. Buckner, in *Proc. of the 1999 International Conference of Future Nuclear Systems* (Jackson Hole, WY, USA, August, 1999).
- [42] C. Wang, M.H. Eisa, H. Shen, L. Zhong, M. Yang, Y. Mi, H. Yao, and Z.Y. Zhou, in *Proc. of 18th International Conference on Ion Beam Analysis* (Hyderabad, India, September, 2000).
- [43] J. R. Alonso, in *Proc. of 7th International Conference on Nucleus-Nucleus Collisions* (Strasbourg, France, July 3-7, 2000).
- [44] R. L. Martin, in *Proc. of the Second European Particle Accelerator Conference* (Nice, France, June, 1990) pp. 1802–1804.
- [45] E. Pedroni, in *Proc. of 7th European Particle Accelerator Conference* (Vienna, Austria, June, 2000) p. 240.
- [46] H. Padamsee, J. Knobloch, and T. Hays, *RF Superconductivity for Accelerators* (John Wiley and Sons, Inc., 1998).
- [47] J. R. Delayen, in *Proc. of the 26th International Linear Accelerator Conference* (Tel-Aviv, Israel, September, 2012) p. 758.
- [48] M. Tinkham, *Introduction to Superconductivity* (Dover Publications, Inc., 1996).
- [49] M. Cyrot, *Rep. Prog. Phys.* **36**, 103 (1973).
- [50] H. K. Onnes, *Commun. Phys. Lab. Univ. Leiden* **120b** (April, 1911).
- [51] H. K. Onnes, *Commun. Phys. Lab. Univ. Leiden* **122b** (May, 1911).
- [52] W. Meissner and R. Ochsenfeld, *Naturwiss.* **21**, 787 (1933).
- [53] F. and H. London, *Proc. Roy. Soc. London* **A149**, 71 (1935).
- [54] A. B. Pippard, *Proc. Roy. Soc. London* **A216**, 547 (1953).
- [55] V. Ginzburg and L. D. Landau, *Zh. Eksp. Teor. Fiz.* **20**, 1064 (1950).
- [56] A. A. Abrikosov, *Soviet Phys. JETP* **5**, 1174 (1957).
- [57] J. Daunt and K. Mendelssohn, *Proc. Roy. Soc.* **A185**, 225 (1946).

- [58] J. Bardeen, *Phys. Rev.* **97**, 1724 (1955).
- [59] L. N. Cooper, *Phys. Rev.* **104**, 1189 (1956).
- [60] P. Bauer, N. Solyak, G.L. Ciovati, G. Ereemeev, A. Gurevich, L. Lilje, and B. Visentin, in *Proc. of the 12th International Workshop on RF Superconductivity* (Ithaca, NY, USA, 2005) pp. 223–229.
- [61] N. Ashcroft and N. D. Mermin, *Solid State Physics* (Brooks/Cole Cengage Learning, 1976).
- [62] L. Gor'kov, *Soviet Phys. JETP* **36(9)**, 1364 (1959).
- [63] H. London, *Proc. Roy. Soc.* **176**, 522 (1940).
- [64] A. B. Pippard, *Proc. Roy. Soc. London* **191**, 370 (1947).
- [65] A. B. Pippard, *Proc. Roy. Soc. London* **191**, 385 (1947).
- [66] A. B. Pippard, *Proc. Roy. Soc. London* **191**, 399 (1947).
- [67] J. Bardeen, L. N. Cooper, and J. R. Schrieffer, *Phys. Rev.* **108**, 1175 (1957).
- [68] D. Mattis and J. Bardeen, *Phys. Rev.* **111**, 412 (1958).
- [69] J. Matricon and D. Saint-James, *Phys. Lett.* **24A**, 241 (1967).
- [70] W.M. Fairbank, J. M. Pierce, and P.B. Wilson, in *Proc. Eighth International Conference of Low Temperature Physics* (London, 1963) p. 324.
- [71] A. Banford and G. Stafford, *J. Nucl. Energy, Part C Plasma Phys.* **3**, 287 (1961).
- [72] L. Rinderer, J. Rufenacht, and A. Susini, *Physics Letters* **2**, 119 (1962).
- [73] J. Rufenacht and L. Rinderer, in *Proc. Eighth International Conference of Low Temperature Physics* (London, 1963) pp. 326–327.
- [74] J. Rufenacht and L. Rinderer, *Zeitschrift für Angewandte Mathematik und Physik* **15**, 192 (1964).
- [75] T.I. Smith, H.A. Schwettman, and W.M. Fairbank, et al, in *Proc. of the 1966 Linear Accelerator Conference* (Los Alamos, NM, 1966).

- [76] J. Turneaure and N. Viet, *Appl. Phys. Letters* **16**, 333 (1970).
- [77] S. Y. Lee, *Accelerator Physics* (World Scientific Pub., 2004).
- [78] T. P. Wangler, *RF Linear Accelerators* (John Wiley and Sons, Inc., 2008).
- [79] U. R. et. al., *Nucl. Instrum. Methods Phys. Res. Sect. A* **415**, 229 (1998).
- [80] J. R. Delayen, in *Proc. of the 11th Workshop on RF Superconductivity* (Travemunde, Germany, September, 2003).
- [81] K. Saito, <http://www.lns.cornell.edu/public/SRF2005/program.html> (2005).
- [82] M. Pekeler, *Untersuchungen der feldbegrenzenden Mechanismen in supraleitenden Niob-Resonatoren*, Ph.D. thesis, University of Hamburg (DESY) (1996).
- [83] J. Knobloch, *IEEE Trans. Appl. Supercond.* **9**, 1016 (1999).
- [84] B. Bonin, in *CERN Accelerator School, Superconductivity in Particle Accelerators* (Meyrin, Switzerland, 1996) pp. CERN 96-03.
- [85] R. H. Fowler and L. Nordheim, *Proc. Roy. Soc. London A* **119**, 173 (1928).
- [86] R. E. Burgess, H. Kroemer, and J. M. Houston, *Phys. Rev.* **90**, 515 (1953).
- [87] J. W. Gadzuk and E. W. Plummer, *Rev. of Modern Phys.* **45**, 487 (1973).
- [88] V. Balandin, R. Brinkmann, K. Flottmann, and N. Golubeva, *Studies of Electromagnetic Cascade Showers Development in the TESLA Main Linac Initiated by Electron Field Emission in RF Cavities*, Tech. Rep. 2003-10 (TESLA Report, 2013).
- [89] R. J. Noer, *Appl. Phys. A* **28**, 1 (1982).
- [90] B. Bonin and R. Roeth, in *Proc. of the 5th Workshop on RF Superconductivity* (Hamburg, Germany, 1991) pp. 210-244.
- [91] K. Schulze, O. Bach, D. Lupton, and F. Schreiber, in *Niobium- Proceedings of the International Symposium* (Warrendale, PA, USA, 1981).
- [92] R.E. Laxdal, R.J. Dawson, K. Fong, A. Grassellino, M. Marchetto, AlK. Mitra, T. Ries, V. Zvyagintsev, and R. Edinger, in *Proc. of the 24th Linear Accelerator Conference* (Victoria, British Columbia, Canada, 2008) pp. 777-779.

- [93] H. Safa, in *Proc. of the 8th Workshop on Superconductivity* (Padua, Italy, 1997) pp. 814–821.
- [94] CST, <http://www.cst.com/Content/Products/MWS/Overview.aspx> (2013).
- [95] L. C. Maier, Jr. and J. C. Slater, *J. Appl. Phys.* **23**, 68 (1952).
- [96] H. Hahn and H. J. Halama, *IEEE Trans. Microwave Theory and Techniques* **MIT-16**, 20 (1968).
- [97] P. McIntosh, in *Proc. of the Fourth European Particle Accelerator Conference* (London, U.K., 1994) pp. 1283–1285.
- [98] J. Byrd, in *USPAS & CCAST* (Beijing, China, 1998).
- [99] H. Padamsee and A. Joshi, *J. Appl. Phys.* **50**, 1112 (1979).
- [100] G. F. Dionne, *J. Appl Phys.* **46**, 3347 (1975).
- [101] C. S. Hopper, R. G. Olave, and J. R. Delayen, in *Proc. of the 3rd International Particle Accelerator Conference* (New Orleans, LA USA, May, 2012) p. WEPPC103.
- [102] F. L. Krawczyk, in *Proc. 10th Workshop on RF Superconductivity* (Tsukuba, Japan, J2001).
- [103] R. P. P. Fernandes and G. Bienvenu, *Nucl. Instrum. Methods A* **320**, 1 (1992).
- [104] P. Fabbriatore, G. Gemme, R. Musenich, R. Parodi and S. Pittaluga, in *Proc. of the 7th Workshop on RF Superconductivity* (Gif sur Yvette, 1995).
- [105] K. Ko et al., in *Proc. of the 2010 Linear Accelerator Conference* (Tsukuba, Japan, 2010) pp. 1028–1032, <http://accelconf.web.cern.ch/accelconf/LINAC2010/papers/fr101.pdf>.
- [106] L. Ge, K. Ko, K. Lee, Z. Li, C. Ng, and L. Xiao, in *Proc. of 11th International Computational Accelerator Physics Conference* (Rostock-Warnemünde, Germany, 2012) pp. 54–58.
- [107] L-Q. Lee, Z. Li, C. Ng, and K. Ko, *Omega3P: A Parallel Finite-Element Eigenmode Analysis Code for Accelerator Cavities*, Tech. Rep. SLAC-PUB-13529 (SLAC National Accelerator Laboratory, 2009).

- [108] L. Ge, K. Ko, Z. Li, C. Ng, and L. Xiao, in *Proc. of North American Particle Accelerator Conference* (Pasadena, Ca, USA, 2013) pp. 216–218.
- [109] W. K. H. Panofsky and W. A. Wenzel, *Rev. Sci. Instrum.* **27**, 967 (1956).
- [110] M. J. Browman, in *Proc. of the 1993 Particle Accelerator Conference* (Washington D.C., USA, 1993) pp. 800–802.
- [111] A. W. Chao, *Physics of Collective Beam Instabilities in High Energy Accelerators* (Wiley, New York, 1993).
- [112] C. L. Bohn and J. R. Delayen, *Phys. Rev. A* **45**, 5964 (1992).
- [113] J. R. Delayen, *Phys. Rev. ST Accel. Beams* **6**, 084402 (2003).
- [114] P. Wilson, *Transient Beam Loading in Electron-Positron Storage Rings*, Tech. Rep. CERN-ISR-TH/78-23 (CERN, 1978).
- [115] P. Craievich, *Short-Range Longitudinal and Transverse Wakefield Effects in FERMI@elettra FEL Project*, Ph.D. thesis, Technische Universiteit Eindhoven (2010).
- [116] K. Mittag, H. Schwettman, and H. D. Schwarz, in *Proc. of the Proton Linear Accelerator Conference* (Los Alamos, NM, USA, 1972) pp. 131–139.
- [117] C. Tennant, F. Hannon, F. He, J. Mammosser, and R. Rimmer, *Regenerative Beam Breakup in a 400 MHz Cavity*, Tech. Rep. JLAB-TN-13-016 (Thomas Jefferson National Accelerator Facility, 2013).
- [118] Andy Wolski, <http://cas.web.cern.ch/cas/Belgium-2009/Lectures/PDFs/Wolski-1.pdf> (2009).
- [119] J. Barranco Garcia et al., in *Proceedings of the 3rd International Particle Accelerator Conference* (New Orleans, LA, 2012) p. 1873.
- [120] Z. Conway, M. P. Kelly, P. N. Ostroumov, and K. W. Shepard, in *Proc. of the 15th International Conference on RF Superconductivity* (Chicago, IL USA, 2011) pp. 943–245.

- [121] D. Passarelli, M. H. Awida, I. V. Gonin, L. Ristori, and V. P. Yakovlev, in *Proc. of the Third International Particle Accelerator Conference* (New Orleans, LA USA, 2012) pp. 2339–2341.
- [122] J. C. Slater, *Rev. Mod. Phys.* **18**, 441 (1946).
- [123] D. Meidlinger, in *Proc. of the 14th International Conference on RF Superconductivity* (Berling, Germany, 2009) pp. 523–527.
- [124] T. L. Grimm, W. Hartung, T. Kandil, H. Khalil, J. Popielarski, J. Vincent, and R.C. York, in *Proc. of the 22nd International Linear Accelerator Conference* (Lübeck, Germany, August, 2004) pp. 763–765.
- [125] J. R. Delayen and L. H. Harwood, in *Proc. of the 2003 Particle Accelerator Conference* (Portland, Oregon, May 12-16, 2003) pp. 992–994.
- [126] J. R. Delayen, S. U. DeSilva, and C. S. Hopper, in *Proc. of the 2011 Particle Accelerator Conference* (New York, NY, 2011) p. TUP100.
- [127] J. J. Wlodarczak, *Fundamental Power Coupler Development for Low-Beta Superconducting Cavities*, Master's thesis, Michigan State University, East Lansing, MI (2008).
- [128] S. Malloy and R. Ainsworth and R. Ruber, in *Proc. of the Second International Particle Accelerator Conference* (San Sebastian, Spain, 2011) pp. 190–192.
- [129] C. Darve, M. Eshraqi, M. Lindroos, D. McGinnis, S. Malloy, P. Bosland, and S. Busson, in *Proc. of the 16th International Conference on RF Superconductivity* (Paris, France, September, 2013) pp. 77–79.
- [130] G. Devanz et al., in *Proc. of the 16th International Conference on RF Superconductivity* (Paris, France, September, 2013) pp. 1212–1216.
- [131] Z. Li, P. Cheng, H. Geng, Z. Guo, Y. He, C. Meng, H. Ouyang, S. Pei, B. Sun, J. Sun, J. Tang, F. Yan, Y. Yang, C. Zhang, and Z. Yang, *Phys. Rev. ST Accel. Beams* **16** (2013).
- [132] J. R. Alonso, in *Proc. of 7th International Conference on Nucleus-Nucleus Collisions* (Strasbourg, France, July 3-7, 2000).

- [133] H. Padamsee, *RF Superconductivity: Volume II: Science, Technology and Applications* (Wiley-VCH, 2009).
- [134] J. Sekutowicz, in *Proc. of the Third Workshop on RF Superconductivity* (Argonne National Laboratory, Illinois, USA, 1987) pp. 597–604.
- [135] P. Kneisel and G. Ciovati and G. R. Myneeni and G. Wu and J. Sekutowicz, in *Proc. of the 2005 Particle Accelerator Conference* (Knoxville, Tennessee, USA, 2005) pp. 4012–4014.
- [136] J. Sekutowicz, in *Proc. of the 2006 Linear Accelerator Conference* (Knoxville, Tennessee USA, 2006) pp. 506–510.
- [137] S. Belomestnykh, in *USPAS* (Albuquerque, NM, USA, 2009).
- [138] T.J. Peterson, H.F. Carter, M.H. Foley, A.L. Klebaner, T.H. Nicol, T.M. Page, J.C. Theilacker, R.H. Wands, M.L. Wong-Squires, and G. Wu, *Niobium as a Pressure Vessel Material*, Tech. Rep. FERMILAB-PUB-09-320-TD (Fermi National Accelerator Laboratory, 2009).
- [139] G. Cheng and M. Wiseman, *C100 Cryomodule Niobium Cavity Structural Analysis*, Tech. Rep. JLAB-TN-10-001 (Thomas Jefferson National Accelerator Facility, 2010).
- [140] G. Olry, J.-L. Biarrotte, T. Junquera, J. Lesrel, C. Mielot, H. Suagnac, P. Maccioni, and M. Gauthier, in *Proc. of the 8th European Accelerator Conference* (Paris, France, June 3-7, 2002) pp. 2271–2273.
- [141] B. Mustapha, P. Ostroumov, and Z. Conway, in *Proc. of the 3rd International Particle Accelerator Conference* (New Orleans, LA, USA, May, 2012) p. WEPPC037.
- [142] R. G. Olave, J. R. Delayen, and C. S. Hopper, in *Proc. of the 2012 Linear Accelerator Conference* (Tel Aviv, Israel, September 9-14, 2012) p. MOPB072.
- [143] P. Berrutti et al, in *Proc. of the International Particle Accelerator Conference* (New Orleans, LA, USA, May 20-25, 2012) pp. 2318–2320.
- [144] G. Myneni and P. Kneisel, *High RRR Niobium Material Studies*, Tech. Rep. JLAB-TN-02-01 (Thomas Jefferson National Accelerator Facility, 2001).

- [145] H. Padamsee, *Supercond. Sci. Technol.* **14**, 28 (2001).
- [146] Niowave Inc., <http://www.niowaveinc.com> (2005).
- [147] HyeKyoung Park, C. S. Hopper, and J. R. Delayen, in *Proc. of the 27th Linear Accelerator Conference* (Geneva, Switzerland, September, 2014).
- [148] K. Wang and R. Reeber, *Material Science and Engineering* **R23**, 101 (1998).
- [149] P. Kneisel, K. Saito, and R. Parodi, in *Proc. of the Eighth Workshop on RF Superconductivity* (Abano Terme, 1997) pp. 463–471.
- [150] P. Kneisel, in *Proc. of the First Workshop on RF Superconductivity* (Karlsruhe, Germany, July, 1980) pp. 27–40.
- [151] A. Burrill, *Buffer Chemical Polishing and RF Testing of the 56 MHz SRF Cavity*, Tech. Rep. BNL-82024-2009-IR (Brookhaven National Laboratory, 2009).
- [152] P. Kneisel, B. Lewis, and L. Turlington, in *Proc. of the Sixth Workshop on RF Superconductivity* (Newport News, VA, USA, 1993) pp. 628–636.
- [153] K. Saito, H. Miwa, K. Kurosawa, P. Kneisel, S. Noguchi, E. Kako, M. Ono, T. Shishido, and T. Suzuki, in *Proc. of the Sixth Workshop on RF Superconductivity* (Newport News, VA, USA, 1993) pp. 1151–1159.
- [154] G. Ciovati, P. Kneisel, G. Myneni, and W. A. Lanford, in *Proc. of the 11th Workshop on RF Superconductivity* (Lubeck/Travemunder, Germany, September 8-12, 2003) pp. 562–571.
- [155] C. Reece, B. Almeida, T. Powers, and J. Susta, in *Proc. of the IEEE Particle Accelerator Conference* (San Francisco, CA, USA, May, 1991) pp. 2325–2327.
- [156] T. Powers, in *Proc. of the 12th International Workshop on RF Superconductivity* (Ithaca, NY, USA, July, 2005) pp. 40–70.
- [157] C. Hovater, in *Proc. of the 24th Linear Accelerator Conference* (Victoria, British Columbia, Canada, 2008) pp. 704–708.
- [158] J. Delayen, *Phase and Amplitude Stabilization of Superconducting Resonators*, Ph.D. thesis, California Institute of Technology (1978).

- [159] J. Knobloch, *Basic Concepts of Measurements Made on Superconducting RF Cavities*, Tech. Rep. SRF 910927-07 (Laboratory of Nuclear Studies, Cornell University, 1991).
- [160] H. A. Schwettman, J. P. Turneaure, and R. F. Waites, *J. Appl. Phys.* **45**, 914 (1974).
- [161] J. Knobloch and H. Padamsee, *Particle Accelerators* **53**, 53 (1996).
- [162] M. Sawamura, R. Hajima, R. Nagai, T. Kubo, H. Fujisawa, Y. Iwashita, and H. Tongu, in *Proc. of the 5th International Particle Accelerator Conference* (Dresden, Germany, 2014) pp. 1946–1948.
- [163] V. Goryashko, A. Opanasenko, and V. Zhaunerchyk, in *Proc. of the 36th International Free Electron Laser Conference* (Basel, Switzerland, 2014) p. TUP079.
- [164] Department of Energy, <http://science.energy.gov/sbir/highlights/2014/sbir-2014-04-d/> (2014).

APPENDIX

Here we list the characteristic properties of the significant HOMs for both the 500 MHz, $\beta_0 = 1$ double-spoke cavity and the 325 MHz, $\beta_0 = 0.82$ single-spoke cavity. The values of Q_0 are calculated by

$$Q_0 = \frac{G}{R_s},$$

where $R_s = R_{BCS} + R_{res}$ where R_{BCS} is given by

$$R_{BCS} = \frac{2 \times 10^{-4}}{T} \left(\frac{f_n}{1.5} \right)^2 \exp(-17.67/T),$$

where T is the temperature (4.2 K in this case) and f_n is the HOM frequency.

TABLE 28: HOM Properties: 500 MHz, $\beta_0 = 1$ Double-Spoke Cavity

Accelerating Modes			Deflecting Modes		
Frequency	R/Q	Q_0	Frequency	R/Q	Q_0
[MHz]	[Ω]	[10^8]	[MHz]	[Ω]	[10^8]
508.76	7.50	20.1	650.31	35.8	13.0
529.57	1.11	20.6	748.92	18.5	13.7
672.22	4.73	11.5	763.18	14.0	15.6
707.47	3.14	13.1	867.64	72.7	14.6
822.51	3.09	12.2	896.86	27.9	12.6
873.56	42.4	13.0	911.03	26.8	12.9
936.67	36.0	11.9	960.96	16.6	12.1
1086.1	20.6	11.7	1030.3	27.0	8.76
1105.0	3.23	11.6	1105.2	4.96	10.2
1213.2	4.02	10.8	1147.2	16.0	9.75
1256.4	6.88	9.87	1161.2	12.1	8.89

TABLE 28

Accelerating Modes			Deflecting Modes		
Frequency	R/Q	Q ₀	Frequency	R/Q	Q ₀
[MHz]	[Ω]	[10 ⁸]	[MHz]	[Ω]	[10 ⁸]
1259.8	12.1	9.55	1191.5	1.16	9.48
1309.8	38.3	8.82	1251.9	6.54	9.67
1323.2	4.00	9.25	1330.9	1.64	7.61
1339.0	8.33	7.65	1355.6	1.12	10.4
1356.0	6.06	8.86	1467.8	3.60	7.52
1357.8	39.1	7.49	1481.7	2.98	7.85
1367.4	2.11	7.55	1505.7	1.02	8.10
1381.6	65.8	6.89	1593.7	3.22	7.42
1403.0	35.7	7.02	1595.7	2.00	6.99
1493.3	2.56	7.22	1606.8	2.59	6.40
1507.3	3.61	6.50	1617.1	5.34	7.01
1537.8	2.85	6.75	1644.8	1.98	6.39
1609.2	2.94	7.96	1660.9	4.21	6.35
1695.9	2.15	7.52	1668.4	9.29	6.38
1704.2	2.42	5.59	1686.9	21.0	5.91
1732.3	1.84	7.45	1701.9	9.31	6.10
1741.4	4.60	8.71	1744.7	8.22	6.66
1820.8	8.66	6.20	1775.4	3.89	5.90
1827.9	7.51	5.82	1804.0	1.68	7.01
1828.5	7.63	5.13	1843.5	4.34	6.48
1878.7	3.21	6.01	1873.2	2.20	7.87
1887.8	1.01	6.36	1950.0	2.34	5.38
1972.9	3.69	5.86	1959.8	1.10	5.99
1982.6	2.34	6.82	1976.9	5.23	6.26
1988.4	16.9	7.18	1995.4	2.73	6.01
1998.7	13.8	5.47	2022.1	6.37	6.40
2016.1	1.53	5.35	2027.2	1.00	6.58
2017.1	2.97	5.27	2034.0	3.24	7.14
2082.3	1.40	6.06	2046.6	1.52	6.34

TABLE 28

Accelerating Modes			Deflecting Modes		
Frequency	R/Q	Q ₀	Frequency	R/Q	Q ₀
[MHz]	[Ω]	[10 ⁸]	[MHz]	[Ω]	[10 ⁸]
2110.4	2.27	5.13	2061.3	2.54	5.81
2187.8	3.25	6.48	2065.2	2.37	5.77
2246.9	1.19	4.89	2085.1	1.82	6.42
2264.3	1.06	3.81	2112.9	3.48	4.93
2283.3	2.00	4.58	2165.3	1.10	5.34
2307.8	1.14	5.24	2178.5	1.51	4.98
2336.5	8.88	6.09	2189.6	1.21	5.47
2343.6	2.59	4.79	2215.4	1.08	4.68
2394.0	1.47	4.75	2284.3	1.02	5.15
2418.8	8.00	5.40	2294.0	9.75	4.50
2432.3	1.47	4.75	2297.7	2.04	5.27
2434.5	5.76	3.93	2306.6	8.76	4.97
2440.9	2.48	5.40	2317.3	1.95	5.44
2455.7	1.40	3.82	2333.7	1.05	5.29
2522.4	3.20	4.76	2345.9	3.04	4.96
2530.4	5.88	4.36	2371.9	1.19	4.04
2531.5	1.73	4.47	2414.1	1.82	4.41
2558.1	2.24	4.45	2451.2	2.32	4.50
2563.5	1.48	4.33	2456.9	1.41	4.85
2606.5	1.23	4.37	2471.3	1.34	4.66
2643.0	1.58	4.04	2499.3	1.10	4.69
2673.0	1.94	3.75	2502.4	2.95	4.38
2676.6	1.37	3.78	2962.8	1.15	3.41
2714.4	2.18	4.50	2978.8	1.56	3.59
2771.9	1.13	3.99	3028.9	1.45	4.26
2803.4	1.37	3.91	3057.4	1.00	3.81
2821.8	2.63	4.68	3065.1	1.69	3.76
2830.9	1.89	4.40	3107.9	1.13	3.94
2841.3	3.81	3.89	3108.5	1.39	3.43

TABLE 28

Accelerating Modes			Deflecting Modes		
Frequency	R/Q	Q ₀	Frequency	R/Q	Q ₀
[MHz]	[Ω]	[10 ⁸]	[MHz]	[Ω]	[10 ⁸]
2851.2	1.83	3.91	3117.9	2.19	3.45
2855.5	7.33	3.84	3297.9	1.57	3.50
2860.8	1.53	4.44	3311.8	2.50	3.12
2867.0	12.7	4.36	3321.0	1.49	3.28
2868.3	6.00	4.05	3352.5	1.80	3.00
2878.1	2.23	4.27	3361.2	1.97	2.84
2881.2	1.17	4.23	-	-	-
2892.8	1.98	3.97	-	-	-
2907.9	3.37	3.80	-	-	-
2958.5	1.45	4.62	-	-	-
2983.3	3.31	3.42	-	-	-
3062.3	3.59	4.19	-	-	-
3075.4	1.20	3.66	-	-	-
3189.4	2.22	3.62	-	-	-
3208.2	2.09	3.72	-	-	-
3211.0	1.14	3.21	-	-	-
3221.0	1.14	2.60	-	-	-
3232.9	1.28	3.50	-	-	-
3258.2	2.24	3.66	-	-	-
3265.8	1.50	3.17	-	-	-
3357.3	1.20	3.82	-	-	-
3445.8	1.10	2.93	-	-	-
3468.3	1.28	3.02	-	-	-

TABLE 29: HOM Properties: 325 MHz, $\beta_0 = 0.82$
Single-Spoke Cavity

Accelerating Modes			Deflecting Modes		
Frequency	R/Q	Q ₀	Frequency	R/Q	Q ₀
[MHz]	[Ω]	[10 ⁹]	[MHz]	[Ω]	[10 ⁹]
337.75	8.66	3.46	452.40	14.4	2.35
692.57	21.7	1.86	531.26	38.8	2.25
703.22	4.68	2.00	555.84	24.8	2.50
827.65	1.51	2.15	594.71	20.2	2.71
852.37	1.34	1.50	626.08	29.5	2.93
860.49	23.6	1.72	846.64	1.32	1.61
874.87	2.80	1.94	848.94	1.29	1.63
933.86	1.24	1.71	886.87	8.16	1.56
935.23	30.2	1.21	946.44	1.55	1.25
964.17	10.9	1.44	1201.6	22.5	1.09
976.14	3.81	1.28	1537.7	1.09	0.76
1047.0	1.10	1.53	1582.6	9.38	1.18
1293.4	2.35	1.23	1602.3	2.10	0.87
1321.2	1.53	1.07	1876.2	1.05	0.92
1372.9	1.14	0.98	-	-	-
1374.9	5.69	1.06	-	-	-
1387.3	2.74	0.95	-	-	-
1517.4	1.08	0.96	-	-	-
1664.8	1.38	0.80	-	-	-
1864.5	6.15	0.80	-	-	-
1915.9	1.32	0.94	-	-	-
2062.7	1.15	0.60	-	-	-
2121.7	1.26	0.72	-	-	-

VITA

Christopher Shawn Hopper
Department of Physics
Old Dominion University
Norfolk, VA 23529

Typeset using \LaTeX .